UNIVERSITAT DE VALÈNCIA
Departament de Física Aplicada i Electromagnetisme

Characterisation of single semiconductor nanowires by non-destructive spectroscopies

By

Eleonora Secco

Supervised by:

Dr. Núria Garro Martínez

Programa Oficial de Doctorat en Física 3026

VALÈNCIA, juliol 2015

Ai miei genitori e ai miei nonni... e soprattutto a tutti i miei amici piú cari.

No pain, no gain.

Contents

1 Introduction **1**
1.1 Towards new semiconductor devices based on NWs 2
1.2 Challenging open problems 5
1.2.1 Controlled growth of semiconductor NWs 5
1.2.2 Tunability and quantum efficiency of the emission of GaN/InGaN NWs 7
1.3 Characterisation techniques at the nanoscale 9
1.4 Objectives of the work 10
1.5 Organisation of the work 11

2 Fundamental physical properties of wide band gap semiconductors **13**
2.1 Crystal structure 13
2.1.1 Stacking faults and dislocations 15
2.1.2 Strain in wurtzite crystals 18
2.2 Electronic properties 20
2.2.1 InGaN alloy band gap energy 21
2.2.2 Pyroelectric and piezoelectric effects 22
2.2.3 Quantum confined Stark effect in InGaN/GaN heterostructures 24
2.3 Vibrational properties 26
2.3.1 Phonons 26
2.3.2 Phonons in wurtzite InGaN alloys 29
2.3.3 Effects of the strain on the phonons of wurtzite crystals 29
2.3.4 Surface optical modes 30
2.3.5 SO in a rectangular NW 30

3 Characterisation techniques **35**
3.1 Raman scattering spectroscopy 35
3.1.1 Theoretical background 36
3.1.2 Raman selection rules 41
3.1.3 Experimental apparatus 42
3.2 Surface Enhanced Raman Spectroscopy 43
3.2.1 Plasmon resonaces 44
3.2.2 Enhancement factor 49

3.2.3 Variability of SERS signal 50
3.3 Photoluminescence spectroscopy 51
3.3.1 Experimental apparatus 53
3.4 X-ray spectroscopies 54
3.4.1 Synchrotron facility and beamlines 57
3.4.2 X-ray nanoprobe beamline ID22NI 58

4 Optical characterisation of selective area growth GaN nanowires and nanopyramids 61
4.1 Introduction 62
4.2 SAG nanostructures grown by MBE 62
4.3 GaN nanowires 65
4.3.1 Description of the sample 65
4.3.2 Fundamental characterisation by Raman scattering . 67
4.3.3 Fundamental characterisation by photoluminescence spectroscopy 69
4.3.4 Effects of the mask geometry on the optical properties of SAG GaN nanowires 74
4.3.5 Discussion 77
4.4 GaN nanopyramids 77
4.4.1 Description of the sample 77
4.4.2 Raman scattering characterisation 79
4.4.3 Photoluminescence characterisation 80
4.4.4 Discussion 81

5 Optical and structural characterisation of single GaN/InGaN core-shell nanowires 83
5.1 Introduction 83
5.2 InGaN core-shell nanowires 84
5.2.1 Metal organic chemical vapour deposition 85
5.2.2 Description of the sample 87
5.2.3 InGaN MQWs in individual NWs 88
5.3 Elemental distribution of individual NWs 91
5.3.1 X-ray fluorescence maps 92
5.3.2 Composition of non-polar GaN/InGaN MQWs 96
5.4 Structural properties of individual NWs 97
5.4.1 X-ray diffraction maps of individual NWs 97
5.4.2 X-ray absorption near edge spectroscopy of individual NWs 101
5.4.3 Raman scattering of individual NWs 102
5.5 Optical properties of single NWs 103
5.5.1 Emission of NW ensembles 103
5.5.2 Emission of single NWs 105
5.6 Discussion 107

6 Surface Enhanced Raman Scattering of individual ZnO nanowires decorated with Au nanorods 111
6.1 Introduction 111
6.2 ZnO nanowires 113
6.2.1 ZnO NWs grown by chemical vapour deposition . . . 113
6.2.2 Raman scattering of an ensemble of ZnO NWs 114
6.3 Hybrid ZnO NW - Au nanorods system 114
6.3.1 Synthesis of the Au nanorods 114
6.3.2 Decoration of the ZnO NWs with Au nanorods 116
6.4 SERS of individual hybrid NWs 117
6.4.1 SERS of Au nanorods 118
6.4.2 Raman scattering of single hybrid ZnO NWs 119
6.5 Discussion 124

Conclusions 127

Resumen 131

Acknowledgements 149

Bibliography 151

Chapter 1

Introduction

Semiconductor nanowires (NWs) have a broad range of potential applications in the field of optoelectronics (light-emitting and laser diodes), nano-electronics (logic circuits and field effect transistors), sensing, and energy harvesting (solar cells) [1, 2]. In broad terms, NWs can be described as elongated nanostructures with diameters and lengths typically ranging from tens to hundreds of nanometers and from a few to tens of microns, respectively. Such morphology offers two main advantages in comparison with thin films: on the one hand, an improvement of the crystal quality thanks to a more efficient relaxation of the strain induced by the mismatch with the substrate allowing the growth on a much wider variety of substrates (Si, transparent conductive oxides, etc.); and on the other hand, a large surface to volume ratio and an enhancement of the surface related effects which can be beneficial for many new applications [3, 4].

Many semiconductors have been obtained in the form of NWs by means of different growth techniques and aiming at different applications. Some of the most studied NWs are based on Si, Ge (IV semiconductors), GaAs, GaP, InP, InAs (III-V semiconductors),GaN, AlN, InN (III-nitride semiconductors) ZnS, ZnSe, CdS, CdSe (II-VI semiconductors), ZnO, MgO, SiO_2, CdO (oxides) and also ternary alloys of many of the previously cited binaries [1]. In particular, the materials that will be studied in this thesis, ZnO, GaN, and GaN-based alloys (InGaN) have direct band gaps, covering the range between the ultraviolet and the infrared. The wide band gaps of ZnO (3.40 eV) and GaN (3.41 eV) are favorable for short-wavelength light emitting devices and high-power devices [5,6]. In the case of GaN-based ternary alloys, i.e. InGaN and AlGaN, it is possible to adjust the fundamental band gap from the near infrared (InN) to the ultraviolet (AlN) of the electromagnetic spectrum which suits the requirements of lightning and photovoltaic solar cells. [7, 8].

Furthermore, NWs bearing heterostructures have been obtained [9–11]. This requires an accurate control of the growth techniques. The columnar morphology of this nano-objects allows to obtain heterostructures with

interfaces perpendicular to the NW axis (axial heterostructures) or parallel to it (radial or core-shell heterostructures).

This work has been supported by the NANOWIRING Marie Curie ITN (EU project No. PITN-GA-2010-265073) [12]. NANOWIRING started in November 2010 and ended in October 2014. Several cutting-edge European institutions have been involved for creating a Network in the field of semiconductor NWs. This project focused on the growth, the characterisation, the simulation and the device integration of NWs as building blocks in the field of sensing, optoelectronics, nanoelectronics, and energy harvesting [13–19].

The purpose of this Chapter is to describe some examples of state of the art research in the field of semiconductor NWs and to introduce the main objectives of this Thesis.

1.1 Towards new semiconductor devices based on NWs

Great advances in the implementation of devices based NWs are being achieved in nano-optoelectronics in recent years. GaN and InGaN NWs, for instance, are interesting building blocks in the field of optoelectronics with better properties than 2D heteroepitaxial layers [6]. The energy tunability of the band gap of group-III nitrides and their alloys points at them as the best candidates for the development of laser diodes, solar cells, and high brightness emitting diodes for UV, blue, and white light. Light-emitting diodes (LEDs) based on wurtzite GaN/InGaN axial quantum wells (QWs) have been successfully developed [20, 21], although their efficiency is strongly limited by the internal electric fields generated by the spontaneous and the piezoelectric polarisations characteristic of these materials [22]. An efficient solution to this problem is to grow core-shell QWs along non-polar directions but, despite the big efforts made in this field, obtaining non-polar luminescent layer structures remains difficult [23]. Current research related to GaN/InGaN core-shell NWs is offering very promising results. As an example of state of the art research, *Koester et al.* [24] obtained GaN/InGaN core-shell NW LEDs with high on/off switching rates. They used GaN NWs grown along the c-axis as template for subsequent growth of radial junction orthogonal to the c-direction that should be polarisation free. The GaN/InGaN multiple QW (MQW) core-shell NW LEDs were grown along the m-direction by catalyst-free metal-organic vapor phase epitaxy (MOVPE). The growth is performed on conductive n-Si(111) substrate in order to enable a later array device fabrication using the conductive substrate as the LED cathode. A SEM image of the core-shell NWs and a sketch of the device are shown in Fig. 1.1. Time-resolved electroluminescence showed that the internal electric field was successfully suppressed, and this explains the fast response of the electroluminescence in the gigahertz regime of m-plane

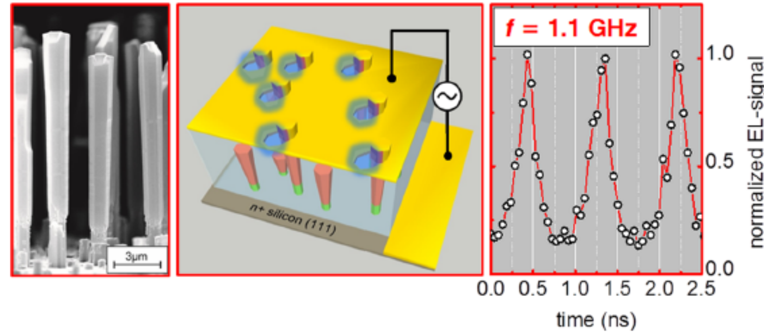

Figure 1.1: Core-shell NW LED grown on Si(111): from left to right, SEM micrograph of the as-grown p-GaN/InGaN MQW(×5)/n-GaN core-shell, sketch of the NW array LED device, and time-resolved electroluminescence signal recorded for $V_{DC} = 8$ V and $V_{Pulse} = 6$ V square pulses for a pulse width of 500 ps and a frequency of 1.1 GHz. Figure adapted from Reference [24].

InGaN/GaN NW based LEDs.

Although very high quality NWs have been grown by self-assembled methods [6,25], the main drawback of this growth processes is the impossibility of precisely controlling the diameter and the position of the NWs, which can be detrimental for the efficiency of the future devices. The selective area growth (SAG) of NWs on a substrate covered with an inert patterned mask appears as a good alternative for the growth of high quality NWs. A very interesting example of the current research in SAG growth is that of *Gao et al.* [26] for InP SAG NWs. Figure 1.2 presents a SEM micrograph of the regular array of InP NWs with diameter of 500 nm. The response of the NWs in terms of the variation of the quantum efficiency as a function of excitation power density and that of very high quality InP layer are shown in Fig. 1.2. The structural and optical characterisation of the NWs was carried out by scanning electron microscopy (SEM), transmission electron microscopy (TEM), photoluminescence and time-resolved photoluminescence. The structural uniformity and the high quantum efficiency of these NWs enable room-temperature lasing from single NWs under optical pumping.

Even more challenging would be the production of devices based on single NWs. As an example of recent research, *Pescaglini et al.* [27] fabricated and characterised a device for near-infrared photongeneratation (650 - 850 nm) of hot electrons in individual ZnO NW field effect transistor (FETs) decorated with Au nanorods. The device is shown in Fig. 1.3. In the proposed hybrid system device, Au nanorods acted as active elements, generating hot electrons that were injected into the wide band gap ZnO NW, which functioned as a passive component for charge collection. This hybrid device presented a two orders of magnitude enhanced photoconductance and a forty times faster response than those of bare ZnO FET. The mechanism of generation of the hot electrons and their injection into the NWs hybrid and the results of the photoresponse are also shown in Fig. 1.3. These

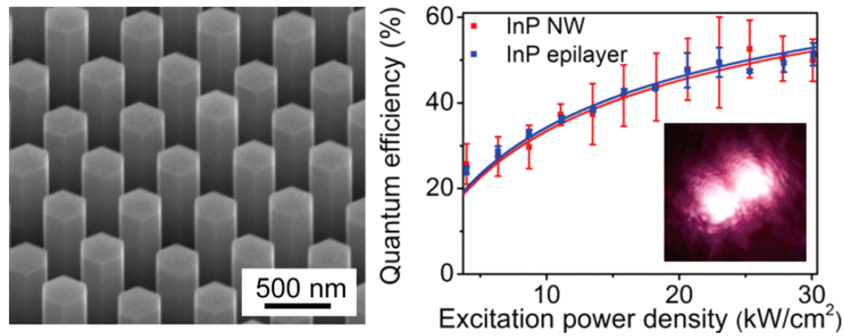

Figure 1.2: SEM of SAG InP NWs grown by MOVPE and the plot of quantum efficiency as a function of excitation power density for NWs and InP epilayer. The inset shows the optical microscope image of the NW emission. Figure taken from Reference [26].

metal nanorod-NW hybrid device architectures are extremely promising for further development of novel miniaturized, tunable photodetectors and for highly efficient plasmonic energy conversion devices. It has to be stressed that very few studies have addressed the use of plasmonic/semiconductor NW hybrid systems for the development of photodetectors and photovoltaic applications [27].

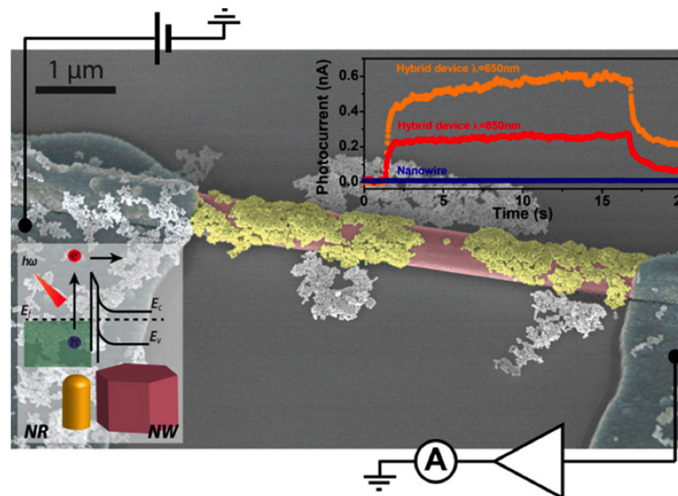

Figure 1.3: SEM image of a ZnO NW - Au nanorods hybrid device. Inset on the left corner: schematic representation of the hot electron generation and the injection process at the nanorod-NW interface. Inset on the right corner shows the photoresponse during exposition to light with $\lambda = 650$ nm (orange curve) and $\lambda = 850$ nm (red curve) of hybrid FET device and of ZnO NW FET (blue curve). Figure adapted from Reference [27].

The three works presented are recent examples of new and challenging scenarios in the field of optoelectronics thanks to the integration of semiconductor NWs and remark, once again, the benefits that this kind of structure

can introduce in the field.

1.2 Challenging open problems

NWs with very good properties have been obtained in recent years. However, there are still open problems related to their growth, structural, and optical properties that can dramatically affect the device performance. An important problem is the difficulty to control the position, the size, and the growth direction of the NWs. On the other hand, NWs enable heterostructures with new orientations, such as those growing on non-polar planes, and, assessing the structural quality, the elemental segregation in the alloy composition of NW heterostructures as well as the existence of internal electric fields are other new specific problems. Such studies add an extraordinary difficulty to the available characterisation techniques which should deal with large ensembles of objects of submicron sizes. This requires new techniques with spatial resolution in the nanoscale, in order to probe individual NWs, and, at the same time, capable of extracting statistically meaningful information from the ensemble.

1.2.1 Controlled growth of semiconductor NWs

Vapour-liquid-solid (VLS) assisted methods of growth are the most common for the growth of NWs. VLS was discovered in 1965 for gold-assisted growth of silicon whiskers and is well understood for this kind of structures [28]. This method is rapid and low cost and gives high crystalline quality NWs [29]. Moreover, the use of a gold catalyst allows to control the diameter, the density and even the position of NWs, as it is depicted in Fig. 1.4. However, the catalyst-assisted growth produces NWs with a higher density of structural defects and impurities than the catalyst-free processes, probably due to the incorporation of catalyst atoms [31]. NWs have been successfully obtained without the use of a catalyst by metal organic chemical vapour deposition (MOCVD) and molecular beam epitaxy (MBE) [6, 25]. However, there are still open problems related to this kind of self-assembled NWs that can dramatically affect the future device processing: the difficulty to control the position, the size, and the growth direction of the NWs. Therefore, the search of new techniques that can allow to overcome these problems is an active field of research.

SAG allows to grow regular arrays of vertically aligned NWs in the holes of a patterned inert mask. In this way, precise control over their position and diameter is achieved. Several groups reported on the successful SAG of GaN NWs by MBE and MOCVD. For example, *Shuman et al.* [32] obtained the selective growth of GaN NWs in the holes of a patterned silicon oxide film covering a Si (111) substrate by MBE. The same growth technique was used by *Urban et al.* [13] (A. Rizzi's group) for obtaining regular arrays of GaN

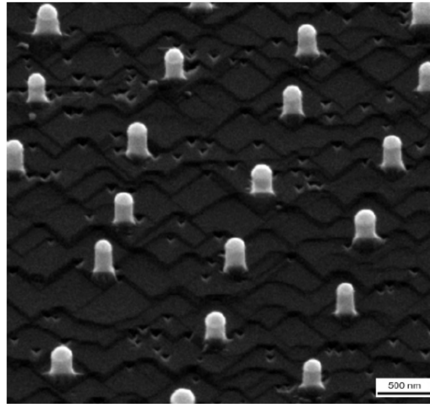

Figure 1.4: SEM image of a Si NW array obtained on a Si(111) wafer with an average diameter of 1320 nm. The diameter of the NWs depends on the size of the Au droplets, which remain on the tips of the wires. Figure taken from Reference [30].

NWs on the apertures of a Mo mask deposited on a GaN (0001) template. On the other side, *Choi et al.* [33] have grown very thin SAG GaN NWs on a GaN template covered by a SiO_2 layer by MOCVD, as it is depicted in Fig. 1.5. They found that the growth is strongly influenced by the mask design.

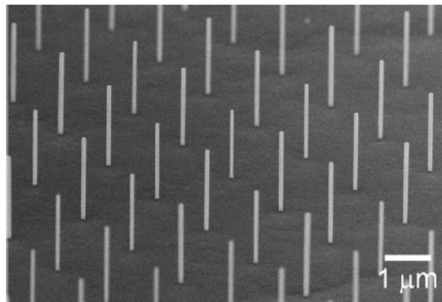

Figure 1.5: SEM image of GaN NWs with a diameter of about 50nm. Figure adapted from Reference [33].

The material quality and the properties of the NWs depend sensitively on the growth parameters, which change according to the growth process: SAG growth process differs consistently from the self-organised one. SAG typically requires higher temperatures and III/V ratios than self-assembled growth, as selectivity is achieved by increasing Ga desorption and diffusion in order to suppress the nucleation outside the apertures of the mask [34]. The mask geometry is another important factor not only for selectivity but also for the vertical growth and the shape evolution of the nanostructures since it affects the local III/V ratio within the mask apertures [35]. While there is extensive literature about the structural and optical quality of self-assembled NWs, less attention has been paid to the quality of SAG NWs.

The first characterisation studies carried out with TEM revealed that SAG growth can also be affected by threading dislocation and basal plane stacking faults [13, 36]. Thus, it would be highly beneficial to study the effects of the SAG mask geometry on the structural and optical properties of SAG NWs.

1.2.2 Tunability and quantum efficiency of the emission of GaN/InGaN NWs

Quantum confined Stark effect (QCSE) [37] can dramatically affect the quantum efficiency of devices based on piezoelectric materials, such as group-III nitrides. Normally III-nitride based QWs are grown along the *c*-axis, because it is easier and cheaper that along other directions, but their optical properties are strongly affected by the QCSE [38, 39]. The internal field induces a spatial separation of the electron and hole wave functions in the QWs, with the consequent decrement of the radiative recombination efficiency [40]. Investigations on the efficiency drop in 2D GaN/InGaN MQWs where performed by *Li et al.* [41] who found that the thicker the QWs are, the lower the relative internal quantum efficiency at room temperatures, as it is shown in Fig. 1.6. The authors attributed this result to the larger electron-hole charge separation induced by internal field in thicker QWs.

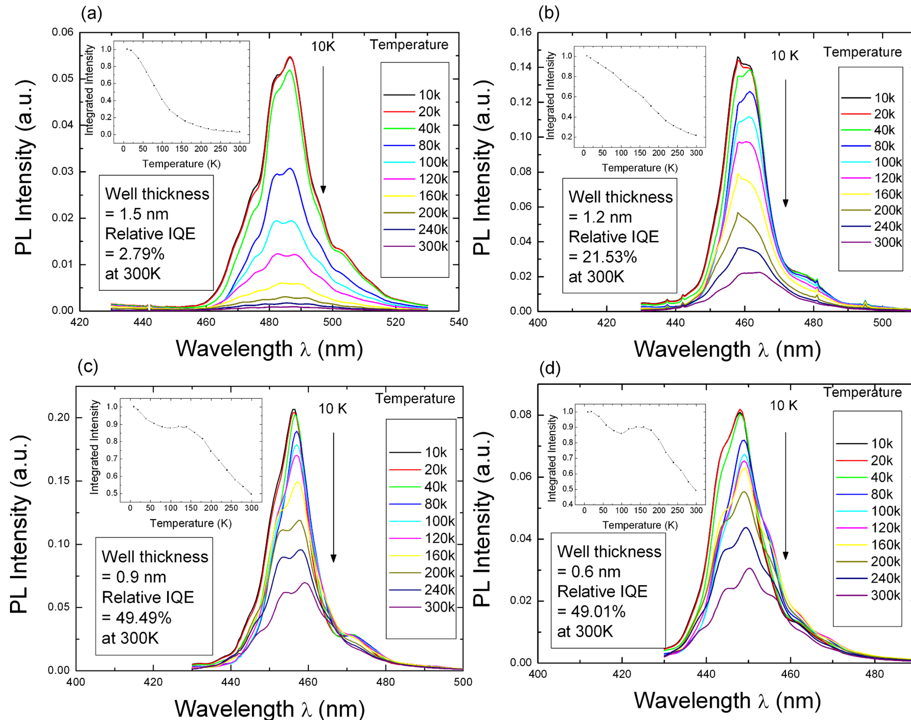

Figure 1.6: PL temperature dependence for the determination of the internal quantum efficiency of GaN/InGaN MQWs with varied QWs thickness: (a) 1.5 nm (b) 1.2 nm (c) 0.9 nm and (d) 0.6 nm. Figure taken from Reference [41].

A possible solution to this problem is the growth on semi- or non-polar

planes of the crystal in order to either diminish or suppress the internal electric field [42]. *Ra et al.* [43] demonstrated that coaxial GaN/InGaN NWs grown in non-polar directions have better quantum efficiency than their *c*-axis grown counterparts. However, controlling simultaneously the crystal quality, the alloy composition and the strain field of these structures has proven to be very difficult [44]. The main problem is related to the InGaN alloy, which normally presents In compositional inhomogeneities. This implies a degradation of the structural quality, presence of strain, and the impossibility to control the alloy composition, and to cover all the spectral range in the future devices [45]. This effect is stronger for the mid compositional range, which is still preventing green lasers with reasonable lifetimes based on these materials. Only few works report on the successful tunability across the entire range of compositions [46]. However, first thorough investigations, such as those by *Segura-Ruiz et al.* [47] reported the elemental segregation in InGaN NWs and its influence on the local atomic structure by X-ray fluorescence (XRF) imaging and X-ray absorption near edge structure (XANES) at the nanoscale. Ga and In elemental maps

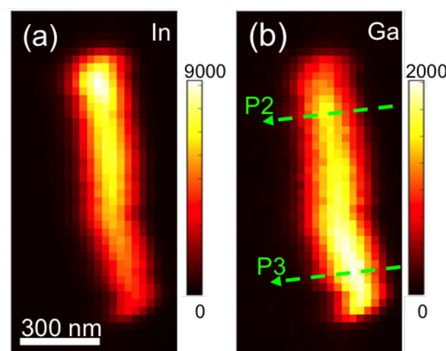

Figure 1.7: Spatial distribution maps of the intensity of two fluorescence peaks corresponding to (a) In and (b) Ga atoms. The intensity ranges are indicated by their colour scale, where dark represents low and bright high photon counts. The XRF maps were taken with a pixel size of 25 $\times$ 25 nm^2 and an accumulation time of 1.5 s per pixel. Figure adapted from Reference [47].

revealed an inhomogeneous distribution along single NWs [48], with a higher Ga concentration at the bottom of the NW, as it is shown in Fig. 1.7. Moreover, they demonstrated that the elemental modulation does not affect the local atomic structure.

These initial studies leave many open questions: how does In incorporate along the NWs? Is there elemental segregation along the NWs? How does it affect the structural and optical properties? Is there an effective strain relief thanks to the election of the 1-D geometry? In order to solve these issues, one should take great advantage from techniques that allow the study of single NWs and that give complementary and simultaneous information on their structural, optical, and elemental properties.

1.3 Characterisation techniques at the nanoscale

The study of single and ensemble of NWs introduces new challenges to carefully and efficiently characterise devices and samples. The properties of the device will be those of an ensemble of many individual NWs. While, single NWs can present slight differences in their optical properties [49] and therefore they exhibit their own individual spectra. Performing single NWs studies is the only way to univocally evidence their individual properties. Thus, techniques that enable the study of ensembles as well as single NWs with spatial resolutions ranging from the micro- to the nano-scale are required. Moreover, in nanoscale functional materials, it becomes very important to determine the relationship between structural and optical properties. This requires the application of different techniques to the same nano-object. Therefore, it is mandatory the use of non destructive and contact-less spectroscopic techniques, which do not require a special preparation of the sample and allow to perform several experiments on the same NWs.

Raman scattering reveals the interaction between the electromagnetic radiation and vibrational and/or rotational normal modes (phonons) in a material and is already a well established technique for the characterisation of NWs [50]. It gives information on the crystal quality and the strain field of the material. Photoluminescence (PL) is based on the emission of photons created from the recombination of an electron-hole pair generated by optical excitation. PL gives information on the material band gap, the presence of optically active defects, the quantum confinement in heterostructures, the presence of strain fields and the general optical quality of the material [51]. PL as well as Raman scattering are widely used in the characterisation of ensembles and individual NWs [52].

X-ray spectroscopy techniques are based on the excitation of atoms with X-rays [53]: X-ray fluorescence (XRF), X-ray diffraction (XRD), and X-ray absorption near edge structure (XANES) are key tools for the determination of the chemical composition (trace element level) and the structural properties of crystalline materials. The sub-micron scale spatial resolution achieved in recent years in Synchrotrons allows the study of not only ensembles but also single NWs [54]. As Raman and PL, these X-ray techniques give information in a non-destructive manner. On the other hand, energy dispersive X-ray spectroscopy (EDS) is another powerful tool complementary to XRF providing information about the internal composition of the material, with high spatial resolution, thanks to the use of electron beams as excitation source [55, 56].

All the above enumerated characterisation techniques enable the study of ensembles and single NWs. However, Raman scattering is generally affected by low scattering rates, therefore the only possibility to detect signal from a single NW often requires resonant excitation conditions (excitation energy equal or superior to the band gap of the semiconductor). Resonant

measurements have many drawbacks such as the heating of the semiconductor, its consequent thermal degradation, and the secondary emission that can hide the Raman signal. A solution for overcoming this problem could be to perform surface enhanced Raman scattering (SERS). SERS exploits the intense electromagnetic fields that are generated by localised surface plasmons at noble metal nano-structures-dielectric interfaces. Metal nanostructures, when illuminated with a light in resonance with their plasmons, enable to localise and strongly enhance the light intensity within a nanoscale volume [57]. Up to now, SERS has been a very efficient technique in the investigation of molecular species down to the single molecule detection [58]. The decoration with nano-metallic particles has been rarely applied to semiconductor NWs [59] and it seems to be a promising technique for the study of their surface properties.

1.4 Objectives of the work

The advent of nanotechnology has brought with it not only an outstanding number of potential applications in many fields but also the need for characterisation techniques capable of correlating the fundamental properties of the nanostructured materials and the performance of the devices. In the field of optoelectronics, determining the relationship between structural and optical properties of nanoscale functional materials necessarily requires applying different complementary techniques to the same nano-object. The main aim of this thesis is the characterisation of single semiconductor NWs by a combination of new and more conventional spectroscopic techniques. All the employed techniques should be non-destructive and have submicron spatial resolution. Studying the same NW with several complementary techniques provides more complete information regarding morphology, crystalline properties, chemical composition, strain fields, and optical response, among other properties. This goal has led to three main objectives that are synthesised into the following items.

1. *Studying the structural properties of GaN selective area grown NWs by optical means.*
   The properties of homoepitaxial and heteroepitaxial SAG GaN NWs grown by molecular beam epitaxy have been studied in order to prove if SAG growth is a valid alternative to catalyst-assisted and self-organised processes. The effects of the SAG mask geometry on the structural and optical properties of GaN NWs, i. e., internal strain, structural defects and optical emission were investigated. The studies were performed both on ensemble and single NWs by micro-Raman scattering and micro-PL spectroscopies.

2. *Determining the compositional, structural, and optical properties of individual GaN/InGaN core-shell NWs.*

This objective has required the use of several optical and X-ray spectroscopies, including Raman and PL, and XRF, XRD and XANES for mapping the elemental distribution and strain fields of InGaN MQWs in individual NWs.

3. *Demonstrating surface enhanced Raman scattering of individual ZnO NWs decorated with Au nanorods.*
   A careful examination of SERS in individual semiconductor NWs has been performed taking hybrid systems composed by ZnO NWs and Au nanorods as a proof of concept. In order to avoid the problems originated by the Raman resonant excitation, SERS with excitation energy below the semiconductor band gap has been performed. The resonance conditions of the effect and the reproducibility of the frequency and the intensity of the SERS peaks have been evaluated.

1.5 Organisation of the work

This thesis is organised as follows. The current Chapter has introduced the state of the art and formulated the main objectives of the work. Chapter 2 reviews the fundamental properties of wurtzite wide band gap semiconductors, in particular GaN and ZnO. Chapter 3 introduces the different characterisation techniques and the experimental setups employed in this work. Starting from the Raman scattering, then describing SERS, followed by photoluminescence and finally X-ray spectroscopy. Chapters 4, 5, and 6 present the results of investigations. Chapter 4 is devoted to the structural and optical characterisation of GaN SAG NWs and their dependence on the inert mask layout. Chapter 5 studies the optical properties of GaN/InGaN core-shell NWs in relation to their structural properties and elemental distribution. Chapter 6 describes the preparation of ZnO NWs decorated with Au nanorods and presents the results of SERS measurements in these hybrid systems. Finally, the conclusions of the doctoral work are drawn.

Chapter 2

Fundamental physical properties of wide band gap semiconductors

In this Chapter the most important properties of the materials studied in this work, GaN, InGaN, and ZnO, are reviewed in order to provide the theoretical background needed for analyzing the results that will be presented. Most of the investigations carried out during this project are focused on GaN and InGaN, therefore the majority of the information that is given in the present Chapter is related to the properties of these materials. ZnO NWs were employed for studying the potentiality of surface enhanced Raman scattering on semiconductor NWs, so only some basic aspects of this material, especially those concerning vibrational properties, are reviewed. First of all, the crystal structure and some of the defects that can affect this structure are presented. Then, the electronic structure with the main focus on those of GaN and its alloys InGaN is described. Finally, the vibrational properties, including vibrational surface effects that are enhanced in NWs compared to their layer counterparts, are presented.

2.1 Crystal structure

The spontaneous crystal structure of GaN and ZnO is, under normal conditions of temperature and pressure, that of wurtzite (WZ). This structure symmetry is given by the space group C^4_{6v}. The unit cell of the WZ structure is composed by four atoms and it is characterised by two lattice constants a and c, that are depicted in Fig. 2.1. The WZ cell is constituted by two interlocking closed-packed-hexagonal (hcp) Bravais lattices, displaced from one another along the [0001] axis by the amount uc. The ideal value of the internal structural parameter u is $\frac{3}{8} = 0.375$. However, III-nitrides do not fulfil the ideal condition, for example GaN shows a value of u equal to 0.377. This is the cause of the spontaneous polarisation in WZ semiconductors (see Section 2.2.2). The direction along the primitive c lattice vector is by convention defined as the c-axis. The WZ crystal structure

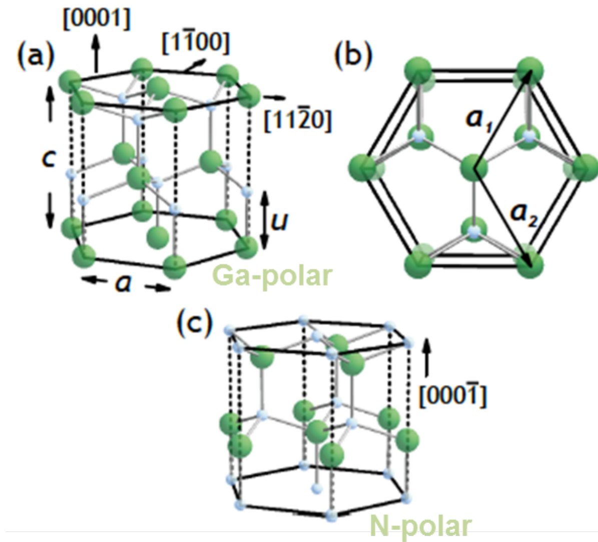

Figure 2.1: Model of the WZ crystal structure, exemplarily shown for GaN. Big and small spheres denote Ga and N atoms, respectively. (a) Ga-polar GaN. (b) Top-view projection of (a) along the c-axis. The N-polar case is shown in (c). Figure adapted from Reference [60].

is non-centrosymmetric: for an arbitrary point (x, y, z) in the unit cell, non equivalent point at (-x, -y, -z) is found. The WZ semiconductors are therefore termed polar. In particular, the Ga-N dimer which is described by the vector pointing from Ga to N can be aligned parallel or antiparallel with respect to the c-direction. The first case corresponds to Ga-polarity, the latter to N-polarity, see Fig. 2.1 (a) and (c), respectively.

In the hexagonal system, Miller-Bravais indices in the form $(hkil)$, with i= -$(h+k)$ define crystallographic planes. The directions of the plane normal vectors are given by $[hkil]$. A commonly used plane in crystal description is the basal plane (0001), named c-plane, as depicted in Fig. 2.2 (a) and its plane normal vector is [0001] (see Fig. 2.1 (a)). Consequently, a will be the in-plane lattice constant and c the out-of plane lattice constant of the basal plane, as it is shown in Fig. 2.1 (a). Other important planes are the $(11\bar{2}0)$ a-plane and the prismatic $(1\bar{1}00)$ m-plane and they are drawn in Fig. 2.2 (a). The c-plane is named polar, while the latter are termed non-polar. Planes in between, are termed semi-polar and they are depicted in Fig. 2.2 (b) and (c), respectively.

During the growth of WZ crystals (in the case of this work of GaN and ZnO) inclusions of cubic structure can appear unintentionally. This cubic structure, known as zinc blende (ZB) and shown in Fig. 2.3, belongs to the space group T_d^2 and can be illustrated by two interpenetrating face-centred-cubic (ccc) sublattices displaced from each other by $(1/4,\ 1/4,\ 1/4)\,a$, where a is the cube edge length (or lattice constant). Each sublattice corresponds to one atomic species which results in two atoms per unit cell.

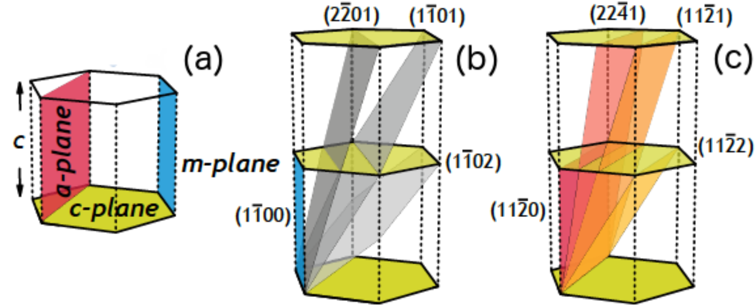

Figure 2.2: Polar, nonpolar (a), and low-indexed semipolar (b,c) planes are shown. Figure adapted from Reference [60].

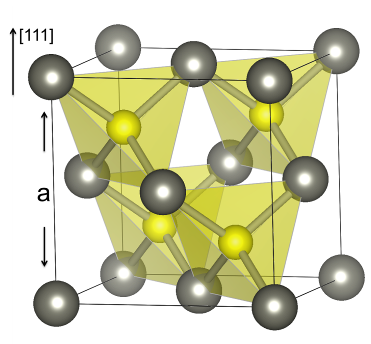

Figure 2.3: Schematic model of the ZB crystal structure along the direction [111].

The stacking sequence along the growth direction consists of repeating AB and ABC layers (containing the elements of both groups each layer) for WZ and ZB structure, respectively, as it is shown in Fig. 2.4.

The GaN and the ZnO hexagonal lattice parameters a and c and the respective cubic lattice parameter c are summarised in Table 2.1.

Table 2.1: Lattice parameters of WZ and ZB GaN [61] and ZnO [62].

WZ	GaN	ZnO
a ($\AA$)	3.189	3.250
c ($\AA$)	5.185	5.207
ZB		
a ($\AA$)	4.50	4.60

2.1.1 Stacking faults and dislocations

Stacking faults (SFs) are extended defects that generate non-uniformities in the stacking sequence: some layers differ from the predominant stacking sequence. Basal plane stacking faults (BSFs) in WZ semiconductors can be

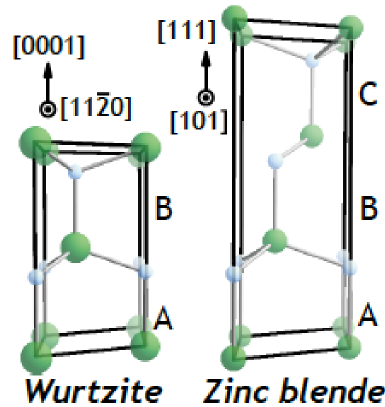

Figure 2.4: Stacking sequence for WZ along [0001], and for zinc blende along [111]. Figure adapted from Reference [60].

seen as planar ZB inclusions into the WZ matrix. BSFs are classified in four categories according to the number of violations to the stacking sequence: the intrinsic type I_1, I_2, I_3 and the extrinsic one E, their crystallographic arrangements are shown in Fig. 2.5. In the case of I_1 the cubic inclusion (between parenthesis) appears in the following way, ABA(BAC)AC and corresponds to a substitution of one basal plane (A or B) with a C plane. In the one of I_2 the stacking sequence contains two violations of the stacking rule, resulting from the substitution of an A plane with a C plane and a B plane with an A plane, respectively, and the stacking sequence is AB(ABCA)CAC. Type I_3 is created by a C plane which occupies a basal plane (A or B) position and leads to a stacking sequence ABA(BACAB)AB. Experimental verification of the type-III BSF by transmission electron microscopy is scarcely reported to the present date. E type is created by an insertion of one basal C-layer into the crystal. The stacking sequence is AB(ABCAB)AB. There are also prismatic stacking faults (PSFs) which involve changes in the stacking sequence but along the direction $(11\bar{2}0)$. It has to be stressed that these extended defects are less common in c-plane GaN, but appear with high density in samples grown along non-polar and semi-polar directions [63–65].

Another type of structural defects are dislocations, that are one-dimensional defects in the crystallographic arrangement with respect to a perfect crystal. Generally, dislocations can be grouped into misfit and threading dislocations (TDs). The former are generated due to strain accommodation in heteroepitaxy, while the latter are related to crystallographic misorientation. Misfits are created by the lattice mismatch between the substrate and the grown material [66]. Misfit dislocations form when there is a missing or dangling bond in the lattice between two layers with different lattice constant (i.e., substrate and semiconductor), as it is shown in Fig. 2.6. Usually, misfit dislocations do not thread up into the layer and are very efficient in relieving strain. However, it has been shown that they can be interconnected to the

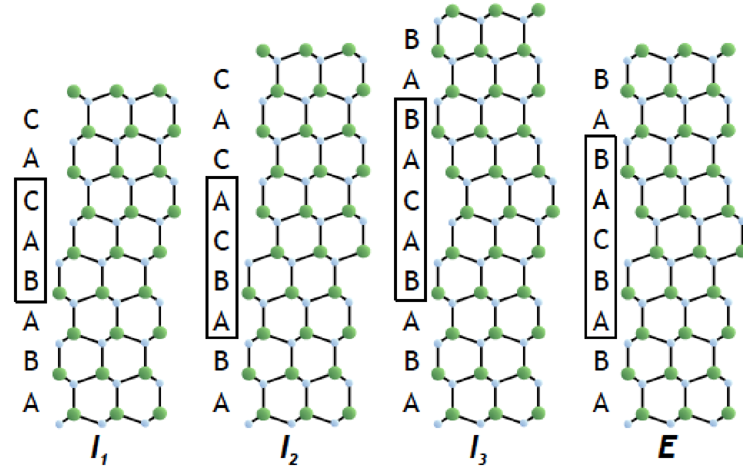

Figure 2.5: Atomic structure of basal plane stacking faults in WZ semiconductor projected along $[11\bar{2}0]$. The reduced stacking sequence is indicated and the fault region marked by rectangles. Figure taken from Reference [60].

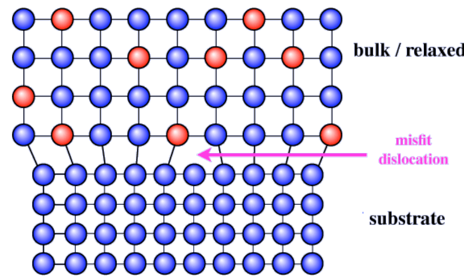

Figure 2.6: Sketch of misfits dislocations between the substrate and the layer. Figure adapted from Reference [67].

TDs network [68]. Transmission electron microscopy investigations have demonstrated the TDs originate at the interface of the epilayer and propagate through the crystal. They are terminated if they reach the crystal surface or annihilate each other. TDs may be formed at coalescence boundaries due to slight deviations of the crystal orientation of one island with respect to the other [66]. Since TDs typically run perpendicular to the interface where they are created, they do not accommodate strain [66]. There are three types of TDs edge (**a**-type), screw (**c**-type) and, mixed varieties of the two (**a**+**c**-type). The type of dislocation is determined only by the Burgers vector **b** and the line direction of **u**. For edge dislocations **b** is perpendicular to **u** and equal to $\frac{1}{3}\langle 11\bar{2}0\rangle$, while for screw dislocations, it is parallel to **u** and obviously equal to $\langle 0001\rangle$. Finally, for mixed type dislocation **b** is equal to $\frac{1}{3}\langle 11\bar{2}3\rangle$. To understand edge disclocation, one can think of a half extra-plane inserted/removed perpendicular to the c-plane that causes distortion of the neighbour planes, as shown in the top-view sketch in Fig. 2.7 (a). On the other hand, screw-dislocations can be visualised as cutting a crystal half-way

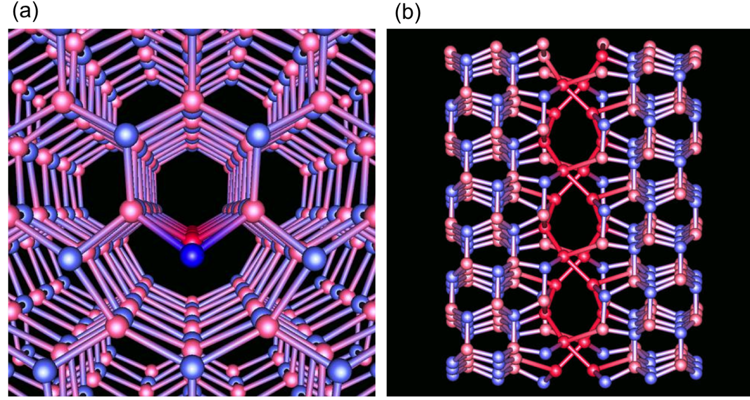

Figure 2.7: Sketch of edge (a) and screw dislocations (b).

along a plane and slipping one half of the plane across the other, causing deformation of the neighbour bonds and the formation of an helical path along the slip-direction as shown in Fig. 2.7 (b).

2.1.2 Strain in wurtzite crystals

Strain generates distortions in the crystal structure and is often produced by the mismatch in the lattice constants between the substrate and the grown material, by defects or by incorporated impurities.

The deformation of a crystal is related to the applied stress by the Hooke's law:

$$\sigma_{ij} = C_{ijkl}\varepsilon_{kl} \qquad (2.1)$$

where σ_{ij} is the stress tensor and it corresponds to a force in the i-direction applied to the unit area of the plane normal to the j-direction, C_{ijkl} is elastic tensor, and ε_{kl} is the strain tensor. The σ_{ij} is symmetric ($\sigma_{ij} = \sigma_{ji}$) and this ensures the absence of rotational torques due to the stress [69]. Intuitively, the normal forces on opposite faces of the crystal must be equal in magnitude and opposite in direction, thus the tractions which would tend to rotate them, must balance each other and the crystal will not spin.

Taking into account the symmetry properties of the WZ crystals, the fourth-rank elastic tensor could be reduced to a 6×6 matrix of elastic constants C_{ij} and using the Voig notation, $xx \rightarrow 1$, $yy \rightarrow 2$, $zz \rightarrow 3$, yz, $zy \rightarrow 4$, zx, $xz \rightarrow 5$, xy, $yx \rightarrow 6$, Eq. (2.1) becomes

$$\sigma_i = C_{ij}\varepsilon_j \qquad i = 1, \ldots, 6 \qquad (2.2)$$

where C_{ij} is

$$\begin{pmatrix} C_{11} & C_{12} & C_{13} & 0 & 0 & 0 \\ C_{21} & C_{22} & C_{23} & 0 & 0 & 0 \\ C_{31} & C_{32} & C_{33} & 0 & 0 & 0 \\ 0 & 0 & 0 & C_{44} & 0 & 0 \\ 0 & 0 & 0 & 0 & C_{44} & 0 \\ 0 & 0 & 0 & 0 & 0 & (C_{11}-C_{12})/2 \end{pmatrix}$$

The elastic constants for WZ GaN are listed in Table 2.2. *Vurgaftman et al.* [70] recommend these theoretical values, because they present the best concordance with the experimental data [71].

Table 2.2: Elastic constants for WZ GaN [70].

WZ	GPa
C_{11}	390
C_{12}	145
C_{13}	106
C_{33}	398
C_{44}	105

The strain-stress relations given above can be simplified making the assumption that a crystal is affected only by pure uniaxial strain or biaxial strain. Normally, III-N binary compounds are grown along the *c*-axis, and in this case, biaxial strain is contained in the plane normal to the growth direction (*c*-plane). Thus, the crystal will be uniformly compressed or expanded in the *c*-plane and separately strained along the *c*-axis. According to Eq. (2.2), the stress tensors will be

$$\sigma_{xx} = \sigma_{yy} = (C_{11} + C_{12})\varepsilon_{xx} + C_{13}\varepsilon_{zz}, \quad \sigma_{zz} = 2C_{13}\varepsilon_{xx} + C_{33}\varepsilon_{zz} \tag{2.3}$$

From Eq. (2.3) within the biaxial approximation (the material grows free along the *c*-axis and σ_{zz}=0), it is possible to obtain the relationship between the normal and in-plain strain components

$$\varepsilon_{zz} = -\frac{2C_{13}}{C_{33}}\varepsilon_{xx} \tag{2.4}$$

Conventionally, ε is greater than zero for tensile strain and less than zero for compressive one.

The strain components can be written in terms of the lattice parameters as

$$\varepsilon_{xx} = \varepsilon_{yy} = \frac{a - a_0}{a_0} \quad and \quad \varepsilon_{zz} = \frac{c - c_0}{c_0} \tag{2.5}$$

where a_0, c_0 and a, c are the values of the unstrained and strained lattice

parameters, respectively. The value of lattice parameter a in the case of crystals grown along non-polar directions may be different along the x and y axis.

2.2 Electronic properties

The electronic properties of semiconductors are determined by their electronic band structure. In crystalline solids, the energy bands are functions of the electron wavevector which takes any value within the Brillouin zone. The first Brillouin zones (BZs) for WZ and ZB lattices are depicted in Fig. 2.8 (a) and (b), respectively. Several methods of computation have been

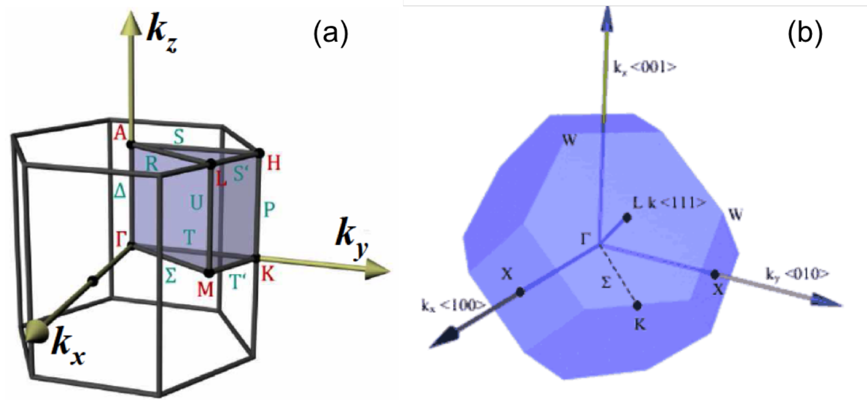

Figure 2.8: First Brillouin zone of (a) WZ and (b) ZB structures showing some of the high-symmetry points and directions according to standard notation.

used for calculating the GaN electronic band structure [72]. The results of the detailed electronic band structure calculations for WZ and ZB GaN by 'empirical pseudo potential method' [72] are presented in Fig. 2.9 (a) and (b), respectively. Figure 2.9 (a) and (b) show that for both the WZ

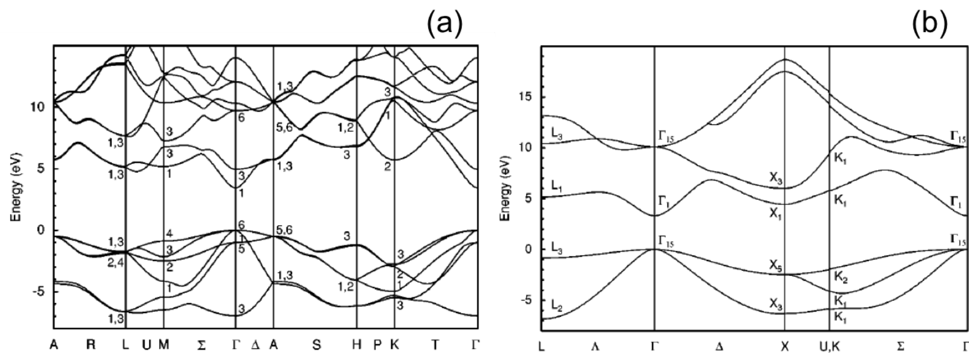

Figure 2.9: (a) and (b) Bulk band structure of WZ and ZB GaN calculated by empirical pseudo-potential method. Figure adapted from Reference [72].

and the ZB structures, the valence band maximum and the minimum of the conduction band are at the Γ point. The conduction bands near the Γ point are parabolic, as expected in wide band gap semiconductors, therefore both GaN and ZnO have direct band gaps. At room temperature, the large energy band gap of WZ GaN and ZnO are equal to 3.41 eV [73] and 3.40 eV [74], respectively. The value of the energy band gap of ZB GaN is 3.23 eV (room temperature) [73].

It has been seen that BSFs in GaN behave as type-II quantum wells with band off-set of ΔE_C = 122 meV and ΔE_V = -62 meV for the conduction and valence band, respectively, and with an effective well width of L = 0.77 nm [75, 76]. Thus, the radiative recombination takes place between electrons confined in the stacking faults and holes localised in their vicinity.

2.2.1 InGaN alloy band gap energy

In the case of InGaN alloys the band gap energy is phenomenologically described by the following equation

$$E_{In_xGa_{1-x}N} = xE_{In} + E_{Ga}(1-x) - b(1-x)x \qquad (2.6)$$

where x is the indium fraction, b is the 'bowing parameter' (1.43 eV) [77], E_{Ga} is the GaN band gap, E_{In} is the InN band gap and is equal to 0.65 eV [78]. Figure 2.10 compares the trend of the InGaN band gap, that Eq.

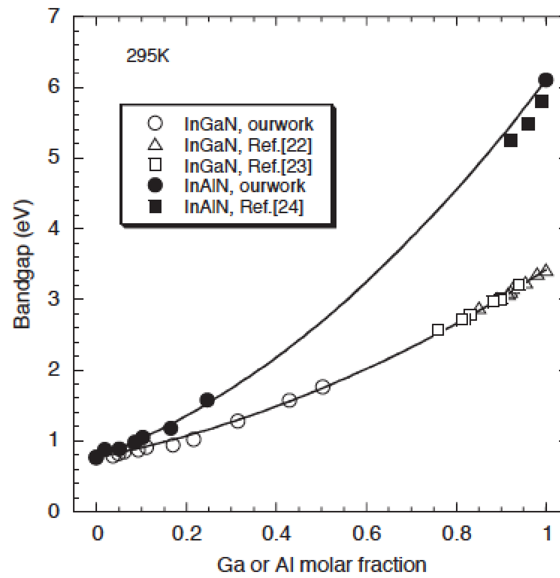

Figure 2.10: Band gaps of InGaN and InAlN alloys plotted as functions of composition. The solid lines are quadratic fits of the band gap energies using bowing parameters of 1.4 eV for InGaN and 3.0 for InAlN, respectively. Figure adapted from Reference [79].

(2.6) foresees for different alloy compositions, with the experimental data.

They show perfect agreement. However, experimental data between $x = 0.5$ and $x = 0.75$ are missing. This is a consequence of the well-know difficulty to control the concentration of In in the alloy, due to In compositional inhomogeneities or segregation, which are reported by all growth techniques both for layers and NWs [80,81]. This implies the impossibility of tuning the energy emission of the alloy within all the range spectra of energies between 0.65 and 3.41 eV.

2.2.2 Pyroelectric and piezoelectric effects

WZ III-V and II-VI compounds are characterised by a small uniaxial macroscopic strain along the [0001] direction, accompanied by microscopic displacements of the ions out of their high-symmetry sites, consequently, the WZ lattice can not be represented by a regular tetrahedron and it is deformed along the c-axis. This is caused by the deviation of u from its ideal value (see Section 2.1). As a result, the interatomic bond lengths are larger along the c-axis which induces a spontaneous polarisation, also named *pyroelectric* polarisation. It is considered that these electrostatic interactions make WZ ZnO and GaN more stable than their ZB counterparts (whose spontaneous polarisation is zero). As it is depicted in Fig. 2.11, the spontaneous polarisation vector P_{SP} points from the negative to the positive charge. This classical description is however only applicable in the case of a solid which is composed of well separated and independently polarisable units, as in the case of ionic crystals. Therefore in covalent materials, like GaN, for which the electronic charge is delocalised, such local-dipole picture is oversimplified and a quantum approach is needed for the description of the electronic system. *King-Smith et al.* [82] developed a quantum theory for

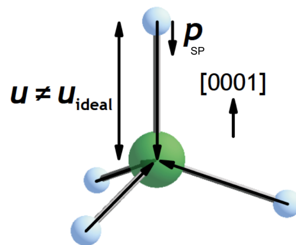

Figure 2.11: GaN tetrahedron (big: Ga, small: N) in the classical dipole moment picture (N negatively charged, Ga positively charged). The resulting net electric dipole moment is given by P_{SP}. Figure adapted from Reference [68].

describing the polarisation charge. *Bernardini et al.* [83] performed ab initio calculations based on this approach for obtaining the values of the P_{SP} for III-V nitrides. The results for GaN and InN are summarised in Table. 2.3. The P_{SP} of the two materials is different, and this is a direct consequence of its dependence on the structural parameters. The value of P_{SP} of InN

Table 2.3: Calculated values of the spontaneous polarisation for GaN and InN [83].

Cm^{-2}	GaN	InN
P_{SP}	-0.029	-0.032

is bigger than the one of GaN, because the u of the former is bigger. For ternary alloys, like $In_xGa_{1-x}N$, P_{SP} can be calculated using Vergard's law:

$$P_{SP}^{InGaN} = xP_{SP}^{InN} + (1-x)P_{SP}^{GaN} \tag{2.7}$$

For arbitrary In concentrations x, the spontaneous polarisation is thus easily calculated.

On the other hand, extrinsic stress fields can also modify u. The consequent structural deformation of the unit cell induces a *piezopolarisation*, P_{PE}. The piezoelectric polarisation is related to the strain tensor by the three rank piezoelectric one e_{ijk} [84]:

$$P_{PEi} = e_{ijk}\varepsilon_{jk} \tag{2.8}$$

The subindexes ijk vary from 1 to 3, that correspond to the spatial directions, therefore e_{ijk} have 27 components, but considering the tensor symmetry, the independent components become 18. Additionally, using the Voigt notation (i.e., 11 $\rightarrow$1 and 22 $\rightarrow$ 2 and 33 $\rightarrow$ 3 and 23,32 $\rightarrow$ 4 and 31,13 $\rightarrow$ 5 and 12, 21 $\rightarrow$ 6) it is possible to reduce the indexes to 2, jk. With these considerations and taking into account that the WZ structure is isotropic in its basal plane, e_{ijk} will have only 5 non vanishing components. So, Eq. (2.8) can be rewritten as

$$P_{PE} = \begin{pmatrix} 0 & 0 & 0 & 0 & e_{15} & 0 \\ 0 & 0 & 0 & e_{15} & 0 & 0 \\ e_{31} & e_{31} & e_{33} & 0 & 0 & 0 \end{pmatrix} \begin{pmatrix} \varepsilon_{xx} \\ \varepsilon_{yy} \\ \varepsilon_{zz} \\ \varepsilon_{yz} \\ \varepsilon_{xz} \\ \varepsilon_{xy} \end{pmatrix} = \begin{pmatrix} e_{15}\varepsilon_{xz} \\ e_{15}\varepsilon_{yz} \\ e_{31}(\varepsilon_{xx}+\varepsilon_{yy}) + e_{33}\varepsilon_{zz} \end{pmatrix}$$

According to this equation, P_{PE} is directed along c if there is no shear (ε_{yz}, ε_{xz} and $\varepsilon_{xy} = 0$) in the material. Thus, P_{PE} is equal to zero along the non-polar directions [11$\bar{2}$0] (x-axis), and [1$\bar{1}$00] (y-axis). The P_{PE} induced by shear strain will be not considered in this work.

Finally, in the case of biaxial strain (ε_{xx}=ε_{yy} and $\varepsilon_{zz} = -2C_{13}/C_{33}\varepsilon_{xx}$) in a strained layer grown along the [0001] direction, the P_{PE} is equal to

$$P_{PE} = 2\varepsilon_{xx}(e_{31} - e_{33}C_{13}/C_{33}) \tag{2.9}$$

Values of the piezoelectric constants (e_{31}, e_{33}) for GaN and InN, which are

in good agreement with the few available experimental data, are reported in Table 2.4.

Table 2.4: Value of the piezoelectric constants of GaN and InN [85].

Cm^{-2}	GaN	InN
e_{33}	0.67	0.37
e_{31}	-0.21	-0.45

2.2.3 Quantum confined Stark effect in InGaN/GaN heterostructures

The consequence of the polarisation in nitrides is the generation of large electrostatic fields inside the heterostructures grown along the *c*-axis. With the purpose of considering the polarisation effects on InGaN/GaN heterostructures, a schematic diagram representing the spontaneous and piezoelectric polarisation vectors with different polarity are presented in Fig. 2.12, where they are indicated with the label P_{SP} and P_{PE}. For this kind of structures only biaxial strain is present, thus, it is expected that the InGaN alloy is under compressive strain because of its bigger lattice constants. The

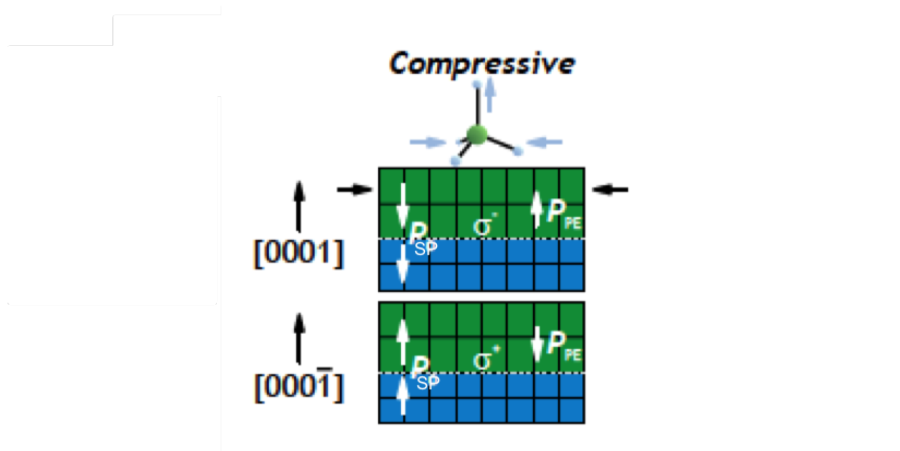

Figure 2.12: Direction of spontaneous and piezoelectric polarisation for InGaN/GaN heterostructures under a compressive biaxial strain. The arrows at the GaN tetrahedra indicate atomic displacements with respect to the unstrained state. Positive and negative induced interface charges are denoted by $\sigma+$ and σ-, respectively. The top and the bottom figure represents the case of heterostructure with N- and Ga-face polarity, respectively. Figure adapted from Reference [60].

macroscopic polarisations are aligned perpendicular to the heterostructure interface. The resulting interface charges induced by the discontinuity in the polarisation give rise to an electric field inside the heterostructure, which is

aligned along the growth direction. Consequently, the conduction and valence bands of the alloy are tilted (see Fig. 2.13). The band bending produces the so-called quantum confined Stark effect (QCSE) [86]. In particular, in the case of InGaN/GaN heterostructures grown along the *c*-axis, *Lefebre et al.* [38] calculated that for QWs with In composition around 0.15-0.20, the internal electric field is around 1MV/cm.

The QCSE has a strong influence on the optical properties of the heterostructures. First of all, the electric field causes a spatial separation in opposite direction between the electrons and the holes towards the interfaces of the QWs. As a direct consequence, the overlap of the wave-functions of electrons and holes diminishes and the probability of radiative recombination decreases [21], implying a detriment of the optical efficiency. Additionally, there is a redshift of the emission and absorption energies in the QW with respect to that in bulk layer [40], that is monotonically enhanced with the well thickness. Figure 2.13 shows the effective band gap of a InGaN/GaN QW and the spatial separation of electrons and holes inside the well.

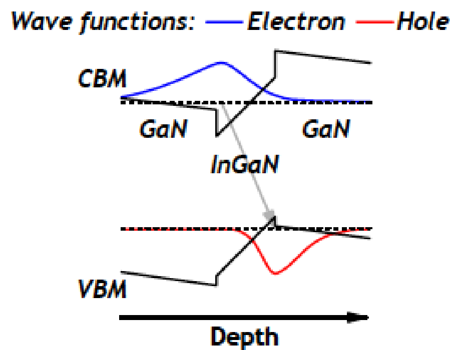

Figure 2.13: Electron and hole wave functions spatially separated (grey arrows). The ground state energy levels of the confined carriers are indicated by dashed lines. Figure adapted from Reference [87].

The QCSE severely affects also polar NWs, even though it would be natural to argue that their particular heterostructure geometry could lead to a strong reduction of the piezoelectric component of the polarisation, due to the strain relaxation typical of these structures. As an example, *Renard et al.* [88] found evidence that GaN/AlN NWs are affected by QCSE.

As it has been seen in the previous Section, the piezoelectric polarisation of heterostructures along non-polar directions is zero, therefore the growth along non-polar directions is considered as a valid alternative for eliminating the QCSE.

2.3 Vibrational properties

The normal modes of vibration of a crystal, called *phonons* in the quantum mechanics approach, provide information on its crystalline structure. In this Section the GaN and ZnO phonon modes for WZ and ZB crystal structure are presented. After that, phonon modes in InGaN alloys are described. Then, it is shown how they are affected by strain. Finally, surface optical phonons, which are normally observed in NWs due to their large surface to volume ratio [89], are introduced and a model for the calculation of their frequency dispersion relations is presented.

The experimental techniques that are commonly used for studying phonons are the inelastic neutron scattering, infra-red absorption spectroscopy and Raman scattering. Only Raman scattering will be employed in this work and its main characteristics will be described in the next Chapter.

2.3.1 Phonons

The number of normal modes of vibration in a crystal with n atoms in the primitive cell is equal to $3n$. In WZ structure n is equal to 4, and in the case of ZB $n = 2$. This results in three acoustic branches both for WZ and ZB structures, for which $\omega_0 = 0$. The rest 3n-3 ones corresponds to optical modes with $\omega_0 \neq 0$ [69], which are 9 and 3 for WZ and ZB structures, respectively. The normal coordinates can be transformed under operations of the crystal symmetry, in the same way that the base functions of the symmetry group. Therefore, the different type of phonons in a crystal can be classified by the irreducible representation of the point group [90]. As it has been described in Section 2.1, the WZ and the ZB structures belong to the $C^4_{6\nu}$ space group and to the T^2_d one, respectively. Thus, the theory predicts in the case of WZ materials that all vibrations at the Γ point of the Brillouin zone have the following irreducible representations [91]: $\Gamma_{ac} + \Gamma_{op} = [A_1(z)+ E_1(x,y)]_{ac}+ [A_1(z)+E_1(x,y)+2B_1+2E_2]_{op}$, with z parallel to the c-axis of the crystal. The letters in parentheses describe the phonon polarisation direction (i. e., direction of vibration of the atoms of the unit cell). If the polarisation direction is parallel to the propagation direction of the phonon, the phonon is longitudinal (L), and if it is perpendicular, it is transversal (T). The optical modes are catalogued as follows: two E_1 modes (LO and TO, polarised along the x and y directions each one), two A_1 (LO and TO polarised along z direction), two B_1 (low and high) and two E_2 (low and high referring to their frequency). The A_1 and the E_1 modes are both Raman and infra-red active, the E_2 modes are only Raman active, and the B_1 modes are silent. Thus, there are six Raman-active phonons in WZ structures, as it is depicted in Fig. 2.14. In the case in which the cations (see Fig. 2.14) move in phase and anti-phase with the anions, a dipole is created, and phonons are polar (A_1 and E_1). While in the case in which the atoms of each element move out of phase, the generated modes are non polar (E_2 and B_1). The

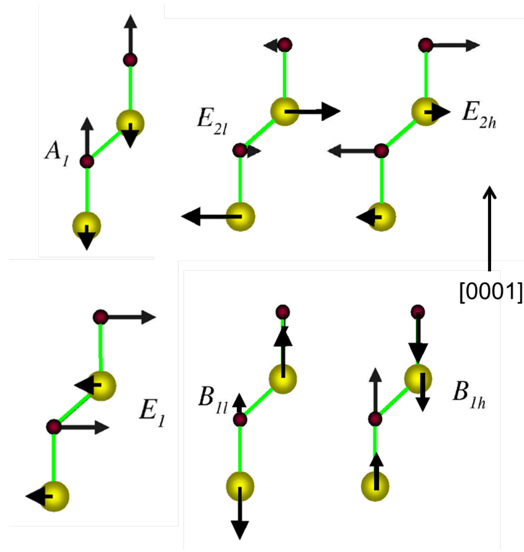

Figure 2.14: Sketch of the vibration of the four atoms of WZ unit cell. The big spheres represent Ga and Zn atoms, while the small ones correspond to N and O in the case of GaN and ZnO, respectively. Figure adapted from Reference [92].

Table 2.5: Phonon frequencies corresponding to WZ GaN [93] and to WZ ZnO [94] at the Γ point.

WZ	GaN (cm^{-1})	ZnO (cm^{-1})
E_{2l}	143	99
$A_1(LO)$	734	574
$A_1(TO)$	531	378
$E_1(LO)$	743	584
$E_1(TO)$	559	410
E_{2h}	567	438

frequencies of Raman active modes of WZ bulk GaN and ZnO at the Γ point are listed in Table 2.5.

In the case of ZB, there are two atoms per unit cell, implying six different vibrational modes: two transverse and one longitudinal acoustical modes (TA and LA) as well as two transverse and one longitudinal optical modes (TO and LO). These double-degenerate optical modes are also in this case Raman-active. The frequencies of ZB bulk GaN and ZnO phonons at the Γ point are listed in Table 2.6. A phonon is described by its wavevector $\vec{q}$ in the first Brillouin zone. The frequencies ω_q associated to it are given by the 3n functions of $\vec{q}$. The variation of the frequency of the phonon with its wavevector ($\omega(\vec{q})$) is known as dispersion relation. As the unit cell length of WZ along the [0001] axis is double with respect to the ZB along the [111], its phonon dispersion can be approximated by folding the one of the ZB structure along the direction [111], see Fig. 2.15. More information about

the stacking sequence of WZ and ZB structure is given in Section 2.1.

Table 2.6: Phonon frequencies corresponding to ZB GaN [95] and to ZB ZnO [96] at the Γ point.

ZB	GaN (cm^{-1})	ZnO (cm^{-1})
TO	555	399
LO	742	581

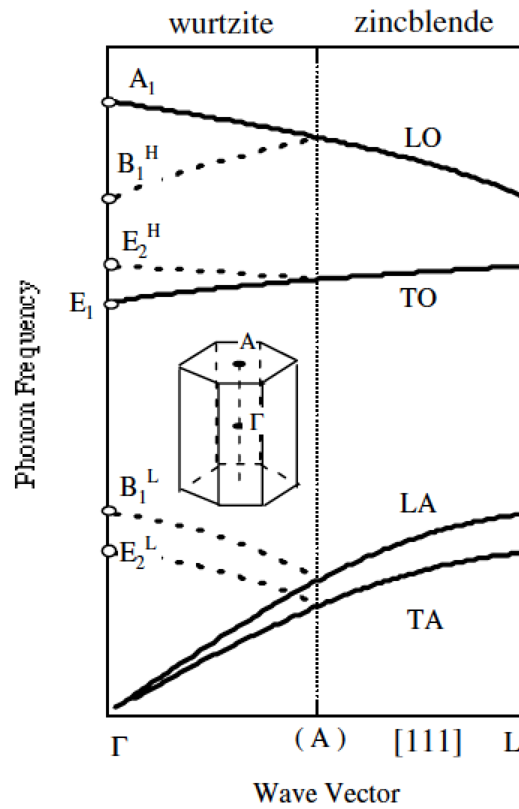

Figure 2.15: Schematic representation of the phonon dispersion. Phonon branches along [111] in the ZB structure are folded to approximate those of WZ structure along [0001]. Figure taken from Reference [95].

2.3.2 Phonons in wurtzite InGaN alloys

The phonon frequencies of InGaN alloy ($\omega_{In_xGa_{1-x}N}$) are given by a compositional linear dependence of the Raman frequencies of InN and GaN. Following [97] the expression will be

$$\omega_{In_xGa_{1-x}N} = x\omega_{InN} + (1-x)\omega_{GaN} \tag{2.10}$$

where x is In fraction in the alloy. Figure 2.16 shows the InGaN phonon frequency evolution as a function of its composition.

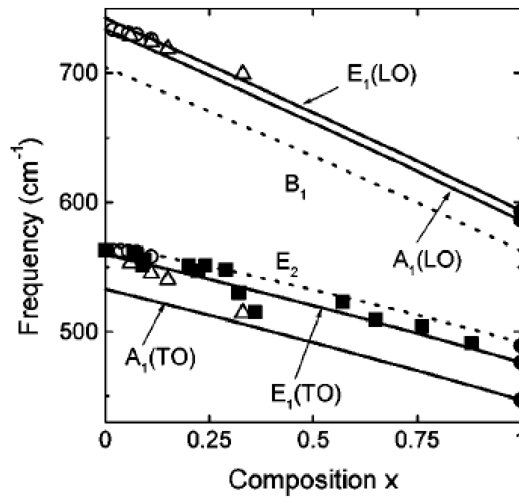

Figure 2.16: Calculated and measured phonon frequencies in InGaN. The theoretical frequencies (solid and dotted lines) are denoted by the mode symmetry. The experimental frequencies are indicated by filled squares, open triangles, open circles and filled circles. Figure adapted from Reference [98].

2.3.3 Effects of the strain on the phonons of wurtzite crystals

Biaxial strain fields typically affect materials grown epitaxially, as already discussed in Section 2.1.2. Such strain fields do not modify the vibration modes but affect their frequencies. Thus, by monitoring the changes in the phonon frequencies, information on the strain values can be extracted. Biaxial strain in the c-plane is probed by observing the non-polar E_2 phonon. Extracting information on strain from the polar modes, i.e., A_1 and E_1 phonons, is more difficult because their frequencies are also affected by free carriers and on their propagation direction which can change with sample misalignment.

The relation between the phonon frequencies and the biaxial strain is given by the linear deformation theory. It describes the shift of the phonon

Table 2.7: Phonon deformation potentials for WZ GaN experimentally determined.

cm^{-1}	a_{E_2}	b_{E_2}
E_{2h}	-850 ± 177 [100]	-963 ± 220 [100]
E_{2l}	-115 ± 25 [101]	-80 ± 35 [101]

frequency by means of the phonon deformation potentials (PDPs). The frequency shift of the E_2 mode ($\Delta\omega_{E2}$) is characterised by two PDPs a_{E_2} and b_{E_2} (that are listed in Table 2.7) [99, 100]:

$$\Delta\omega_{E2} = 2a_{E_2}\varepsilon_{xx} + b_{E_2}\varepsilon_{zz} \tag{2.11}$$

In the case of biaxial strain, substituting Eq. (2.4) and the elastic constants reported in Table 2.2 for GaN in Eq. (2.11), the biaxial strain of WZ GaN can be obtained from the frequency shift of the E_2 mode.

2.3.4 Surface optical modes

The surface optical modes (SO) are polarised lattice vibrations localised at the near-surface and they strongly decay with distance towards the bulk. As mentioned before, they are normally observed in NWs and other nanostructures due to their large surface to volume ratios [89]. The vibrational frequency of these modes are different from those of the bulk states, in fact, the surface atoms are less bound and experience a different local field compared to those of the bulk. For any q vector, their frequency is comprehended between the LO and TO phonons ones [102]. Their frequency and intensity depend on the dielectric constant of the environment in which the nanostructure is immersed and on its radius. SO modes are as interface modes and they appear due to the presence of an interface between two different materials with different dielectric constants (semiconductor - environment). They are observed experimentally when the translational symmetry of their potential is broken (e.g. surface roughness, diameter modulation) [102]. Therefore, once again, they are more intense for nanostructures, like NWs.

2.3.5 SO in a rectangular NW

The cross-sectional shape of the NW influences the SO phonon dispersion relation, which has to be calculated taking into account of the geometrical constraints and the dielectric medium.

The NWs studied in this work are hexagonal and in a first approximation they are assimilable to a rectangular shape. In this Section an expression for the dispersion relation of SO modes of NWs with rectangular shape will be described, giving focus to the particular case of 'large diameter' NWs.

Xiong et al. [103] used the dielectric continuum (DC) approximation introduced for rectangular NWs by *Stroscio et al.* [104], which neglects the exponentially decaying electrostatic fields generated at the corner regions of the NWs, and predicted the SO frequencies in the case of rectangular ZnS NWs. The next theoretical description will follow mainly Reference [103] with some additional details extracted from References [104,105]. Figure 2.17 depicts the considered system: the NW c-axis is assumed to be parallel to z-axis of the reference system. The dielectric functions of the NW and of the surrounding medium are labeled with ε_w and ε_m, respectively. The potential

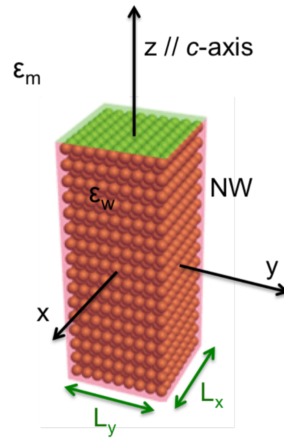

Figure 2.17: Sketch of the modelled NW.

describing the optical-phonon modes along the z-direction, in which the system is translationally invariant, can be written as

$$\Phi(x, y, z) = \Phi(x, y)e^{iq_z z} \tag{2.12}$$

where q_z is the phonon wave vector in the z direction. The potential in Eq. (2.12) in a region of dielectric function ε has to satisfy Poisson's equation

$$\varepsilon\left(\frac{d^2}{dx^2} + \frac{d^2}{dy^2} - q_z^2\right)\Phi(x, y) = 0 \tag{2.13}$$

where $\varepsilon = \varepsilon_w$ inside the NW and $\varepsilon = \varepsilon_m$ outside (as depicted in Fig. 2.17). Assuming, as in the model of *Stroscio et al.*, that the potentials are separable in the plane perpendicular to the c-axis (x,y), i.e. $\Phi(x, y) = \phi_x(x)\phi_y(y)$, Eq. (2.13) becomes

$$\frac{1}{\phi_x(x)}\frac{d^2\phi_x(x)}{dx^2} + \frac{1}{\phi_y(y)}\frac{d^2\phi_y(y)}{dy^2} - q_z^2 = 0 \tag{2.14}$$

Eq. (2.14) has a symmetric and an antisymmetric solution, respectively. Requiring the continuity of the potential and of the normal component of the electric field at the NW boundaries to the solutions of Eq. (2.14), the

SO dispersion relations are derived

$$\varepsilon_w(\omega)tanh(q_iL_i/2) + \varepsilon_m(\omega) = 0 \tag{2.15}$$

and

$$\varepsilon_w(\omega)coth(q_iL_i/2) + \varepsilon_m(\omega) = 0 \tag{2.16}$$

one for the symmetric (S) and one for the asymmetric solution (A), respectively, where L_i (i=x,y) is the edge width of the rectangular NW (see Fig. 2.17) and q_i (i=x,y) is the phonon wavevector. L_i and q_i have to satisfy

$$q_x^2 + q_y^2 = q^2 \tag{2.17}$$

$$q_xL_x = q_yL_y \tag{2.18}$$

The dielectric function ε_w can be expressed as

$$\varepsilon_w(\omega) = \varepsilon_\infty \frac{\omega^2 - \omega_{LO}^2}{\omega^2 - \omega_{TO}^2} \tag{2.19}$$

where ω_{TO} and ω_{LO} are the the transversal and the longitudinal optical phonon frequency, respectively, and ε_∞ is the high frequency dielectric constant of the semiconductor. The TO and LO optical phonon frequencies are related by the Lyddane-Sachs-Teller relation [105]

$$\frac{\varepsilon_0}{\varepsilon_\infty} = \frac{\omega_{LO}^2}{\omega_{TO}^2} \tag{2.20}$$

where ε_0 is the static constant of the semiconductor. Now, substituting Eq. (2.17), (2.18), (2.19), (2.20) in Eq. (2.15) and (2.16), and considering ε_m constant with the frequency, the S and the A phonon dispersion relations are obtained

$$\begin{aligned} \omega_{SO}^2(q)_S &= \omega_{LO}^2 \left[\frac{\varepsilon_\infty[\varepsilon_0 tanh(q_iL_i/2) + \varepsilon_m]}{\varepsilon_0[\varepsilon_\infty tanh(q_iL_i/2) + \varepsilon_m]} \right] \\ &= \omega_{TO}^2 \left[\frac{\varepsilon_0 tanh(q_iL_i/2) + \varepsilon_m}{\varepsilon_\infty tanh(q_iL_i/2) + \varepsilon_m} \right] \end{aligned} \tag{2.21}$$

$$\begin{aligned} \omega_{SO}^2(q)_A &= \omega_{LO}^2 \left[\frac{\varepsilon_\infty[\varepsilon_0 coth(q_iL_i/2) + \varepsilon_m]}{\varepsilon_0[\varepsilon_\infty coth(q_iL_i/2) + \varepsilon_m]} \right] \\ &= \omega_{TO}^2 \left[\frac{\varepsilon_0 coth(q_iL_i/2) + \varepsilon_m}{\varepsilon_\infty coth(q_iL_i/2) + \varepsilon_m} \right] \end{aligned} \tag{2.22}$$

Figure 2.18 shows the SO dispersion relation for a rectangular cross section ZnO NW for a dielectric surrounding media with dielectric constant $\varepsilon_m = 1.7$. The SO dispersion relation is calculated from Eq. (2.21) and Eq. (2.22), corresponding to symmetric and asymmetric modes, respectively. The two branches of the SO phonon dispersion relation converge for values

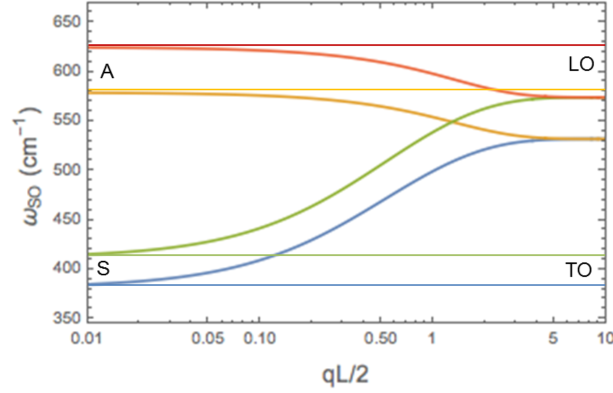

Figure 2.18: SO phonon dispersion relation for rectangular cross section ZnO NWs for a dielectric medium composed by air and Si/SiO_2 (substrate) calculated from Eq. (2.21) and Eq. (2.22), corresponding to symmetric modes (S) and asymmetric (A), respectively. Four horizontal solid lines represent LO (red and orange ones) and TO (green and blue ones) frequencies.

of $qL/2$ greater than 1 (see Fig. 2.18). For 'large dimensions' NWs, i.e. $qL/2 > 1$, the analytical expression for the relation dispersion of the SO phonon is given by

$$\omega_{SO}^2 = \omega_{TO}^2 \frac{\varepsilon_0 + \varepsilon_m}{\varepsilon_0 + \varepsilon_\infty} \tag{2.23}$$

The ZnO NWs studied in this work satisfy this condition (q is typically of the order of 10^7-10^9 m^{-1} [106] and r between 100 - 150 nm (that is the average radius of the NWs)), therefore Eq.(2.23) will be used for the theoretical calculations of the frequency value of the SO phonons.

Chapter 3

Characterisation techniques

This Chapter provides the physical basis and the experimental details of the different spectroscopic techniques used for the characterisation of the structural and optical properties of the investigated samples.

In the first Section, the fundamental physics ground of Raman scattering process, Raman selection rules for WZ and ZB structure and the used experimental setup are presented. In the second one, the theoretical basis for surface enhanced Raman spectroscopy and important characteristics of this technique are given. The third Section is devoted to the main characteristics of photoluminescence spectroscopy and the employed experimental apparatus. In the last, the theoretical background of X-ray spectroscopy techniques, i.e., X-ray fluorescence, X-ray diffraction and the X-ray absorption near edge structure, and the description of the X-ray nano-probe beamline ID22NI are reported. All these techniques enable the study of ensembles and single NWs.

3.1 Raman scattering spectroscopy

The Raman scattering is an effect that was discovered by Chandrasekhara Venkata Raman in 1921 in India [107]. He observed with a really rudimental experiment what is named today 'anti-stokes Raman scattering' that has really low probability to occur. All that involves the measurement of photons arising from the Raman effect is called *Raman spectroscopy.*

Raman spectroscopy techniques analyses the inelastic scattering of light by elementary excitation of solids or molecules. It is a powerful, non-destructive, contact-less technique that is used for obtaining information on the chemical composition, the crystalline quality and the strain fields of crystals, mainly semiconductors. A similar technique originating from elastic processes is referred to as Rayleigh scattering. Since inelastic scattering involves an excitation of the material, the scattering cross-section is typically much smaller than that of infrared absorption or secondary emission ones, thus, Raman spectroscopy has an intrinsically low detection sensitivity.

Because of its low detection limit, it has taken decades before it became as widely used as today. Starting from 1970, its detection sensitivity was significantly improved by the invention of lasers, that are used as very powerful source of light for Raman spectroscopy.

3.1.1 Theoretical background

The description below follows Chapter 17 of reference [108] by Daniel Wolverson, where a more detailed description can be found.

Classical approach

The electric field of light inside a dielectric medium induces a macroscopic polarisation ($\mathbf{P}$) of the material itself, that can be described by the following equation:

$$\mathbf{P} = \varepsilon_0 \chi \mathbf{E} \tag{3.1}$$

where $\mathbf{E}$ is the in-coming electric field, χ is the dielectric susceptibility of the material (which depends on the frequency of the in-coming light and it is a second rank tensor χ_{jk}), and ε_0 is the vacuum permittivity. The time and space variation of the electric field of light is of the form

$$\mathbf{E}(\mathbf{r}, t) = \mathbf{E}(\mathbf{k}_I, \omega_I) cos(\mathbf{k}_I \cdot \mathbf{r} - \omega_I t) \tag{3.2}$$

where ω_I is the angular frequency and $\mathbf{k}_I$ the wave vector. In the medium there are fluctuations of the susceptibility generated by vibrational excitations of the atoms, i. e., *phonons*. The atomic displacement of the media due to phonons is described as

$$\mathbf{u}(\mathbf{r}, t) = \mathbf{u}(\mathbf{q}, \omega_{ph}) cos(\mathbf{q} \cdot \mathbf{r} - \omega_{ph} t) \tag{3.3}$$

where ω_{ph} is the angular frequency of the phonon and $\mathbf{q}$ its wavevector. Assuming that the variation of the susceptibly by the displacement u is small, we can expand χ_{jk} in Tayolr series in u keeping only the first two lowest order terms (representing the first-order Raman scattering), and we obtain

$$\chi_{jk}(\mathbf{k}_I, \omega_I) \approx \chi_{jk}(\mathbf{k}_I, \omega_I)_{\mathbf{u}=0} + \left(\frac{\partial \chi_{jk}(\mathbf{k}_I, \omega_I)}{\partial u_l} \right)_{\mathbf{u}=0} u_l + \dots \tag{3.4}$$

Note that Eq. (3.4) could be easily extended to second or even higher orders, causing induced polarisation at higher orders, and therefore, second order Raman scattering or Raman overtones.

Substituting Eq. (3.2) and Eq. (3.4) in Eq. (3.1), the expression of the polarisation becomes

$$P(\mathbf{r}, t, \mathbf{u}) = P_0(\mathbf{r}, t) + P_{ind}(\mathbf{r}, t, \mathbf{u}) \tag{3.5}$$

where

$$P_0(\mathbf{r},t) = \chi_0(\mathbf{k}_I,\omega_I)\mathbf{E}_I(\mathbf{k}_I,\omega_I)cos(\mathbf{k}_I\mathbf{r} - \omega_I t) \tag{3.6}$$

is the polarisation vector vibrating in phase with the incident radiation, i. e., the term responsible for the elastic light scattering (*Rayleigh scattering*), and

$$\begin{aligned} P_{ind}(\mathbf{r},t,\mathbf{u}) &= \left(\frac{\partial\chi}{\partial\mathbf{u}}\right)_0 \mathbf{u}(\mathbf{r},t)\mathbf{E}_I(\mathbf{k}_I,\omega_I)cos(\mathbf{k}_I - \omega_I t) \\ &= \left(\frac{\partial\chi}{\partial\mathbf{u}}\right)_0 \mathbf{u}(\mathbf{q},\omega_{ph})cos(\mathbf{q}\cdot\mathbf{r} - \omega_{ph}t)\times \\ &\times \mathbf{E}_I(\mathbf{k}_I,\omega_I)cos(\mathbf{k}_I - \omega_I t) \end{aligned} \tag{3.7}$$

is the polarisation vector induced by the phonon. We are interested only in Eq. (3.7), that represents the term of first-order Raman scattering, and could be rewritten as

$$\begin{aligned} P_{ind\ j}(\mathbf{r},t,\mathbf{u}) = \frac{1}{2}\varepsilon_0\left(\frac{\partial\chi_{jk}(\mathbf{k}_I,\omega_I)}{\partial u_l}\right)_{\mathbf{u}=0} u_l(\mathbf{q},\omega_{ph})E_k(\mathbf{k}_I,\omega_I)\times \\ \times\left\{cos[(\mathbf{k}_I+\mathbf{q})\cdot\mathbf{r} - (\omega_I+\omega_{ph})t] + cos[(\mathbf{k}_I-\mathbf{q})\cdot\mathbf{r} - (\omega_I-\omega_{ph})t]\right\} \end{aligned} \tag{3.8}$$

Eq. (3.8) contains oscillating terms at $\omega_I+\omega_{ph}$ and $\omega_I-\omega_{ph}$ frequencies. This implies that the intensity of the emitted radiation will contain two sidebands, that are the Raman-scattered light waves: conventionally, the terms + is referred to 'anti-Stokes' and the one − to the 'Stokes' scattered light, as it is depicted in Fig. 3.1. Anti-Stokes scattering has lower probability to occur, because the scattered light is more energetic than the incoming one. The prefactor in Eq. (3.8)

$$R_{jk,l}(\mathbf{r},t,\mathbf{u}) = \left(\frac{\partial\chi_{jk}(\mathbf{k}_I,\omega_I)}{\partial u_l}\right)_{\mathbf{u}=0} u_l(\mathbf{q},\omega_{ph}) \tag{3.9}$$

is defined as the Raman tensor (R) which determines the amplitude of the scattered wave for a given vibrational mode l. Therefore, we can now define the intensity (I) of the scattered radiation (with polarisation e_j) coming from the in-coming one (with polarisation e_k), when scattered by the l-mode as

$$I \propto \mid e_j^S \cdot R_{jk,l} \cdot e_k^I \mid^2 \tag{3.10}$$

If the l-th mode is degenerate, a summation over all $\mathrm{R}_{jk,l}$ corresponding to the set of degenerate modes is required.

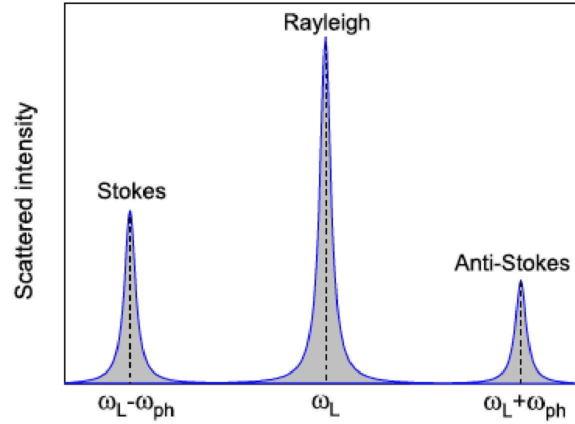

Figure 3.1: Diagram showing Rayleigh, Stokes, and anti-Stokes scattering of light. Stokes scattered light is always more intense than anti-Stokes.

Quantum approach

The classical formalism of Raman scattering cannot account of two important aspects: the effect of resonances and the phonon statistics. In the quantum approach the normal modes of atomic vibrations in a crystal are quantised and they are properly referred to as phonons, like in the classic approach. In this picture, a photon excites the electronic system to a higher energy state (real or virtual). The whole process can be explained following both the Feynman diagrams of Fig. 3.2 or the band structure diagram of Fig. 3.3. These present three possible steps: first of all, the creation of an electron-hole pair (see Fig. 3.2 a) or an exciton (see Fig. 3.2 b) in the state $|n\rangle$ in the crystal through the absorption of a photon; second, the creation or the annihilation of a phonon, leaving the system in the state $|m\rangle$; and finally, the recombination of the hole-pair, returning the system to its original ground state $|i\rangle$ (taken as the zero energy) and generating the scattered photon. The scattering process must comply with conservation laws, which impose requirements that are evident from Fig. 3.3. Thus, in a first-order scattering process involving only a single quantum of excitation the following relations have to be fulfilled:

$$\hbar\omega_S = \hbar(\omega_I \pm \omega_{ph}) \tag{3.11}$$

$$\hbar\mathbf{k}_S = \hbar(\mathbf{k}_I \pm \mathbf{k}_{ph}) \tag{3.12}$$

where ω_I, ω_S and ω_{ph} are the energies of the in-coming and the scattered light, and energy released in the scattered system (that correspond to the energy of the phonon) and $\mathbf{k}_I$, $\mathbf{k}_S$ and $\mathbf{k}_{ph}$ are the wavevector of the in-coming and scattered radiation and of the phonon. The sign minus applies to cases where a phonon is generated in the scattering process (Stokes scattering). On the contrary, if the phonon is annihilated the sign plus applies (anti-Stokes

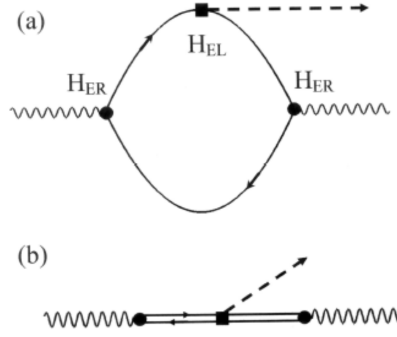

Figure 3.2: Feynman diagrams representing phonon Raman scattering. Time flows from left to right. Wavy lines: photons; solid lines: electrons and holes; dashed lines: phonons; solid circles: electron-radiation interaction vertex; solid squares: electron-lattice interaction vertex. Intermediate states: (a) electron-hole pair; (b) exciton. Figure taken from Reference [108].

scattering). $\hbar\omega_{ph}$ is normally referred to as *Raman shift* or *Raman frequency*. The first-order processes access only elementary excitation near the Γ point, while in higher order processes, the scattering wavevector is a sum of single wavevectors $\mathbf{k}_i$ which span the whole Brillouin zone.

Since the interactions in Raman scattering are weak, it is possible to calculate via third-order perturbation theory the scattering probability in terms of the electron-radiation H_{ER} and electron-lattice H_{EL} coupling strengths [109]. In the following, only Stockes processes are taken into account. The Fermi's golden rule allows to calculate the probability P_{ph} for scattering an electron from the initial state $|i\rangle$ to the final state $|f\rangle$ [110], that in case of Raman scattering are the same as it is shown in Fig. 3.3:

$$P_{ph}(\omega_S, \omega_{ph}) = \frac{2\pi}{\hbar} \left| \sum_{n,m} \frac{\langle i| H_{ER}(\omega_S) |m\rangle \langle m| H_{EL}(\omega_{ph}) |n\rangle \langle n| H_{ER}(\omega_I) |i\rangle}{[\hbar\omega_I - (E_n - E_i)][\hbar\omega_S - (E_m - E_i)]} \right|^2 \delta(\hbar\omega_I - \hbar\omega_S - \hbar\omega_{ph}) \tag{3.13}$$

where $|n\rangle$ and $|m\rangle$ are intermediate electronic states. Eq. (3.13) can be simplified considering a real discrete intermediate state $|s\rangle$ of energy E_s and finite lifetime τ_s, thus, the scattering probability can be re-written as [109]

$$P_{ph}(\omega_S) \propto \frac{2\pi}{\hbar} \left| \frac{\langle i| H_{ER} |s\rangle \langle s| H_{EL} |s\rangle \langle s| H_{ER} |i\rangle}{[E_s - \hbar\omega_I - i\Gamma_s][E_s - \hbar\omega_S - i\Gamma_s]} \right|^2 \tag{3.14}$$

where Γ_s is the damping constant and is equal to $\Gamma_s = \hbar/\tau_s$.

If the incoming radiation or the scattered light is close to E_s, the probability of exciting a phonon through the intermediate state $|s\rangle$ increases considerably, because the denominator of Eq. (3.14) goes to zero. This

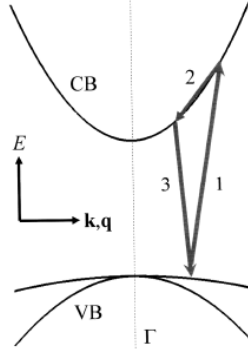

Figure 3.3: The scattering process shown in Fig. 3.2 (a), now represented as transitions on the diagram showing the band structure near the Γ point (k=0) of a zinc blende semiconductor. The transitions are numbered 1-3 in the sequence in which they appear (from left to right) in Fig. 3.2 (a) and in the text. Figure taken from Reference [108].

process is called resonant Raman scattering (RSS). The RRS becomes vital when the signal in off-resonance conditions is weak (e. g., in case of NWs).

The second aspect introduced by the quantum mechanical nature of the Raman process is the probability of annihilating a phonon in an anti-Stokes process, which depends on the temperature of the sample and is given by the probability occupation of a given phonon state following Bose-Einstein statistics. The Raman scattering efficiency η_{RS} in the case of one phonon is defined as the ratio (S) of scattered to incident power per unit path length L and unit solid angle Ω (see Fig. 3.4) [111] and is proportional to

$$\eta_{RS} = \frac{\partial S}{L \cdot \partial \Omega} \propto \frac{\omega_S^2}{c^3} \left| \mathbf{e}^I \cdot R \cdot \mathbf{e}^S \right|^2 \frac{\hbar}{\omega_{ph}} \begin{Bmatrix} (n_B + 1) & Stokes \\ n_B & anti - Stokes \end{Bmatrix} \tag{3.15}$$

where n_B is the Bose-Einstein statistical factor

$$n_B = \frac{1}{e^{\frac{\hbar \omega_{ph}}{k_B T}} - 1} \tag{3.16}$$

Thanks to Eq. (3.15) it is possible to calculate Stokes and anti-Stokes scattering intensities ratio (I_{AS}/I_A) under non-resonant conditions

$$\frac{I_{AS}}{I_S} = \left(\frac{\omega_I + \omega_{ph}}{\omega_I - \omega_{ph}} \right)^4 exp\left(-\frac{\hbar \omega_{ph}}{k_B T} \right) \tag{3.17}$$

Eq. (3.17) implies that Stokes scattering is Stokes scattering can take place at any temperature, while the anti-Stokes one takes place only if T is high enough so a high density of phonons are present in the material.

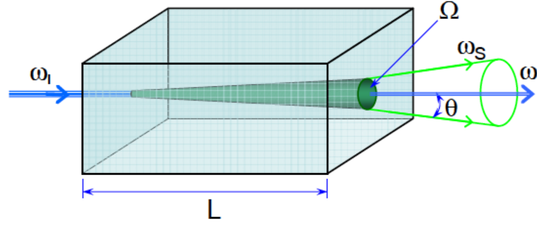

Figure 3.4: Illustration of the elastics and inelastic light scattering in a path length L and solid angle Ω. ω_I and ω_S represents the incoming and the scattered photon frequency, respectively.

3.1.2 Raman selection rules

According to Eq. (3.10), the intensity of the Raman scattered light depends on the polarisation of the incident and the scattered light and on the Raman tensor, which is related to the crystal symmetry. The Raman tensor contains the selection rules for the phonons. The Raman selection rules for ZB and WZ structures will be given in this Section.

In ZB crystal, with point group T_d, x, y and z are equivalent and therefore the phonons are three-fold degenerate. The related Raman tensors must have the same symmetry properties, therefore they should have the following form [108]

$$R_x = \begin{pmatrix} 0 & 0 & 0 \\ 0 & 0 & d \\ 0 & d & 0 \end{pmatrix}; R_y = \begin{pmatrix} 0 & 0 & d \\ 0 & 0 & 0 \\ d & 0 & 0 \end{pmatrix}; R_z = \begin{pmatrix} 0 & d & 0 \\ d & 0 & 0 \\ 0 & 0 & 0 \end{pmatrix} \tag{3.18}$$

The suffixes x, y and z indicate the direction of polarisation of the mode.

In WZ crystal, with point group C_{6v}, x and y are equivalent to each other but are normal to the non-equivalent direction of the six-fold rotation axis z (c-axis of the WZ structure). The three Raman-active symmetry types are usually labelled A_1, which is non-degenerate and it corresponds to a displacement in the z direction and E_1 and E_2 (each of them two-fold degenerate) corresponding to a displacement perpendicular to the z direction (as it is shown in Fig. 2.14). The corresponding Raman tensors are represented by the following (3×3) matrices with the non-zero elements a, b, c, d [112]

$$\begin{aligned} R_z^{A_1} &= \begin{pmatrix} a & 0 & 0 \\ 0 & a & 0 \\ 0 & 0 & b \end{pmatrix}; R_x^{E_1} = \begin{pmatrix} 0 & 0 & c \\ 0 & 0 & 0 \\ c & 0 & 0 \end{pmatrix}; R_y^{E_1} = \begin{pmatrix} 0 & 0 & 0 \\ 0 & 0 & c \\ 0 & c & 0 \end{pmatrix}; \\ R^{E_2} &= \begin{pmatrix} d & 0 & 0 \\ 0 & -d & 0 \\ 0 & 0 & 0 \end{pmatrix}; R^{E_2} = \begin{pmatrix} 0 & 0 & -d \\ 0 & -d & 0 \\ 0 & 0 & 0 \end{pmatrix} \end{aligned} \tag{3.19}$$

Therefore the Raman selection rules are calculated solving Eq. (3.10) for each of the tensors above and with a set of $\mathbf{e}^I$ and $\mathbf{e}^S$. The selection rules for the phonons for WZ and ZB structures in back-scattering configuration are summarised in Table 3.1.

Table 3.1: Raman selection rules in backscattering configuration. The modes for WZ structure are given for different polarisation configurations x = [100] and y = [010], x$'$=[1$\bar{1}$0] and y$'$=[$\bar{1}$10] (Table taken from [113]) and those for the ZB structure for the polarisation x$''$=[111] and y$''$=[1$\bar{1}$1] (Table taken from [110]).

Surface	$\hat{e}_i$	$\hat{e}_s$	Porto notation	Allowed Modes	
				Cubic	Hexagonal
(001)	[$\bar{1}$10]	[$\bar{1}$10]	$z(y',y')\bar{z}$		A_1(LO), $E_{2l,h}$
	[110]	[$\bar{1}$10]	$z(x',y')\bar{z}$		$E_{2l,h}$
	[100]	[100]	$z(y,y)\bar{z}$		A_1(LO), $E_{2l,h}$
	[010]	[100]	$z(x,y)\bar{z}$		$E_{2l,h}$
(110)	[001]	[001]	$x'(z,z)\bar{x}'$		A_1(TO)
	[$\bar{1}$10]	[001]	$x'(y',z)\bar{x}'$		E_1(TO)
	[$\bar{1}$10]	[$\bar{1}$10]	$x'(y',y')\bar{x}'$		A_1(TO), $E_{2l,h}$
(111)	[11$\bar{2}$]	[11$\bar{2}$]	$x''(z'',z'')\bar{x}''$	TO, LO	
	[11$\bar{2}$]	[1$\bar{1}$0]	$x''(z'',y'')\bar{x}''$	TO	

Pure LO and TO phonons are observed in a semiconductor only when the in-coming or the scattered radiation are parallel or perpendicular to the optical axes. For other directions of propagation, Raman signal shows a polar angle dependence resulting from a mixture of modes known as *quasi-modes* or *q-modes* [114]. In the case of WZ semiconductors, mixing of A_1 or E_1 modes occurs for intermediate propagation direction, giving quasi-TO and quasi-LO modes. The frequency ω_Q of these modes follows [95]

$$\omega_Q(TO) = \omega^2(E_1[TO])cos^2\theta + \omega^2(A_1[TO])sin^2\theta \tag{3.20}$$

$$\omega_Q(LO) = \omega^2(A_1[LO])cos^2\theta + \omega^2(E_1[LO])sin^2\theta \tag{3.21}$$

where θ is the angle between the c-axis and the phonon propagation direction.

3.1.3 Experimental apparatus

The basic elements of a Raman set-up are: a light source, the optical instrumentation for the excitation of the sample and the collection of the scattered light, a spectrometer for dispersing the scattered signal and to separate the intense Rayleigh contribution (generally a factor 10^{10} stronger than the Raman signal) and a highly sensitive photodetector. The optical path and the different components of the set-up are illustrated in Fig. 3.5. The light source is a laser, that is monochromatic, polarised, collimated

and has high intensity, so that the problem of the low intensity of the Raman signal can be overcome. For eliminating unwanted plasma-lines and sidebands of the laser, an holographic filter is used. A confocal optical microscope (equipped with 100× and 40× objectives in the case of visible and UV light, respectively) focuses the excitation light on the sample and collects the scattered one. The diameter of the laser spot on the sample is of 1μm or 4 μm when using the 100× and the 40× objectives, respectively. The microscope is coupled to a Jobin Yvon T64000 triple spectrometer, equipped with a liquid-nitrogen-cooled charge couple device (CCD). The spectrometer can be operated in single configuration, with an edge filter placed at the entrance slit for rejecting the Rayleigh scattered light. The focal distance of the T64000 system is of 0.64 m and a set of 900/1800/2400 groove/mm grating are used to disperse the light. The spectral resolution of the whole system is around 1 cm^{-1}.

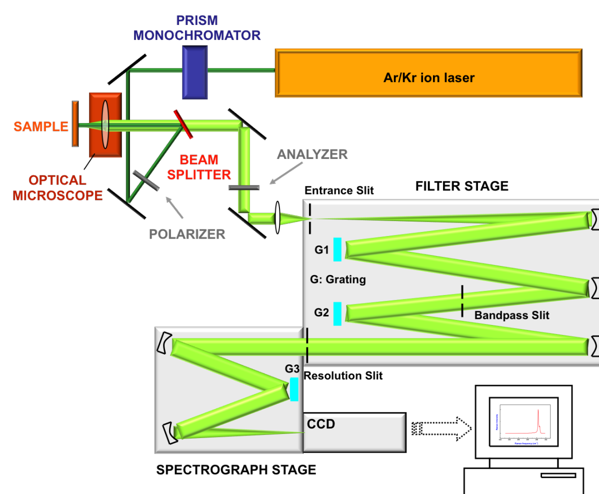

Figure 3.5: Schematic experimental Raman set-up used for Raman and SERS measurements.

This set-up enables the study of nanostructures, in particular ensembles and single NWs, due to the microsize of the laser spot.

3.2 Surface Enhanced Raman Spectroscopy

In the early 70s many research teams were investigating how to detect a single monolayer of molecules. *Fleischmann et al.* [115] reported the first observation of surface enhanced Raman spectroscopy (SERS) in 1974. They were studying the Raman scattering of the molecule pyridine adsorbed from an aqueous solution by a silver electrode. The increased intensity of the signal that they detected was wrongly interpreted as the effect of the augmented surface area of the electrode, that implies a larger number of molecules adsorbed and, consequently, sampled. In 1977, two independent

papers by *Jeanmaire and Van Duyne* [116] and *Albrecht and Creighton* [117], demonstrated that the reason of the enhancement was directly connected to the presence of the noble metal. Therefore, SERS consists in the amplification of the Raman signal through the electromagnetic interaction of light with metals, which produces large amplifications of the laser field through excitations known as plasmons. If a probe (i. e., molecule, crystal, ...) produces Raman signal, in principle it can be amplified by the excitation of localised surface plasmon resonances of the metallic substrate (that are not pure plasmons, see Section 3.2.1).

The SERS-active substrates are usually in the form of metal films or particles [58]. The magnitude of the SERS enhancement is directly dependent on the SERS substrate. Nowadays, the investigation is mostly focusing on silver and gold nanoparticles due to their outstanding capabilities compared to their film counterpart. Very good results have been achieved in the synthesis of nanoparticles with high yield and tunable aspect ratio from 1 (spherical particles) to more than 10 (nanorods) [58]. Moreover, using nanoparticles allows to have better control on their assembly for optimising SERS enhancement factor.

Up to now, the outstanding capabilities of SERS have been vastly used for non-destructive characterisation and detection of chemical species down to single-molecule resolution [118, 119]. Although molecules represent the ideal targets to demonstrate the enhanced capabilities of SERS compared to standard Raman spectroscopy, also semiconductor nanostructures can benefit from this technique [59]. In fact, SERS analysis can potentially provide meaningful information on crystal defects, surface states, interface crystal quality in heterostructures, etc.

It is important to evaluate how much the SERS signal can be boosted with respect to normal Raman conditions. The magnitude that quantifies the SERS effect is called *enhancement* factor (EF), which can have electromagnetic (EM) and chemical (CH) origin. Theoretical calculations predict that the EM-EF can be as large as $\sim 10^4 - 10^6$ at plasmon resonances, this typically happens in very specific regions of the SERS substrate known as hot spots [57]. The CH-EF is important for understanding the SERS mechanism but, in general, it does not contribute significantly to the SERS EF [57].

3.2.1 Plasmon resonaces

Some relevant optical properties of metals (like other properties) are due to the presence of free electrons in the conduction band (*plasma*). In order to model the optical response of the plasma, a system of equations that describes the relation between electromagnetic field and currents and charges inside the plasma is needed.

A simple and effective model for describing the free electron plasma is the Drude model [120], where a complex dielectric function depicts exhaustively

the optical response of the metal:

$$\epsilon(\omega) = \epsilon_\infty \left(1 - \frac{\omega_p^2}{\omega^2 + i\gamma_0\omega}\right) \tag{3.22}$$

where ω is the angular frequency of the interacting light wave, the damping term γ_0 corresponds to the collision rate of free electrons with crystal or impurities, that is small compared to ω, and

$$\omega_p = \sqrt{\frac{ne^2}{m\epsilon_0\epsilon_\infty}} \tag{3.23}$$

is called the *plasma frequency*, and the corresponding wavelength is $\lambda_p = 2\pi c/\omega_p$, giving the natural oscillation frequency of the free-electron plasma, n is the number of free electrons per unit volume and m their mass. In a first approximation the contribution of the ions can be considered constant, leading to a constant background real dielectric function $\epsilon_\infty \geq 1$. The real and the imaginary part of Eq. (3.22) are

$$Re(\epsilon(\omega)) = \epsilon_\infty \left(1 - \frac{\omega_p^2}{\omega^2 + \gamma_0^2}\right) \tag{3.24}$$

and

$$Im(\epsilon(\omega)) = \frac{\epsilon_\infty\omega_p^2\gamma_0}{\omega(\omega^2 + \gamma_0^2)} \tag{3.25}$$

For Au, that is the metal which has been used as SERS substrate for samples studied in this work, $\omega_p = 13.8 \times 10^{15} s^{-1}$ and $\gamma_0 = 1.075 \times 10^{11} s^{-1}$. Equations (3.24) and (3.25) for Au parameters are plotted in Fig. 3.6. The monotonous decay of $Re(\epsilon(\omega))$ from small values in the UV to negative values in the visible and very negative values in the infrared is common to all metals. In the region where $\omega < \omega_p$, therefore the radiation wavelength is grater than λ_p, $Re(\epsilon(\omega)) < 0$ and if ω is not too small, the absorption, that is characterised by $Im(\epsilon(\omega))$, is also small. This condition originates interesting optical effects, including *plasmon resonances*. For all metals, the plasma frequency is in the UV part of the electromagnetic spectrum.

This model, despite its simplicity, is valid for describing part of the optical response of Au and Ag. However, there are few cases in which this approximation is unsuccessful in providing an explanation to the experimental observation [107]. Free conduction electrons also experiment intra-band optical transitions, since the excited electrons remain in the conduction band and in a real metal, additional optical processes are contributing to the optical properties. However, in the case of SERS the Drude model is still valid.

A *plasmon* is a quantum quasi-particle representing the elementary excitations, or modes, of the charge density oscillations in a plasma [107].

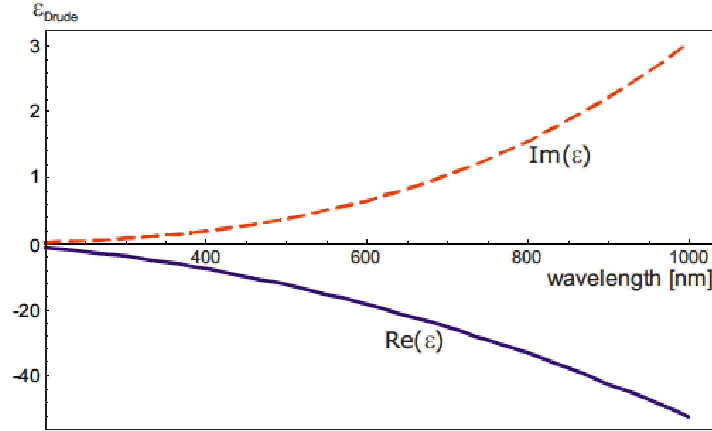

Figure 3.6: Real and imaginary part of the dielectric function for Au according to the Drude free electron model. The blue solid line represents the real part and the red dashed line is the imaginary part. Note the different scales for real and imaginary part. Figure adapted from Reference [121].

When an electromagnetic wave propagates in a medium holding plasmons, this excites the internal degree of freedom of the medium, and new modes called *plasmon-polaritons* appear, which would not exist without the presence of interfaces, and their properties depend on the optical properties of the outside medium. Localised surface plasmon-polaritons (LSP) are dispersive electromagnetic waves confined at the metal/dielectric interface in systems with dimensions smaller than the incident radiation wavelength. Due to their not propagative nature, they are defined as localised.

As mentioned previously, the negative real part of $\epsilon(\omega)$ is strictly linked to the existence of plasmons and plasmon resonances. To understand it, the problem of a metallic nano-sphere of radius r smaller than the light wavelength is considered. In this case, the problem can be solved in the *quasi-static approximation*. Thus, it is equivalent to the electrostatic problem of a sphere of radius r in a medium with dielectric constant ϵ_M and in a uniform external electric field E_0. The considered system is depicted in Fig. 3.7. The field inside and outside the sphere, E_{In} and E_{out}, respectively, can therefore be extracted directly solving the Laplace equation [107]:

$$E_{In} = \frac{3\epsilon_M}{\epsilon_p(\omega) + 2\epsilon_M} E_0 \tag{3.26}$$

$$E_{out} = E_0 + \frac{3\mathbf{n}(\mathbf{n} \cdot \mathbf{p}) - p}{4\pi\epsilon_0\epsilon_M r^3} \tag{3.27}$$

where E_0 is the intensity of the external field, $\epsilon_p(\omega)$ the complex dielectric function (Drude's model) of the particle, ϵ_M the dielectric constant of the medium, ε_0 is the vacuum permittivity, r the radius of the particle, $\mathbf{n}$ the unit vector representing the direction of r and $\mathbf{p} = \epsilon_M \alpha(\omega)\mathbf{E}_0$ the dipole

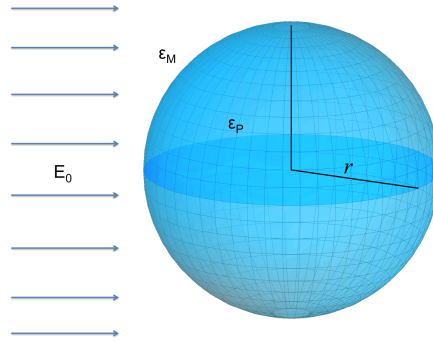

Figure 3.7: Sketch of a spheric particle with radius r and dielectric function ϵ_p immersed in a uniform medium with dielectric constant ϵ_M and uniform electric field E_0.

moment with polarisability $\alpha(\omega)$

$$\alpha(\omega) = 4\pi\epsilon_0 r^3 \frac{\epsilon_p(\omega) - \epsilon_M}{\epsilon_p(\omega) + 2\epsilon_M} \tag{3.28}$$

E_{out} has two terms, one is the external applied field and the second is identical to that generated by a dipole **p** located at the centre of the sphere, and it shows a fast spatial decay with the distance from the metal surface $\propto r^{-3}$.

The denominator of Eq. (3.28) goes to zero if $\epsilon_p(\omega) \approx -2\epsilon_M$, that implies

$$Re(\epsilon_p(\omega)) \approx -2\epsilon_M \tag{3.29}$$

and

$$Im(\epsilon_p(\omega)) \approx 0 \tag{3.30}$$

In this case the optical response of the electron plasma (absorption and scattering) at this particular wavelength will correspond to a *resonance*. Using the dielectric function of Drude's model (Eq. (3.24)), the resonance frequency ω_{LSP} that satisfies Eq. (3.29) is

$$\omega_{LSP} = \frac{\omega_p}{\sqrt{1 + 2\epsilon_M}} \tag{3.31}$$

This corresponds to a LSP resonance which is now in the visible ($\omega_p/\sqrt{3}$ in air) and redshifts as ϵ_M increases.

Similar effects exist for other geometries and configuration, but with different resonance conditions: optical resonance conditions in small objects do not depend only from the material, but also strongly from the **geometry** of the object. Therefore, two objects of the same material but with different geometries have different resonances, that always correspond to the negative real part of $\epsilon(\omega)$. The quasi-static approximation shows that, in resonant

conditions, the field amplitude is strongly enhanced near the surface of the particle and is homogeneous inside it, as it is shown schematically in Fig. 3.8.

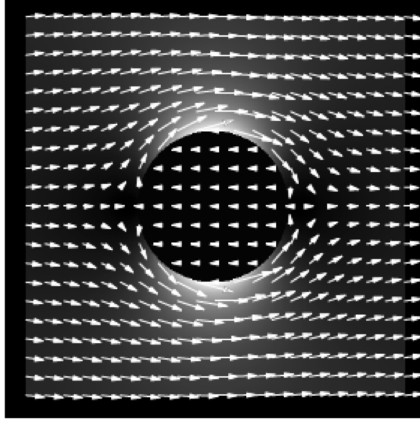

Figure 3.8: Sketch of the field distribution around a section of a nanosphere. Figure taken from Reference [121].

The scattering σ_{scatt} cross-section of the sphere is given by

$$\sigma_{scatt} = \frac{k^2}{6\pi\varepsilon_0^2}|\alpha(\omega)|^2 \tag{3.32}$$

However, the power removed from the incident radiation due to the presence of a particle is not only due to scattering process but also due to absorption. The absorption cross-section σ_{abs}, which takes into account the dissipated power inside the nanoparticle, is

$$\sigma_{abs} = \frac{k}{\varepsilon_0} Im[\alpha(\omega)] \tag{3.33}$$

where k is the wave-vector in the surrounding medium. Figure 3.9 shows the normalised scattering cross-section of Au and Ag particles with $r = 20$ nm in different media. The resonance for the Ag particles is in the ultraviolet spectral range, while for Au the maximum scattering occurs around 530 nm. A redshift of the resonance is observed if the dielectric constant of the environment is increased.

In the case of nanoparticles with ellipsoidal geometry, like nanorods, which have been used as SERS active elements in the fabrication of the sample studied in this work, solving Laplace equation in the quasi-static approximation [122] results in two spectrally separated plasmon resonances, corresponding to the oscillation of the electron plasma along the long and short axes of the nanorod, respectively. They will be referred to as longitudinal plasmonic resonance (LPR) and transversal plasmonic resonance (TPR).

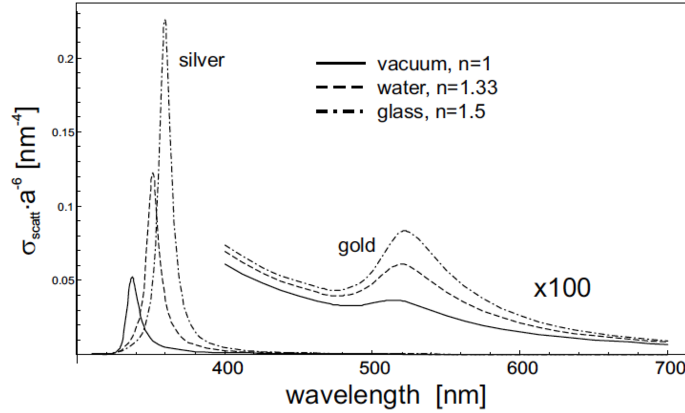

Figure 3.9: Plots of the scattering cross-section of spherical Au and Ag particles with radius of 20 nm in different environments. Solid line: vacuum (n=1). Dashed line: water (n=1.33). Dash-dotted line: glass (n=1.5). Figure taken from Reference [121].

3.2.2 Enhancement factor

As mentioned above, the magnitude that measures how much the Raman signal is boosted by SERS is the EF. Thus, it has a central role in SERS and it needs to be clearly defined in order to correctly compare the SERS of identical substrates. Still nowadays, there is a big variability in the literature on the EF, this makes difficult (impossible, even) to compare different SERS substrates.

Two multiplicative contributions give the EF: the EM-EF and the CH-EF. The former, which is the main contribution, is due to the coupling of the incident and scattered electromagnetic fields with the SERS substrate. Thus, it can be separated into two multiplicative EFs

$$EM - EF = EF_{E_0} \cdot EF_{E_{scatt}} \tag{3.34}$$

where EF_{E_0} takes into account the incident field (E_0) and $EF_{E_{scatt}}$ the re-emitted (scattered) one. It depends directly on the intense electromagnetic fields generated when LSP resonance is excited at noble metal nanostructure/dielectric interfaces. The CH-EF, on the other hand, is still subject to controversy [107] and its contribution is considered to be smaller than that of the EM-EF. The CH is generally thought to rely on the modification of the electronic polarisability of the probe, which can induce resonant-Raman scattering and therefore enhanced signals at wavelengths where the probe would not be resonant. The mechanism that enables this enhancement is called *charge transfer* [107].

The EF strongly depends on several factors: the characteristics of the laser excitation (wavelengths, angle of incidence, ...), detection set-up (scattering configuration, solid angle for collection, ...), metal of the SERS substrate

(shape, size, refractive index of the surrounding medium) and, Raman cross-section and distance between the metallic surface and the probe. It is difficult to take into account all these parameters for giving a universal definition of the EF, on the contrary, a simpler definition would fit for almost all the cases, even though it would be approximated. Before giving the definition, it is important to stress that the EF is highly non-uniform on the SERS substrate. Points of very large enhancement, the so-called 'hot spots' are generally highly localised and not always reproducible, and they are placed within tens of nanometers of points with little or negligible enhancement. Therefore, there are two categories of EF: the averaged EF, that represents an average property of the substrate and the single-point EF, which corresponds to the enhancement only at specific positions of the substrate. Each type of definition is relevant depending on the application/experiment. Taking into account that only probes that are in direct contact with the metal or at least at a distance less than $\sim$ 10 nm contribute to the SERS signal, the following definition for the EF is given for the case of molecules [107]

$$EF = \frac{I_{SERS}/N_{Surf}}{I_{RS}/N_{Vol}} \tag{3.35}$$

where N_{Vol} is the average number of probes in the scattering volume Vol for the non-SERS Raman and N_{Surf} is the average number of both adsorbed or really near probes present in the volume Vol. Equation (3.35) is considered the best estimation of the average EF for a SERS substrate. However, in the case of SERS on semiconductors NWs, a unique and clear definition of EF has not been encountered, yet. Normally, an estimation of the EF is given calculating the ratio between the SERS signal and the Raman one obtained from the decorated and bare semiconductor material, respectively.

3.2.3 Variability of SERS signal

SERS signal, contrary to the traditional Raman one, often presents fluctuations in the intensity, in the peak position and width and in the relative intensity of the peaks [107]. The fluctuations on different points of the SERS substrate are ascribed to its non-uniformity, however in most cases, temporal fluctuations remain and their causes are still under study. Some possible causes could be:

- changes in the environment, due to large laser powers, further locally enhanced, can alter the roughness of the surface of the probe or induce mechanical movements of the metallic nanoparticles (change in the hotspots);

- photochemistry and photoblenching induced directly by the laser or indirectly by the heating of the substrate, resulting in desorption, re-

orientation, chemical transformation or destruction/partial destruction of the probe.

For minimising these effects it is recommended to, if possible, varying the power density and making a suitable choice of the SERS substrate. However, even following the previously mentioned recommendations, the fluctuations in SERS spectra are still not negligible. The origin of SERS fluctuations is still unknown and should be assessed on a case-by-case basis. Consequently, the reproducibility and the reliability of the results is poor, therefore, it is mandatory to use a statistical approach to correctly interpret and extract reliable results from SERS experiments.

3.3 Photoluminescence spectroscopy

As Raman spectroscopy, photoluminescence (PL) spectroscopy is a non destructive technique that is widely used for the study of the optical, structural and electronic properties of semiconductors, e.g., crystal quality, impurities, defects, electronic band structure. Moreover, the study of PL as a function of temperature or power, gives additional information about some properties (such as identification of defects). Additionally, PL allows to obtain very useful information on the properties of semiconductor heterostructures, such as internal efficiency.

PL in a semiconductor is the process of re-emission of light by inter band transitions after the excitation by a photon with greater energy than that of band-gap. This process is composed by three separate steps:

- *Excitation*: electron-hole (e-h) pairs are created by the absorption of a photon.

- *Thermalisation*: the excited e-h pairs relax towards quasi-thermal-equilibrium distributions. This process usually involves the emission of phonons.

- *Recombination*: the thermalised e-h pairs recombine radiatively emitting photons.

Band-to-band transitions

In an ideal semiconductor the e-h pair will thermalise and accumulate at the conduction (C. B.) and valence (V. B.) band extrema, usually at $k = 0$. As can be seen in Fig. 3.10, The emission takes place near $k = 0$, and corresponds to a photon energy E_g. No matter how we excite the electrons, luminescence energies close to the band-gap are always obtained.

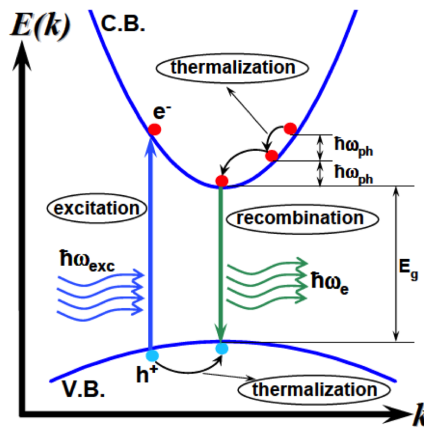

Figure 3.10: Photoluminescence in a direct bandgap semiconductor optically excited. $\hbar\omega_{ph}$ corresponds to the energy of the phonon created during the thermalization process.

Excitonic transitions

In high quality semiconductors at low temperature, it is expected that photo-excited electrons and holes are attracted to each-other by Coulomb attraction. This quasi-particle is called *exciton*. When an exciton recombines it emits a spectral line with energy

$$E_{FX} = E_g - E_X \tag{3.36}$$

where E_g is the band gap energy and E_X the exciton binding energy. See transition (3) in Fig. 3.11.

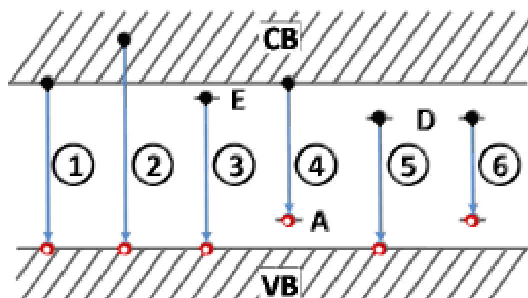

Figure 3.11: Possible radiative transitions in semiconductors. The transitions (1) and (2) correspond to band-to-band transitions, (3) is an excitonic transitions, (4) and (5) are free-to-bound transitions and (6) represents the donor-acceptor pair transition (E: exciton, D: donor, A: acceptor). Figure adapted from Reference [123].

Free-to-bound transitions

Free-to-bound transitions are recombination between an electron and a hole bound to an impurity, see transitions (4) and (5) in Fig. 3.11. At very low temperature, carriers are frozen on the impurities.Thus, low temperature PL is a simple way for measuring impurity binding energy. The excitons can be trapped by neutral or ionised donors or acceptors via Van der Waals interaction. The excitons formed due to the trapping of excitons by impurities are called *bound excitons.* They are usually denoted as (D^0X_A) and A^0X_A for the neutral impurities, and D^+X_A and A^-X_A for ionised ones. When they recombine, the energy of the emitted photon is given by

$$E_B = E_g - E_{BX} \tag{3.37}$$

where E_{BX} is the energy required for removing the exciton from the impurity.

Donor-Acceptor Pair Transitions

Quite often semiconductors contain both donors and acceptors. These carriers can then be trapped at the D^+ and A^- sites to produce neutral centres. The process of recombination of electrons on neutral donors to holes on the neutral acceptors is called *donor acceptor pair transition* (or DAP transition). See transition (6) in Fig. 3.11.

$$D^0 + A^0 \rightarrow \hbar\omega + D^+ + A^- \tag{3.38}$$

and taking in account the Coulomb interaction between the ionised donors and acceptor, the photon emitted in DAP transition will have an energy given by

$$E = E_g - E_A - E_D + e^2/(\varepsilon R) \tag{3.39}$$

where E_A and E_D are the binding energy of the hole and the electron to the acceptor and the donor impurities and $e^2/(\varepsilon R)$ is the Coulomb interaction between the impurities that are separated by a distance R. Thus, the emitted photon energy is increased by the Coulomb contribution, that lower the energy of the final state. Finally, the energy contribution given from the interaction between the donors and the acceptors (similar to van der Waals interaction) can be neglected, because it is small.

3.3.1 Experimental apparatus

The PL measurements both at room and liquid Helium temperature have been performed with the same setup presented in Section 3.1.3. Particularly, in the case of low temperature measurements, a He microstat cryostat model Leybold instrument was used to control the sample in the range from 5K to 300K.

3.4 X-ray spectroscopies

X-rays are a powerful probe of the structure of matter. They are an essential tool for non-destructive investigations in archeology, biology, chemistry, materials, medicine, paleontology, physics and many other scientific disciplines. The synchrotron radiation emitted from charged particles circulating in storage rings are an intense and versatile source of X-ray. A typical electron accelerator emits synchrotron radiation in a very broad range of photon energies, from microwaves to hard X-rays and γ-rays. The wavelengths range corresponding to these energies goes from 10^3 to $10^{-1}\mathring{A}$ [124]. This range is very important, because the sizes of the atoms, molecules and proteins fall in the same range, as do the lengths of chemical bonds and the minimum distances between atomic planes in crystals. Thus, the above photons have the right wavelengths for studying the atomic structure of solids, molecules, and important biological structures and understanding their physical and chemical properties.

X-Ray Fluorescence

X-ray fluorescence (XRF) is a very efficient technique for the elemental analysis of samples. The shells of atoms are labelled with capital letters: K, for the innermost ones, followed by L-shells, M-shells, etc. The L- and M-shells are divided in sub-shells: L_1, L_2 and L_3 and M_1, M_2, M_3, M_4 and M_5, respectively. Each shell is filled by a certain number of electrons determined by the Pauli exclusion principle. Four quantum numbers describe the electron and consequently the shell it can occupy: the principal quantum number (n), that describes the electron shell or the energy level of the atom, the azimuthal quantum number (l) describing the angular momentum of the electron and the subshell that is occupying, the magnetic quantum number (m_l) that gives the projection along a specified direction of the angular momentum and specify a particular orbital within a subshell, and the spin quantum number (m_s) that describes the spin of the electron within that orbital. XRF phenomenon consist in the emission of a secondary photon after shining the material with the X-ray beam: when an atom is irradiated by an X-ray photon with sufficient energy, it will eject an electron from an inner shell, leaving a vacancy (hole). The hole state of the core shell has a short lifetime of 10^{-15} s, in fact by this time it will be refilled by an electron from an outer shell. This transition from the outer shell to the inner shell occurs via two competitive processes: the X-ray fluorescence and Auger effects. In the X-ray fluorescence, that is subjected to selection rules ($\Delta n \geq 1$, $\Delta l = \pm 1$ and $\Delta j = \pm 1$, where $j = l + s$), an electron with energy E_m from an outer shell will fill an inner shell with energy E_l, creating a characteristic X-ray emission photon with energy $E = E_m - E_l$. The Auger effect consists in the ejection of an electron in the transition from an outer shell to an inner one. Figure 3.12 depicts the most common X-ray

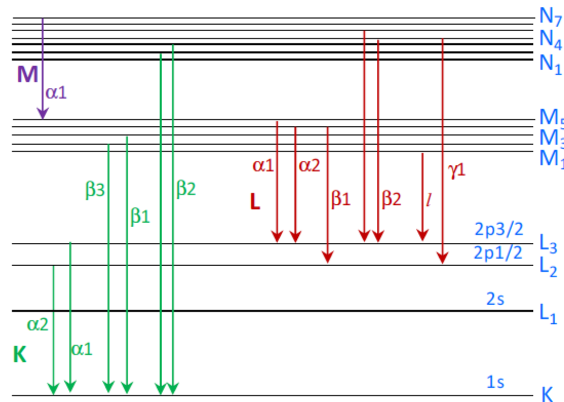

Figure 3.12: Different X-ray fluorescence emission lines in an atom after K-shell ionisation. The Greek letter nomenclature define most probable electron transitions to the K, L and M shells.

characteristic lines with their allowed transitions.

Each atom has a characteristic X-rays spectrum, therefore the detection of an element in a sample can be identified from the overall XRF of the latter.

X-Ray Diffraction

XRD is a versatile, non-destructive technique that permits the study of the crystal structure of materials in the long range order.

The basic principle of XRD is that crystalline materials under monochromatic X-ray irradiation produce typical patterns of reflected X-ray peaks. This was explained by modelling the crystal as a set of discrete parallel planes separated by a constant parameter d, as it is depicted in Fig. 3.13. It was suggested that the incident X-ray radiation would produce a Bragg peak if X-rays are specularly reflected by the ions in one plane, i.e. the angle of incidence has to be equal to that of reflection and the reflected X-rays from successive planes interfere. The interference is constructive when the phase shift is a multiple of 2π; this condition can be expressed by Bragg's law:

$$n\lambda = 2dsin(\theta) \tag{3.40}$$

where n is an integer representing the order of reflection, θ is the angle of incidence (equal to that of reflexion) and λ is the wavelength of the incident radiation. XRD gives direct information on the d-spacing between planes, therefore any change in the crystal sequence or structure can be directly observed.

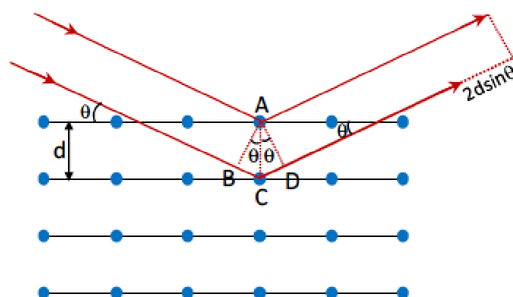

Figure 3.13: Schematic of a Bragg reflection from planes separated by a distance d. Incident and reflected rays are shown for the two neighbouring planes.

X-ray Absorption Spectroscopy

XAS is a very powerful tool for the study of short-range order and/or electronic structure of a broad range of crystalline materials. It provides quantitative structural information at the atomic scale about the local environment around the absorbing atom (i.e., near-neighbour species, interatomic distances, coordination chemistry, valence state and coordination number).

The X-ray absorption process is based on the photoelectric effect: tuning the energy of incident photons to a value that is equal or larger than the binding energy of an atom, an electron from an inner core level is ejected to a vacant excited state or to the continuum. This phenomenon results in a sharp rise in the absorption intensity, which is called 'absorption edge'. XAS is the measurement of the X-ray absorption coefficient μ(E) of a material as a function of energy. The μ(E) is defined as:

$$\mu(E) = \frac{I_f}{I_0} \tag{3.41}$$

where I_f is the intensity of the X-ray fluorescence lines and I_0 is the intensity of incoming X-rays.

A XAS spectrum is generally divided into two parts: the X-ray absorption near edge structure (XANES) and the extended X-ray absorption fine structure (EXAFS), as it is shown in Fig. 3.14. XANES zone is separated from the EXAFS at a value of energy that corresponds to the wavelength of the excited electron that is equal to the distance between the absorbing atom and its nearest neighbour. The XANES covers a region of the XAS spectrum of about 50 eV across the absorption edge, that includes pre-edge and edge regions. On the other hand, EXAFS covers the region from 50 to 1000 eV above the edge. The pre-edge structure provides information on the local geometry and on the absorption sites (they typically involve transition from the level 1s to the 3d, that are forbidden by the selection rules, but the phenomena of orbital *hybridisation* makes them observable [125]). The absorption edge gives information on the electronic structure of the absorber

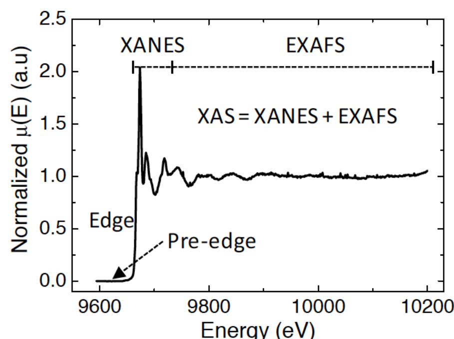

Figure 3.14: Example of a Zn K-edge XAS of ZnO:Co NWs. Figure taken from Reference [125].

atom (its position corresponds to the threshold to the continuum). Finally, the region above the edge provides information on the first coordination shells around the absorbing atom and bond angles. The region of a XAS spectrum starting around 50 eV is generated by the interaction of the ejected electron from the absorber atoms with a neighbour atom, which scatters back the electron. In a classic view, the electron can be described as a wave. Thus, the interaction between the outgoing and backscattered photoelectron waves produces the oscillations in the spectrum of the X-ray absorption coefficient. If the interference is constructive a maximum will appear and in the case of destructive interference a minima. Therefore EXAFS gives information on the average structure around the absorbing atom.

3.4.1 Synchrotron facility and beamlines

There are three types of magnetic structures commonly used to produce synchrotron radiation: bending magnets, undulators and wigglers [126–128] (the last two are made of permanent blocks which force the electron beam onto a sinusoidal trajectory and therefore stimulate radiation). The *European Synchrotron Radiation Facility* (ESRF) [126, 127] storage-ring light source was built in the early nineties in Grenoble (France): a schematic view of it is presented in Fig. 3.15. The accelerator consists of the pre-injector, the booster and the storage ring. The relativistic electrons are injected into the ring from a linear accelerator and a booster synchrotron. Various magnetic lenses keep the electrons traveling along the desired trajectory. Electron beam energy lost to synchrotron radiation is refilled with a radiofrequency accelerator (a cavity with an axial electric field oscillating at the frequency of arrival of sequential electron bunches). The photon beam is extracted tangentially to the source and sent on the studied sample through the beamlines. The beamline [126, 127] conveys the radiation emitted by dipole magnets and insertion devices to user's experimental chambers. They also enable the user to select from the total synchrotron radiation spectrum

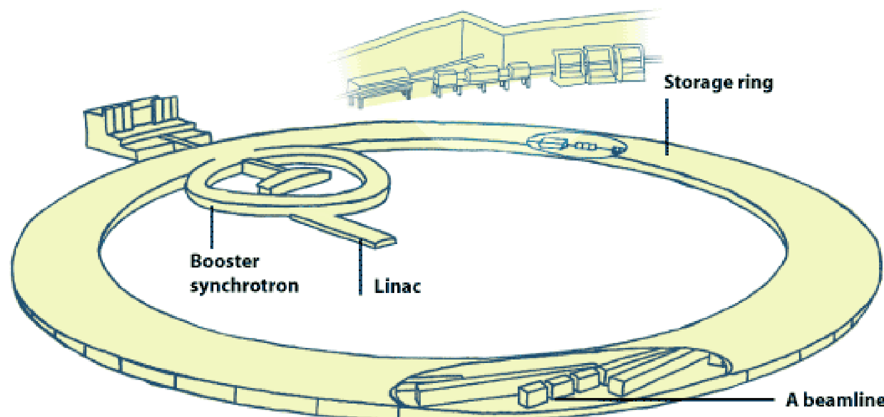

Figure 3.15: Schema of the Synchrotron.

the particular photon energy required for each experiment. The major components of a beamline are: the monochromator, the vacuum system, mirrors and the experimental chamber.

3.4.2 X-ray nanoprobe beamline ID22NI

The results of the measurements presented in this thesis were performed at beamline ID22NI (upgraded to ID16B after 2014), in collaboration with Dr. Jaime Segura-Ruiz, Dr. Mahn-Hung Chu and Dr. Gema Martínez-Criado. This beamline is enabled to perform, among others, the following kinds of measurements: X-ray fluorescence (XRF), X-ray diffraction (XRD) and X-ray absorption spectroscopy (XAS). The nano-meter scale resolving power of beamline ID22NI allows to perform characterisation of single NWs.

A schema of the beamilne ID22NI is shown in Fig. 3.16. The vertical mirror is a Si crystal coated with Si, Pd, Pt used at 2.5 mrad to remove high harmonics. The Si (111) monochromator allows the selection of the working energy with a spectral resolution of 1 eV. Multilayer coated Kirkpatrick-Baez mirrors are used to focus the X-ray beam down to nanometer length scale.

The XRF and XANES data are collected by an energy dispersive Si drift detector, as it is shown in Fig. 3.17, while the XRD data are registered by a fast readout low noise (FReLoN) CCD detector, that is positioned in front of the sample holder behind the microscope detector, as depicted in Fig. 3.17. This setup allows to perform simultaneous measurements of XRF and XRD allowing to spatially correlate elemental composition and structural information.

The nano probe of this beamline combines high lateral spatial resolution with deep escape depth and intense photon flux and gives information on

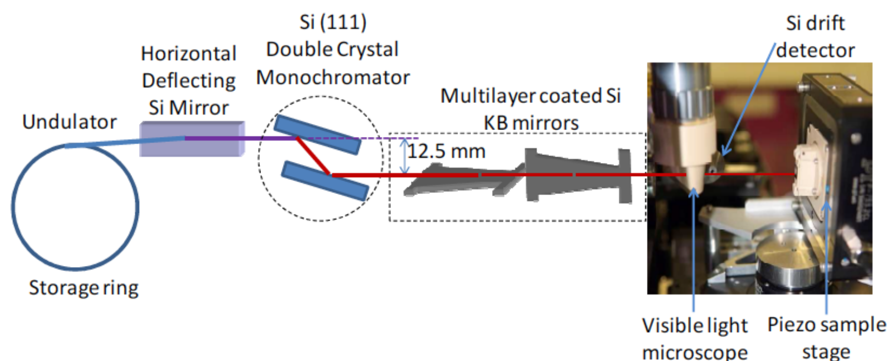

Figure 3.16: Schematic of the experimental setup for recording X-ray fluorescence and X-ray absorption using a synchrotron X-ray nano-beam at the beamline ID22NI.

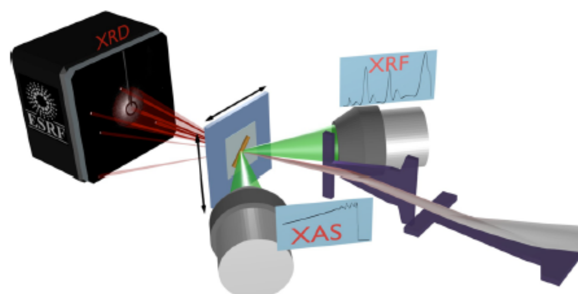

Figure 3.17: Schematic of the experimental setup for recording XRD. Figure adapted from Reference [81].

the chemical speciation and its distribution along the nanostructures. In pink-beam conditions (quasi-monochromatic) the beam size was 50×50 nm^2 and the energy bandwidth was about 10^{-2}. The step size used in this mode was of 25 nm, and the integration time of 500 ms per point.

For the results presented in this thesis the monochromatic beam was used (bandwidth of 10^{-4}). XRF maps were recorded exciting with a beam energy equal to 29.6 keV, the beam size was 120×97 nm^2 (H×V), and the integration time was 0.2 s per point. For XRD mapping the beam energy was equal to 28.03 keV, the beam size to 154×136 nm^2 (H×V), and the integration time to 0.2 s per point (as for XRF). In the first case the maps were recorded with a 25 nm step size and in the latter with a 100 nm one.

The XRF and XRD data are processed by the PyMCA program [129]. PyMCA is a very versatile tool that has been created for the analysis of XRF spectra and gives very good identification and quantification of the elements present in a sample. With PyMCA is possible to build XRF and XRD maps and to study the two at the same time, avoiding possible errors in attributing XRD reflections that do not come from the sample [129]. The raw XRD data are preprocessed with Fit2D program [130] for being

correctly interpreted by PyMCA. Fit2D allows to perform the calibration using a XRD pattern obtained measuring a standard powder of Al_2O_3 and to correctly identify the XRD diffraction peaks (more precisely, the use of a standard sample enables to determine all the geometric parameters required to integrate the XRD CCD image and, thus, obtaining reliable and interpretable diffraction patterns) and to perform a first noise subtraction. The processing of XANES data is performed using ATHENA [131], which is a highly interactive graphical utility that allows to easily convert the raw data to the X-ray absorption coefficient in function of energy and to perform fits, among other several options.

Chapter 4

Optical characterisation of selective area growth GaN nanowires and nanopyramids

In this Chapter the effects of the mask geometry on the structural and optical properties of ensembles and single selective area growth (SAG) GaN NWs are investigated by means of Raman scattering and photoluminescence. Often in the past, studies of the structural quality of SAG NWs have been carried out by transmission electron microscopy, which requires a sophisticated preparation, and usually implies the partial destruction of the sample and is quite time-consuming. Thus, the use of non-destructive and contact-less techniques for the detailed characterisation of the properties of SAG NWs appears highly beneficial.

The Chapter is organised as follows: Section 4.1 contains brief introduction to SAG NWs, underlying the main achievements in the field of GaN NWs. In Section 4.2, molecular beam epitaxy growth technique, with a focus on the growth of SAG GaN nanostructures, is described. Section 4.3 is dedicated to the first investigated sample, which is homoepitaxial SAG NWs. After giving the details on the growth and morphology of the SAG NWs, the results of Raman scattering and photoluminescence measurements carried out on ensembles and single NWs are presented. Then, effects of changing the SAG mask lay-out are described in a separated Subsection. Finally, the results are summarised. In the last part of the Chapter, Section 4.4, hetero-epitaxial SAG nanopyramids are presented. The comparative description of the properties characterised by Raman scattering and photoluminescence of nanopyramids and NWs is given. Concluding, the results are discussed.

The samples studied in this Chapter were grown by Dr. Arne Urban of the University of Göttingen.

4.1 Introduction

In the last decade, self-assembled growth of high quality GaN NWs has been achieved by MBE [132–134] and MOCVD [6,135,136]. *Brandt et al.* [49] characterised self-assembled GaN NWs grown by MBE by low-temperature PL and found that they presented a crystal quality even higher than that of state-of-the-art homoepitaxial layers. Despite the very encouraging results obtained, self-assembled growth produces fluctuations in the diameter, position, and height of the NWs. Future optoelectronic applications will need regular arrangement of vertical standing NWs with well-defined height homogeneity for efficient device processing.

Catalyst-assisted growth could be an alternative for the growth of ordered and regular NW arrays. By vapor-liquid-solid process, that will be described in next Chapter, the catalyst seeds drive the formation of NWs in a given position. The diameter of the NWs can be controlled by the seed diameter. However, this kind of growth produces NWs with a higher density of structural defects and impurities, probably due to the incorporation of catalyst atoms, as it has been exhaustively demonstrated by *Chéze et al.* [31].

The fabrication of regular GaN NW arrays by epitaxial SAG was reported by *Hersee et al.* in 2006 [137]. SAG GaN NWs have been grown successfully on different substrates by MOCVD and, more recently, also by MBE [32, 34, 138, 139]. In SAG the substrate is covered by a mask with an array of holes were the NWs nucleate. Growth parameters and the mask design are crucial for SAG. Typically, SAG requires higher temperatures and III/V ratios than self-assembled growth, as selectivity is achieved by increasing Ga desorption and diffusion in order to suppress the nucleation outside the apertures of the mask [34]. The mask geometry is another important SAG parameter not only for selectivity but also for the vertical growth and the shape evolution of the nanostructures since it affects the local III/V ratio within the mask apertures [35]. The majority of the studies in literature are focused on the study of the growth process in order to establish the optimal conditions to achieve and to control selectivity and homogeneity of SAG NWs [140, 141].

4.2 SAG nanostructures grown by MBE

MBE is a growth technique that consists in the controlled deposition of thin crystalline layers on a heated semiconductor substrate with a precise control of its thickness, composition, and morphology. The growth chamber is under ultra high vacuum conditions (10^{-12} mbar) which reduces the incorporation of impurities during growth. The molecular beams are created in separated effusion cells that allow the direct irradiation of the substrate by the constituents. Generally, the distance between the cells and the sample is of 30 cm and the growth-rate around 1 μm h^{-1}. Such low growth rates allow to obtain high quality crystalline structures with impurity concentration

below one part per million.

The GaN samples studied in this thesis were grown in a Veeco Gen II MBE system equipped with a radio frequency (RF)-plasma source and an effusion cell for gallium. The schema of the apparatus is shown in Fig. 4.1. Nitrogen is a very inert gas and has to be dissociated for the reaction to occur. Due to its high binding energy, it is not possible to do it thermally. Therefore, a RF plasma source is used to excite the nitrogen to the plasma state. The cells temperature, their geometry, and their internal vapour pressure control the molecular beam fluxes. Each cell has a shutter positioned at its front. Furthermore, the ultra high vacuum conditions allow for in situ monitoring of the growth and characterisation techniques, such as reflection high energy electron diffraction (RHEED).

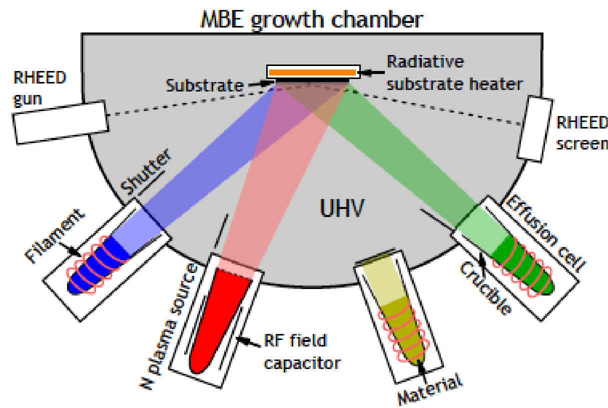

Figure 4.1: Schema of an MBE growth chamber. Figure taken from Reference [60].

The V/III rate is the crucial parameter for the growth of GaN: high V/III ratios are necessary to obtain GaN self-assembled nanostructures with high aspect ratios, while Ga-rich conditions enable the growth of GaN layers. In fact, the high V/III ratio controls the nucleation density on the substrate and allows to suppress coalescence of neighbouring nucleation sites, by reducing the diffusion length of Ga atoms [6].

In the case of SAG growth, the position and the size of the nanostructures is controlled by the dimensions and the relative position of apertures in a patterned layer that covers the substrate. These apertures act as nucleation centres for the growth of the nanostructures. The materials usually employed as masks are Ti, Mo, SiN, and SiO_2, because of their stability at high temperatures. The SAG growth is performed at higher temperatures than the conventional self-assembled growth in order to favour the Ga desorption and diffusion, and thus, suppress the parasitic nucleation on the mask itself [32, 34, 35, 137–139].

The study of the growth mechanism of SAG nanostructures analysed in this work was carried out by Dr. Arne Urban performing time dependent

growth series. This study reveals the following process: first, multiple GaN nuclei grow within the holes, as shown in Fig. 4.2 (a). Then they coalesce to form a compact pedestal like that of Fig. 4.2 (b). At this stage, the shape of the holes does not influence the GaN crystal shape, since the apertures are much larger than the critical radius for stable GaN nuclei. With increasing the growth time, semipolar facets start growing at the pedestal edges, and they grow from the outside of the column to its inner part. This mechanism is reported in Fig. 4.2 (c), (d) and (e). Finally, the semipolar facets fully form on the pedestal with hexagonal cross section and the vertical growth of NWs can start, see Fig. 4.2 (f).

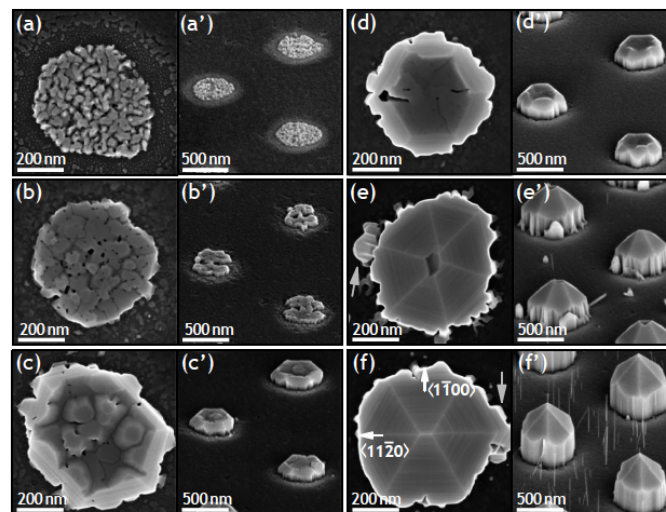

Figure 4.2: SEM top-view (a - f) and bird's eye view (a'-f') micrographs of SAG GaN NWs with diameters in the range of 500 to 700 nm. The growth times are t =10, 20, 40, 60, 120, and 180 min for (a - f), respectively. Crystallographic directions are given in (f). Gray arrows indicate non-uniform radial overgrowth. Figure taken from Reference [60].

The two samples analysed in this Chapter were grown by homo- and hetero-epitaxial growth, respectively. In the former case the growth of NWs (see Section 4.3.1) was achieved and in the latter nanopyramids were obtained (described in Section 4.4.1). Prior to epitaxy, the substrate surfaces of the two samples were covered by a 10 nm thick Mo layer by evaporation (with a deposition rate of about $1\mathring{A}$ s^{-1}). The Mo mask was patterned by e-beam lithography (EBL). The SAG growth was performed under N-rich conditions with V/III rate $\sim$ 8 for a total of 3 hours and with substrate temperature (T_S) of 780 °C and of 840 °C for the NWs and the nanopyramids, respectively.

4.3 GaN nanowires

In this section the details on the sample and results of the measurements performed on the first sample by Raman scattering and PL are presented.

4.3.1 Description of the sample

The SAG GaN NWs studied in this Chapter were grown on a GaN MOCVD template covered by a 10 nm thin Mo mask. The mask patterned region has an area of 700 × 900 μm^2. The mask is constituted by 48 individual patterns of an area equal to 80 × 80 μm^2, as shown in Fig. 4.3. Each individual pattern contains periodic triangular arrays of circular apertures with diameter (d) and *pitch* (p) (see inset of Fig. 4.3), nominally ranging from 30 to 500 nm and 0.25 to 8 μm, respectively.

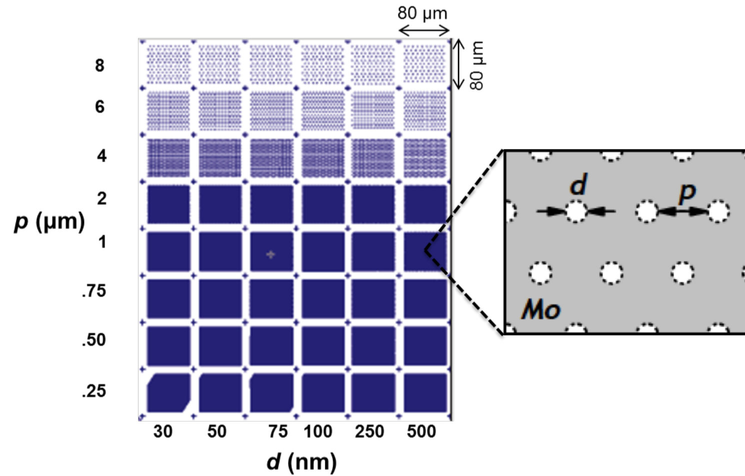

Figure 4.3: Schematic layout of the hexagonal arrays of the Mo mask. The individual pattern size (constant aperture diameter and constant aperture pitch) have an area of 80 × 80 μm^2. Figure modified from Reference [60].

It has been found, as it will be discussed later, that p has a strong effect on the selectivity of growth, since SAG mechanism is Ga-diffusion assisted, as already observed by *Gotschke et al.* [140]. Two growth regimes have been identified depending on the ratio between p and Ga diffusion length (λ). For $p \leq 2\lambda$ the first regime which is defined *competitive* is found, where adjacent NWs compete for the Ga atoms diffusing on the mask surface. For $p > 2\lambda$ a regime which is named *isolated* occurs when the growth of NWs is independent from one another.

The SAG NWs growing on this patterned substrate have hexagonal cross section and end in pyramidal tips defined by semi-polar facets, corresponding to $(1\bar{1}02)$ planes (r-plane). The identification of the exact semipolar facets family was performed by TEM. In Fig. 4.4 (a) a bird SEM view of the SAG

NWs is shown. From the TEM studies performed by the growers it was concluded that the NWs are located preferentially at the apertures of the Mo mask, except for diameter equal to 30 nm, where an incomplete growth took place (thus, no measurements were performed on it). The diameter of

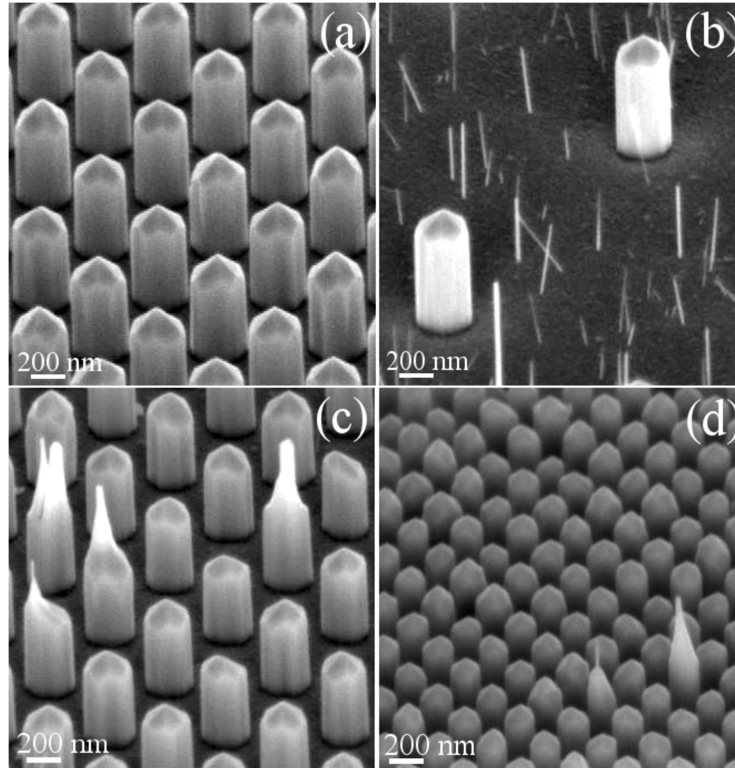

Figure 4.4: SEM images of GaN NWs. Sample code: G1225. (a) Side view of GaN NWs ending with a pyramidal tip defined by $\{1\bar{1}02\}$ facets for d = 500 nm and p = 0.25 μm and (b) side view of SAG and parasitic NWs for d = 500 nm and p = 2 μm and (c) and (d) Additional structures growing on the NWs apex. GaN NWs with p = 0.50 μm and d = 250 and d = 100 nm.

the SAG NWs exceeds the aperture diameter, revealing that radial growth is low but never completely suppressed. On the other hand, the NW height, which is an indicator of the axial growth rate, increases with $p < 1\mu$m from 425 nm to the saturated value of 750 nm for $p > 1$ μm, as it is shown in Fig. 4.5. For $p \leq 1$ μm the growth regime is the so-called competitive and for p > 1 μm the isolated regime occurs. The behaviour of the NWs height clearly identifies the transition from the competitive regime to the isolated one. In the first regime when increasing p, the same amount of growth species is consumed by a decreasing growth area and, therefore, the height of the NWs increases. The Ga diffusion length can be estimated from the intersection of these two regimes and is equal to $\lambda = 435 \pm 30$ nm. In the latter regime, much thinner self-organised GaN NWs (diameter $\sim$ 10 - 20 nm) also grow on the Mo mask with a density of 30 NWs per μm^2, see Fig. 4.4 (b). The

self-organised NWs end with a flat c-plane and their density is comparable to that in the un-patterned regions. Occasionally, some of the NWs present

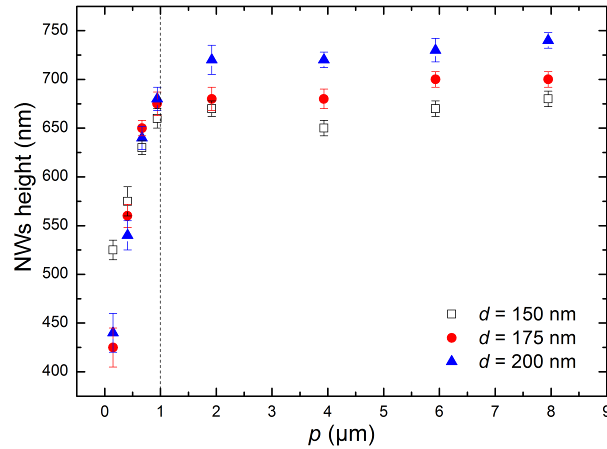

Figure 4.5: Average NW height as a function of p for d = 150, 175 and 200 nm. The error bars indicate the standard deviation. The dashed line shows approximately the transition from the competitive to the isolated regimes.

additional structure growing from the NW apex (see Fig. 4.4 (c) and (d)). These structures have been identified as zinc-blende GaN material by TEM measurements. TEM measurements also allowed to observe TDs in the base region of the NWs that are caused by the process of coalescence of the GaN nuclei during the first step of the growth (described in Section 4.3.1). Moreover, it has been found that for the largest aperture diameter of 500 nm (that corresponds to the NWs with real diameter $\sim$ 350nm) the NWs show a hollow core. This is attributed to the failure of the EBL which produced an incorrect and imprecise etching of the Mo from the holes of the mask. For this reason, the results on this diameter have been considered not representative and therefore not reported in this work.

In the following Sections, the real values of the d and of the p measured by SEM will be indicated.

4.3.2 Fundamental characterisation by Raman scattering

The quality of the GaN material has first been investigated by Raman scattering spectroscopy. Figure 4.6 displays a representative non-resonant Raman spectrum measured in backscattering configuration of an ensemble of SAG NWs, along with the fitting curves (dashed lines). The results of the fit are summarised in Table 4.1. The most intense peak is that associated to the E_{2h} phonon of wurtzite GaN. At $\sim$ 736 cm^{-1} a q-LO phonon mode is detected, which comes from the overlapping between the A_1(LO) and the E_1(LO) modes (refer to Eq. (3.21)). Another distinctive feature of the

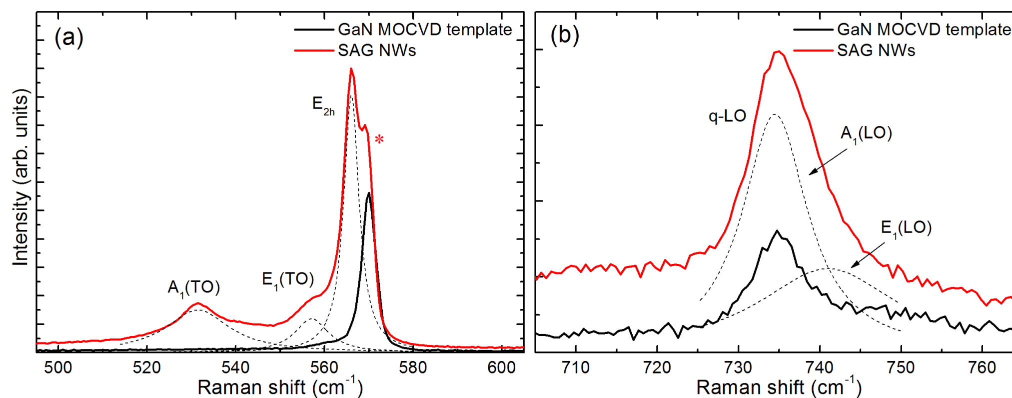

Figure 4.6: Non resonant Raman scattering spectra of ensemble of NWs with $p = 0.15$ μm and $d = 160$ nm around (a) the E_{2h} and (b) A_1(LO) modes. All measurements were carried out at room temperature in backscattering configuration, and with 488 nm laser line excitation. The peak marked with an asterisk corresponds to the GaN template. The scale of (a) is 13 times bigger in intensity than that of (b).

Table 4.1: Results of the fit for the curves displayed in Fig 4.6.

	SAG NWs (cm^{-1})	GaN MOCVD template (cm^{-1})
A_1(TO)	531.4 ± 17.5	-
E_1(TO)	557.1 ± 9.2	-
E_{2h}	566.1 ± 4.2	570.0 ± 8
A_1(LO)	734.5 ± 9.8	735.0 ± 8.4
E_1(LO)	741.2 ± 21.1	-

spectrum is the appearance of two additional peaks at ~ 533 cm^{-1} and ~ 557 cm^{-1}, matching the frequencies of the A_1(TO) and E_1(TO) modes, respectively.

The partial opacity of the Mo mask (92% and 72% measured for UV and visible light, respectively) allowed a weak peak attributed to the E_{2h} mode of the GaN MOCVD template to appear in the Raman spectrum (labeled by an asterisk in Fig. 4.6 (a)). This peak is centred at 570 cm^{-1}, revealing that the slight residual compression (around -0.2% assuming biaxial strain) of the substrate is not transmitted into the NW material. The observation of TO modes in backscattering measurements has been reported for vertically standing self-organised NWs and is attributed to deviations from the nominal geometry due to the slight tilt of the NWs relative to the laser excitation direction [142]. Such reason cannot be invoked for the perfectly vertical SAG nanostructures. Instead, the refraction of the excitation light at the pyramidal facets of the nanostructures, which form a $40° - 50°$ angle with respect to the c-plane, changes the internal scattering configuration enabling an oblique internal excitation geometry with an internal in-coming angle

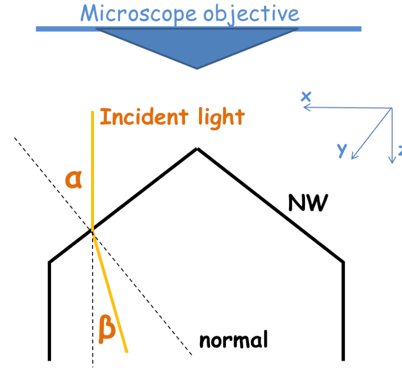

Figure 4.7: Sketch of the Raman geometry, where 40°<α<50° and 25°<β<30°.

25° − 30°, see the sketch of Fig. 4.7. Furthermore, the high refractive index of GaN (2.44) can cause multiple internal reflections and therefore additional deviations from the backscattering geometry. It should be pointed out that the peaks at $\sim$ 557 cm^{-1} and at $\sim$ 741 cm^{-1} could also correspond to the TO and LO modes of cubic GaN, but the oblique penetration of light into the NWs makes difficult to track the Raman selection rules and hampers the discrimination of the zinc-blende phase.

A closer analysis of the E_{2h} phonon of the GaN NWs can provide information about residual strain fields and the crystal quality of the material [143]. The E_{2h} peak is centred at a frequency of $\sim$ 566.5 cm^{-1} for all p and d, which is in good agreement with the value of strain-free bulk samples [93, 144], indicating that SAG NWs grow free of macroscopic strain and are not lattice matched to the substrate.

4.3.3 Fundamental characterisation by photoluminescence spectroscopy

PL spectroscopy is another very efficient and powerful technique for the study of the optical properties of the NWs. A representative low temperature PL spectrum of an array of SAG GaN NWs ($\sim$ 40 scanned NWs) is shown in Fig. 4.8. Two distinctive UV peaks are observed at 3.471 eV and 3.42 eV, while no yellow luminescence, associated to nitrogen vacancies and other defects has been observed. The most intense peak is attributed to the recombination of donor-bound excitons (D^0X_A) and its energy confirms that the SAG NWs are free from strain. This peak presents a slight asymmetry at both the high and low energy sides which are compatible with traces of free A-exciton emission and two electron satellite processes [49], respectively. The large FWHM ($\sim$ 5.5 meV) measured for this transition exceeds by almost an order of magnitude that of strain-free GaN. *Jenichen et al.* [145] found that even though self-organised GaN NWs grow free from strain at

the macroscopic scale, the FWHM of the D^0X_A transition is larger than that of high quality films and attributed it to the presence of a micro-strain field generated by the coalescence of NWs during growth. As described in Section 4.2, SAG NWs experiment as well coalescence, in particular the GaN nuclei coalescence in the first stage of growth. Thus, the large broadening of the SAG PL peak can be attributed to micro-strain. The energy of the excitonic transitions changes linearly with strain component, so according to the work of *Fernández-Garrido et al.* [146], the micro-strain value of the studied SAG sample should be of the order of $\pm$ 0.04%. Additionally, the PL broadening could also arise from the random separation of the donor sites with respect to the lateral surfaces of the NWs, suggested as the cause of the broadening of their GaN NWs by *Corfdir et al.* [65]. However, as it will be discussed in Section 4.3.4 the latter is a minor contribution.

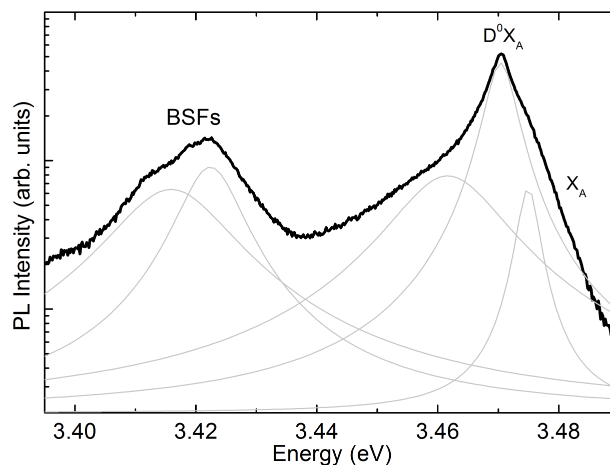

Figure 4.8: Representative 5K PL spectrum measured at low excitation power (2 μW) of NWs with $d = 220$ nm and $p = 0.15$ μm.

The second band of Fig. 4.8 is a partially resolved doublet, composed of one peak at 3.416 eV and another at 3.422 eV, attributed to the radiative recombination between electrons confined in BSFs and holes localised in their vicinity, similarly to previous observations [76, 147, 148]. The energies of emission of Fig. 4.8 are in excellent agreement with the ones reported in literature for I_1-type BSFs (see Section 2.1.1) [147, 149]. These extended defects are rare in GaN grown on the c-plane, but appear with high density in non-polar and semi-polar samples [63, 64].

In order to confirm the assignation of the peaks in the PL spectrum, a power dependence characterisation was carried out, see Fig. 4.9. The band related to D^0X_A maintains a fixed position (only one spectrum slightly deviates from the expected position, see spectrum taken at 109 μW in Fig. 4.9) and becomes broader in function of the power. During the measurements the laser spot position on the sample was not totally stable due to the vibrations of the sample stage that are transmitted by the vacuum pump.

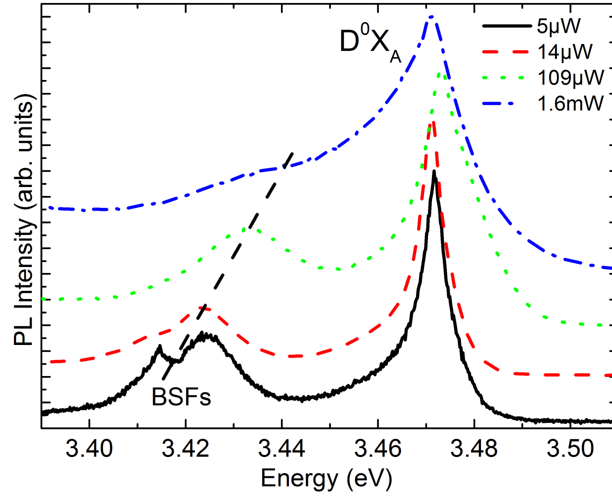

Figure 4.9: Power dependence of PL spectrum of ensemble of NWs of $p = 0.15\ \mu$m and $d = 160$ nm taken at 5 K.

This implies that not always the same ensemble of NWs was scanned. It is well know that single NWs generally present their own PL spectrum, due to slight differences in their optical properties [49], thus, the change in position of the D^0X_A can be attributed to the averaging of NWs spectra coming from different zones of the array. On the other side, the emission related to BSF blue-shifts by about 18 meV as the excitation power increases: the ZB inclusions (i.e., BSFs) inside the WZ matrix of the NW form quantum wells (QWs) grown along the c-axis which is affected by QCSE (see Section 2.2.2). With increasing power, the generated carriers accumulate at the interface of the QWs and an electric dipole is formed. This dipole screens partially the internal electric field of GaN NWs and suppresses the QCSE contributing to the blue-shift of the BSFs transition [150].

The temperature dependence of the PL spectrum has been recorded between 5 and 300K with a power of $0.15\mu W/\mu m^2$. Representative spectra showing the evolution with increasing sample temperature are reported in Fig. 4.10. Increasing T, the D^0X_A intensity progressively quenches. The decay of integrated intensity of the D^0X_A transition (plus the contribution peaked at 3.46 eV, that is an asymmetry of the donor-bound transition, see Fig. 4.8, plus the X_A emission) has to be fitted considering two different quenching mechanisms for the PL with activation energies E_1 and E_2. In fact, taking into account only one energy the curve does not fit the data, see Fig. 4.11 (a). The fitting function will therefore be

$$I(T) = \frac{I_0}{1 + Ae^{-E_1/kT} + Be^{-E_2/kT}} \tag{4.1}$$

If the radiative lifetime is assumed temperature independent, A and B are proportional to the scattering rate of each mechanism. The results of the

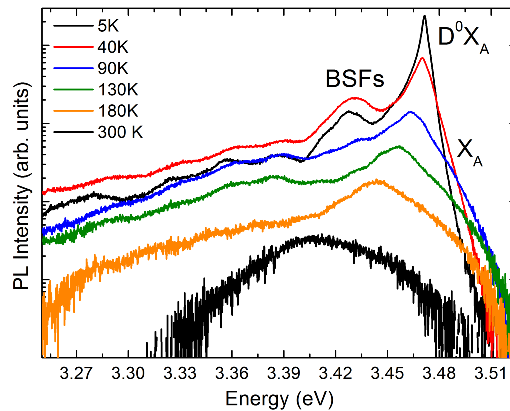

Figure 4.10: Representative PL spectra taken between 5 K and 300 K of ensemble of NWs of $p = 0.40$ μm and $d = 160$ nm.

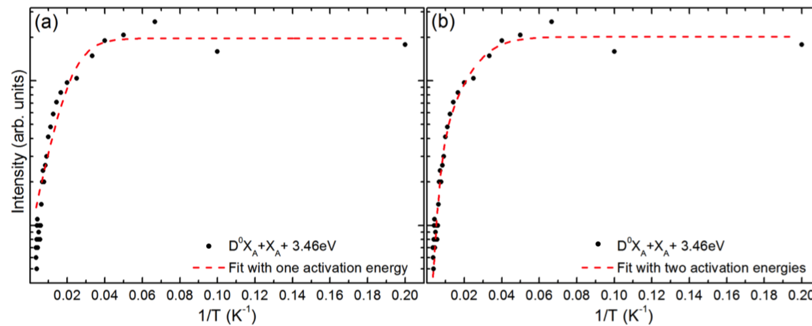

Figure 4.11: Arrhenius plot of integrated PL intensity of the D^0X_A plus the contribution peaked at 3.46 eV plus the X_A transition and its corresponding fitting of ensemble of NWs of $p = 0.40$ μm and $d = 160$ nm with its fitting considering (a) one quenching mechanism and (b) two quenching mechanisms, respectively.

fitting are shown in Fig. 4.11 (b) and summarised in Table 4.2. D^0X_A quenches to the benefit of free exciton A line firstly with a weak activation energy $\sim$ 9 meV and at higher temperature, a second mechanism starts acting with an activation energy of $\sim$ 49 meV. Thus, at high temperature, the spectra are dominated by free A exciton. Parameter B presents a very big

Table 4.2: Parameters of the fit of Fig. 4.11 (b) with Eq. (4.1).

A	E_1 (meV)	B	E_2 (meV)
9.4 ± 5.0	9.2 ± 0.2	252 ± 500	49±3

error, which suggests that a third activation energy could be introduced in the fit. However, this solution did not give better results. Consequently, the parameter B has to be considered with great care. The obtained energies, $\sim$ 9 meV and $\sim$ 49 meV for the first and second activation energies, respectively,

are somehow bigger than those reported by *Leroux et al.* [151] and other authors: 5 - 7 meV for the first activation energy and 34 - 36 meV for the second one. This discrepancy is not expected a priori, and it can be attributed to an effect due to the high surface to volume ratio of NWs or to the fact that the considered integrated intensity for building the Arrhenius curve is given by the contribution of both D^0X_A and X_A, instead of only that of D^0X_A. This is consequence of the fact that X_A is not observable as a separated peak. Therefore, further studies are needed for understanding better this problem. The first activation energy represents the optical binding energy of D^0X_A excitons, while the second one is the sum between the D^0X_A exciton binding energy and the activation energy for free exciton A, which is normally around 26.7 meV, i. e., of the order of the Rydberg energy for free exciton A [151].

Figures 4.12 (a) and (b) display the temperature dependence of the D^0X_A and BSFs energies, respectively, obtained by deconvolution of the spectra recorded at different T. Experimental points are compared with the result of Varshni's empirical formula

$$E(T) = E(0) - \frac{\alpha T^2}{T + \beta} \tag{4.2}$$

where we obtained the best fit for the value E(0) = 3.47 eV and E(0) = 3.45 eV for D^0X_A and BSFs, respectively, with $\alpha = 0.80$ meV/K and $\beta = 800$ K [147]. D^0X_A data follow Varshni's behaviour, while the deviation at low T of the BSFs one is attributed to the localisation of the holes intervening in the transitions. As already mentioned, BSFs are QWs for the electrons, while the holes are free, but can be localised in the vicinity of the defects. On the other hand, at high T, this transition takes place between electrons and free holes, so that it follows the standard behaviour. The difference between the Varshni's curve and the experimental results is of $\sim$ 20 meV at T $\sim$ 0 K, this should correspond to the localisation energy of the hole [147].

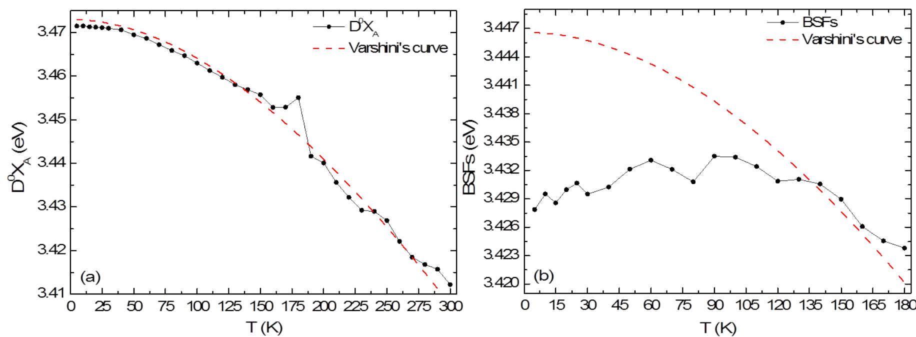

Figure 4.12: Energy position of D^0X_A (a) and BSFs (b) vs temperature. The dashed line correspond to the results of Varshini's semi-empirical model.

4.3.4 Effects of the mask geometry on the optical properties of SAG GaN nanowires

As it was already discussed in Section 4.3.1, the mask geometry has important effects in the process of growth. In this Section its influence on the quality of the material is discussed. The FWHM of the E_{2h} peak and its dependence with p and d is a good indicator of the crystal quality of the material as a function of the mask layout. Figure 4.13 (a) shows the

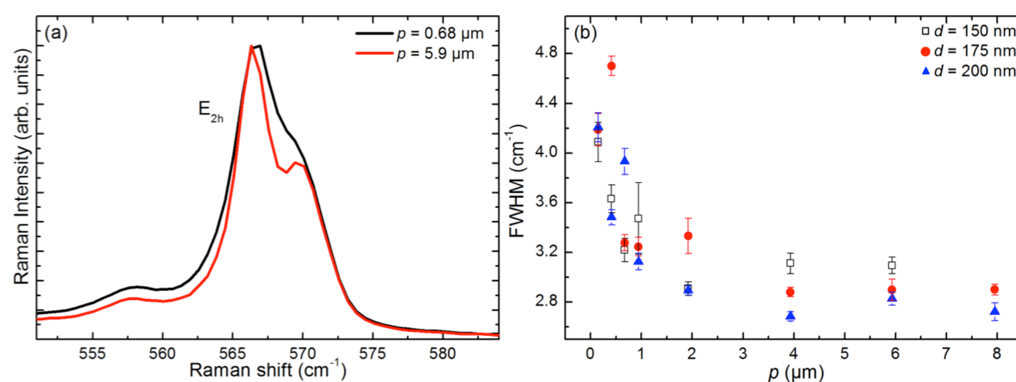

Figure 4.13: (a) Comparison between two Raman spectra in the region of E_{2h} mode of a low pitch ($p = 0.68$ μm) and an high one ($p = 5.9$ μm) for a fixed $d = 200$ nm. (b) Trend of the FWHM of the E_{2h} mode vs different pitches. The average diameter of the NWs is given.

comparison between the E_{2h} mode of a low pitch ($p = 0.68$ μm) and a high one ($p = 5.9$ μm) for a fixed $d = 200$ nm. Figure 4.13 (b) shows the evolution of the FWHM as a function of p, while there is no change as function of d. An abrupt change is observed for $p \sim 1$ μm when the growth changes from isolated to competitive regimes. For $p > 1$ μm, FWHMs are similar to those measured for high quality self-organised NWs [152], revealing a high crystalline quality of the SAG NWs. It should be pointed out that the contribution of the self-organised NWs to the Raman signal is negligible due to their much smaller overall volume (between 7.5 and 13 times lower than the volume of one SAG NW). The measured phonon broadenings are below the FWHM of the E_{2h} phonon of the GaN MOCVD template (8 cm^{-1}) and correlate perfectly with the evolution of the NW height reported in Fig. 4.5. This suggests a decreasing density of the structural defects with increasing NW height. This is in good agreement with the TEM images of *Urban et al.* [13] showing how the threading dislocations originated in the base region bend and terminate at the non-polar lateral surfaces of the NWs. Consequently, longer NWs should present a lower density of dislocations. The origin of these defects is attributed to the coalescence of multiple nuclei in the initial stages of the growth, which will very probably lead to the generation of micro-strain. This was the most probable cause for

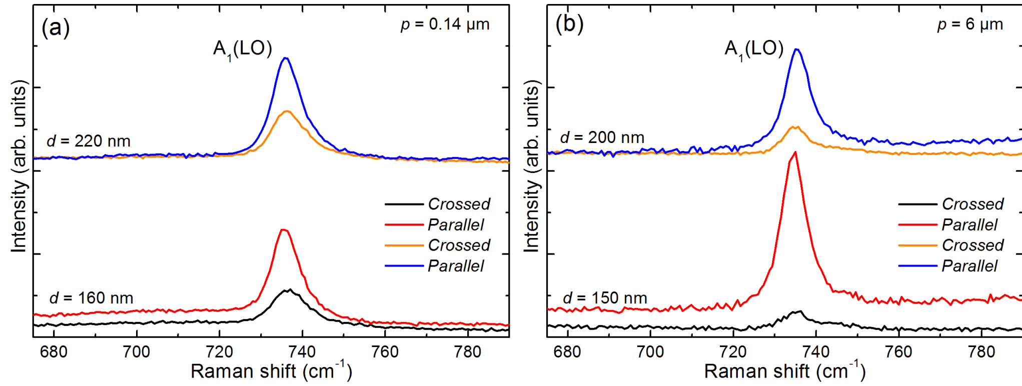

Figure 4.14: Trend of the degree of polarisation with d and p. (a) and (b) Non resonant Raman scattering spectra measured with 488 nm laser line of arrays with $d = 220$ nm and $p = 0.15$ μm and 6 μm, respectively, with excitation light polarised parallel or perpendicular to the detected light (see Fig. 4.7).

the broadening of the PL reported in Section 4.3.3. Assuming a micro-strain field compatible with the PL linewidth, which is of the order of $\pm$ 0.04%, the phonon broadening would be of $\pm$ 1 cm^{-1} which is lower than the observed increase in the phonon broadening. Micro-strain cannot account for the measured FWHMs by itself, therefore the increasing broadening of the FWHMs could be attributed to the contribution of both micro-strain and TDs, which are mostly placed in the bottom part of the NW and whose densities decrease with NW height.

Even though the pyramidal shape of the nanowire tips prevented the study of the Raman scattering selection rules, experiments were performed with the excitation light polarised parallel or perpendicular to the detected light. The laser polarisation was controlled and rotated by a $\lambda/2$ plate. It is evident that the polarisation degree of the Raman peak is constant with d and that it is stronger for higher p, as is depicted in Fig. 4.14 (a) and (b), respectively. It has to be stressed out that in crossed polarisation configuration, and according to the selection rules, no contribution of the polar mode $A_1(LO)$ is expected. However, as it is shown in Fig. 4.14, this is not true for the studied sample partly due to the angle of the semi-polar top surfaces of the studied NWs. Nevertheless, it is evident that the degree of polarisation is higher for higher pitches, while there is no evidence of a trend with d, and this indicates that part of the violation of the Raman selection rules can be attributed to the presence of structural defects. NWs grown with higher p, which show larger heights, also present improved crystal quality.

Let us turn the attention to the effect of the mask geometry on the emission properties of SAG NWs. The PL studies were limited to $p \leq 1$ μm, as for higher p self-organised NWs contributed significantly to the PL

spectrum and invalidated any trend. Representative PL spectra dependence of d and p are presented in Fig. 4.15 and they show a clear dependence on the mask geometry. The PL spectra and the relative PL intensities recorded

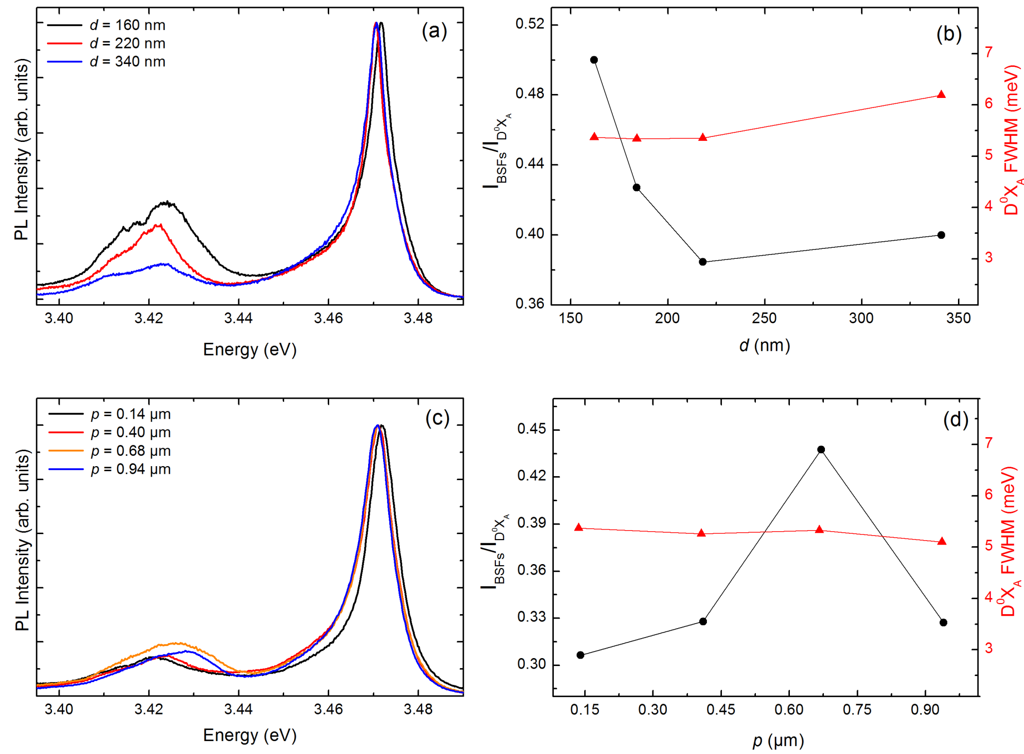

Figure 4.15: (a) PL trend with d (fixed $p = 0.14$ μm) and (b) integrated intensity of the emission from BSFs normalised to that from D^0X_A excitons as a function of d (fixed $p = 0.14$ μm) and FWHM of the D^0X_A as a function of d. (c) PL trend with p (fixed $d = 220$ nm) and (d) integrated intensity of BSFs normalised to that of D^0X_A as a function p (fixed $d = 220$ nm) and FWHM of the D^0X_A as a function of p.

as a function of d are presented in Fig. 4.15 (a) and 4.15 (b), respectively. Similar studies as a function of p are shown in Fig. 4.15 (c) and 4.15 (d). Each of these spectra are the result of an average of many spectra recorded at different points of the same individual pattern. In this way it is possible to take into account and average all the variations in the optical properties that NWs always present, as previously mentioned. According to the same criteria used for the spectra, each point of Fig. 4.15 (b) and Fig. 4.15 (d) was obtained by averaging the integrated intensities coming from several spectra measured at different points of the sample (with same d and p) in order to make the study statistically relevant. Figure 4.15 (b) shows how the ratio between the transitions involving BSFs and donor-bound excitons decreases with increasing d. However, the ratio is not consistently affected by the mask p. In fact, no clear trend was detected, as shown in Fig. 4.15 (d).

Figure 4.15 (b) shows that the variation of the FWHM of the D^0X_A with increasing d is negligible. If the greater contribution to the PL broadening would have been produced by the random separation of the donor sites, an increasing FWHMs for smaller d would have been observed, i.e., the broadening D^0X_A band is expected to be larger for thinner NWs, since the fraction of donors close to the surface increases quadratically with the diameter. The lack of such a trend suggests that micro-strain is the most probable cause for the large FWHM of the NWs emission.

4.3.5 Discussion

In this Section, the growth selectivity and structural quality of ensemble and single GaN NWs are investigated by means of Raman scattering and PL. Optimum control over the NW arrangement requires a p below twice the diffusion length of Ga atoms. Low p, however, seems to diminish the structural quality of the material, as revealed by the increase of the Raman peak line-widths, while it is not influenced by the d. This is in good agreement with the results of TEM studies performed by *Urban et al.* [13] and *Hersee et al.* [153] showing how the threading dislocations, originated in the base region, bend and terminate at the non-polar lateral surfaces of the NWs. Consequently, shorter NWs, which correspond to $p \leq 1\mu m$, present a higher density of TDs. The origin of these defects is attributed to the coalescence of multiple GaN nuclei in the initial stages of the growth.

The PL spectra of the NWs show a considerable presence of basal plane stacking faults, whose density increases for decreasing NW d. In fact, the dependence of the PL on the NWs d points out the preponderance of the growth direction in the formation mechanism of BSFs: thinner NWs, for which most of the growth takes place on semi-polar facets, statistically present a higher BSFs density. On the other hand, the variations in the local growth conditions derived from the arrangement of p in the mask have a negligible impact on the density of BSFs. The broadening of the FWHMs of the D^0X_A emission is attributed to micro-strain generated by coalescence of the multiple GaN nuclei in the first stages of the growth.

4.4 GaN nanopyramids

A comparative study between the properties of the SAG NWs, analysed in the previous Section, and those of SAG GaN nanopyramids grown on SiC substrate are presented in this Section.

4.4.1 Description of the sample

The SAG GaN nanopyramids studied in this Section were grown on a 6H-SiC(0001) substrate covered by a pre-patterned 10 nm thick Mo mask (see

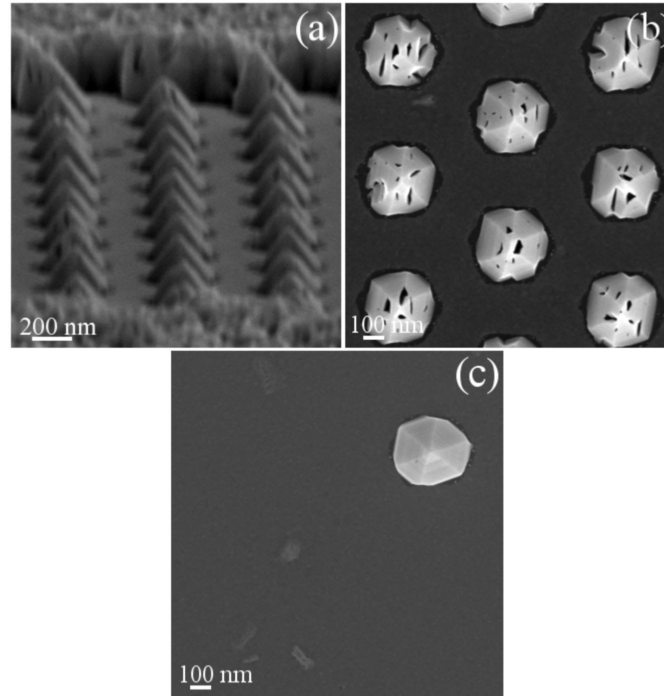

Figure 4.16: SEM images of GaN nanostructures. (a) Side view of the GaN nanopyramids growing in openings of $d = 500$ nm and $p = 0.25$ μm and a porous layer covering the unmasked SiC substrate. The pyramidal facets are $\{11\bar{2}4\}$ planes and (b) and (c) top view of nanopyramids growing in $d = 500$ nm and $p = 0.25$ μm and $p = 6$ μm, respectively.

Section 4.2). The growth of pyramids was performed at higher temperature (840 °C) than that of the NWs (780 °C). The layout of the mask is the same of that of the NWs described in Fig. 4.3, but with an important difference: the overall substrate is not covered by the mask, neither the space between individual square patterns (region with the aperture with same d and same p). The non-patterned region of the substrate is covered by a GaN rough layer-like structure (porous GaN), as shown Fig. 4.16 (a), since the absence of the mask enlarges the probability of GaN nucleation. Also in this case, the mask layout contains periodic triangular arrays of circular apertures with diameter (d) and pitch (p) ranging from 100 to 500 nm and 0.25 to 6 μm, as depicted in Fig. 4.3. All the SAG nanostructures have pyramidal shape defined by r-plane semi-polar facets.

This second sample also presented clear effects of the mask geometry. Figure 4.16 (b) shows how large voids are left inside the nanopyramids for smaller inter-hole spacings ($p < 1$ μm). For $p > 1$ μm the nanopyramids are composed of fully coalesced GaN, as it is shown in Fig. 4.16 (c). The mechanism of growth can justify the structure of the nanopyramids. Like in the case of NWs, two growth regimes have been identified (see Section 4.3.1). Most probably, the uncoalesced nature with $p < 1$ μm is due to the very high

growth temperatures and the consequent lower Ga material supply, that implies a lower growth rate which prevents the completion of the coalescence. For larger pitches more Ga is supplied, because of the decreasing influence and competition for material of the other nanopyramids. Differently from the NWs, no parasitic growth is observed and it is also a consequence of the higher Ga desorption rate due to the higher growth temperature.

4.4.2 Raman scattering characterisation

Representative Raman spectra of the porous nanopyramids and of the fully coalesced GaN nanopyramids are shown in Fig. 4.17. As in the case of NWs, the most intense peak in all the spectra is that associated to the E_{2h} phonon and it is centred at the same frequency, ~ 566.5 cm^{-1}, for all p and d. The measured frequency is in good agreement with that of bulk

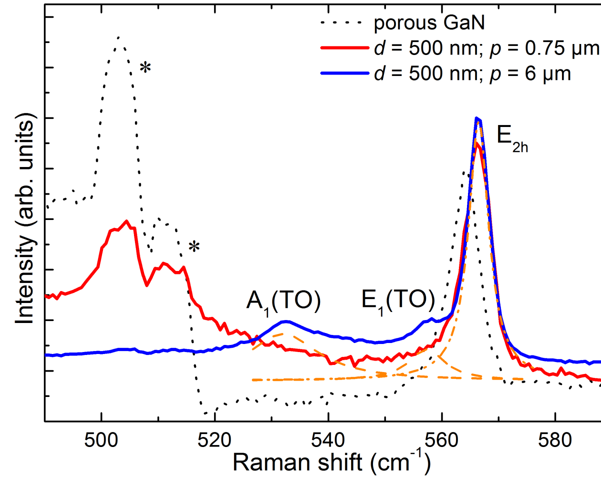

Figure 4.17: Non resonant Raman scattering spectra of arrays ($p = 0.75$ μm) and single ($p = 6$ μm) nanopyramids with $d = 500$ nm measured with 514 nm laser line excitation. The peaks marked with an asterisk correspond to the SiC substrate.

samples [93], therefore also nanopyramids grew free of macroscopic strain and are not lattice matched to the substrate SiC. The 30% transparency of the Mo mask explains why the signal of the SiC substrate is present in the spectra. Like for NWs, due to the semipolar facets (see Section 4.3.2), Raman scattering spectra present two additional peaks at ~ 533 cm^{-1} and ~ 557 cm^{-1}, matching the frequencies of the A_1(TO) and E_1(TO) modes, respectively, see Fig. 4.17. Their intensity decreases for smaller pitches while the signal from the SiC substrate becomes more intense. The LO of GaN modes overlap with those of the SiC, thus it is not possible to detect them. The FWHM of the E_{2h} reduces marginally from 5.6 cm^{-1} to 4.3 cm^{-1} when going from porous ($p < 1\mu$m) to fully coalesced ($p > 1\mu$m) nanopyramids, proving a slight improvement in the crystal quality when the coalescence is

completed. This effect can be understood as consequences of the existence of voids in the nanopyramids for $p < 1\mu$m.

A significant difference in FWHMs of the E_{2h} mode between nanopyramids and NWs is observed, the results of the fit for arrays of nanopyramids with same $p = 6$ μm are reported in Table 4.3. This Table also shows the value of the FWHM associated to the phonon frequency. This trend confirms the lower density of extended defects in the NWs and, thus, its higher crystal quality.

Table 4.3: Comparison between the results of the fit of the Raman spectra of nanopyramids and NWs with $p = 6$ μm and $d = 500$ nm and $d = 220$ nm, respectively. To each value of the phonon frequency is associated the one of the FWHM.

	Nanopyramids (cm^{-1})	NWs (cm^{-1})
A_1(TO)	532.0 ± 15.4	531 ± 12
E_1(TO)	557.3 ± 7.7	557.5 ± 7.9
E_{2h}	566.5 ± 4.3	566.4 ± 2.9

4.4.3 Photoluminescence characterisation

The comparison between a characteristic low temperature PL spectrum of nanopyramids ($p = 0.50$ μm and $d = 500$ nm) and one of NWs ($p = 0.14$ μm and $d = 220$ nm) is presented in Fig. 4.18. The spectrum related to

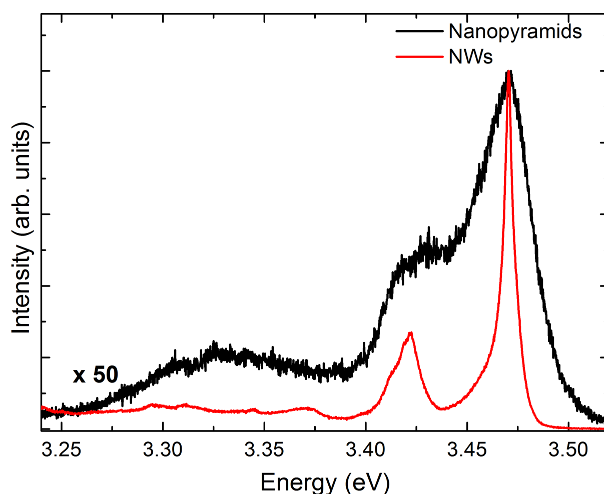

Figure 4.18: Low temperature (5 K) normalized PL spectra of the nanopyramids (multiplied by a factor 50) and NWs with $d = 500$ nm and pitch to $p = 0.50$ μm and $d = 220$ nm and $p = 0.14$ μm, respectively.

nanopyramids presents three distinctive UV bands at 3.47 eV, 3.42 eV, and

3.25 eV. No yellow luminescence, associated to nitrogen vacancies and other defects, has been observed as in the case of NWs. The first and most intense peak is attributed to the recombination of donor-bound excitons (D^0X_A) and its energy confirms that the nanostructures are free from macroscopic strain. The second band composed of one peak around 3.42 eV is related to BSFs [76, 147] and the third band is associated with prismatic stacking faults (PSFs), which often take place during the growth along non-polar planes [63].

There are remarkable differences with the NWs trends, PL peaks of NWs are considerably much brighter ($\sim$ 50 times) and sharper than those of nanopyramids. The FWHMs of D_0X_A peaks in nanopyramids (p $<$ 1 μm) are sixfold (30 meV) those of NWs (5 meV). According to [146], since the energy transitions changes linearly with the strain component, the micro-strain value expected for the nanopyramids should be of the order of $\pm$ 0.3%.

4.4.4 Discussion

The comparative study of the structural and optical properties of NWs and nanopyramids carried out in this Section points out the higher crystal quality of NWs. Raman scattering spectra reveal the absence of macroscopic strain fields in both cases and the higher crystal quality of NWs with respect to nanopyramids (narrower FWHMs), which confirms that TDs bend with the formation of the semi-polar pyramidal facets, leaving most of the NW volume virtually free of defects. Finally, the relative intensity of BSFs and of PSFs (only present in nanopyramids) bands relative to D^0X_A is higher for nanopyramids than in NWs. This indicates that most of the defects appear in the initial nanopyramid formation and the subsequent vertical growth of the NWs carries on virtually free of defects.

Chapter 5

Optical and structural characterisation of single GaN/InGaN core-shell nanowires

This Chapter focuses on the determination of the elemental distribution, structural properties and optical response of individual GaN/InGaN core-shell NWs by means of optical and X-ray spectroscopies. Current research in NWs focus on how to obtain high quality GaN/InGaN core-shell NWs with precise control of the In content. Thus, a careful and complete characterisation of their properties is crucial and highly beneficial.

The Chapter is organised as follows: a brief introduction for motivating the study presented in this Chapter is given in Section 5.1. In Section 5.2, the growth technique is introduced and the investigated sample is described and studied by energy dispersive X-ray spectroscopy. The study of the elemental distribution and the In composition of single GaN/InGaN core-shell NWs by X-ray fluorescence is presented in Section 5.3. Then, the results of the structural characterisation of single GaN/InGaN core-shell NWs by X-ray diffraction, X-ray absorption near edge spectroscopy and Raman scattering are shown in Section 5.4. The optical properties of ensembles and single GaN/InGaN core-shell NWs are compared in Section 5.5. In the final part of the Chapter, Section 5.6, the results previously presented are discussed with the aid of a theoretical simulation of the strain in this kind of heterostructures.

5.1 Introduction

GaN/InGaN heterostructures, such as QWs, are promising material support for highly efficient solid-state lightning. However, their potential is severely limited by two remaining problems. First of all, the difficulty in controlling the In concentration in the InGaN alloy, which normally shows compositional inhomogeneities and phase segregation which are particularly

severe in the mid compositional range (green emission) [154, 155] . Secondly, the strong piezoelectric fields present in polar III-nitride based QWs [156]. These fields cause the QCSE (see Section 2.2.3), which dramatically diminishes QWs emission and efficiency [157]. A solution to the QCSE problem is the growth on semi-polar and non-polar planes of the crystal in order to suppress the internal electric fields. However, semipolar and non-polar QWs show, contrary to the predictions, a quantum efficiency that is comparable with that of their polar counterparts. This fact is attributed to the presence of a larger number of SFs and TDs in non polar heteroepitaxial layers [87]. All these factors prevent the growth of high quality two-dimensional QWs covering the entire range of In compositions, thus, the tunability within all spectral range (from 0.67 eV to 3.42 eV). It should be mentioned as well that, despite their applications, GaN layers still present a rather poor structural quality, with high densities of crystallographic defects, caused by the large mismatch with the substrate [158]. NW-based QWs have attracted great interest in the last few years, since they represent an interesting option to overcome the difficulties described above.

GaN NWs offer a very high crystal quality base for the growth of polar and non-polar GaN/InGaN QWs with low density of defects. In fact, as described in the previous Chapter, GaN NWs, grown by MOCVD and MBE, have high crystal quality, with a reduced presence of structural defects, such as dislocations, and are usually strain free. Moreover, vertically standing NWs offer a large surface for the growth of layers on the non-polar direction, therefore a larger active area, enhanced light output and extraction efficiency, and stronger carrier confinement [43].

Although the QCSE has been successfully suppressed in this way [159] other problems have appeared: the semi-polar and non-polar QWs show, contrary to the predictions, structural defects, i. e., SFs and TDs [160], local well-width fluctuations and inhomogeneity in the alloy composition, and elemental segregation [161, 162]. On top of these, strain fields arise from the large lattice mismatch between the InGaN of the QW and the GaN of the barrier, which generate a change in the electronic band structure and consequently in the emission properties [163]. Although NW morphology is expected to reduce In compositional inhomogeneities and In segregation and to improve the general structural crystal quality [81, 164], only one group reported on the growth of high crystal quality GaN/InGaN NWs covering the entire compositional range [46] and similar results have not been reproduced, yet.

5.2 InGaN core-shell nanowires

In this Section GaN/InGaN core-shell NWs grown by vapour-liquid-solid Au-assisted metal organic chemical vapour deposition process are presented. The GaN/InGaN heterostructure is formed by a thick GaN core, followed

by a six period multiple QW active region, which contains three thin InGaN wells and three thin GaN barriers. New optoelectronic devices, such as multijunction solar cells and light emitting diodes, would benefit from the tunability of InGaN band gap, its high stability and its resistance to intense current and illumination [165].

5.2.1 Metal organic chemical vapour deposition

MOCVD is a versatile technique as it allows the growth of a wide spectrum of compound semiconductors with excellent properties (e.g., high purity, high luminescence efficiency) [166]. Compared to MBE, MOCVD is less costly as it does not require ultra-high vacuum, has faster growth rate (μm per hour), and is scalable at an industrial level for mass production. On the down side, there are toxic gases to be handled, the reactions do not occur only at the substrate, and therefore, parasitic reactions can take place, in-situ monitoring is more complicate, and long term reproducibility and accurate growth parameters are more difficult to obtain.

MOCVD is a gas phase technique at low pressure (e.g., 25 torr). It is a non-equilibrium process that proceeds by flowing gaseous precursors (in ratios calibrated to yield the desired compound composition) over a heated single-crystal substrate. In the elevated temperature environment of the reactor chamber, the gases undergo a complicated series of reactions that cause the precursor to dissociate and to deposit the required elements on the surface of the substrate. It has to be stressed that most of the group-III precursors are liquids and only common group-V precursors are gaseous. The liquid are evaporated and transported via a carrier gas to the substrate. There are six steps involving gas phase and surface reactions during this kind of growth, as depicted in Fig 5.1: (1) the carrier gasses transport the precursor molecules from the sources to the hot zone where they decompose and diffuse to the substrate; (2) the species can desorb or react with the other species on the surface; the species can react with the growing layer either (3) by step-down diffusion or (4) terrace processes; finally, (5) desorption and (6) by-products processes simultaneously occur. The gaseous desorbed by-products diffuse in the carrier gas away from the deposition zone towards the reactor exhaust. In principle, the terrace diffusion is more probable than the step-down diffusion and generally atoms are bound tighter at the bottom of a step. Furthermore, the step-down diffusion is kinetically only significant at very high temperature. The MOCVD process is complex, and the products of growth strongly depend on the reactor configuration, the growth rate, the growth pressure, and the substrate temperature.

Semiconductor NWs can be obtained by vapour-liquid solid (VLS) Au-assisted MOCVD growth. A sketch of growth process is depicted in Fig. 5.2. The VLS process can be divided in two main steps: the formation of liquid droplets acting as catalysts and the alloying, the nucleation and

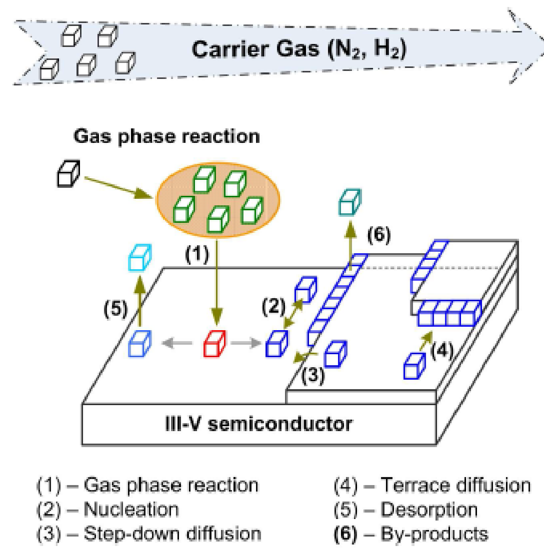

Figure 5.1: Schematic view of the MOCVD fundamental steps. Figure adapted from Reference [167].

the growth of NWs. First, a thin (few nm) gold layer is deposited on a semiconductor substrate surface, which is tempered prior to growth in order to form Au particles or droplets. The temper conditions (i. e., temperature, pressure, temper time) as well as the thickness of the initial gold layer decide on size and distribution of the catalyst droplets. During growth, the precursors decompose to yield group III and N elements and deposition of III-N material occurs preferentially at the Au particle-substrate interface, so that nanowire nucleation takes place. With continual supply of group III and N reactants, deposition of III-N material proceeds at the Au particle NW interface. The Au particle, located at the growing tip of the nanowire, drives highly anisotropic growth, which enables the growth of one dimensional structures: the axial growth rate is higher than the radial one. There are two contributions to the axial NW growth: the reaction species which directly impinge on the Au particle and the species adsorbed on the substrate or the NW side-walls, as it is illustrated in Fig. 5.2. The latter adatoms diffuse towards the Au particle, where they are incorporated into the axial growth. Group III adatoms have significantly larger diffusion lengths than N ones, that normally incorporate near to the adsorption position. The radial growth is led by the deposition of material on the NWs side-walls. This deposition does not directly involve the Au particle. As it is depicted in Fig. 5.2, radial growth occurs when species adsorbed on the substrate and NWs, diffuse and incorporate on the NWs side-walls. Therefore, the radial growth competes with axial growth, and strongly depends on the growth parameters, mainly V/III ratio. High V/III ratios favour the radial growth. The position and the diameter of the grown NW are governed by the diameter of the Au

particle. The average length of the NWs is set by the growth times. In

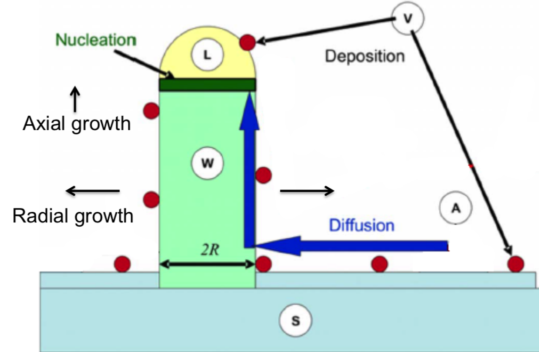

Figure 5.2: Sketch of VLS process for NW: diffusion induced VLS growth of wire (W) from the vapor phase (V) on the (S) through the liquid (L) in the Au drop and through the surface adatoms (A). Figure adapted from Reference [168].

MOCVD Au catalyst-assisted growth, the conditions (e. g., the temperature of the substrate, the precursor and working pressures, V/III ratios, growth rate) are crucial for the successful growth of high quality NWs [169].

5.2.2 Description of the sample

Coaxial GaN/InGaN NWs were grown by MOCVD in an AIXTRON 3x2″ close-coupled showerhead reactor. The standard precursors were triethylgallium (TEGa) and trimethylindium (TMIn) for the metal species and ammonia (NH_3) for the nitrogen supply. N_2 was used as the carrier gas. The VLS Au catalyst initiated growth of GaN NWs was realised by utilising the sapphire substrate coated ex-situ with an Au film of 1 nm of nominal thickness. At the beginning of the growth process, after reaching the growth temperature of around 1020 °C, TEGa supply was applied for the first two minutes to allow Ga enrichment of the Au catalyst. This pre-deposition step was followed by the simultaneous introduction of both TEGa and ammonia supply. The V/III ratio was of around 3 and promoted the vertical growth of the NWs. Three layers of InGaN were deposited at a lower temperature of 730 °C and followed by three GaN layers. The expected structure of the GaN/InGaN multi-QWs (MQWs) is depicted in Fig. 5.3. Each NW should contain MQWs growing along the c-direction, which are *polar*, and the ones along the m-direction, *non-polar*, that will be also referred to as *core-shell* MQWs. Finally, the cooling down was carried out under NH_3 stabilisation to avoid excess N desorption. A SEM bird's eye view micrograph of the sample is shown in Fig. 5.4 (a), while an HR-TEM image of a single dispersed NW is presented in Fig. 5.4 (b). The NWs have diameters and heights ranging from 150 to 230 nm and 1.5 to 3 μm, respectively.

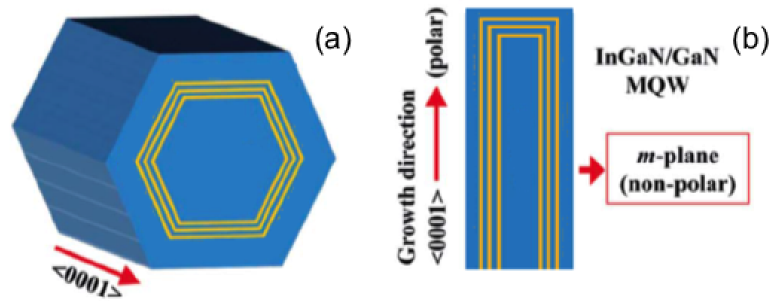

Figure 5.3: (a) and (b) sketches of the growth of core-shell GaN/InGaN MQWs c-plane and m-oriented, respectively. The width of the wells (InGaN in yellow) and the barriers (GaN in blue) is not realistic. Figure adapted from Reference [43].

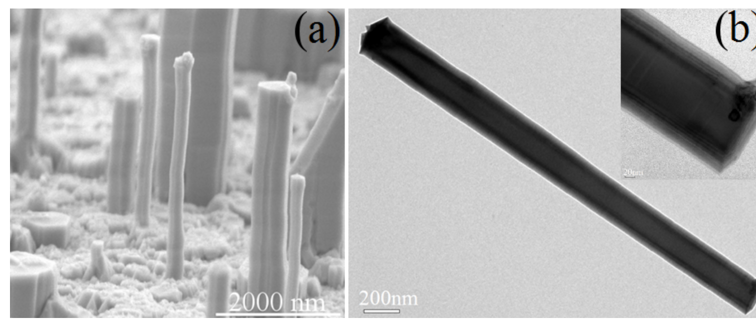

Figure 5.4: (a) SEM view of the sample and (b) HR-TEM of a single dispersed NW. The inset is a magnification of the bottom part of the NW.

5.2.3 InGaN MQWs in individual NWs

In order to check if the polar and non-polar MQWs correctly formed during growth, energy dispersive X-ray spectroscopy (EDS) was performed on individual NWs. EDS has been preferred to HR-TEM measurements, since it can be carried out on individual NWs dispersed on a TEM grid without the need of cutting them in lamellas. In the case of NWs, this process would have been costly and difficult. Furthermore, it would have destroyed a large number of NWs. EDS is based on the emission of characteristic X-rays from an atom through its excitation by an electron beam in a TEM system. The processes experienced by electrons of the atom during EDS are the same than in the case of XRF (for more details See section 3.4). EDS enables the study of the elemental composition of the NWs with high spatial resolution. The EDS measurement of this work were carried out with a FEI Tecnai G^2 TEM system, operated at 200 kV and the signal is recollected by a Si(Li) detector. The sample support is placed at 30° with respect to the electron beam for optimising the detection of the emitted X-rays. EDS linear scans, where the intensity of the integrated fluorescence lines of the elements of interest are recorded at each point of the scan, have been carried out.

The non-polar MQWs were studied performing the scan along the radial

direction in the top and medium heights of the NW. The TEM image of a representative scanned NW and the scanned zones are shown in Fig. 5.5 (a), while the integrated intensities of Ga K-line and In L-line are presented in Fig. 5.5 (b) and (c) for the top and the medium heights of the NW, respectively. The core-shell MQWs and the barriers appear as regular oscillations in the In fluorescence signal. Slight variations in the intensity and periodicity of these oscillations are observed between the top and medium regions.

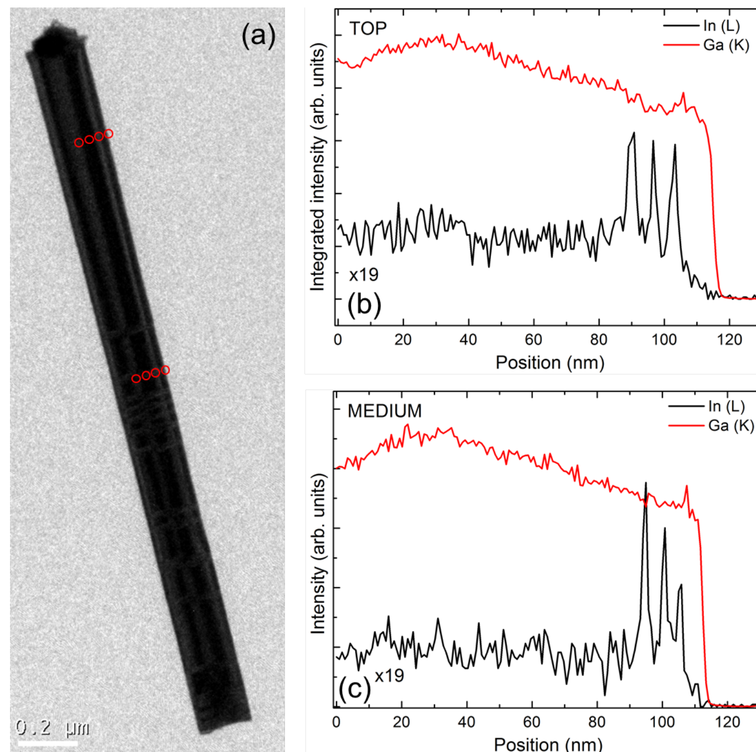

Figure 5.5: (a) TEM image of the scanned NW. The red circles identify the scanned linear zones, top and medium heights of the NW ($d = 200$ nm). Integrated intensities linear profiles of the L line of In and the K line of Ga at the (b) top position and (c) at the medium one, respectively.

Figure 5.6 shows the integrated intensities of Ga K-line, In L-line, and Au M-line along the axial direction; the inset corresponds to a TEM image of top region of the NW where the scan was performed. The signal of Au and In have been multiplied by appropriate factors in order to make it comparable to the more intense Ga fluorescence. There is no evidence of the formation of the polar MQWs at the top surface of the NW. Au is mixed with Ga and In within the first 220 nm of the NW (which corresponds to the shadowed part of the TEM image in the inset of Fig 5.6), as a result of the alloying during the first step of the VLS process. Then, a region extended for 200 nm is composed by In and Ga. The maximum concentration of In is found right after the part that accommodates the alloy of Ga and Au.

In order to estimate the widths of the wells and the barriers, the spectra

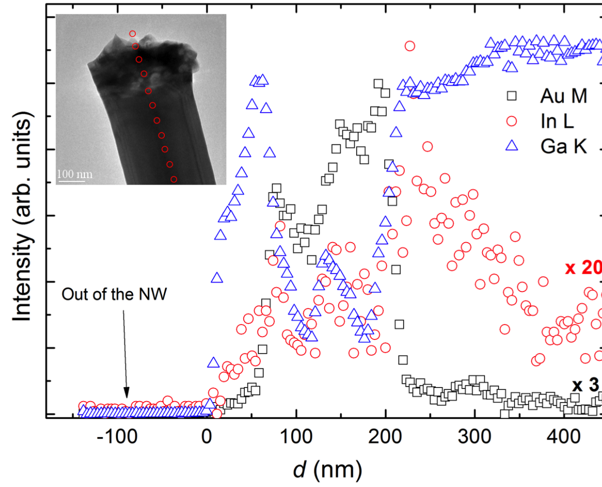

Figure 5.6: Integrated intensities linear profiles of the M line of Au (multiplied by a factor 3), L line of In (multiplied by a factor 20) and the K line of Ga at the top position of the NW along the c-axis. The inset is the TEM image of the top part of the scanned NW. The red circles identify the scanned linear zone.

of the lateral scans have been fitted to the model depicted in Fig. 5.7. R is the diagonal of the hexagonal core, t and s are the thickness of the

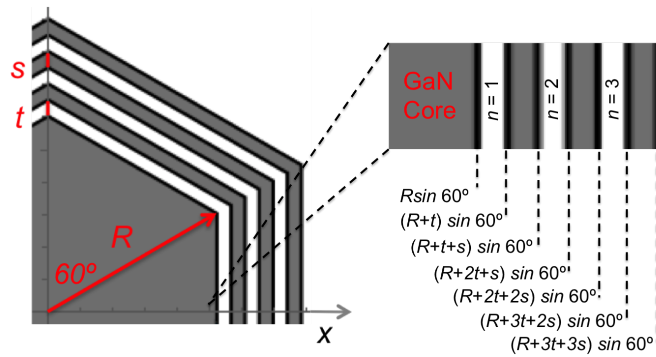

Figure 5.7: Schema of a quarter of the transversal section of the GaN/InGaN NW, where R is half of the diagonal of the GaN core, t and s are the thickness of the InGaN MQWs and the GaN barriers, respectively.

core-shell MQWs and the barriers, respectively. This fitting does not give a reliable value of the In concentration, due to the low chemical sensitivity of EDS. Thus, assuming that the In fluorescence emission is proportional to the illuminated volume, and defining C_{In} as the In concentration, the fluorescence intensity in correspondence to the region of the GaN core (labeled in Fig. 5.7) is proportional to

$$I_{In} \propto 3C_{In}t \tag{5.1}$$

and in correspondence to the wells, which are depicted in white in Fig. 5.7,

is

$$I_{In} \propto C_{In}\left[\frac{x}{tan60^{\circ}} + R + nt + (n-1)s - \frac{x}{sin60^{\circ}} + (3-n)t\right]$$

were $n = 1, 2, 3$ for the first, the second and third well, respectively. While for the barriers (coloured in grey in Fig. 5.7) a minimum in the In concentration is found (as in the case of the GaN core)

$$I_{In} \propto 2C_{In}t \quad \& \quad I_{In} \propto C_{In}t$$

Figure 5.8 (a) and (b) show the fit of the EDS radial line scans measured at the top and the medium heights of the NW, respectively. The profiles were fitted using Eq. (5.1) convoluted with a Gaussian of $\sigma = 4$ nm, which takes into account the real dimension of the EDS electron beam. The results of the fit allows to extract the radius, the width of the wells, and the barriers. They are summarised in Table 5.1. The error is given by the convolution of the error obtained from the fit with a Gaussian of $\sigma = 4$ nm.

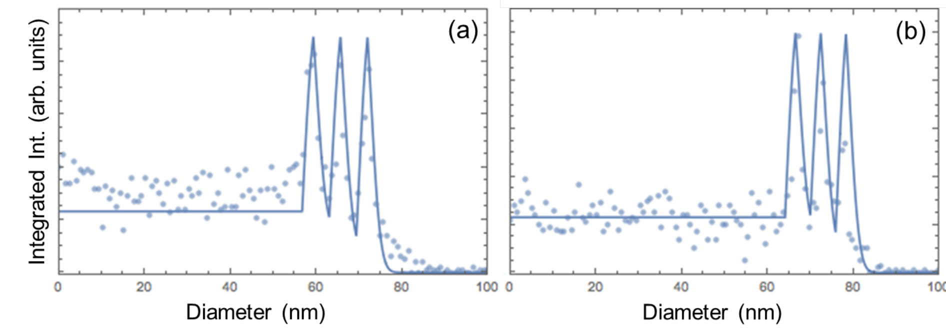

Figure 5.8: (a) and (b) present the fit of the EDS radial profiles measured at the top and middle heights, respectively.

Table 5.1: Results of the fit of the top and the middle EDS In transverse profiles.

	Top	Middle
s	4.9 ± 2.3 nm	4.0 ± 2.9 nm
t	5.7 ± 3.2 nm	5.0 ± 3.8 nm
R	65.6 ± 1.3 nm	71.1 ± 1.5 nm

5.3 Elemental distribution of individual NWs

The purpose of the measurements presented in this Section is to examine the compositional distribution of elements in the GaN/InGaN core-shell NWs. In particular, verifying if there is no incorporation of the Au catalyst and of

other impurities along the NWs that would imply a deterioration of their crystal quality, and checking the homogeneity of the In distribution along the core-shell MQWs, estimating the concentration of the alloy in the wells. Direct measurement of catalyst concentration in the NWs is experimentally very challenging, as it implies detecting concentrations below 1% with spatial resolution of nanometers. To this aim, the chemical sensitivity of EDS is not sufficient, despite its high spatial resolution.

X-ray fluorescence measurements were performed at the X-ray nano-probe beamline ID22NI of the ESRF, which provides high elemental sensitivity and a spatial resolution determined by the beam size (120×97 nm^2).

5.3.1 X-ray fluorescence maps

The average XRF spectrum of several individual NWs dispersed on a SiN thin windows was recorded to identify the different elements in the scanned area, which encloses the NW and its surrounding region. Only the results corresponding to a representative NW are presented. The spectrum was fitted using PyMCA program code (Section 3.4.2). This program allows to calibrate the XRF spectrum, to build elemental distribution maps, to subtract the noise through a baseline, and to prepare an optimised fitting function starting from the fit of the average XRF spectra. The overall XRF data are processed automatically with this function for obtaining high precision elemental distribution maps, that can be displayed and manipulated. Figure 5.9 shows the XRF spectrum of a full NW. Within the scanned area, the strongest peaks are those corresponding to In, Ga, and Au present in the NW. XRF peaks associated to Ag, Fe and Pb are also observed, with much weaker intensities.

The XRF spectrum described above comes from the averaged XRF spectra taken within the whole area of the NW and its surrounding with a pixel size of 25×25 nm^2 and an accumulation time of 0.2 s/pixel. In order to elucidate whether the elements observed in this scanned area are incorporated in the NW or not, the XRF spectrum of each pixel has been fitted with the function obtained from the spectrum in Fig. 5.9. The spatial distribution of Ga, In, Au, Ag, Fe, and Pb are shown in Fig. 5.10. Ga and In are clearly incorporated in the NW, since they present NW morphology, as it is depicted in Fig. 5.10 (a) and (b), respectively. Au catalyst, as well as Ag, were detected only on the top of the NWs implying no incorporation along the NWs, as it is shown in Fig. 5.10 (c) and (d), respectively. Ag can be present in very low levels in Au. The estimated concentration of Ag in the Au droplet given by PyMCA is around 0.02%. This is a proof of the high chemical sensitivity of XRF. Fe and Pb have a density of counts less intense and are present both in the NW and outside the scanned region. They cannot be a font of contamination of the MOCVD chamber where the samples were grown, because they were never used in it. The signals most

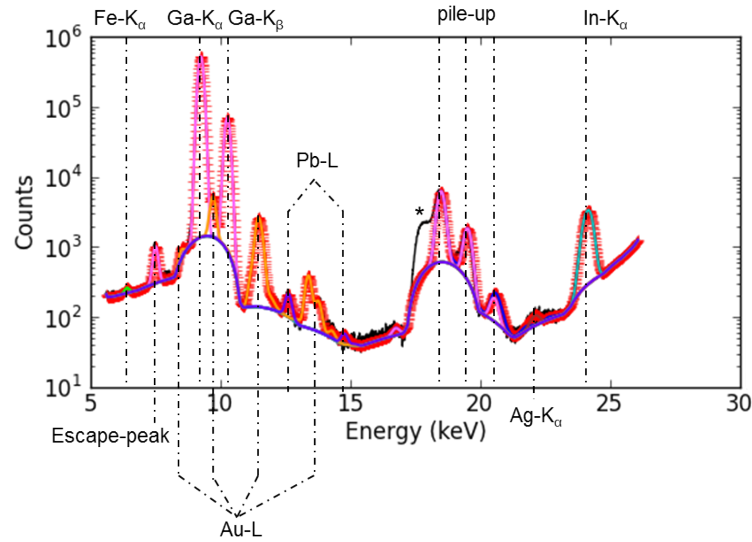

Figure 5.9: Average XRF spectrum of the full scanned area and fits obtained by PyMCA indicating each elemental distribution. The asterisk represents an artefact coming from the measurements.

probably come from second order processes of scattering from the shielding system around the sample or from the frame of the SiN thin window were the NWs are dispersed, and they will not be further considered.

Figure 5.10 (a) shows that Ga is homogeneously distributed along the NW axis. Radially, it is more intense in the centre (corresponding to the GaN core) and less in the outer surfaces (where only barriers and QWs are illuminated by the X-ray beam). On the other hand, the intensity of In increases from the bottom to the top end of the NW, as it is depicted in Figure 5.10 (b). The higher intensity of In at the top of the NW does not correspond to the formation of polar MQWs, as previously demonstrated by EDS.

In order to gain further insight, longitudinal and radial spatial profiles at the top, medium and bottom ends of the NWs were studied. The profiles confirm the trends that were previously found in the XRF maps: there is an increasing distribution of In and an accumulation of it at the top of the NW (see Fig. 5.11 (a)). Ga atoms, on the other hand, are more evenly distributed, as it is shown in Fig. 5.11 (b). The radial distribution of Ga shows similar intensities at the top, middle and bottom positions, as can be observed in Fig. 5.11 (d), (f), and (h). On the other hand, the In scans present slight variation in intensity, which is correlated with the increasing concentrations found from the bottom to the top of the NW (see Fig. 5.11 (c), (e), and (g)).

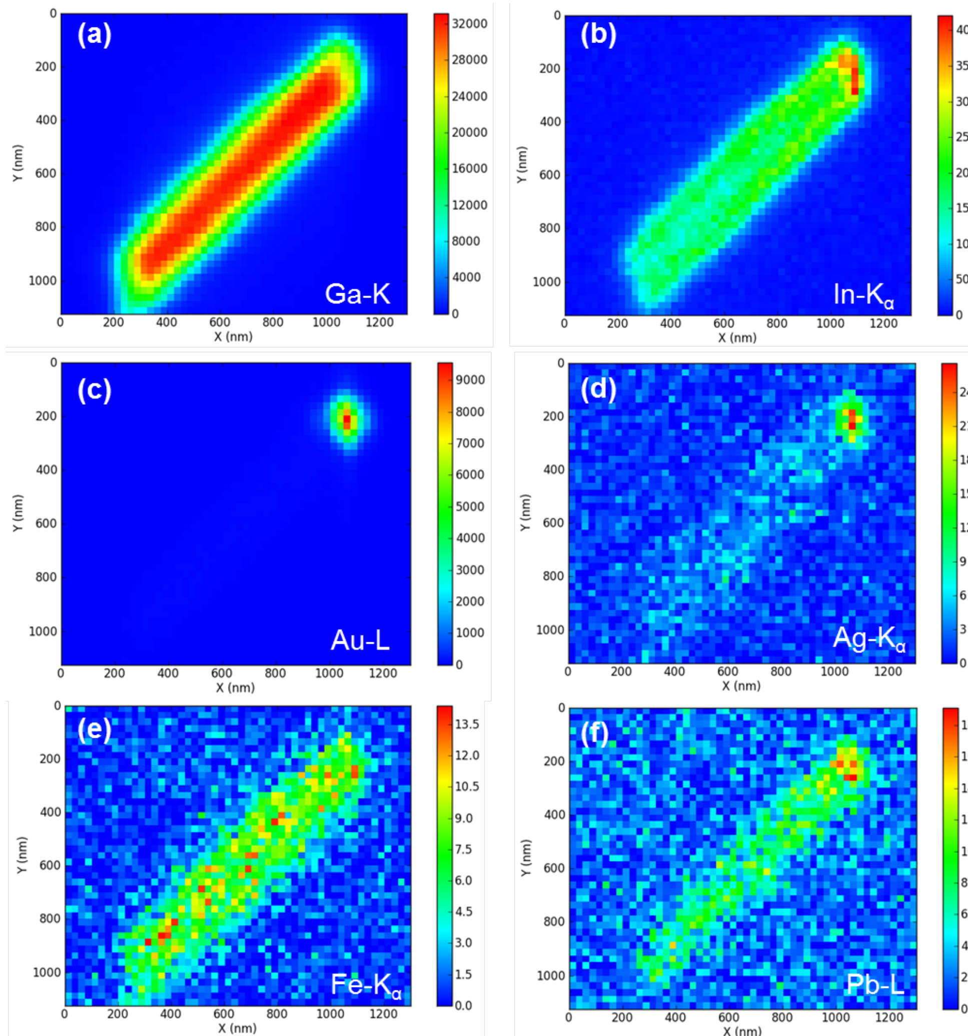

Figure 5.10: XRF colour map distribution of (a) Ga, (b) In, (c) Au, (d) Ag, (e) Fe and (f) Pb along the representative NW. The colour scale indicates the XRF intensity in photon counts.

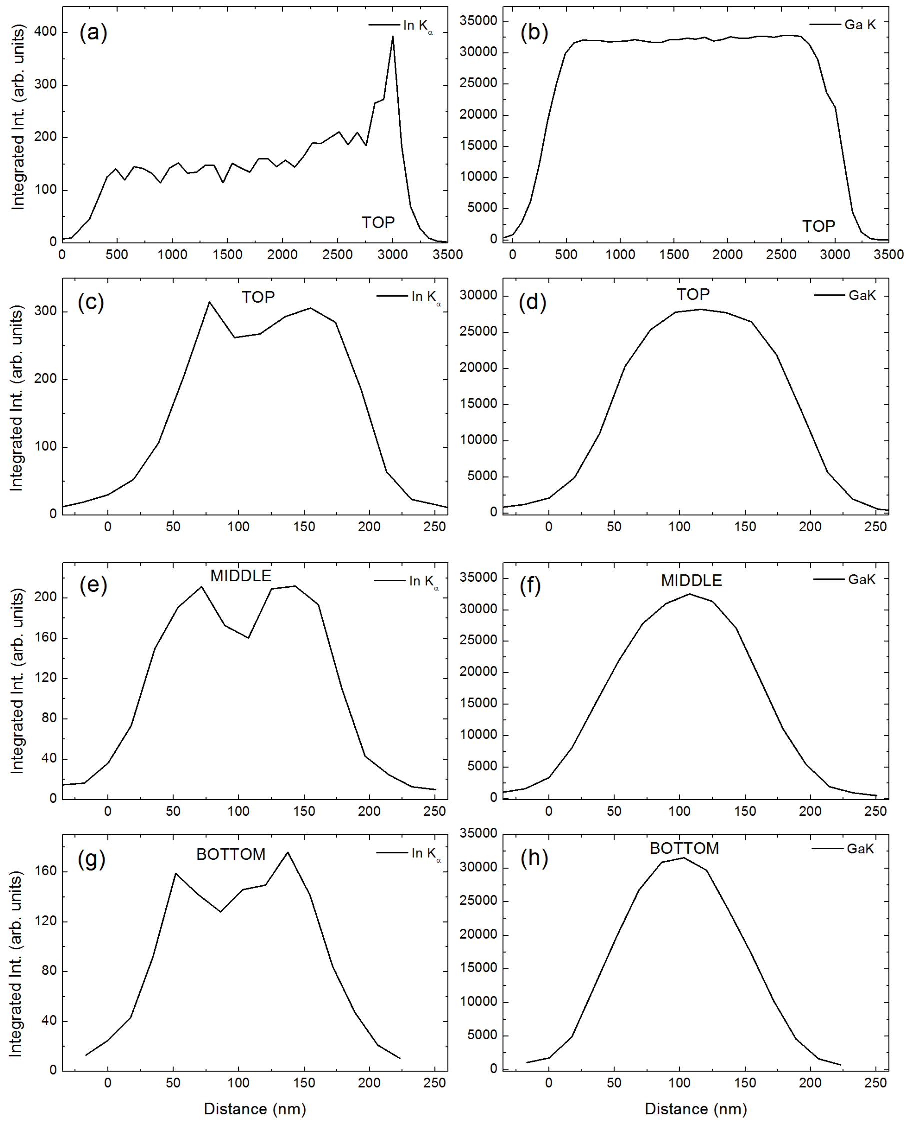

Figure 5.11: The profiles are relative to the NW presented in Fig. 5.10. (a) and (b) are the axial profiles of the In-K_α and Ga-K fluorescence intensity, respectively. (c), (e), (g), and (d), (f) and (h) are the In and Ga radial profiles at the top, middle and bottom of the NW, respectively.

5.3.2 Composition of non-polar GaN/InGaN MQWs

The In concentration in the core-shell MQWs can be extracted from the maps using PyMCA software. The relation between the intensity of the XRF emission of an element, I_i, and its concentration, C_i, for a flat sample excited by a monochromatic X-ray beam is given by [170]

$$I_i = I_0 k_i C_i \int_0^d e^{-[\mu(h\nu)/sin\theta_1 + \mu(hE_i)/sin\theta_2]y} dy \qquad (5.2)$$

where d is the thickness of the sample; I_0 is the intensity of the incoming beam; k_i accounts for the fluorescence yield, solid angle, and detection efficiency; μ is the total mass absorption coefficient at the energy of the fluorescence E_i; $h\nu$ is the excitation energy; and $\theta_{1,2}$ are the excitation and detection angles. In the current experimental conditions (i. e., small diameter of the NWs), the 'thin layer approximation' can be assumed, in fact the contribution to the fluorescence spectrum of the terms of reabsorption for the considered NW thicknesses is around 1% and it can be neglected. Thus, Eq. (5.2) can be rewritten as [170]

$$I_i \propto I_0 k_i C_i d \qquad (5.3)$$

which for the case of InGaN ternary alloy, has to satisfy the following condition: the sum of In and Ga concentrations has to be equal to one, $\sum_i C_i = 1$.

First of all, the In and Ga composition of the NW was calculated assuming that all the volume of the NW is composed by InGaN. In a second step, the In concentration of the core-shell MQWs was estimated using the values for the thickness of the wells, barriers, and NW core extracted from the EDS analysis (see Table 5.1). Finally, the In concentration of the MQW of several points along the c-axis of the NW can be estimated. Figure 5.12 depicts the six regions in which the concentration was deduced. The obtained values

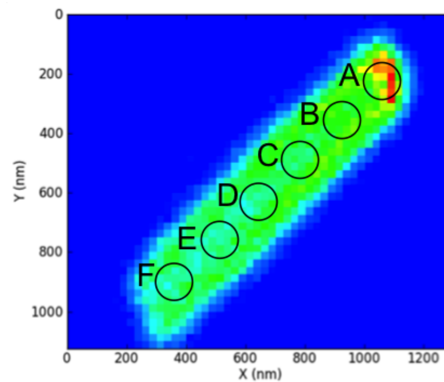

Figure 5.12: Regions along the c-axis in which the In concentration was measured.

Table 5.2: Values of the In concentration of the core-shell MQWs estimated by PyMCA along the *c*-axis of the NW.

Point	In Concentration (%)
A	11.6 ± 3.3
B	9.2 ± 2.7
C	7.4 ± 2.1
D	6.3 ± 1.8
E	5.4 ± 1.6
F	5.4 ± 1.6

for the In concentrations are reported in Table 5.2. The In concentration along the axis decreases from point A to point F, revealing that the alloy composition of the MQWs is not homogeneous. The error is the result of the propagation of the error on the In concentration given by PyMCA (around 5 %) and the error on the well thickness ($\pm$ 2.7 nm). The error of PyMCA is given by the errors on the parameters of renormalisation which the program uses for the calculations of the concentrations and represents the main contribution to the total error of the program. The error on the intensity of the XRF maps is around 0.13% and it can be neglected. The value of In concentration obtained for point A is 20% higher than in point B, according to the results of XRF spatial profiles (see Fig. 5.11 (a) and (b)). The correlation of the XRF and its fitting was rather low for point F, thus the In concentration in this point is less reliable than the others.

5.4 Structural properties of individual NWs

The structural properties at the nano- and micro-scale of single NWs were studied by the combination of three techniques: XRD, XANES, and Raman scattering. The structural quality of NWs can be affected by defects, such as TDs and BSFs, inhomogeneities in the alloy composition and In concentration or In segregation in some regions of the NW, and by strain fields due to the lattice mismatch between GaN (core and barriers) and InGaN (MQWs).

5.4.1 X-ray diffraction maps of individual NWs

Nano-XRD measurements were performed on the same NWs characterised by XRF in order to study their crystal phase, determine the lattice parameters at local level, and map their potential variation across the NWs. The XRD results related to the representative NW presented in Section 5.3.1 are reported.

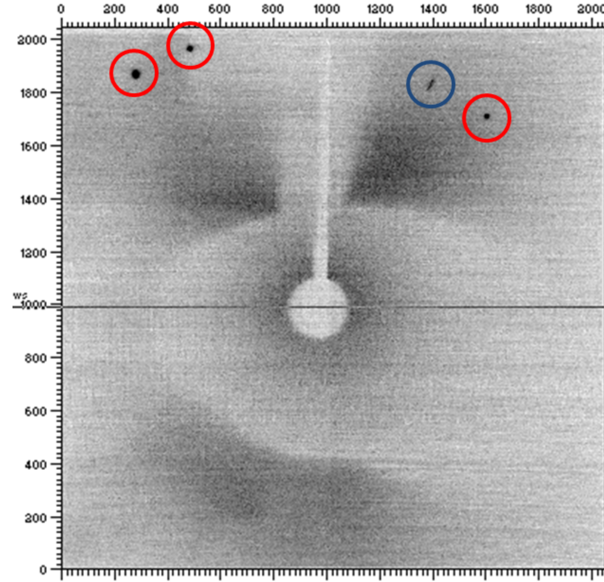

Figure 5.13: Representative CCD image of the XRD pattern. The black spots circled in red identify the diffraction peaks, while that in blue is an artefact. The white shadow in the central part of the XRD image is a region were no signal is detected, since a beam stop is placed on the XRD detector for protecting it from the direct X-ray beam, as depicted in Fig. 3.17.

A representative CCD image of the XRD pattern is shown in Fig. 5.13. The reflection at the right corner and the two reflections at the left corner circled in red correspond to $2\theta = (21.76 \pm 0.04)^\circ$, $2\theta = (24.54 \pm 0.08)^\circ$ and $2\theta = (25.03 \pm 0.08)^\circ$, respectively. The identification of these peaks, performed with Fit2D and PyMCA programs as described in Section 3.4.2, pointed out that they correspond to (104), (210) and (211) reflections of unstrained wurtzite GaN. The last two diffraction peaks are shown in Fig. 5.14. The error of the calibration (for further details see Section 3.4.2) is the main contribution to the error of the diffraction angles. The error of the fit performed by Fit2D program is three order of magnitude smaller than the calibration error, and has not been taken into account. The value of the GaN wurtzite reflections expected in this case were calculated with PowderCell program [171]. From these reflexions it is possible to calculate the interplanar distance d using the Bragg's law (Eq. (3.40)). Then, the lattice parameters of the studied NWs can be extracted from the relation between the interplanar distance, d, the Miller indices (hkl) and the lattice parameters a and c of the wurtzite structure:

$$d_{hkl} = \left[\frac{4}{3a^2}(h^2 + hk + k^2) + \frac{l^2}{c^2} \right]^{-1/2} \tag{5.4}$$

Symmetric reflections, such as (210), allow to extract the lattice parameter

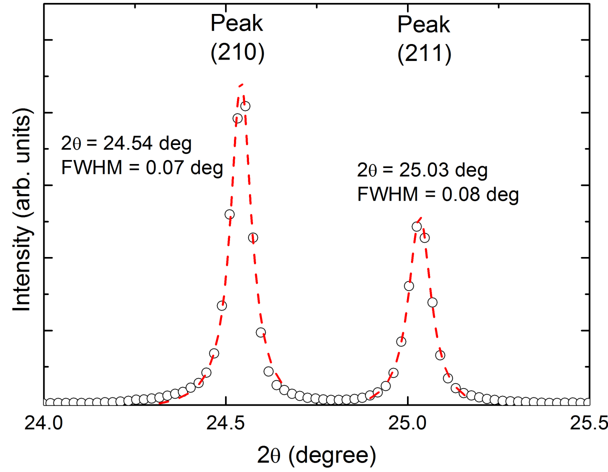

Figure 5.14: Representative XRD peaks. (210) and (211) along with their best Gaussian fit. The peak position and the FWHM are indicated for each fit.

a directly from Eq. (5.4) by substituting the reflection Miller index and the related d. Then, from non-symmetric reflections, such as (211), it is possible to calculate the lattice parameter c. The values obtained from the XRD data are summarised in Table 5.3. The errors were calculated propagating

Table 5.3: Lattice parameters.

Parameters	Å
a	3.18 ± 0.01
c	5.1 ± 0.6

the error on the angle θ. It has to be noted that the error obtained for the c parameter is one order of magnitude higher than the error on a due to error propagation. The obtained values for the lattice parameters match the values of strain-free wurtzite GaN of the literature (reported in Table 2.1 in Chapter 2).

XRD scans of the entire area of the NWs allowed to perform a structural study of all the NW in the nano-scale. The obtained map is shown in Fig. 5.15 (a). The points of the map represent the intensity of the XRD reflection coming from each spot of the NW. There are significant differences in the intensity (number of counts), moreover there are points in which no signal is registered. This occurs when the Bragg condition is lost along the scan due to imperfections on the NW surface. The diffraction peaks position have been measured and the lattice parameters of the NW have been calculated at each point of the map using Eq. (5.4). The variation of the lattice parameters along the NW axis is presented in Fig 5.15 (b). This analysis shows no systematic changes in the crystal structure and no detectable strain in the GaN material.

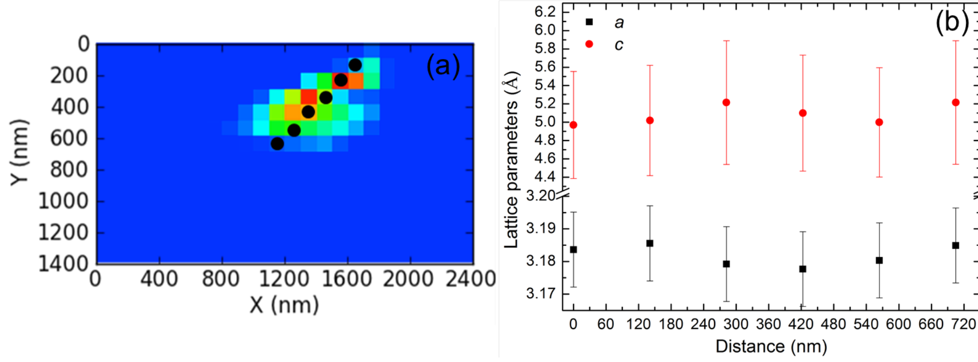

Figure 5.15: a) XRD map of a single NW. Only a part of the NW emitted XRD signal. The black circles indicated the reflection points along the c-axis. b) Evolution along the c-axis of the wurtzite lattice parameters a and c starting from the lowest black point that corresponds to the centre of the NW of Fig. (a).

Figure 5.16 shows the variation of the XRD peaks in logaritmic-scale along the axis of the NW from the middle height to the top (as depicted in Fig. 5.15 (a)). All of them come at the diffraction angle of the diffraction peak (210) of unstrained GaN. Similar results are obtained for (211) refraction. The individual spectra show a slight variation in the angle positions which falls within the error ($\sim 0.08°$). Neither additional reflections nor asymmetry of the peaks are observed. Therefore, only diffraction peaks corresponding to unstrained GaN reflections were detected studying the XRD signal of the whole NW. This fact suggests that the core-shell InGaN MQWs are completely lattice matched to the strain-free GaN core. Otherwise they would have appeared as distinct peaks or asymmetries of the GaN XRD peaks. The expected XRD reflection angles of unstrained InGaN MQWs can be predicted indirectly. The expected values of the unstrained lattice parameters of the InGaN MQWs can be calculated using Vergard's law

$$a_{In_xGa_{1-x}N} = xa_{InN} + (1-x)a_{GaN} \tag{5.5}$$

Using Eq. (5.5) and the averaged value for the alloy composition in the region scanned by XRD ($x = 0.076$ as obtained from Table 5.2), the lattice parameters are $a_{In_xGa_{1-x}N}$= 3.215 $\AA$ and $c_{In_xGa_{1-x}N}$= 5.225 $\AA$. Now, substituting the value of the lattice parameters in Eq. (5.4), d can be extracted and thus, from Bragg's law the diffraction angles corresponding to the reflections (210) and (211) of InGaN can be calculated and they correspond to $2\theta_{210} = 24.262°$ and $2\theta_{211} = 24.757°$, which are depicted as dashed lines in Fig. 5.16. No distinctive XRD peak coming from the core-shell MQWs has been observed in the expected region, confirming that the core-shell MQWs are completely matched with the GaN core and therefore completely strained (compressed along a and c directions and expanded along m-direction).

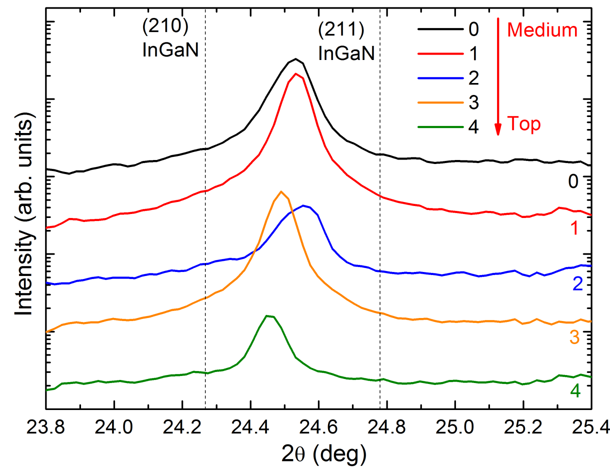

Figure 5.16: Variation of the (210) GaN XRD diffraction peak from the middle height to the top of the NW. In Fig. 5.15 (a) the reflections points are circled in black. The dashed curves indicate the position of unstrained InGaN with In concentration of $x = 0.076$.

5.4.2 X-ray absorption near edge spectroscopy of individual NWs

XANES measurements were performed for studying the local disorder of the GaN present in the NWs. The maps were taken with a step size of 1 eV near the Ga K-edge, that matches the energy resolution provided by the double-crystal monochromator. The representative X-ray absorption near edge spectra of a single NW taken with the polarisation of the X-ray parallel and perpendicular to the axis of the NW are shown in Fig. 5.17 (a) and (b), respectively. The XANES spectra of the NW where compared with

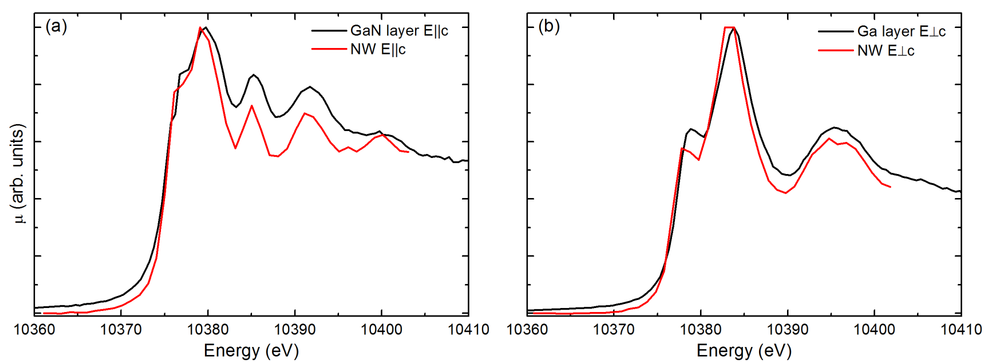

Figure 5.17: Comparison between a reference GaN layer for different X-ray beam incident angles (a) parallel polarisation to the axis of the NW and (b) perpendicular polarisation.

those measured in a high quality GaN reference layer, measured for polarised X-rays either parallel or perpendicular to the wurtzite c-axis. The spectra of

the NW match the reference one, therefore it can be concluded that the NW has wurtzite structure and there is no mixture of phases (see Section 2.1.1). Moreover, it can be argued that the axis of the NW coincides with the *c*-axis of the wurtzite structure. The small difference between the absorption edge of the NW and that of the layer is attributed to the calibration, since the measurements were carried out in different moments and therefore not in exactly the same experimental conditions.

5.4.3 Raman scattering of individual NWs

Raman measurements were carried out for studying the structural properties of the core-shell GaN/InGaN NWs. The measurement were performed on several single NWs dispersed onto a Au-patterned substrate with different laser wavelength in the visible (488nm, 514nm and 647nm) and the results show no variations with the excitation energies in this range. A representative Raman spectrum is shown in Fig. 5.18 (a). The observed Raman peaks

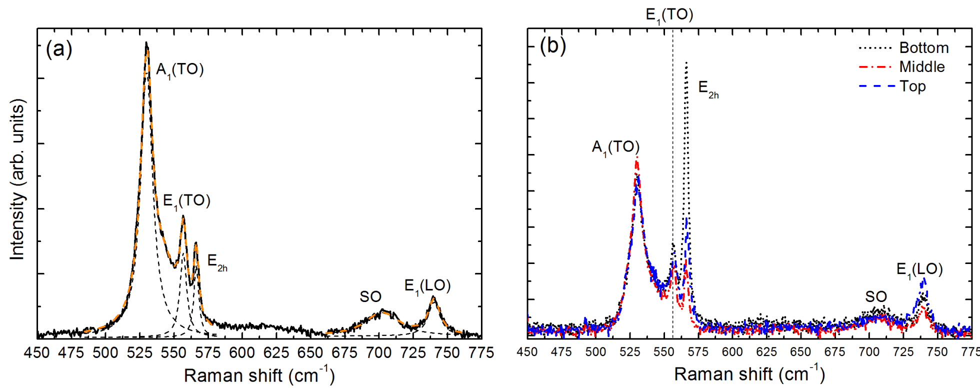

Figure 5.18: (a) Representative unpolarised Raman spectrum of a single NW taken at 514 nm and (b) Raman spectra taken at the bottom (black curve), middle (red curve) and top (blue curve) and of the NW measured with 647nm laser line.

have been fitted by Gaussians and the results are summarised in Table 5.4. Their values match those of wurtzite strain-free GaN. Although A_1(TO) and E_{2h} phonon modes are allowed in the back-scattering configuration (see Table 3.1) , and therefore they are expected to be seen more intensely, additional modes are observed, such as E_1(TO) and E_1(LO). The observation of these modes is attributed to deviations from the nominal geometry: the studied NWs have hexagonal cross-section, so the excitation light does not impinge at completely flat lateral surfaces, but on the oblique facets whose angle depends on how the NW is laying on the substrate. Therefore the refraction of the excitation light enables the detection of these ‘forbidden modes’, as it was observed for SAG NWs due to the semi-polar facets of their tips (as it is described in Section 4.3.2). An additional peak centred around 701cm^{-1} can be attributed to a surface optical mode (SO), since its frequency belongs to

Table 5.4: Raman active modes of the GaN/InGaN NWs.

	Mode (cm^{-1})	FWHM (cm^{-1})
$A_1(TO)$	530	10
$E_1(TO)$	557	6
E_{2h}	566	3.5
$E_1(LO)$	740	10

the range in between the TO and LO phonons frequencies, as it is described in Section 2.3.4. This peak cannot be attributed to a mode of the InGaN core-shell MQWs, because the frequency does not match the In content of the quantum wells. In fact, according to Eq. (2.10) and for the concentrations obtained in Section 5.3.2, the position of the SO corresponding to the $A_1(LO)$ phonon would be around 725cm^{-1}.

Several spectra were recorded along different points of the NWs for checking if there were any changes due to the non-uniform growth of the core-shell MQWs, similar to those revealed by the XRF and EDS measurements (see Section 5.3). There are no changes in the frequency of the peaks as it is shown in Fig. 5.18 (b). The intensity of all the peaks generally keeps constant along the NWs, except for the E_{2h} mode that in many cases shows a dramatical change in intensity. The FWHMs of the E_{2h} mode measured on several NWs is around 3.6 cm^{-1} confirming the good quality of the GaN core.

Resonant Raman scattering measurements (with laser line 365 nm) were performed for exciting directly the core-shell MQWs. The Raman signature was hidden by the really intense PL signal. Thus, no information could be extracted.

5.5 Optical properties of single NWs

The optical properties of individual GaN/InGaN core-shell NWs will be studied in this section by PL. A statistically relevant number of individual NWs have been measured. Only representative results are showed. First, the results of PL at low temperature of the NW ensemble are presented. Then, the internal quantum efficiency of individual NWs is studied.

5.5.1 Emission of NW ensembles

Low temperature (7 K) macro-PL has been measured on the ensemble of GaN/InGaN core-shell NWs with 325 nm laser line, whose spot diameter was of 100 μm. Therefore a large zone of the sample was probed, as it becomes clear looking at Fig. 5.4 (a). A representative low temperature PL spectrum is shown in Fig. 5.19. The spectrum is dominated by the excitonic

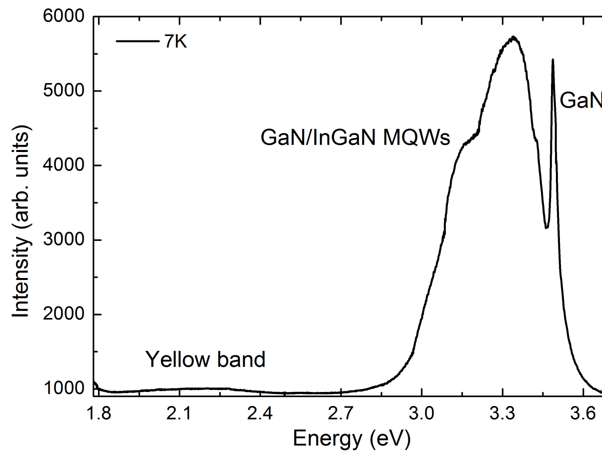

Figure 5.19: Low T PL spectrum of the ensemble of NWs.

emission of GaN/InGaN MQWs and GaN core centred around 3.33 eV and 3.48 eV, respectively. A much weaker third broad band centred at 2.2 eV corresponds to yellow luminescence and is attributed to nitrogen vacancies or the presence of impurities, such as oxygen or carbon [172]. The emission shows large FWHM (around 300 meV for the MQWs and 20 meV for the GaN core), attributed to the inhomogeneity of In composition of the MQWs and of the ensemble, as already reported in Fig. 5.4 (a). In the case of the GaN core the PL broadening can be related to structural defects, as was discussed in Chapter 4 for the case of GaN SAG NWs.

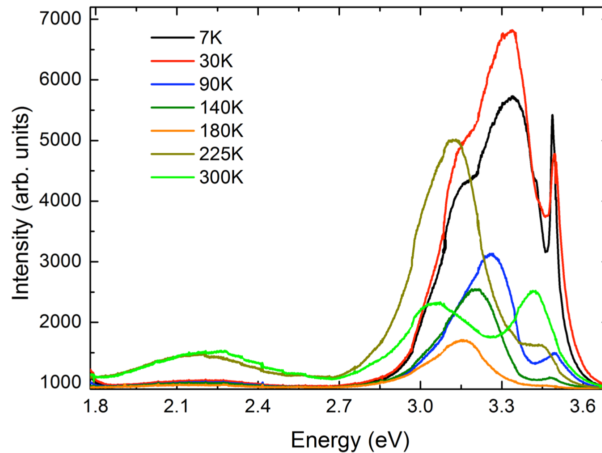

Figure 5.20: Temperature dependence of the PL of the ensemble of NWs.

Figure 5.20 shows the variation of the PL spectra of the ensemble of the NWs measured at different temperatures. The PL bands progressively redshift with increasing temperature, as expected. There are sudden changes in intensity and energy of the bands which are also due to inhomogeneities of the ensemble, as previously reported for the FWHM. Moreover, the stage in which the sample is fixed during the measurements can change its position

slightly due to thermal expansion with increasing temperature. The lack of reproducibility of the PL spectra from one area to another makes it difficult to study the ensemble and to extract conclusive information from its spectrum. Thus, single NW characterisation is highly beneficial as it would provide a more fundamental understanding of the optical processes and more control over the experimental conditions.

5.5.2 Emission of single NWs

Hundreds of NWs were dispersed on a Au-patterned substrate for measuring their individual emission. Representative PL spectra taken at 5 K with the laser light focused either at the tip or the base ends of the NWs are showed in Fig. 5.21 (a) - (d). All the spectra are dominated by excitonic

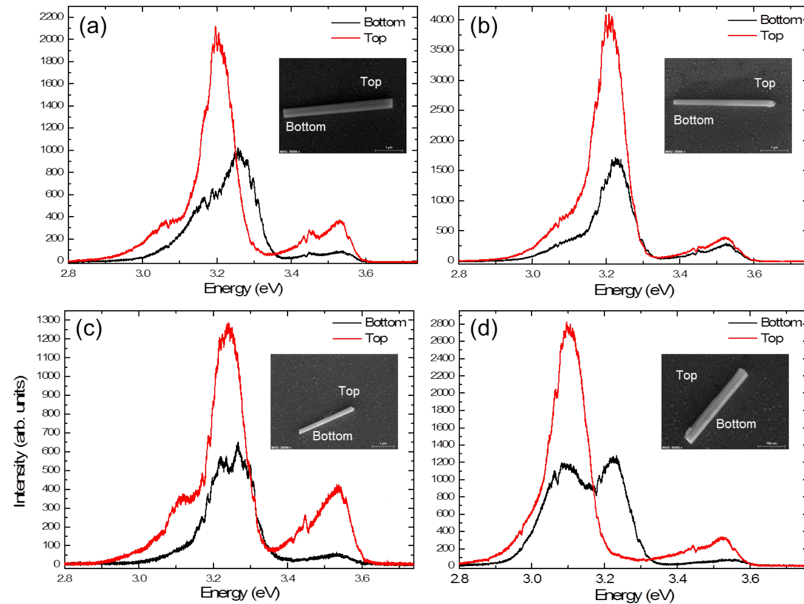

Figure 5.21: (a), (b), (c) and (d) are representative PL spectra taken at the top and bottom ends of different NWs at 5 K with the same experimental conditions: laser power ($\sim$ 10 μW), accumulation time (60 s), and experimental setup.

transitions of the GaN/InGaN core-shell MQWs with energies between 3.1 - 3.3 eV. The large FWHM ($\sim$ 34 meV) of this peak is attributed to the variation of the alloy composition along the NWs (see Section 5.3.2). The peak centred around 3.47 eV is attributed to emission from GaN and it is originated by the overlapping of the D^0X_A (FWHM $\sim$ 50 meV) and X_A emissions (FWHM $\sim$ 20 meV). Comparing the core emission spectra of the core-shell NWs to the ones of the SAG GaN NWs grown by MBE studied in the previous Chapter (see Section 4.3), the latter have narrower FWHMs, revealing a higher crystal quality. There is a feature appearing at 3.45 eV

present in all the spectra which has been attributed to an artifact coming from the gratings of the spectrometer.

When comparing the spectra taken at the tip and the base of each NW, the PL band of InGaN MQWs increases its intensity and red-shifts from the bottom to the top of the NW. This again could be due to the higher In concentration towards the top end of the NW. This effect is attributed to the inhomogeneous In concentration along the core-shell structure of each individual NW, which was demonstrated by the XRF measurements. Despite the inhomogeneities present in each single NW, the FWHM of the MQWs of individual PL spectra are smaller (one order of magnitude less) than those of the ensemble. In the case of the emission of the GaN core, similar FWHMs, around 20 meV, are measured for the ensemble and the individual NWs. On the other hand, the MQWs emission peak of the ensemble is blue-shifted of 0.1-0.2 eV compared to that of the individual spectra. Thus, the overall inhomogeneities of the ensemble mask the real properties of the individual NWs and single NW characterisation is demonstrated to be necessary.

Figure 5.22 shows two room temperature spectra of the same individual NW taken at its top and bottom. The GaN/InGaN core-shell MQWs emission around $\sim$ 3.05 eV dominates the spectra. The emission from the tip is slightly redshift ($\sim$0.5 eV) and broader than that of the bottom due to the higher concentration of In. The small peak at $\sim$ 3.42 eV corresponds to band to band transitions of GaN. PL measurements as a function of the

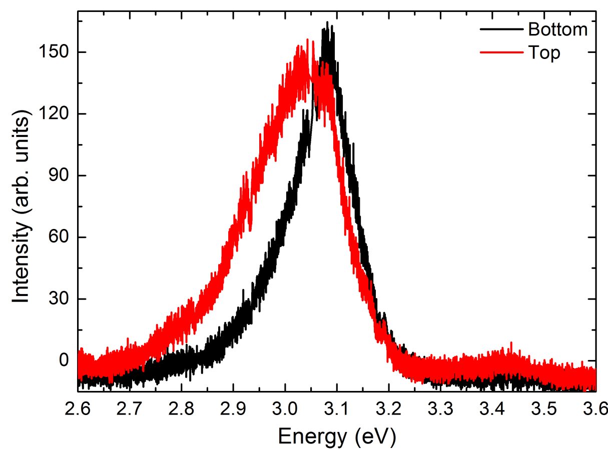

Figure 5.22: Room temperature PL taken at the top and bottom part of the single NW in Fig. 5.21 (a) in the identical experimental conditions than for low temperature measurements.

temperature allow to calculate the relative internal quantum efficiency (IQE) of the optical transitions at room temperature. This can be done under the assumption that, at low temperature, non-radiative processes are suppressed and they are activated at room temperature. Thus, the relative IQE is given by the ratio between the PL integrated intensity at room temperature and low temperatures. Then, the IQE at low temperature is equal to 1, while at

room temperature, IQE of the tip and of the base of the core-shell InGaN MQWs is around 20% and 15%, respectively. On the other hand, the IQE of the core is less than 1%, as it is expected for the absence of quantum confinement.

5.6 Discussion

The detailed studies of individual NWs performed by a combination of non-destructive techniques (EDS, XRF, XRD, XANES, and Raman scattering) presented in the first part of this Chapter have provided a complete picture of the structure and chemical composition of the GaN/InGaN core-shell NW heterostructures. The EDS spectroscopy on single GaN/InGaN core-shell NWs shows that non-polar MQWs formed correctly at their lateral surface. Linear EDS scans along the axial direction of the NW detect an In accumulation at the tip of the NWs, but no QWs are observed. The XRF maps performed at the nanoscale confirm these results and the In concentration increase from the bottom to the top with values between 5% and 12%. Since the control of all the growth conditions at the nanoscale is complex, the accumulation of In towards the top part of the NW can be attributed to various causes, e. g., temperature difference between the bottom and the top of the NW; local different V/III-ratios; or more efficient diffusion of In along the axial direction. In fact, adatoms are incorporated by two mechanisms: direct impingement on the NW surface and diffusion from the substrate to the top of the NW.

The material of the core-shell NWs does not present disorder at the local level, as shown by the XANES results. On the other hand, no distinctive signature from InGaN MQWs is observed by XRD measurements. Since these are performed illuminating all the material present in the NW, a signal from the MQWs would be expected if they grew with the lattice parameters of InGaN. This suggests that the MQWs are strained and completely matched to the GaN core, otherwise some resolved peaks or asymmetry in the GaN XRD refractions would have been observed.

In order to support our conclusions, the results of a theoretical simulation are presented. These allow to calculate the expected energy band gaps of these strained QWs which can be then compared with the results obtained in the PL measurements presented in the previous Section. *Mengistu et al.* of the University of Valencia performed finite-difference-time domain (FDTD) simulations in order to investigate these points. The FDTD calculations were performed using the COMSOL-Multiphysics software platform [173] following the approach described in Reference [174] for a core-shell NW. Being numerical simulations of 3D elastic problems (e.g., calculation of strain) generally time- and CPU-expensive, the 2D simplification under specific conditions is preferred. The general hypothesis is that the strain field depends only on the in-plane coordinates (x,y), and therefore, all the

cross sections along z can be considered identical (see Fig. 5.23). The employed approximation gives good results in the case of finite but long 3D system, i.e., $L >> R$. This perfectly matches the case of NWs.

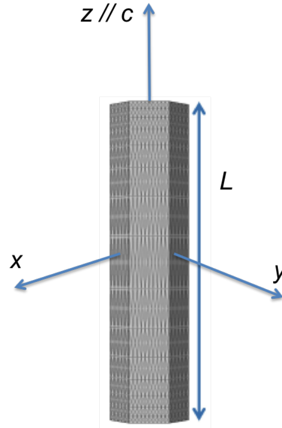

Figure 5.23: Sketch of the GaN/InGaN MQW NW. Adapted from [174].

The numerical calculations were made for an GaN/InGaN MQW NW with cross section like that displayed in Fig. 5.7 and with averaged values of the thickness of the wells (4.5 nm) and the barriers (5.4 nm) (as summarised in Table 5.1) and In concentration of 10% (compatible with those of Table 5.2). It is assumed that the only source of strain is given by the lattice-mismatch between InGaN and GaN.

The results for the strain field are given in cylindrical coordinates, where the components of the strain tensor are the radial one, ε_{rr}, the angular one, $\varepsilon_{\phi\phi}$, and the one along z (that in the studied case is parallel to the c-axis), ε_{zz}. Figures 5.24 (a), (c) and (e) show maps of the strain fields, ε_{rr} and $\varepsilon_{\phi\phi}$, and ε_{zz} for the the NW cross section. The GaN core is almost completely relaxed (all strain components are in the range 0 - 0.2%). Similarly, the GaN of the MQW barriers is slightly expanded except for the radial direction ($\varepsilon_{rr} \sim -0.1\%$). Two strain components, $\varepsilon_{\phi\phi}$ and $\varepsilon_{zz} \sim -0.8\%$, show that the InGaN wells are under compressive strain, obviously due to the larger lattice parameter of the InGaN than that of GaN. The radial component is tensile strained as a result of the compression along the angular and c-axis directions ($\varepsilon_{rr} \sim 0.4\%$). The distribution of the strain is homogeneous except for the corners where, due to their particular shape, the strain field has a more complicated expression. These results confirm the observations made by XRD: GaN/InGaN MQWs grow strained and matched to the GaN material.

Figures 5.24 (b), (d) and (f) show the evolution of the strain components along the x-direction for each material (i. e., core, QWs and barriers). The effect of changing the In concentration has been modelled for the strain components and a linear dependence is observed.

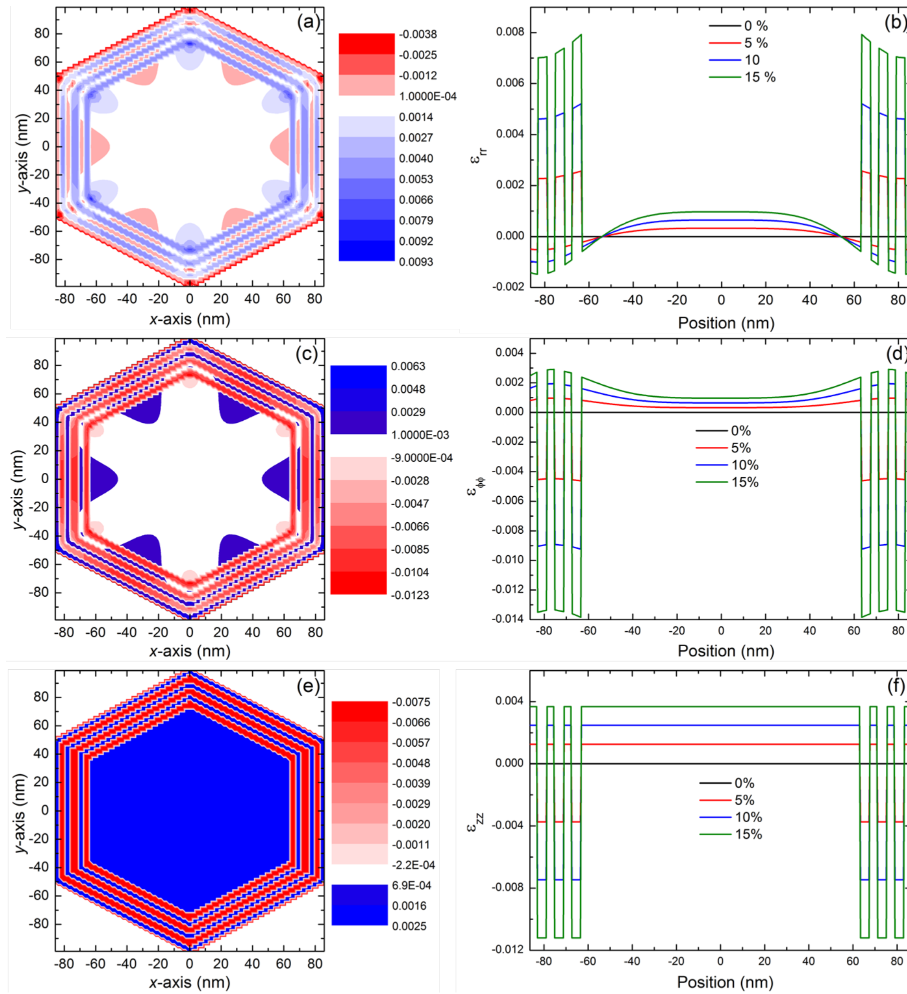

Figure 5.24: Strain field maps of the NW cross-section for InGaN MQWs with 10% In concentration for the components (a) ε_{rr}, (c) $\varepsilon_{\phi\phi}$ and (e) ε_{zz}, respectively. (b), (d) and (f) evolution of the strain components related to each material (i. e., core, QWs and barriers) along the x-direction ($y = 0$) for different In concentrations.

Once, the strain field distribution is obtained, the electronic band structure of strained InGaN can be calculated. Figure 5.25 shows the trend of InGaN band gap energy (E_g) for different In concentrations for unstrained and strained InGaN, respectively. As expected, due to the compressive character of the strain field, strained InGaN has band gap energies higher than those of relaxed material. The values of In concentration in the GaN/InGaN core-shell MQWs, calculated thanks to the XRF measurements, are in the range of 5%-12% and the corresponding band gap energies, taking into account that the MQWs are strained, are between 3.05 - 3.29 eV. This result is in very good agreement with the PL measurements. Thus, the redshifting of the PL band from the base to the tip of the MWQs is related to the greater In concentration present in the top of the NW. Moreover, the inhomogeneous distribution of In along the NWs can also justify the broadening of the PL

spectra.

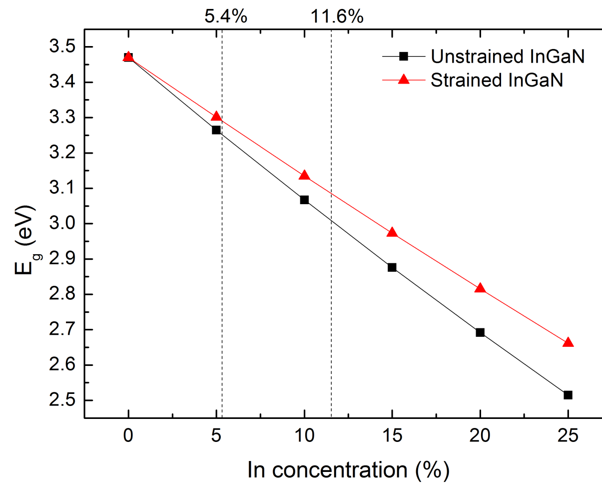

Figure 5.25: InGaN energy band gap variation with In concentration. The dashed lines represents the minimum and the maximum In concentrations that have been observed in GaN/InGaN core-shell MQWs studied in this Chapter.

Chapter 6

Surface Enhanced Raman Scattering of individual ZnO nanowires decorated with Au nanorods

This Chapter is devoted to the study of surface enhanced Raman scattering (SERS) in hybrid systems composed of Au-nanorods and ZnO NWs. Despite the outstanding results obtained for molecular species, the understanding of the real capabilities of SERS for characterising semiconductor NWs is still vastly unexplored.

The Chapter is structured as follows: in Section 6.1 the state of the art of SERS research is described. In Section 6.2, the first investigated sample and the results of its characterisation by Raman scattering are presented. Then, the synthesis of the Au-nanorods and the process of fabrication of the Au-nanorods ZnO NWs hybrid systems are described in Section 6.3. Afterwards, the results obtained by SERS both on bare Au nanorods and on single hybrid systems are shown in 6.4. Finally, in Section 6.5, the results are discussed.

6.1 Introduction

In the last decades, the potentiality of SERS compared to the traditional Raman scattering has been proved [175]. As presented in Section 3.2, it exploits the intense electromagnetic fields generated by localised surface plasmons at noble metal/nanostructure-dielectric interfaces. The incident electromagnetic field is amplified by a factor 10^2-10^4 in close proximity of the metal nanostructure and this produces an amplification of the Raman signal of about 4-8 orders of magnitude [107]. In order to exploit this field enhancement effect the probe has to be close or in contact with the metal surface (maximum 30 nm away [107]). The discovery of SERS resolved the

main disadvantage of Raman spectroscopy, its intrinsically low detection sensitivity, opening many opportunities in fields such as chemistry, biology, and nano-structured materials. Up to now, SERS have been mostly used for detecting molecular species with very impressing results: from low concentration down to the single molecule [119,176]. SERS is very efficient in the investigation of molecules, which can be adsorbed directly on the surface of metal nanoparticle. The variety of the molecular categories that have been successfully studied is very wide. For example, *Khaing Oo et al.* [177] built tailored gold nanoparticles SERS substrate for the detection of vapours of explosive substances. This work is promising for the development of ultra-fast and ultra-sensitive SERS devices for explosive identification and monitoring. *Zhang et al.* [178] proposed a highly sensitive and reliable SERS substrate formed by gold silver core-shell nanorods for detection and characterisation of low concentration pesticides and contaminants in fruits. *Sanles et al.* [179] designed and fabricated an optically stable SERS substrate comprising silver-coated carbon nanotubes for the safe detection and quantification of highly toxic sources in low concentration in the environment or in biological fluids.

The possibility to investigate the vibrational surface properties of single semiconductor NWs by SERS is more intriguing [180]. Due to the low detection signal, normally Raman characterisation of individual nanostructures is performed in resonant conditions, that cause the heating of the semiconductor material, its consequent degradation and the excitation of the secondary emission which could alter or hide Raman signals. Thus, SERS performed at excitation energies corresponding to the plasmonic resonances of the metal components and below the semiconductor band gap would allow to overcome these critical issues. However, only few authors have reported SERS on hybrid semiconductors nanostructures [59, 181–183] and, in some cases, they fulfilled SERS conditions with illumination wavelength corresponding to those of resonant Raman scattering. For example, *Peng et al.* [184] demonstrated that the decoration of Si NWs with Ag nano particles produced an enhancement of the Raman signal by a factor 7. A similar approach was used by *Chen et al.* [185] who decorated Si NWs with Au nano particles of different morphologies demonstrating enhancement of Raman signal by a factor of 24 compared to the bare NWs. In these studies, however, the resonance conditions for SERS correspond to those of resonant Raman scattering.

There are two main issues affecting SERS. The first one is related with the enhancement of the SERS signal and the second issue concerns the reproducibility of the measurements. In fact, SERS can present fluctuations in the intensity of the signal, in the peaks positions and widths, and in the relative intensity of the peaks, as already discussed in Section 3.2.3.

6.2 ZnO nanowires

ZnO NWs provide a very attractive candidate for short-wavelenght optoelectronic devices, such as light emitting diodes, laser diodes [186] and photodetectors for the UV spectral range [187]. This is due to low cost and ease of manufacturing, its large band gap, thermal and chemical stability and its large excitonic binding energy. ZnO NWs with high quality crystalline structure have been obtained, nearly free of stacking faults and dislocation [188].

6.2.1 ZnO NWs grown by chemical vapour deposition

ZnO NWs studied in this chapter were synthesised by vapor transport technique [189] enabled by VLS method, which has been already described in Section 5.2.1). Initially, a substrate is covered by a catalyst, generally a thin layer of gold (thickness $<$10nm) and is heated to a temperature between the melting point of ZnO and that of the catalyst. The catalyst becomes liquid and forms droplets. The ZnO is supplied in a gaseous phase and is absorbed by the catalyst droplet. ZnO is supplied until the supersaturation is reached and starts to nucleate in solid phase at the interface between the catalyst and the substrate. The catalyst does not incorporate in the ZnO due to its low solubility and it remains on top of the growing NW. The size of the NWs is controlled by the size of the catalyst droplet and its length by the time of the ZnO vapour supply.

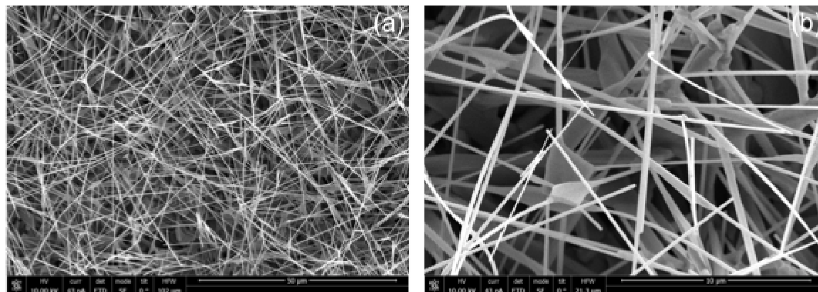

Figure 6.1: SEM view of as-grown ‘spaghetti-like’ ZnO NWs.

ZnO NWs studied in this chapter were synthesised by Davide Cammi of the Institute of Solid State Physics, Friedrich-Schiller-University (Jena) within a horizontal tube furnace at a temperature of 1350 °C. The evaporated material is transported by argon gas flow of 40 sccm at a pressure between 300 and 400mbar towards the growth substrates (Si chips covered with a nominal 5 nm Au film) at the cooler end of the furnace, where NWs grow at 960-1150 °C. The as-grown NWs typically have random orientation with respect to the substrate (‘spaghetti-like’), as depicted in Fig. 6.1. The NWs have mean length of 5 μm and diameters of 200 nm [29].

6.2.2 Raman scattering of an ensemble of ZnO NWs

Raman scattering measurements were performed first on the as-grown 'spaghetti-like' ensemble of ZnO NWs in order to have a reference of the Raman active phonons of these nanostructures. Figure 6.2 shows the Raman spectrum of the ensemble of ZnO NWs obtained with an excitation wavelength of 647 nm. The spectrum is characterised by the entire range of ZnO modes, labeled in Fig. 6.2, including the most intense peak at 438 cm^{-1} corresponding to the E_{2h}, the A_1(TO) at 378 cm^{-1}, E_1(TO) at 410 cm^{-1}, and a q-LO at 577 cm^{-1} (refer to Eq. (3.21)). The latter peak presents an asymmetry at the low frequency side which is compatible with a surface optical (SO) mode centred at 554 cm^{-1} (see Section 6.5). In fact, the random orientation of the NWs with respect to the direction of the incident and scattered light (which is perpendicular to the substrate in backscattering geometry) enables the detection of all the possible optical modes of ZnO. The intense peak centred at 519 cm^{-1} is attributed to the Si/SiO_2 substrate.

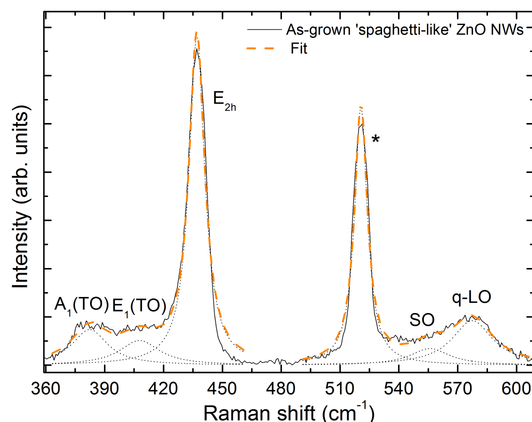

Figure 6.2: Raman spectrum of an ensemble of as-grown 'spaghetti-like' ZnO NWs (hundreds of NWs) measured at 647 nm taken with an accumulation time of 300 s. The asterisk point the TO mode of the Si substrate at 519.5 cm^{-1}.

6.3 Hybrid ZnO NW - Au nanorods system

6.3.1 Synthesis of the Au nanorods

Gold nanorods have been synthesised by a standard seed-mediated method described in [190]. I was trained in the nanorods synthesis by Alfonso Martín in occasion of my stay at Tyndall Institute in May 2012. For the seed solution, 3.75 mL of an aqueous hexadecyltrimethylammonium bromide (CTAB) solution (0.2 M) were mixed with 1.25 mL of an aqueous $HAuCl_4$ solution (1 mM). This was added to a stirred solution 0.3 mL of ice-cold $NaBH_4$ (0.01 M), resulting in the formation of a pale brown solution.

Mild stirring of the seed solution continued for 40 min. After this, the solution was kept at 30°C. For the growth of nanorods, a volume of 35μl of seed solution was added to an aqueous solution containing CTAB (12.5 mL, 0.20 M), $AgNO_3$ (0.5 mL, 4 mM), $HAuCl_4$ (25 mL, 1 mM) and ascorbic acid (0.35 mL, 0.0788 M), and kept at 30°C. After one hour, the growth of standard nanorods was carried out by the addition of 5μl of ascorbic acid (0.0788 M) in drops every 5 minutes. Excess CTAB was removed by successive steps of centrifugation and dispersion in water. CTAB molecules form a double layer around gold-nanorod metallic core, thus stabilising nanorods in solution. Its thickness is estimated to be around 2 - 3 nm. A schematic view of the nanorods with the double CTAB layer is presented in Fig. 6.3.

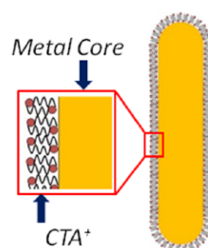

Figure 6.3: Scheme of the Au nanorods surrounded by the CTAB double layer. Picture modified from [191].

Morphological characterisation of the nanorods is done by SEM (see inset of Fig. 6.4) showing that they have a mean diameter of 29 ± 5 nm and length of 68 ± 5 nm. Figure 6.4 shows the absorption spectrum of a colloidal solution of nanorods and evidences that the Au nanorods two absorption peaks at 524 and 657 nm. They correspond to a transversal plasmon resonance (TPR) and a longitudinal plasmon resonance (LPR), respectively. These measurements were performed by Dr. Andrea Pescaglini of the Tyndall Institute.

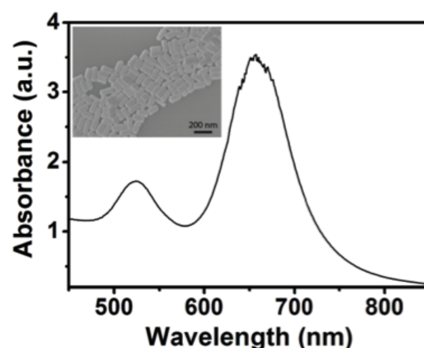

Figure 6.4: Absorbance spectrum of Au nanorods in water solution performed with a UV-VIS Agilent 8453 spectrometer. In the inset, SEM picture of Au synthesised nanorods deposited on a Si/SiO_2 substrate.

6.3.2 Decoration of the ZnO NWs with Au nanorods

Decoration of semiconductor NWs with metal nano-particles has been demonstrated by a variety of different procedures: surface functionalisation [192], drop-and-dry process [193] and sputtering deposition [194]. Following the promising results reported in the literature, the first set of samples were assembled by drop and dry process. However, these gave no reproducibility of SERS signature, which was attributed to the limited control on the density of Au nanorods and their distribution on the NWs surface. Therefore, a new approach that allowed high-yield and reproducible fabrication of hybrid NWs was designed by Dr. Andrea Pescaglini. In particular, this process was designed for maximising the particle deposition on the upper surface of the NW, that is a relevant requirement for the success of the SERS mechanism, since the probability of creating hot spots increases (see Section 3.2).

The novel process of fabrication is shown in Fig. 6.5. First of all ZnO NWs are mechanically dispersed on a substrate of n-type Si covered by a 300 nm SiO_2 layer. Then, they are covered by a layer of spin-coated resist, that is dried putting it on a hot plate at 120°C. The thickness of the resist, 1.4 μm at the centre, is set to be much larger than the diameter of the NWs. The

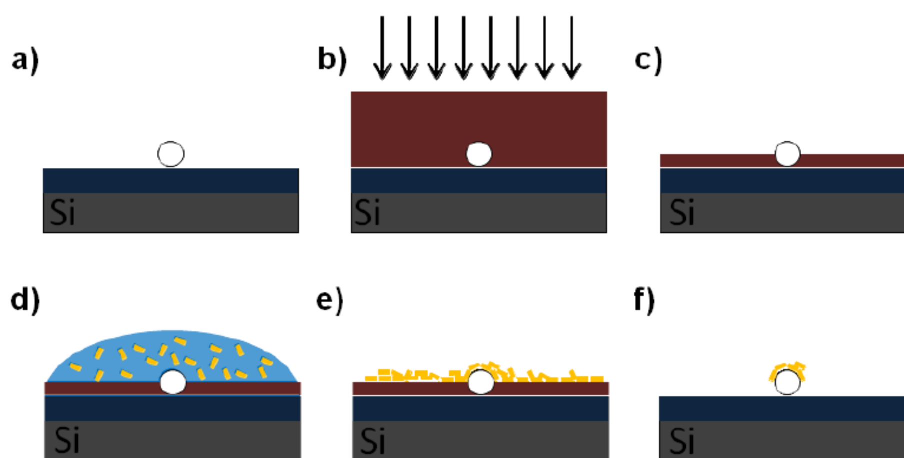

Figure 6.5: Scheme of the hybrid NW system assembly: (a) ZnO NWs are deposited on Si/SiO_2 substrate; (b) resist deposition by spin-coating and O_2 plasma; (c) after etching the layer thickness is smaller than the nanowire diameter; (d) drop and dry deposition of colloidal metal nanorods; (e) Au nanorods cover the entire surface and the nanowires; (f) after the lift-off, the resist is completely removed and only nanorods attached on the nanowire are left. Figure taken from Reference [191].

resist layer is etched down to a thickness lower than the NWs diameter. Two different techniques are employed: reactive ion etching (RIE) and exposition to UV light after loading it on a mask-aligner, followed by the development of the resist with an alkaline corrosive solution (i. e., MF-319 developer).

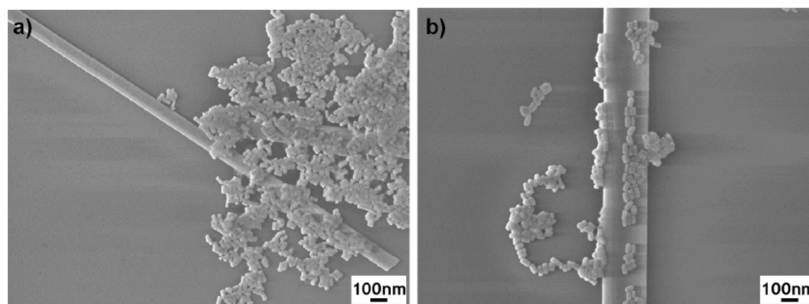

Figure 6.6: SEM image of Au nanorods-ZnO NW hybrid device obtained with the RIE process (a) and with the UV one (b).

The obtained thickness of the resist is in the range of 700 - 900 nm. The process is repeated a second time (UV exposition and development) and the final resist thickness is around 100 - 200 nm.

The first technique gives more reproducible results, although some residual resist is found on the NW surface, moreover, it could damage the surfaces. However, SEM images of a statistically relevant number of NWs did not give any evidence of damages. The second method is less reproducible, but produces cleaner surfaces, free of any residual of resist, as confirmed by SEM images. For the further discussion of this Chapter, the sample processed with the RIE will be referred to as Sample A and that with the UV light will be Sample B. The Au nanorods are deposited on the NWs surface by droplet evaporation. For minimising the coffee stain effect and obtaining the maximum coverage, the deposition is carried out heating the sample up to 110°C. Finally, the sample is chemically cleaned for removing the excess of CTAB and the resist. The result is the coverage of the NWs mostly on its top surface, as shown Fig. 6.6. However, as it is clear from Fig. 6.6 (a), only a part of the NW have been efficiently covered. Both techniques described above allow to deposit the nanorods on the top surface NW, but not all along its axis in an homogeneous way.

The nano-fabrication of the hybrid ZnO NWs - Au nanorods systems was performed by Dr. Andrea Pescaglini at Tyndall Institute. I participated in the fabrication of some of the devices during my stay at Tyndall Institute.

6.4 SERS of individual hybrid NWs

In this Section, the SERS measurements on tens of hybrid Au-nanorods ZnO NW systems belonging to two different samples, sample A and sample B, are presented. All the measurements were performed with a power of 0.55 mW/μm^2 and for an integration time of 120 s. This value of power is the highest that can be used in order not to melt the Au nanorods.

It has to be stressed out that of the nearly one hundred hybrid systems

investigated, only the most representative results have been reported. SERS measurements have been carried out in several samples (around 30) fabricated with different deposition techniques of the rods, size of nanorods (but with the same dimensions rate for obtaining the same plasmon resonances), and way of cleaning the CTAB.

6.4.1 SERS of Au nanorods

SERS measurements of bare Au nanorods deposited on a Si/SiO_2 substrate were performed. CTAB molecules attached on the Au nanorods surface show a Raman peak centred at 174 cm^{-1} that is attributed to the Br-Au bond [195]. The intensity of this mode can be used to verify the wavelength of the plasmonic resonances. Figure 6.7. shows that under excitation at 647 nm (red line), the Br-Au peak is clearly enhanced indicating the condition of resonance with the LPR of the nanorods. This mode is not visible for excitation wavelength at 514 nm (green line), suggesting that the field enhancement generated by the TPR is negligible.

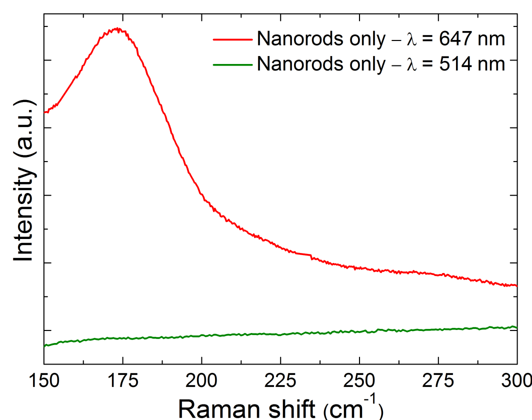

Figure 6.7: Raman spectra of Au bare nanorods measured at 647 nm (red curve) and 514 nm (green curve).

This result is also supported by finite-difference time domain simulations that Dr. Andrea Pescaglini performed in order to investigate the plasmonic resonances of the Au nanorods used in this work. He modelled an Au nanorod 29 × 68 nm surrounded by a 3 nm CTAB layer in contact with a ZnO surface. A schema of the modelled system is presented in the inset of Fig. 6.8 (a). For light propagating along the y-axis, the LPR is found at 642 nm (black curve in Fig. 6.8 (a)), while the TPR at 529 nm (red curve in Fig. 6.8 (a)) for light polarised parallel to the z-direction and the x-direction, respectively.

The Raman spectra of bare Au nanorods in the region of interest for the detection of ZnO Raman modes, between 380 and 600 cm^{-1}, are shown in Fig. 6.9. The spectra are rather featureless, except for weak peaks attributed to

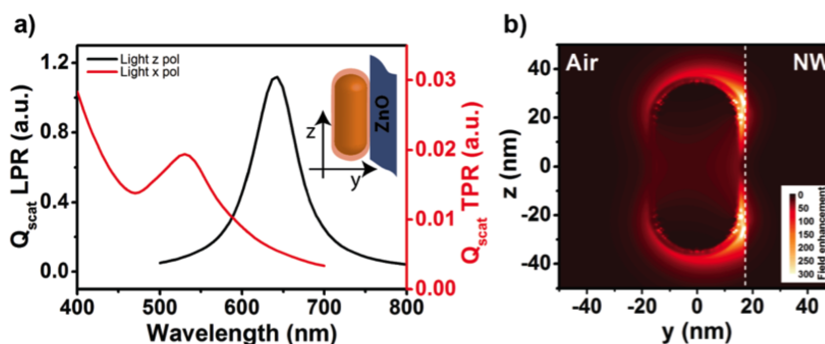

Figure 6.8: (a) Finite-difference time domain simulation of scattering cross section normalised to the geometrical cross section of a Au nanorod 29x68 nm with 3 nm dielectric shell (refractive index n=1.4) on a ZnO nanowire under light polarised along the main axis (black curve) and short axis (red curve). (b) FDTD simulation of the electric field enhancement factor under light polarised along the z-axis.

the CTAB molecule. It is well known that the SERS peaks are not perfectly reproducible (Section 3.2.3) and in order to make their attribution in a reliable way, a careful statistical approach is needed over tens of spectra. The results will be presented in the following Section together with the results on the hybrids NW-Au nanorods systems.

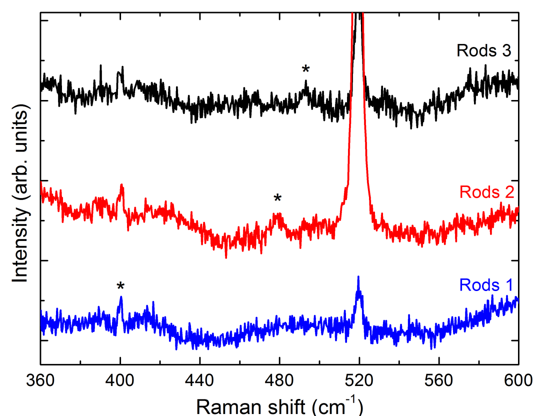

Figure 6.9: Raman spectra of Au bare nanorods taken at different points and measured at 647 nm. The asterisks indicate peaks coming from CTAB molecule.

6.4.2 Raman scattering of single hybrid ZnO NWs

SERS spectra of individual Au-nanorods and ZnO NW hybrid systems exciting at 514 nm and 647 nm, in resonance with the TPR and LPR resonances have been measured. As Figure 6.10 reports, the spectra recorded at 514 nm shows no Raman features, while the spectra at 647 nm excitation wavelength presents a few clear and reproducible peaks (labeled by asterisks). Thus, as in the case of bare nanorods, SERS signal was only collected for

excitation of the hybrid NWs in resonance with the LPR. Therefore, the stronger capabilities of the LPR compared to the TPR corroborate the dominant role played by the former in the SERS mechanism. According to the simulation reported in Subsection 6.4.1, a field enhancement factor larger than $\sim$ 300 times is found concentrated in the nanorod-NW inter-space under excitation of the LPR, although a factor of $\sim$ 70 is calculated inside the ZnO NW surface (Fig. 6.8 (b)) and just below the surface it is found decreasing to 1 within 20 nm. On the other hand, for the TPR resonance (results not shown) the generated field enhancement factor is calculated to be around $\sim$ 3 in proximity of the metal surface and it barely penetrates inside the semiconductor surface (less than a factor 2). This is in perfect agreement with the observed results reported in Fig. 6.10.

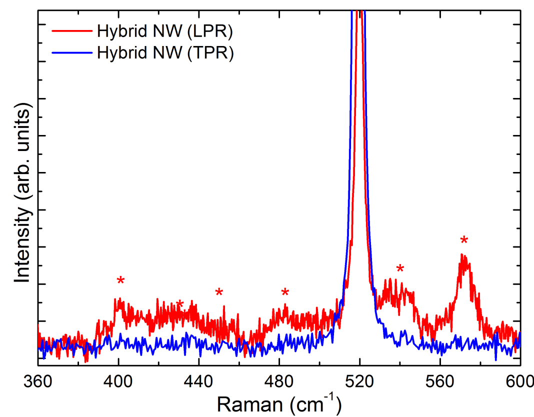

Figure 6.10: SERS spectra of a single hybrid NW at 514 nm (blue curve) and 647 nm (red curve) in resonance with the TPR and LPR resonates, respectively. Asterisks indicate the observed clear and reproducible features of SERS under excitation at 647 nm.

Figure 6.11 contains some representative spectra of SERS of hybrids NWs of sample A. All measurements were carried out at 647 nm excitation, in resonance with the LPR of the nanorods. The spectra showed a clear feature peaked at 572 cm^{-1} that is shadowed in black.

The measurements performed on different NWs show slightly different optical features: fluctuation in the intensity of the peaks and presence of additional peaks. In order to correctly assign the peaks and extract valid conclusions, a careful statistical analysis of these spectra was carried out among tens of NWs. The results are presented in Fig. 6.12, where the y-axis reports the frequency-weighted intensity (FWI) of the observed Raman peaks. This is calculated multiplying the average measured intensity of the peaks by their frequency. In Figure 6.12 (a) the complete set of peaks observed in the overall measurements both of the hybrid NWs and of the Au nanorods substrate are shown. The peaks centred in 390 cm^{-1}, 414 cm^{-1}, 456 cm^{-1}, 480 cm^{-1}, 493 cm^{-1}, 592 cm^{-1} have been previously reported for ordered

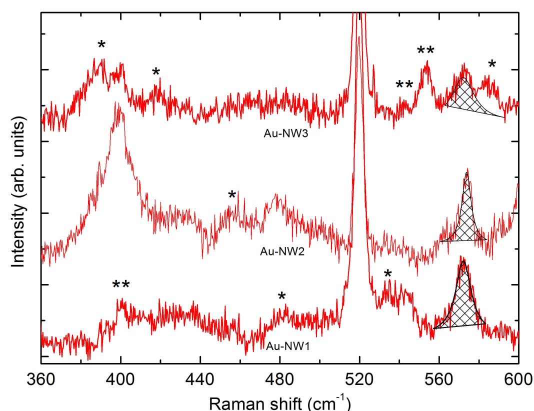

Figure 6.11: Representative Raman spectra taken at laser wavelengths of 647 nm of different single hybrid nanostructures. The mode of the hybrid NWs is shadowed in black, the single asterisk indicate the peaks associated to crystalline CTAB and the double asterisk those associated to Au nanorods deposited on Si/SiO_2 substrate.

CTAB [196, 197]. The remaining peaks at 390 cm^{-1}, 401 cm^{-1}, 414 cm^{-1},

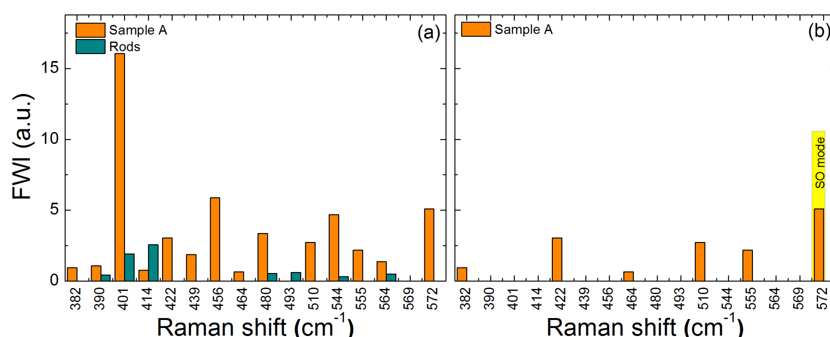

Figure 6.12: Weighted distribution of the observed Raman peaks in several spectra. (a) All observed peaks in the hybrid NWs and the related substrate containing only Au nanorods and (b) the Raman peaks of the hybrids presented in (a) subtracting the peaks attributed to CTAB and to the substrate.

480 cm^{-1}, 493 cm^{-1}, 544 cm^{-1} and 564 cm^{-1} were found both in the spectra of hybrid nanostructures and in the substrate containing Au nanorods only, therefore are attributed to the vibrational transitions of the CTAB adsorbed on the Au nanorods. It is well-known that molecules adsorbed on metal surfaces show shifted Raman modes or new modes due to the interaction between the molecule and the surface [198]. Moreover CTAB molecules on the Au nanorod surface form a double layer that can introduce new vibrational resonances with respect to the isolated molecule [199]. Figure 6.12 (b) is the result of the subtracting from the statistics of all the peaks that are univocally assignable to the Au-nanorods or to CTAB.

After the process of direct comparison, a few peaks remained centred at: 382 cm^{-1}, 422 cm^{-1}, 464 cm^{-1}, 510 $cm^{-1}$and 555 cm^{-1}. In order to

establish whether or not they were related to the NWs, further analysis was carried out: sample A was immersed in a methanol-based solution of 4-aminobenzenethiol (4-ABT) (1 mM) in order to replace most of the CTAB on the nanorod surface with the 4-ABT molecule. The successful adsorption of 4-ABT on the nanorods was demonstrated by recording two SERS spectra, one measured on a hybrid structure and a second one on the substrate containing nanorods only. Both of them are shown in Fig. 6.13 (a). The distinctive features of 4-ABT Raman transitions, centred

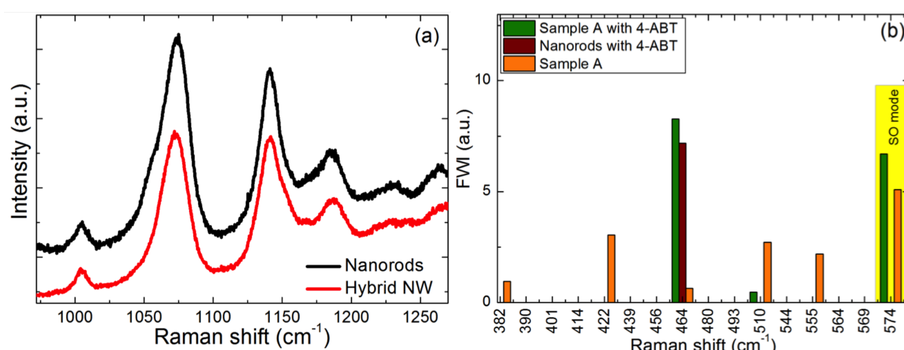

Figure 6.13: (a) Representative Raman spectra of 4-ABT detected from Au nanorods (black curve) and from a single hybrid NW after its functionalisation with 4-ABT (red curve). (b) Statistical analysis of Raman peaks found in sample A, and on sample A and on its substrate after their functionalization with 4-ABT molecule.

at 1004 cm^{-1}, 1073 cm^{-1}, 1139 cm^{-1} and 1187 cm^{-1}, are observed with comparable intensity in both spectra demonstrating the effective attachment of the new molecule on the Au nanorods and the substitution of a good part of the CTAB. A direct comparison between the statistical analysis of the SERS peaks before and after the 4-ABT substitution on the same set of hybrid NWs is reported in Fig. 6.13 (b). The peak centred at 464 cm^{-1} can be disregarded, because it is also observed in the bare Au nanorods. The peaks at 382 cm^{-1}, 422 cm^{-1} and 555 cm^{-1} can be attributed to CTAB, because they do not appear in the the sample after the immersion in 4-ABT. The remaining centred at 510 cm^{-1} can be disregarded as well, because its intensity decreases considerably upon CTAB substitution and can be, therefore attributed to CTAB. Finally only one peak remains, centred at 572 cm^{-1}, whose nature shall be discussed in the following Section.

In order to demonstrate the reproducibility of the results, new measurements were performed on a second sample, sample B, which was assembled in a slightly different way (see Section 6.3.2). The same procedure of analysis was followed for this sample and representative Raman spectra of the hybrid NWs and their substrate are presented in Fig. 6.14 (a). The results of the overall statistics are presented in Fig. 6.14 (b), while in Fig. 6.14 (c) the peaks related to CTAB and to the bare nanorods are subtracted, following

the same criteria that was used in the case of sample A. The remaining peaks centred in 382 cm^{-1}, 464 cm^{-1} and 555 cm^{-1} can be attributed to CTAB according to the analysis that was carried out in sample A functionalised by the molecule ABT. The peak at 572 cm^{-1} remained almost unchanged, corroborating its attribution to the ZnO and demonstrating the reproducibility of the results.

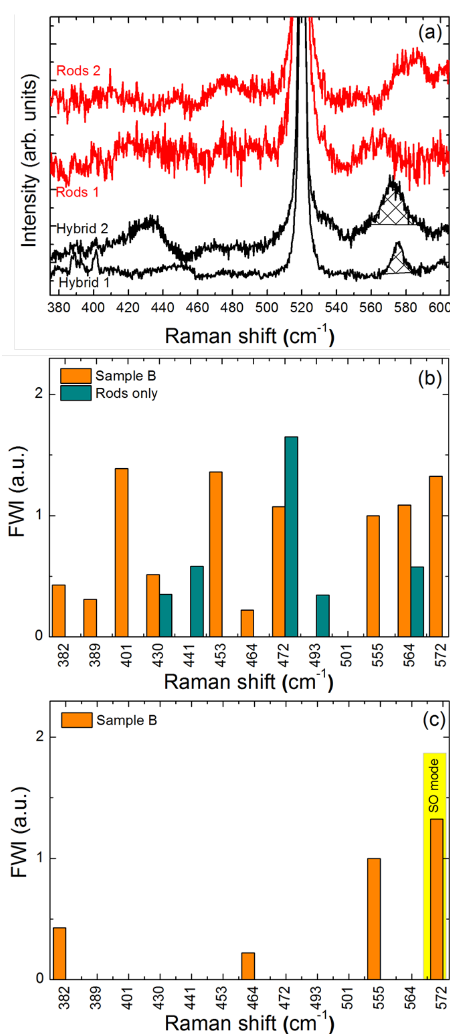

Figure 6.14: (a) Representative SERS spectra of a single hybrid NWs and of bare Au nanorods taken at laser wavelength of 647 nm. The mode of the hybrid NWs is shadowed in black. Wighted distribution of the observed Raman peaks in several spectra. (b) All observed peaks in the hybrid NWs and the related substrate containing only Au nanorods and (c) the Raman peaks of the hybrids presented in (b) subtracting the peaks attributed to CTAB and to the substrate.

6.5 Discussion

The nature of the peak centred at 572 cm^{-1} will be discussed in this Section. This peak cannot correspond to a bulk mode, because it would be accompanied by the simultaneous appearance of the other bulk modes, that are allowed in the geometry of this experiment and that have higher cross sections, like the non-polar mode E_{2h}. Instead the 572 cm^{-1} peak appears as an isolated feature and its frequency is compatible with a SO mode.

The calculations of the expected SO frequency are performed following the model described in Section 2.3.5 for the case of large NWs, i. e., $qL > 1$, where q is the wave-vector of the phonon and L the length of the side of the NWs. The NWs studied in this work fulfil this condition: q is typically of the order of 10^7-10^9 m^{-1} [106] and L between 100 - 150 nm (that is the average radius of the ZnO NWs).

First of all, the case of the single hybrid system is analysed. According to Eq. (2.23), the SO of the single hybrid NW should have its frequency in the range 532-574 cm^{-1}, taking the static dielectric constant $\varepsilon_0 = 10.29$ and the high frequency one $\varepsilon_\infty = 4.47$ of ZnO, and the one of the medium $\varepsilon_m = 1.7$. The dielectric constant of the medium was calculated averaging among the different components of the surrounding medium, which is composed by air and Si/SiO_2 (substrate). The peak centred at 572 cm^{-1} effectively lays within the predicted range of frequencies for SO mode and thus, it can be definitely attributed to a SO mode.

The frequency of the SO mode of the hybrid NW differs from that reported in Section 6.2.2 for the ensemble of 'as-grown' NWs centred at 554 cm^{-1}. This attribution was correct, since the surrounding medium is now composed by air and ZnO. Equation (2.23) predicts a frequency for the SO mode of the ensemble of 'as-grown' NWs in the range 515-556 cm^{-1}, with the dielectric constant of the surrounding medium of $\varepsilon_m = 2.45$.

The origin of the two observed SO modes, one centred in 572 cm^{-1} and the other in 554 cm^{-1} belonging to the single hybrid NW and to the ensemble, respectively, are ascribed to the same surface vibrational mode, since they experiment a shift due to the variation of the dielectric constant of the surrounding medium. This shift is about 20 cm^{-1} and exactly corresponds to the expected one for the dielectric change that the two samples experience.

For concluding, the results demonstrate the enhancement and the reproducibility of the ZnO SO mode in hybrid NWs only under excitation at 647 nm, in resonance with the LPR of the Au nanorod components. Extensive statistical analysis was used to support this attribution, due to the variability of the frequency and the intensity of the SERS peaks related to the presence of the double layer of CTAB around the nanorods. This observation is also supported by the previously discussed FTDT simulations performed in Tyndall.

These results are not as outstanding as those reported for molecules.

In fact, the enhancement of the signal of the probe is several orders of magnitude smaller than the EF found in SERS of molecules. This is a natural consequence of the fast decay of the electromagnetic field intensity away from the metal surface that limits the volume of the semiconductor within the plasmonic enhancement range. For this reason, despite the advantages offered by SERS of single semiconductor NWs compared to resonant Raman scattering, further optimisation is needed. For instance, the CTAB shell should be substituted by other dielectrics in order to reduce the intense and variable background. This would help to avoid the mandatory and time-consuming statistical analysis for the peaks attribution, which was carried out in this work. Additionally, improvements in nanorods distribution along the NW surface (in terms of density and location) could lead to an increase of the signal intensity, which is expected to be proportional to the number of nanorods ('hot-spots').

Conclusions

This work mostly deals with the investigations of the optical and structural properties of ensemble and single selective area growth (SAG) GaN nanostructures and GaN/InGaN core-shell nanowires (NWs). On the other hand, in the final part of the work, ZnO NWs have been employed as a proof of concept of surface enhanced Raman scattering (SERS) on semiconductor NWs. The main conclusions of these investigations are summarised as follows.

In Chapter 4, the effects of the mask geometry on the structural and optical properties of SAG GaN nanostructuctures are investigated by means of Raman scattering and photoluminescence. Both techniques are sensitive probes for residual strain, structural defects and impurities. Homo- and hetero-epitaxial SAG of GaN nanostructures has been carried out by molecular beam epitaxy (MBE) on two different substrates: GaN(0001) MOCVD template on sapphire and 6H-SiC(0001) both covered by a patterned thin Mo mask. This mask contains different periodic arrays of apertures with diameter (d) and pitch (p), which represent the distance between two holes.

The Raman measurements proved that SAG NWs and nanopyramids grow free of macroscopic strain and are not lattice matched to the substrate. The structural quality of the material diminishes for $p < 1$ μm, as revealed by the increase of the Raman peak line-widths, while it is not influenced by d. In the case of NWs, it is attributed to the higher density of TDs present in shorter NWs and for nanopyramids proves that the process of coalescence generates an improvement in the crystal quality.

The PL spectra of the NWs show a considerable presence of basal plane stacking faults, whose density increases for decreasing NW d. In fact, the dependence of the PL on the NWs d points out the preponderance of the growth direction in the formation mechanism of BSFs: thinner NWs, for which most of the growth takes place on semi-polar facets, statistically present a higher BSFs density.

The comparative study of NWs and nanopyramids points out the higher crystal quality of NWs with respect to nanopyramids (narrower FWHMs), which confirms that TDs bend with the formation of the semi-polar pyramidal facets, leaving most of the NW volume virtually free of defects. Finally, the relative intensity of BSFs and of PSFs (only present in nanopyramids) bands relative to D^0X_A is higher for nanopyramids than in NWs. This indicates

that most of the defects appear in the initial nanopyramid formation and the subsequent vertical growth of the NWs carries on virtually free of defects.

The elemental, structural and optical properties of individual core-shell GaN/InGaN NWs were studied by non-destructive spectroscopy techniques with spatial resolution in the nanoscale and the results are presented in Chapter 5. Energy dispersive spectroscopy (EDS) and X-ray fluorescence measurements (XRF) were performed on single GaN/InGaN core-shell NWs. Combining the high spatial and the elemental resolutions of EDS (around 4 nm) and XRF (1ppm), respectively, it has been possible to confirm that the GaN/InGaN multi-quantum-wells (MQWs) formed correctly at the lateral surface of the NWs, to check the In distribution in the NWs area, and to calculate the In concentration in the wells. There is an In accumulation in the tip of the NWs, but no QWs are observed, and the In concentration increase from the bottom to the top with values between 5% and 12%, respectively.

The GaN material of the core-shell NWs grows with the lattice constants of strain-free GaN, as confirmed by the XRD and Raman characterisation. The material does not present disorder at the local level as shown by XANES results. On the other hand, no signature of InGaN MQWs is observed. Since XRD measurements have been performed illuminating all the material present in the NW, a contribution to the spectra from the MQWs is expected. This suggests that the MQWs are strained and completely matched to the GaN core, otherwise some resolved peaks or asymmetry in the GaN XRD refractions would have been observed.

The low temperature PL spectra performed both on ensemble and single NWs are dominated by band transitions of the GaN/InGaN core-shell MQWs with energies between 3.1 - 3.3 eV. The large FWHM ($\sim$ 34 meV) of this band is attributed to the variation of In concentration along the NWs, which shifts the emission. Thus, the overlapping of the different energy emissions produces a large broadening.

The XRD and PL results were supported by finite-difference-time domain (FDTD) simulations. The strain field distribution inside a InGaN/GaN core-shell NW was calculated using the barrier and well width and the In concentration obtained from the EDS and XRF results, respectively. Moreover, the expected energy band gaps of strained InGaN were extracted. The InGaN/GaN are found completely matched to the GaN core and the emission of strained InGaN is calculated in the range 3.05 - 3.29 eV. These results confirm the ones obtained from the experimental data.

Finally, Chapter 6 is dedicated to the study of the potential use of SERS for the characterisation of the vibrational surface properties of single semiconductor NWs. SERS measurements were performed on individual Au-nanorods ZnO NWs hybrid systems.

ZnO surface optical (SO) modes were observed via the excitation of the longitudinal localised surface plasmons resonance (LPR) of Au nanorods,

otherwise no signal was detected in bare single ZnO NWs for incident radiation energies below the band gap. Extensive statistical analysis was necessary to support the assignation of the Raman peak at 572 cm^{-1} to ZnO, and the other features to the hexadecyltrimethylammonium bromide (CTAB) surfactant covering the nanorods.

These results are not as outstanding as those reported for molecules. In fact, the enhancement of the signal of the probe is drastically smaller and the variability of the frequency and the intensity of the SERS peaks related to the background makes it mandatory to carry on systematic and time consuming statistical analysis. In fact, SERS enhancement factor (EF) of the SO in the studied system is predicted to be several orders of magnitude smaller than the EF found in SERS experiments on molecules adsorbed on metal nanostructures. This is a natural consequence of the fast decay of the electromagnetic field intensity away from the metal surface which limits the volume of the semiconductor within the plasmonic enhancement range. For this reason, despite the proved advantages offered by SERS of single semiconductor NWs, further optimisation is still required to improve the reproducibility and stability of this approach. For instance, CTAB double-layer has to be substituted by thinner dielectric layers. This would result in a drastic reduction of the background and, thus, a simplification of the processing of the results. Additionally, improvements in nanorods distribution along the nanowire surface (in terms of density and location) could lead to an increase of the signal intensity that is expected to scale up proportionally the number of nanorods. Nevertheless, this work provides evidence of the enhanced performance afforded by plasmonic-active rod-shaped elements for the surface characterisation of individual semiconductor NWs in non-resonant conditions, extending the capabilities of traditional Raman spectroscopy for semiconductor NWs.

Resumen

Este resumen contiene una breve descripción de los objetivos de esta tesis, las técnicas experimentales utilizadas, los resultados obtenidos y las conclusiones. Por lo tanto, debido a la evidente falta de espacio, no pretende ser exhaustivo.

Los nanohilos semiconductores (NWs, de su nombre inglés, nanowires) tienen una amplia gama de aplicaciones en el campo de la optoelectrónica (emisores de luz y diodos láser), nano-electrónica (circuitos lógicos y transistores de efecto de campo), detección y producción de energía (células solares) [1, 2]. En términos generales, los NWs pueden ser descritos como nanoestructuras de forma alargada con diámetros y longitudes que van típicamente de decenas a cientos de nanómetros y de pocas a decenas de micras, respectivamente. Dicha morfología ofrece dos ventajas principales en comparación con las capas: su alta razón superficie-volumen y su mayor calidad cristalina, ambas beneficiosas para muchas nuevas aplicaciones [3, 4].

En los últimos años se han crecido NWs con muy buenas propiedades, sin embargo, hay aún problemas relacionados con su crecimiento y sus propiedades estructurales y ópticas que pueden afectar dramáticamente el rendimiento de los futuros dispositivos. Un ejemplo de estos problemas específicos es la imposibilidad de controlar la posiciśon, el diámetro y la dirección de crecimiento de los NWs. Por otra parte, aunque la morfología de los NWs permite crecer heteroestructuras con nuevas orientaciones, aprovechando, por ejemplo, los planos no polares de sus superficies laterales, la calidad estructural y la composición de la aleación en estas heteroestructuras siguen presentando algunos inconvenientes.

El advenimiento de la nanotecnología no sólo ha traído consigo aplicaciones potenciales muy interesantes en muchos campos, sino también nuevos retos para las técnicas de caracterización, que deben permitir correlacionar las propiedades fundamentales de los materiales nanoestructurados y el rendimiento de los dispositivos. En el campo de la optoelectrónica, por ejemplo, la determinación de la relación entre las propiedades estructurales y ópticas de los materiales a nivel nanonométrico requiere la aplicación en un mismo nano-objeto de diferentes técnicas complementarias.

El objetivo principal de esta tesis es la caracterización de NWs semiconductores individuales con una combinación de técnicas espectroscópicas nuevas y alguna más convencionales. Todas las técnicas empleadas deben ser

no-destructivas y han de tener una resolución espacial submicrómetrica. El estudio del mismo NW con diferentes técnicas complementarias proporciona información más completa sobre la morfología, las propiedades cristalinas, la composición química, los campos de deformación, y la respuesta óptica, entre otras propiedades. Por tanto los objetivos principales de este trabajo se pueden resumir como sigue.

1. *Estudio de las propiedades de NWs de GaN crecidos de forma controlada a través de una máscara (SAG NWs) mediante caracterización óptica.*
   Las propiedades de los SAG NWs de GaN obtenidos mediante crecimiento epitaxial por haces moleculares (MBE) han sido estudiadas con el fin de comprobar si el crecimiento SAG es una alternativa válida al asistido por un catalizador o al auto-organizado. Los efectos de la geometría de la máscara de crecimiento SAG en las propiedades estructurales y ópticas de los NWs de GaN han sido investigados. Los estudios se realizaron tanto en conjuntos como en NWs individuales por micro-dispersión Raman y micro-fotolumineciencia (micro-PL).

2. *Determinación de la composición, la estructura y las propriedades ópticas de NWs individuales de GaN/InGaN con estructura núcleo-corteza.*
   Este objetivo ha requerido el uso de varias técnicas espectroscópicas tanto ópticas, como de rayos X, incluyendo Raman y PL, y fluorescencia a rayos X, difracción a rayos X y espectroscopía XANES, respectivamente. Se ha conseguido así el mapa de la distribución de las diferentes especies químicas y de los campos de deformación en NWs individuales.

3. *Demostración de dispersión Raman amplificada en la superficie (SERS) de NWs de ZnO individuales funcionalizados con nanopartículas de oro.*
   Un examen cuidadoso de la SERS en NWs semiconductores individuales se ha realizado utilizando sistemas híbridos compuestos por NWs de ZnO y nanopartículas de Au como una prueba de concepto. Con el fin de evitar los problemas que origina la dispersión Raman resonante, se ha realizado SERS con longitudes por debajo de la banda de energía prohibida. Se han tenido en cuenta las condiciones de resonancia de las nanopartículas y la reproducibilidad de la frecuencia y la intensidad de los picos SERS.

Caracterización óptica de nanohilos y nanopirámides de GaN crecidos de forma controlada mediante de una máscara

Los efectos de la geometría de la máscara sobre las propiedades estructurales y ópticas tanto de conjuntos de SAG NWs de GaN como de NWs individuales han sido investigados por medio de dispersión Raman y PL. En el pasado, la mayoría de los estudios de calidad estructural de SAG NWs se han llevado a cabo por microscopía electrónica de transmisión (TEM), que requiere una preparación sofisticada de la muestra que por lo general, implica su destrucción parcial, y consume mucho tiempo para su analisis. Por lo tanto, el uso de técnicas no destructivas y de no contacto (con la muestra) para la caracterización detallada de las propiedades de los SAG NWs es altamente beneficioso.

La primera muestra de SAG NWs de GaN que se ha estudiado ha sido crecida por MBE sobre un sustrato de GaN recubierto por un máscara de Mo con grosor de 10 nm. Ésta contiene matrices triangulares periódicas de aberturas circulares con diámetro (d) y paso entre las aberturas (p), que van desde 30 a 500 nm y de 0.25 a 8 μm, respectivamente. Como se muestra en la Fig. 6.15 (a), los NWs que crecen en las aberturas tienen sección hexagonal y terminan en puntas piramidales definidas por facetas semi-polares (r-plane). Los NWs se encuentran preferentemente en las aberturas de la máscara de Mo. El diámetro de los SAG NWs excede el diámetro de las aberturas,

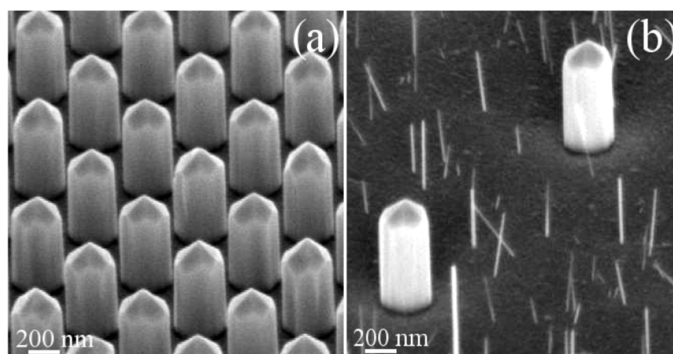

Figure 6.15: Imágenes SEM of SAG NWs de GaN. (a) Vista lateral de NWs de GaN que terminan en una punta piramidal definidas por facetas $\{1\bar{1}02\}$ para $d =$ 500 nm y $p = 0.25$ μm y (b) vista lateral de SAG NWs de GaN y de NWs de GaN auto-organizados para $d = 500$ nm y $p = 2$ μm.

revelando que el crecimiento radial tiene una tasa baja, pero nunca está completamente suprimido. Por otro lado, la altura de los NWs, que es un indicador de la tasa de crecimiento axial, aumenta con $p < 1$ μm desde 425 nm hasta el valor saturado de 750 nm para $p > 1$ μm. Además, como muestra la Figura 6.15 (b), para $p > 1$ μm, los auto-organizados crecen directamente sobre la máscara de Mo con una densidad de 30 NWs por μm^2

y tienen diámetros entre 10 y 20 nm.

En la Figura 6.16 (a) se muestra un espectro representativo de dispersión Raman de un conjunto de NWs. El pico más intenso que se observa en el espectro está centrado en $\sim$ 566.1 cm^{-1} y se asigna al modo E_{2h} del GaN con estructura wurtzita. Alrededor de 736 cm^{-1} (región que no se muestra en la Figura 6.16 (a)) se detecta un modo q-LO mucho menos intenso que el E_{2h}, que corresponde a la superposiciíon de los modos A_1(LO) y E_1(LO). Aparacen también otros dos modos en $\sim$ 533 cm^{-1} y $\sim$ 557 cm^{-1}, que tienen frecuencias que se corresponden a las de los modos A_1(TO) y E_1(TO), respectivamente. La opacidad parcial de la máscara de Mo (92% y 72% medidas para el UV y luz visible, respectivamente) permite que aparezca en el espectro Raman un pico débil atribuido al modo E_{2h} del sustrato (marcado por un asterisco en la Figura 6.16 (a)). Este pico está centrado en 570 cm^{-1}, revelando que la compresión residual leve del sustrato (alrededor de -0.2% asumiendo que la deformación sea biaxial) no se transmite al material de los NWs. La observación de los modos TO en geometria de retrodispersión se debe a la refracción del haz de luz en las facetas piramidales de los NWs, que forman un ángulo de 40 - 50° con respecto al plano c, lo que se traduce en una geometría de excitación interna oblicua a través de las facetas con un ángulo entre 25 - 30°. Además, el alto índice de refracción del GaN (2.44) puede causar reflexiones internas múltiples y, por lo tanto, desviaciones adicionales de la geometría de retrodispersión. La Figura 6.16 (b) muestra

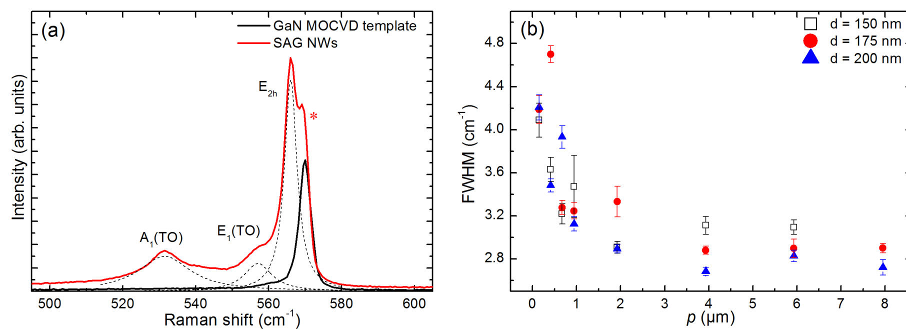

Figure 6.16: (a) Espectro de dispersión Raman de un conjunto de NWs con p = 0.15 μm y d = 160 nm medido con línea láser de 488 nm. La línea discontinua muestra el ajuste del espectro mediante Lorentzianas. (b) Evolución de la FWHM del modo E_{2h} vs diferentes p. Se da el diámetro medio de la NWs.

la evolución de la anchura a media altura (FWHM) en función de p del pico E_{2h}. Para $p > 1$ μm, las FWHMs son similares a las que se miden en los NWs auto-organizados [152], revelando una calidad cristalina alta de estos SAG NWs. El ensanchamiento de los fonones aumenta progresivamente a medida que p disminuye para $p < 1$ μm. Este comportamiento se correlaciona perfectamente con la disminución de la altura de los NWs. Esto sugiere que los defectos estructurales tienen una densidad decreciente con el aumento de la altura de los NWs. De hecho, NWs más largos presentan una menor

densidad de dislocaciones.

Espectros de emisión representativos en función de d y p se presentan en la Figura 6.17. Los espectros de PL en las Figuras 6.17 (a) and (c) son dominados por dos picos centrados en 3.47 eV y 3.42 eV. El pico más intenso se atribuye a la transición que corresponde a la de la recombinación del excitón ligado a un donor neutro (D^0X_A) y su energía confirma que los SAG NWs están libres de deformaciones. Este pico presenta una ligera asimetría en ambos lados que es compatible, en el de alta energía, con el excitón libre A y, en el de baja energía, con procesos a dos electrones satélites [49], respectivamente. La FWHM es muy grande ($\sim$ 5.5 meV) ya que excede en un orden de magnitud las de los NWs auto-organizados de GaN. Este ensanchamiento se puede atribuir a campos de deformación micrométricos que se generan por la coalescencia de los núcleos de GaN durante la primera etapa de crecimiento. Otra contribución puede venir de la separación aleatoria de los donantes con respecto de las superficies laterales de los NWs [65]. La segunda banda de las Figuras 6.17 (a) and (c) es un doblete (parcialmente resuelto) compuesto por un pico a 3.416 eV y otro a 3.422 eV, que se atribuyen a la recombinación entre los electrones confinados en los defectos cristalinos denominados fallos de apilamiento (BSFS) y los huecos localizados en su proximidad. La Figura 6.17 (b) muestra cómo el ratio entre las intensidades integradas relativas a BSFs y D^0X_A disminuye con el aumento d. Sin embargo, esta proporción no se ve afectada por p. De hecho, no se ha detectado una tendencia clara, como se puede ver en la Figura 6.17 (d). Adicionalmente, como se puede observar en la Fig. 6.17 (b), la variación de la FWHM de los D^0X_A es despreciable con el aumento del diámetro. Esto sugiere que los campos de deformación micrométricos son la causa más probable de la anchura de la FWHM de la emisión de los NWs. De hecho, si la mayor contribución al ensanchamiento de la PL se produce por la separación aleatoria de los sitios donantes, se observaría un aumento de las FWHMs con la disminución de d.

La segunda muestra de SAG NWs de GaN que se ha estudiado ha sido crecida por MBE sobre un sustrato de SiC recubierto también por un máscara de Mo con grosor de 10 nm. Esta muestra se creció a temperatura más alta con respecto a la de los NW, que inhibió el crecimiento axial y por tanto se formaron nanopirámides. Se ha llevado a cabo un estudio comparativo entre las propiedades estructurales y ópticas de los NWs y las nanopirámides. Los espectros de la dispersión Raman revelan la ausencia de campos de deformación macroscópicos en ambos casos y un nivel de calidad cristalina superior de los NWs con respecto a la de las nanopirámides (FWHMs más estrechos), esto confirma que los defectos estructurales se curvan con la formación de las facetas piramidales semi-polares, dejando la mayor parte del volumen del NW prácticamente libre de defectos. Finalmente, la intensidad integrada de BSFS y de PSFs (presentes sólo en nanopirámides) relativa a D^0X_A es mayor para nanopirámides que para NWs. Esto indica que la

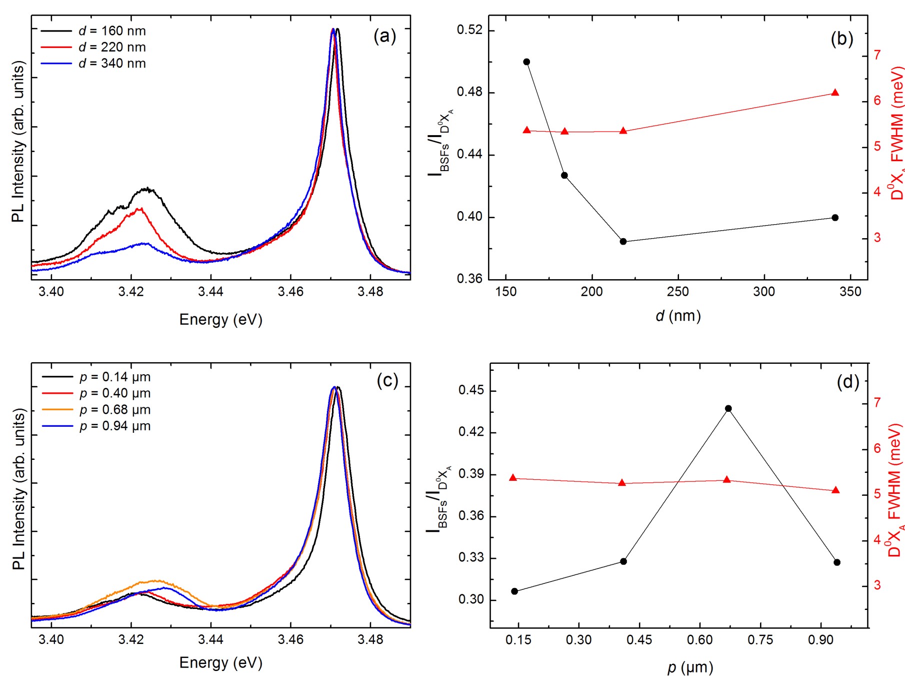

Figure 6.17: (a) Variación de la emisión de PL en función de d ($p = 0.14$ μm) y (b) intensidad integrada de la emisión de BSFS normalizada con la de la emisión del excitón ligado a un donor neutro (D^0X_A) como una función de d ($p = 0.14$ μm) y tendencia de la FWHM de la D^0X_A como una función de d. (c) Variación de la emisión de PL en función de p ($d = 200$ nm) y (d) la intensidad integrada de BSFS normalizada a la de D^0X_A como una función de p ($d = 200$ nm) y tendencia de la FWHM de la D^0X_A como una función de p.

mayoría de los defectos aparecen en la formación de las facetas en la fase inicial del crecimiento y que posteriormente el crecimiento vertical de la NWs continúa prácticamente libre de defectos. Esto confirma otra vez que los NWs tienen mejor calidad cristalina de las nanopirámides.

Caracterización óptica y estructural de NWs núcleo-corteza de GaN/InGaN individuales

Mediante espectroscopía óptica y de rayos-X se han estudiado la distribución elemental, las propiedades estructurales y la respuesta óptica de NWs núcleo-corteza de GaN/InGaN individuales. Las investigaciones actuales en NWs se enfocan en cómo obtener nanohilos núcleo-corteza de GaN/InGaN de alta calidad con un control preciso del contenido en In de las aleaciones. Por lo tanto, una caracterización cuidadosa y completa de sus propiedades es crucial y altamente beneficiosa.

Los NWs de GaN/InGaN que se estudiaron en este trabajo fueron crecidos mediante epitaxia metalorgánica en fase de vapor (MOCVD) en el centro de investigación y desarrollo de AIXTRON, siguiendo la técnica de crecimiento

denominada vapor-líquido-sólido (VLS). Antes de la epitaxia, se revistió ex-situ el sustrato de zafiro con una película de Au de 1 nm de espesor. Los núcleos de GaN de los NWs se crecen a 1020 °C. A continuación, se depositaron tres capas de InGaN seguidas por tres capas de GaN a una temperatura de 730 °C. Un esquema de la estructura que se quería conseguir para los GaN/InGaN multi-QW (MQWs) se representa en la Figura 6.18 (a): cada NW debe contener MQWs que crecen perpendicularmente a su eje (eje c). La Figura 6.18 (b) muestra una micrografía SEM de la muestra. Los NWs tienen diámetros y alturas que están entre 150 - 230 nm y de 1.5 a 3 μm, respectivamente.

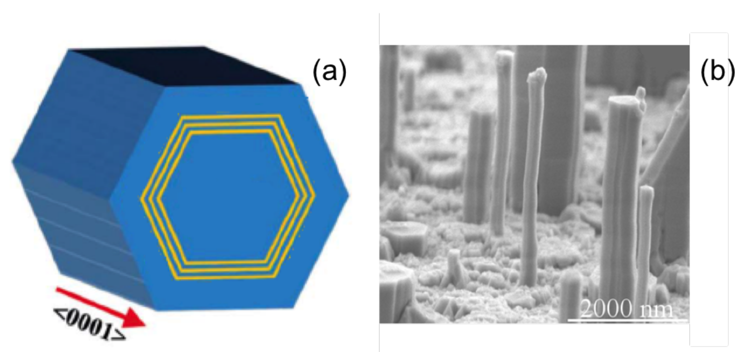

Figure 6.18: (a) Esquema de la estructura esperada por los NWs núcleo-corteza de GaN/InGaN a lo largo del eje c. La anchura de los pozos (InGaN en amarillo) y las barreras (GaN en azul) no es realista. Adaptado de [43] y (b) vista lateral SEM de la muestra.

Con el fin de comprobar si los MQWs no-polares se han formado correctamente durante el crecimiento, se han realizado mediciones de espectroscopia de energía dispersiva de rayos X (EDS) en NWs individuales, que tiene un altísima resolución espacial ($\sim$ 4 nm). La anchura de los MQWs y de las barreras se calculó a partir de estas medidas, y se obtuvieron los siguientes valores: 4.9 y 5.7 nm por los pozos y las barreras, respectivamente.

La distribución elemental de los NWs de GaN/InGaN se ha estudiado por medio de la fluorescencia a rayos X (XRF), que tiene una elevadisíma sensibilidad química (1ppm). En particular, se ha verificado si hay incorporación del catalizador de Au o de otras impurezas en los NWs, que implicaría un deterioro de la calidad cristalina, se ha comprobado si el In se distribuye de forma homogénea en el NW y se ha estimado la concentración del In en los MQWs. Mapas de XRF de varios NWs individuales dispersos sobre un substrato de zafiro recubierto de Al fueron grabados para identificar la distribución de los diferentes elementos en el área barrida. Sólo se presentan los resultados correspondientes a un NW representativo. Los datos se procesaron utilizando el programa PyMCA [129]. La Figura 6.19 muestra las distribuciónes espaciales de Ga, In, Au y Ag en la región del barrido. El Ga y el In se incorporan claramente sólo en el NW, ya que presentan

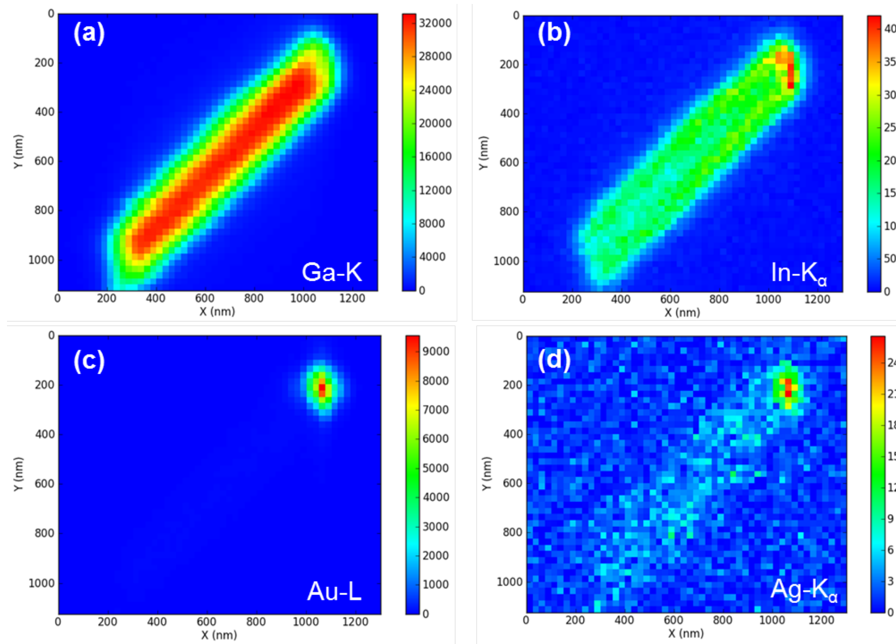

Figure 6.19: (a) Mapa de distribución de (a) Ga, (b) In, (c) Au and (d) Ag a lo largo del NW. La escala de colores indica la intensidad de la XRF en cuentas de fotones.

su morfología, (véasen las Figuras 6.19 (a) y (b)). El catalizador de Au, así como el Ag, se detectan sólo en la parte superior de los NWs. Ésto implica que no hay incorporación de estos elementos a lo largo de los NWs, como se muestra en las Figuras 6.19 (c) y (d), respectivamente. El Ag puede estar presente en niveles muy bajos en el Au y la concentración de Ag estimada por PYMCA es alrededor de 0.02%. Fe y Pb tienen una densidad de cuentas menos intensa y están presentes tanto en el NW como fuera de la región explorada (resultados no mostrados). Éstas señales provienen muy probablemente de procesos de segundo orden de dispersión del sistema de blindaje alrededor de la muestra. El Ga se distribuye homogéneamente a lo largo de la dirección axial del NW. Radialmente, la señal es más intensa en el centro (correspondiente a la región del núcleo de GaN) y menos en las superficies exteriores (donde sólo hay barreras y QWs). Por otra parte, la intensidad del In aumenta desde la base hasta el extremo superior del NW. La mayor intensidad de In en la parte superior de la NW no se corresponde a la formación de MQWs polares, ya que éstos no han sido observados en las medidas de EDS.

La concentración de In en los MQWs se extrae de las mapas utilizando el software PYMCA. En las condiciones experimentales de las medidas de XRF (NWs de diámetro pequeño), se puede asumir la aproximación de *capa fina*, por lo tanto, la intensidad de la emission de XRF por cada elemento es dada por [170]

$$I_i \propto I_0 k_i C_i d \tag{6.1}$$

donde C_i es la concentración de cada elemento; d es el espesor de la muestra; I_0 es la intensidad del haz entrante; k_i tiene en cuenta la eficiencia de detección. En el caso de la aleación ternaria InGaN, la Eq. (6.1) tiene que satisfacer la siguiente condición: la suma de las concentraciónes de In y Ga tiene que ser igual a uno, $\sum_i C_i = 1$. La concentración en los MQWs se estima para 6 puntos a lo largo del eje c del NW, considerando como espesor de los MQWs el que se extrae de los datos de EDS. Los valores obtenidos para las concentraciones se presentan en la Tabla 6.1. La concentración

Table 6.1: Valores de la concentración de In en los MQWs a lo largo del eje c del NW calculado con PYMCA.

Point	In Concentration (%)
A	11.6 ± 3.3
B	9.2 ± 2.7
C	7.4 ± 2.1
D	6.3 ± 1.2
E	5.4 ± 1.6
F	5.4 ± 1.6

disminuye a lo largo del eje, desde el punto A al punto F, revelando que la composición de la aleación de los MQWs no es homogónea y que hay una mayor concentración de In en la parte superior del NW.

Las propiedades estructurales de NWs individuales fueron estudiadas a escala micrométrica y nanométrica mediante tres técnicas: XRD, XANES, y dispersión Raman. La calidad estructural de los NWs puede verse afectada por los defectos, como BSFs, por la falta de homogeneidad en la composición de la aleación o por la segregación de In en algunas regiones del NW, y por el campo de deformaciones que se crea debido a la falta de correspondencia entre los parámetros de red del GaN (presente en el núcleo y las barreras) y el InGaN (MQWs). Mediciones de nano-XRD se realizaron en varios NWs con el fin de estudiar su fase cristalina, determinar los parámetros de red a nivel local, y monitorizar su variación a lo largo del NWs. En la Figura 6.20 (a) se presentan los ángulos de reflexión que se han detectado y son $2\theta = (24.54 \pm 0.08)^\circ$ y $2\theta = (25.03 \pm 0.08)^\circ$. Éstos se corresponden a las reflexiones (210) y (211) de GaN con estructura wurtzita. La identificación de estos picos se ha realizado con los programas Fit2D [130] y PyMCA. A partir de estas reflexiones es posible calcular la distancia interplanar d utilizando la ley de Bragg. Por tanto, los parámetros de red de los NWs estudiados pueden ser extraídos de la relación entre d, los índices de Miller (hkl) y los parámetros a y c de la estructura wurtzita:

$$d_{hkl} = \left[\frac{4}{3a^2}(h^2 + hk + k^2) + \frac{l^2}{c^2} \right]^{-1/2} \tag{6.2}$$

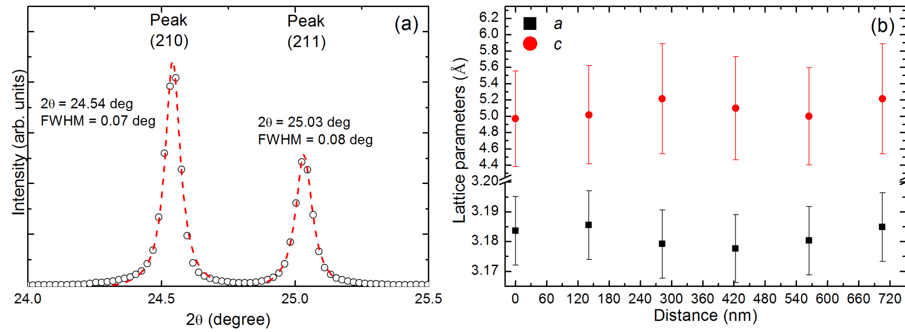

Figure 6.20: (a) Picos en el espectro de XRD en un punto representativo de un NW individual. (210) y (211) son las reflecciónes que se corresponden a los ángulos del espectro. La posición del pico y la FWHM son indicados para cada ajuste. (b) Evolución a lo largo del eje de un NW individual de los parámetros de red a y c.

Las reflexiones simétricas, como las (210), permiten extraer directamente el parámetro a de la ecuación (6.2), y , a partir de reflexiones no simétricas, tales como las (211), es posible calcular el parámetro de red c. Los valores obtenidos se resumen en la Tabla 6.2. Las mediciones de XRD en el área de

Table 6.2: Lattice parameters.

Parámetros	$\mathring{A}$
a	3.18 ± 0.01
c	5.1 ± 0.6

los NWs permite realizar un estudio estructural de todo el NW en la nano escala. Los ángulos de reflexión medidos en cada punto del NW permiten extraer los parámetros de red asociados al punto mismo. De esta manera se puede calcular la variación de éstos a lo largo del NW. Ésta tendencia en dirección axial se muestra en la Figura 6.20 (b).

Puesto que no se observan reflexiones adicionales ni asimetrías en los picos XRD y éstos corresponden a reflexiones del GaN relajado, concluimos que los MQWs de InGaN están totalmente acoplados al núcleo de GaN.

Los resultados de XANES sugieren que el NW tiene estructura de wurtzita y no hay mezcla de fases, y que el eje de la NW coincide con el eje c de la estructura wurtzita (resultados no mostrados).

Un espectro Raman represenativo se muestra en la Figura 6.21 (a). Los picos Raman observados han sido E_{2h}, A_1(TO), E_1(TO) and E_1(LO), y sus frecuencias coinciden con las del GaN wurtzita. La observación de los modos E_1(TO) and E_1(LO) se atribuye a desviaciones de la geometría nominal, como en el caso de los SAG NWs, debido a las facetas no-polares de sus superficies laterales. Un pico adicional centrado alrededor de 701 cm^{-1} se atribuye a un modo óptico de superficie (SO). Éste no puede ser un modo del InGaN, ya que su frecuencia no coincide con la que se habría debido

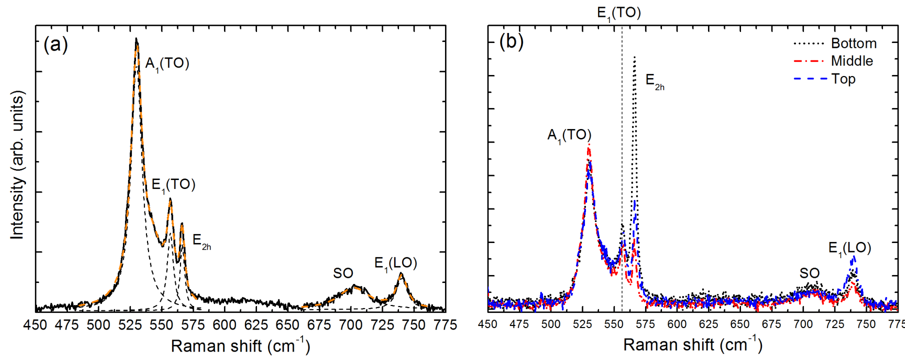

Figure 6.21: (a) Espectro Raman representativo de un NW individual tomado con línea de 514 nm y (b) espectros Raman tomados en la parte inferior (curva negra), en el medio (curva roja) y en la parte superior (curva azul) del NW (línea de láser de 647 nm).

al contenido de In en los pozos cuánticos que se ha obtenido con la XRF. No hay cambios en la frecuencia de los picos en función de la posición a lo largo del NW, como se se muestra en la Figura 6.21 (b). Los FWHMs del modo E_{2h} medidos en varios NWs es de alrededor de 3.6 cm^{-1}, confirmando la buena calidad del núcleo de GaN.

Cientos de NWs se han dispersado sobre un sustrato recubierto de Au para medir su emisión individual. Espectros de PL tomada a una temperatura de 5 K en los extremos de los NWs se muestran en Figura 6.22 (a) - (d). Todos los espectros están dominados por bandas correspondientes a transiciones de los MQWs con energías entre 3.1 - 3.3 eV. La anchura ($\sim$ 34 meV) de estas bandas está relacionada a la variación de la composición de la aleación a lo largo del NWs. La banda centrada alrededor de 3.47 eV se atribuye a las emisiones del GaN y se origina por la superposición de las emisiones D^0X_A (FWHM $\sim$ 50 meV) y X_A (FWHM $\sim$ 20 meV). Al comparar los espectros tomados en la punta y la base de cada NW, respectivamente, los picos de la PL relativos a los MQWs aumentan su intensidad y se desplazan hacia el rojo desde la parte inferior hacia la superior del NW. De nuevo, esto se atribuye a la mayor concentración de In encontrada en la parte superior de la NW y a la falta de homogeneidad en la aleación a lo largo de la dirección axial. Se han realizado mediciones de PL en función de la temperatura (los resultados no se muestran en este resumen) que permiten calcular la eficiencia cuántica interna relativa (IQE) de las transiciones ópticas a temperatura ambiente. Esto se puede hacer bajo el supuesto que, a baja temperatura, los procesos no radiativos se suprimen y se activan a temperatura ambiente. Por lo tanto, la IQE se calcula dividiendo la intensidad integrada de la PL a temperatura ambiente por la de baja temperatura. Entonces, si la IQE a baja temperatura es igual a 1, a temperatura ambiente la IQE será alrededor de 20% y 15% en la punta y en la base del NWs, respectivamente. Por otro lado, la IQE del núcleo es de menos del 1%.

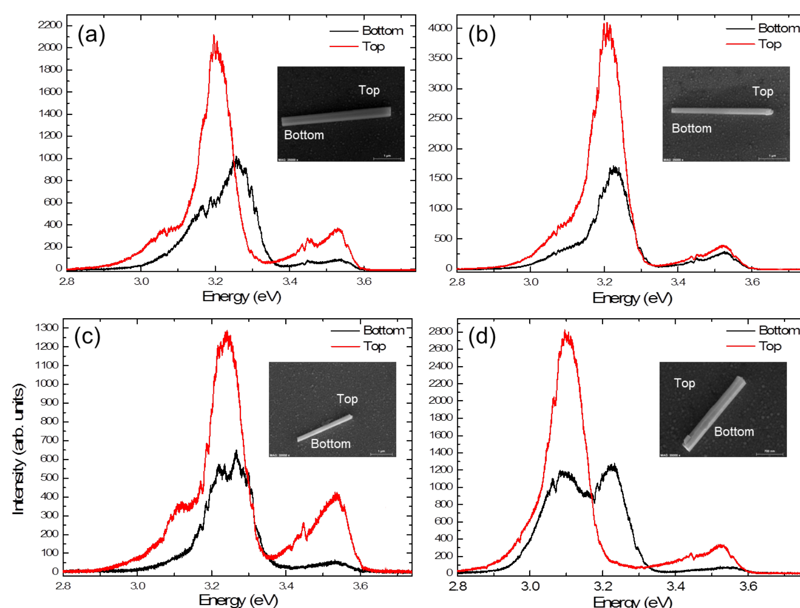

Figure 6.22: (a), (b), (c) y (d) son espectros representativos de PL tomados en los extremos de diferentes NWs a una temperatura de 5 K en las mismas condiciones experimentales.

Dispersión Raman amplificada en la superficie en NWs semiconductores individuales funcionalizados con nanopartículas de oro

Se han explorado las potencialidades de la dispersión Raman amplificada en la superficie (SERS) en NWs semiconductores individuales funcionalizados con nano-varillas (en inglés, nanorods) de Au. A pesar de los excelentes resultados obtenidos para las moléculas, la comprensión de las capacidades reales de la SERS para la caracterización de NWs semiconductores está todavía enormemente inexplorada.

Los nanorods han sido sintentizados mediante un método estándar y se estabilizan en solución gracias a una doble capa de bromuro de hexadeciltrimetilamonio (CTAB) que envuelve toda su superficie [190]. Estos nanorods tienen una razón ancho-largo que implica un espectro de absorción con dos máximos centrados en 524 y 657 nm, que se corresponden a una resonancia plasmonica transversal (TPR) y longitudinal (LPR) al eje del nanorod, respectivamente. La funcionalización de NWs semiconductores con nanorods de metal ha sido demostrada por diferentes procedimientos. Las muestras que se han estudiado en este trabajo han sido obtenidas con un nuevo método de fabricación que ha permitido maximizar la deposición de nanorods en la superficie superior de los NWs (diseñado por Andrea Pescaglini del Instituto Tyndall). Se eligió un nuevo método porque los

de literatura no dieron los resultados esperados. Maximizar el numero de nanorods en la superficie de los NWs es un requisito fundamental para el éxito del mecanismo de SERS, ya que aumenta la probabilidad de crear centros de muy alta dispersión denominados 'hot spots'. El resultado de esta nueva técnica de deposición se muestra la Figura 6.23.

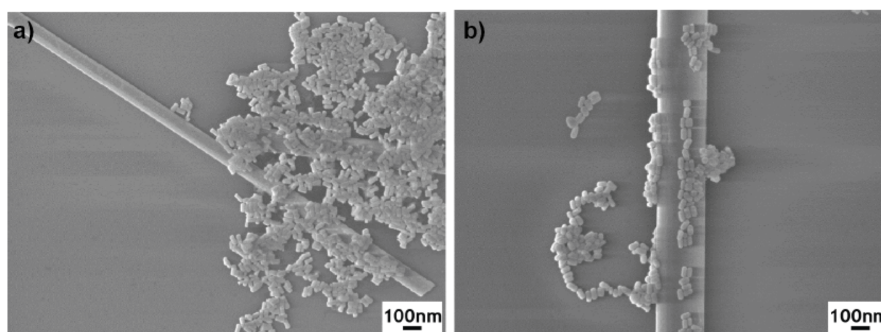

Figure 6.23: (a) and (b) imagenes SEM de los dispositivos híbridos de nanorods de Au y NW de ZnO.

Para confirmar las frecuencias de resonancia plasmónica de los nanorods se realizaron mediciones SERS de nanorods de Au depositados en un sustrato de SiO_2/Si. Las moléculas de CTAB muestran un pico Raman centrado en 174 cm^{-1} y que se atribuye al enlace Br (presente el CTAB)-Au [195]. La intensidad de este modo se ha utilizado para verificar la longitud de onda de las resonancias plasmónicas. La Figura 6.24 muestra que bajo excitación a

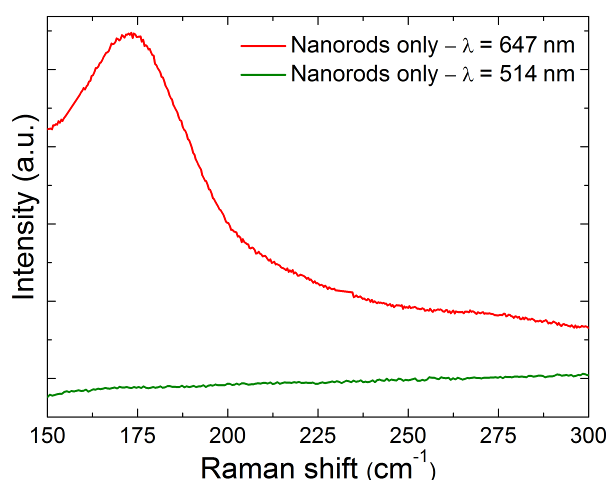

Figure 6.24: Espectros Raman de nanorods de Au medidos a 647 nm (curva roja) y 514 nm (curva verde).

647 nm (línea roja), aparece el pico Raman del enlace de Br-Au y esto indica claramente la condición de resonancia a esta frecuencia, que se corresponde a los plasmones de superficie longitudinales (LPR). Por otro lado, este mismo

modo no es visible para la longitud de onda de excitación a 514 nm (línea verde), lo que sugiere que la magnificación de campo generado por el plasmon transversal es insignificante.

Este resultado está también contrastado por simulaciones que Andrea Pescaglini ha llevado a cabo.

La Figura 6.25 muestra algunos espectros representativos de SERS de los sistemas híbridos nanorods-NWs. Todas las mediciones se realizaron con la línea 647 nm, en resonancia con la LPR de los nanorods. Los espectros mostran un pico claro en 572 cm^{-1} (que está sombreado en negro). Los

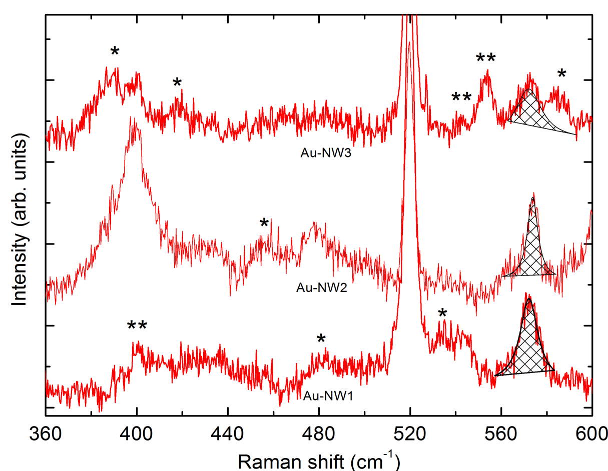

Figure 6.25: Espectros SERS representativos tomados con línea de 647 nm en diferentes NWs híbridas individuales. El modo de la NWs híbrido está sombreado en negro, con el asterisco se indican los picos asociados al CTAB y con el doble asterisco aquellos asociados a nanorods de Au.

espectros de las mediciones realizadas en diferentes NWs muestran diferentes características ópticas: fluctuación en la intensidad y en la frecuencia de los picos y aparición de picos adicionales. Con el fin de asignar correctamente los picos y extraer conclusiones válidas, se ha realizado un análisis estadístico cuidadoso de todos los espectros medidos. Los resultados se presentan en la Figura 6.26 (a), donde el eje y representa la intensidad ponderada (FWI) de los picos SERS observados. Éste se calcula multiplicando la intensidad de los picos por su frecuencia de aparición. Los modos centrados en 390 cm^{-1}, 414 cm^{-1}, 456 cm^{-1}, 480 cm^{-1}, 493 cm^{-1}, 592 cm^{-1} han sido reportados previamente para CTAB cristalino [196, 197]. El resto de los picos a 390 cm^{-1}, 401 cm^{-1}, 414 cm^{-1}, 480 cm^{-1}, 493 cm^{-1}, 544 cm^{-1} y 564 cm^{-1} se encuentran tanto en los espectros de las nanoestructuras híbridas como en el sustrato (que contiene sólo nanorods de Au), por lo tanto, se atribuyen a las transiciones vibracionales del CTAB adsorbido en los nanorods de Au. Es bien sabido que las moléculas adsorbidas en la superficie de un metal muestran modos Raman desplazados o nuevos modos debido a la interacción entre la molécula y la superficie [198]. En la Figura 6.26 (b) se

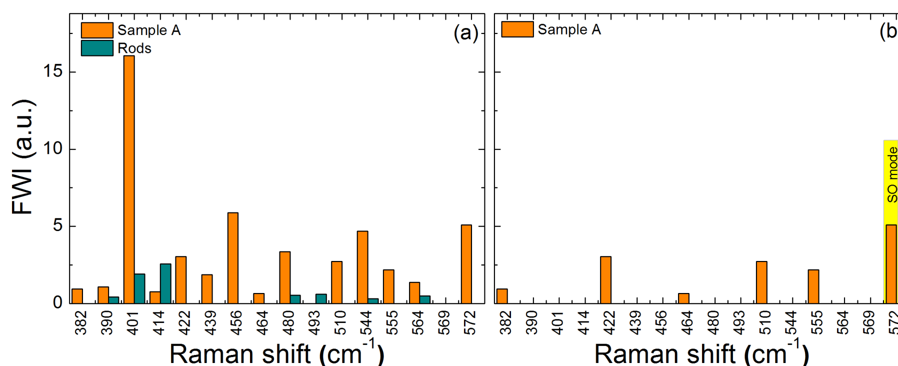

Figure 6.26: Distribución ponderada de los picos SERS observados en los espectros medidos. (a) Picos observados en los híbridos y en el substrato. (b) Picos Raman de los híbridos presentados en (a) y restando los picos atribuidos al CTAB y al sustrato.

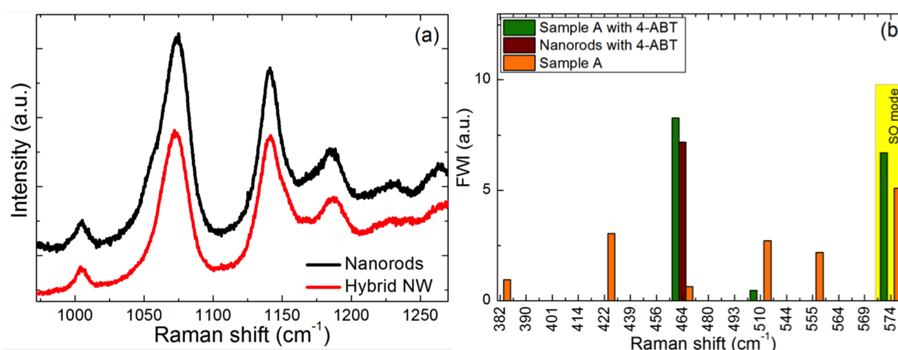

Figure 6.27: (a) Espectros SERS representativos de 4-ABT detectada en un conjunto de nanorods de Au (curva negro) y de un NW híbrido individual después de su funcionalización con 4-ABT (curva roja). (b) Análisis estadístico de los picos Raman encontrado en la muestra sin y con funcionalización con la molécula de 4-ABT.

muestra el resultado final depués de haber restado todos los picos que son unívocamente asignables al CTAB. Después de este proceso de comparación directa, quedan algunos picos centrados en 382 cm^{-1}, 422 cm^{-1}, 464 cm^{-1}, 510 $cm^{-1}$and 555 cm^{-1}. Al fin de determinar si están relacionados con los NWs se ha llevado a cabo un análisis adicional. Se sumergió la muestra en una solución basada en metanol de 4-aminobencenotiol (4-ABT) (1 mM) con el fin de reemplazar en la superficie de los nanorods a la mayor parte de la CTAB con la molécula de 4-ABT. En la Figura 6.27 (a) se muestran los espectros SERS en estructuras híbridas y en el sustrato que contiene nanorods de Au solamente. Señales Raman del 4-ABT, centradas en 1004 cm^{-1}, 1073 cm^{-1}, 1139 cm^{-1} y 1187 cm^{-1}, se observan con intensidad comparable en ambos espectros. Esto demuestra la adsorción efectiva de la nueva molécula a las nanorods de Au y la sustitución de una buena parte del CTAB. Una comparación directa entre el análisis estadístico de los picos

SERS antes y después de la sustitución de 4-ABT en el mismo conjunto de NWs híbridos se muestra en la Figura 6.27 (b). El pico centrado a 464 cm^{-1} puede despreciarse, ya que se observa también en el sustrato. Los picos a 382 cm^{-1}, 422 cm^{-1} y 555 cm^{-1} pueden atribuirse al CTAB, porque no aparecen en la muestra después de la inmersión en 4-ABT. El pico restante centrado en 510 cm^{-1} puede despreciarse también, porque su intensidad disminuye mucho tras la sustitución del CTAB y puede ser por lo tanto atribuido a esta molécula. Finalmente, el pico centrado en 572 cm^{-1} es el único pico que queda. Con el fin de demostrar la reproducibilidad de los resultados, las mediciones se realizaron sobre una segunda muestra, y se conseguierón resultados en perfecto acuerdo con los obtenidos en la muestra precedente. En ambas muestras se midieron decenas de NWs para que los resultados fueran estadísticamente significativos. El pico centrado en 572 cm^{-1} no puede corresponder a un modo del GaN masivo, ya que habría de ir acompañado por otros modos del material que están permitidos en la geometría de este experimento y que tienen probabilidad más grandes, e.g., el modo no polar E_{2h}. En su lugar aparece el pico 572 cm^{-1} como una característica aislada y su frecuencia es compatible con un modo de SO. Esta afirmación está apoyada por cálculos teóricos que no se muestran en este resumen por brevedad.

Conclusiones

Las principales conclusiones de esta investigación se resumen a continuación.

Las medidas Raman demostraron que los nanohilos (NWs) y nanopirámides obtenidos por SAG crecen libres de campos de deformación macroscópicos. La calidad estructural del material disminuye para $p < 1$ μm, mientras que no está influenciada por d. En el caso de los NWs, este efecto se atribuye a la mayor densidad de dislocaciones presentes en NWs más cortos (que se corresponden a $p < 1$ μm) y para las nanopiramdes se demuestra que el proceso de coalescencia (que occurre a $p > 1$ μm) genera una mejora en la calidad del cristal.

Los espectros de PL muestran una considerable presencia de defectos estructurales (en particular, fallos de apilamiento basal, BSFs) en los NWs, cuya densidad aumenta al disminuir d. Por tanto, la dependencia de la PL con d señala la importancia de la dirección de crecimiento en el mecanismo de formación de los BSFs: NWs más delgadas, por las que la mayor parte del crecimiento se lleva en las facetas semi-polares, estadísticamente presentan una mayor densidad de BSFs.

El estudio comparativo entre NWs y nanopirámides muestra que las primeras tienen una calidad cristalina superior (FWHM más estrechos). Eso confirma que las dislocaciones se forman en la base de las nanoestructuras y se doblan terminándose en las facetas non-polares, dejando la mayor parte del

volumen de los NWs prácticamente libre de defectos. Por último, la intensidad relativa de los BSFs y de PSFs (sólo presentes en las nanopirámides) en relación con D_0X_A es mayor para las nanopirámides que en las NWs. Esto indica otra vez que la mayoría de los defectos aparecen en la formación inicial de las facetas y que el crecimiento vertical posterior del NWs continúa libre de defectos.

La caracterización elemental, estructural y óptica de GaN/InGaN NWs individuales con estructura núcleo-corteza se ha llevado a cabo mediante técnicas de espectroscopía no destructivas con resolución espacial nanométrica. En particular, combinando las altas resolución espacial de la espectroscopía de energía dispersiva de rayos X (EDS) (alrededor de 4 nm) y la elemental de la fluorescencia a rayos X (XRF) (1 ppm), se ha observado que los MQWs de GaN/InGaN se han formado correctamente en la superficie lateral de los NWs, que hay una mayor concentración de In en la punta de los NWs y que la concentración de In en los pozos no es uniforme: crece a lo largo del eje de los NWs desde la base hacia la punta.

Los NWs tienen las constantes de red del GaN masivo relajado, tal y como confirman las caracterizaciónes XRD y Raman. El material no presenta desorden cristalino a nivel local como demuestran los resultados del XANES. Por otro lado, no se observa ninguna señal proveniente de los MQWs de InGaN. Siendo que las mediciones de XRD se realizaron iluminando todo el material presente en el NW, se espera una contribución a los espectros de XRD por parte de los MQWs. Esto sugiere que los MQWs están tensionados y se acoplan al núcleo de GaN, de lo contrario se resolverían algunos picos adicionales o la difracción correspondiente al GaN presentaría asimetrías que no se han observado en los espectros de XRD.

Los espectros de PL a baja temperatura obtenidos en conjuntos y en NWs individuales están dominados por las transiciones de los MQWs, con energías entre 3.1 y 3.3 eV. La FWHM $\sim$ 34 meV de esta banda se atribuye a la variación de la concentración a lo largo de los NWs, que desplaza la emisión. Por lo tanto, la superposición de las diferentes emisiones produce una ampliación de esta banda.

Los resultados obtenidos por las medidas de XRD y PL están contrastados por simulaciones teóricas. La distribución de campos de deformación en los NWs se ha calculado utilizando los resultados de EDS y XRF (anchura de los pozos y concentración del In), y se han calculado también los valores de emissión que se esperan del InGaN bajo el campo de deformaciones calculado. La simulaciónes demuestran que los MQWs se encuentran completamente acoplados al núcleo de GaN y la emisión del InGaN comprimido se calcula en el rango 3.05 - 3.29 eV. Éstos resultados coinciden en gran medida con las observaciones experimentales.

Finalmente, se estudió el potencial de la utilización de la dispersión Raman amplificada en la superficie (SERS) para la caracterización de las propiedades vibracionales de superficie de los NWs semiconductores. Las

mediciones de SERS se realizaron en NWs de ZnO individuales funcionalizados con nanorods de oro.

Se observaron modos ópticos de superficie (SO) del ZnO a través de la excitación de la resonancia plasmonica longitudinal (LPR) de los nanorods. Se llevó a cabo un análisis estadístico extenso para apoyar la asignación del pico Raman en 572 cm^{-1} al ZnO, y de los otros al surfactante bromuro de hexadeciltrimetilamonio (CTAB) que recubre los nanorods.

Los resultados obtenidos no son tan excepcionales como los reportados para el SERS de moléculas. De hecho, la amplificación de la señal del semiconductor es drásticamente menor, y la variabilidad de la frecuencia y de la intensidad de los picos relacionados con el sustrato obligan a llevar a cabo un análisis estadístico sistemático que consume mucho tiempo. El factor de mejora (EF) del SO del sistema estudiado en este trabajo se prevé que sea varios órdenes de magnitud más pequeño que el EF tipico de los experimentos SERS sobre moléculas adsorbidas directamente el la superficie de las nanoestructuras metálicas. Esto es una consecuencia natural del rápido decrecimiento de la intensidad del campo electromagnético fuera de la superficie del metal que limita el volumen del semiconductor que se puede excitar. Por esta razón, a pesar de las ventajas ofrecidas por la SERS en NWs semiconductores, se requiere un optimización futura para mejorar la reproducibilidad y la estabilidad. Por ejemplo, la doble capa de CTAB que envuelve los nanorods tiene que ser sustituida por capas dieléctricas más delgadas. Esto daría lugar a una reducción drástica del fondo y, por tanto, a una simplificación del procesamiento de los resultados. Adicionalmente, la mejora de la distribución de los nanorods de Au sobre la superficie de los NWs (en términos de densidad y posición) podría llevar a un aumento de la intensidad de la señal, que se espera sea proporcional al número de nanorods. No obstante, este trabajo proporciona la evidencia de la potencialidad que ofrece el SERS para la caracterización de la superficie de los NWs semiconductores en condiciones no resonantes, extendiendo las capacidades de la espectroscopia Raman tradicional para NWs.

Acknowledgements

Finally, I would like to thank all the people who accompanied me during this wonderful journey of my PhD experience and empowered me to write this work.

First of all, I would like to start by expressing my deepest gratitude to my supervisor Núria Garro for supporting, helping and teaching me in my PhD time. I especially thank her for trusting me with the opportunity to join her group and for making my work fruitful and my stay pleasant due to her friendly character.

Special thanks to Andrés Cantarero for his laboratory and to Arne Urban, Andrea Pescaglini, Alfonso Martínez, Davide Cammi, Carsten Ronning, Bartosz Foltynski and Cristoph Giesen for the samples, and Alberto García-Cristóbal and Heruy Taddese Mengistu for the simulations. Without them, this work would not have been possible.

I would like to thank Ana Cros for her helpfulness, availability, deep expertise and positive attitude, Mauricio Morais for his interesting chats about Brasil, Europe and politics, especially the Italian one, and for sharing with me curious news all the time.

Many thanks to Jaime Segura-Ruiz and Gema Martínez-Criado who offered me the possibility to spend one month at the ID22NI beamline in Grenoble, allowing me to live this unique experience and to learn a lot in a cutting edge institution like ESRF.

I would like to thank Daniela Iacopino and Andrea Pescaglini for the wonderful stay in Cork, in particular Andrea (again), who has not only been a close, competent and always available collaborator during all my PhD, but also a loyal and generous friend. I want to thank all the colleagues in Cork for their support and closeness as well, especially Ethel Noonan.

Special thanks to all my collaborators of the Marie Curie network 'Nanowiring' for both professional experience and friendly one. In particular, I would like to thank Arne Urban (again), Joerg Malindetros and Angela Rizzi (project coordinator) for their availability, expertise and interesting discussions. Many many thanks to Carla Oppo, Davide Cammi (again), Andrea Pescaglini (again), Manh Hung Chu and Bartosz Foltynski (again) for the wonderful time we had together and for the support to my work. In particular to Carla, for articulate conversations, her strong character and her close friendship.

I want to thank all my colleagues of the Institute of Material Science: Antonio, my first friend in Valencia, with whom I had long walks and chats, Maria José for her funny jokes, Sandra for her kindness and helpfulness, Jonathan for his love for music, Albert for always listening and giving me good advises, Raoul for the long chats on politics while speaking Valencian, Guillermo, Luis, Carlos, Rubén, Elena, Pedro, Michael, Rafa, . . . , Maribel for her wise counsels and good time shared together. Pascual for his precious help in the laboratory, for his friendly and positive character and funny breaks and chats.

I cannot forget to mention my friends who accompany, motive and support and stay with me in good and hard times in my private life and make it beautiful every day: Enrico, Eva, Julio, Pablo, Francesca, Albert (again), Elena and Surinder.

Special thanks to all the persons who helped and supported me during my time in Valencia.

Thanks to my Mom, Dad, grandmother and grandfather for their patience, teachings and infinite love.

Thanks! Grazie! Gracias! Gràcies! Merci!

Valencia, July 2015

Eleonora

Bibliography

[1] Matt Law, Joshua Goldberger, and Peidong Yang. Semiconductor nanowires and nanotubes. *Annual Review of Materials Science*, 34(1):83, 2004.

[2] Wei Lu and Charles M Lieber. Semiconductor nanowires. *Journal of Physics D: Applied Physics*, 39(21):R387, 2006.

[3] Hui Pan and Yuan Ping Feng. Semiconductor nanowires and nanotubes: Effects of size and surface-to-volume ratio. *ACS Nano*, 2(11):2410, 2008.

[4] Ruoxue Yan, Daniel Gargas, and Peidong Yang. Nanowire photonics. *Nature Photonics*, 3(10):569, 2009.

[5] Yangyang Zhang, Manoj K. Ram, Elias K. Stefanakos, and D. Yogi Goswami. Synthesis, characterization, and applications of ZnO nanowires. *Journal of Nanomaterials*, 2012:624520, 2012.

[6] Shunfeng Li and Andreas Waag. GaN based nanorods for solid state lighting. *Journal of Applied Physics*, 111(7):071101, 2012.

[7] Lifan Yan, Shafat Jahangir, Scott A. Wight, Babak Nikoobakht, Pallab Bhattacharya, and Joanna M. Millunchick. Structural and optical properties of disc-in-wire InGaN/GaN LEDs. *Nano Letters*, 15(3):1535, 2015.

[8] Bryan M. Wong, François Léonard, Qiming Li, and George T. Wang. Nanoscale effects on heterojunction electron gases in GaN/AlGaN core/shell nanowires. *Nano Letters*, 8(11):3074, 2011.

[9] Jerome K. Hyun, Shixiong Zhang, and Lincoln J. Lauhon. Nanowire heterostructures. *Annual Review of Materials Research*, 43:451, 2013.

[10] Christophe Durand, Catherine Bougerol, Jean-François Carlin, Georg Rossbach, Florian Godel, Joël Eymery, Pierre-Henri Jouneau, Anna Mukhtarova, Raphaël Butté, and Nicolas Grandjean. M-plane GaN/InAlN multiple quantum wells in core-shell wire structure for UV emission. *ACS Photonics*, 1(1):38, 2014.

[11] N. A. Sanford, P. T. Blanchard, M. Brubaker, K. A. Bertness, A. Roshko, J. B. Schlager, R. Kirchhofer, D. R. Diercks, and B. Gorman. Laser-assisted atom probe tomography of MBE grown GaN nanowire heterostructures. *physica status solidi (c)*, 11(3):608, 2014.

[12] *http://nanowiring.eu/index.html.*

[13] A. Urban, J. Malindretos, J.-H. Klein-Wiele, P. Simon, and A. Rizzi. Ga-polar GaN nanocolumn arrays with semipolar faceted tips. *New Journal of Physics*, 15(5):053045, 2013.

[14] M. H. Chu, J. Segura-Ruiz, G. Martinez-Criado, P. Cloetens, I. Snigireva, S. Geburt, and C. Ronning. Synchrotron fluorescence nanoimaging of a single Co-implanted ZnO nanowire. *physica status solidi (RRL)*, 5(8):283, 2011.

[15] D. Cammi, R. Röder, and C. Ronning. Gate modulation of below-band-gap photoconductivity in ZnO nanowire Field-Effect-Transistors. *Journal of Physics D: Applied Physics*, 47(39):394014, 2014.

[16] D. Calestani, M. Villani, R. Mosca, L. Lazzarini, N. Coppedè, S. C. Dhanabalan, and A. Zappettini. Selective response inversion to NO_2 and acetic acid in ZnO and CdS nanocomposite gas sensor. *Nanotechnology*, 25(36):365502, 2014.

[17] K. K. Korir, G. Cicero, and A. Catellani. Piezoelectric properties of zinc oxide nanowires: an ab initio study. *Nanotechnology*, 24(47):475401, 2013.

[18] Andrea Pescaglini, Alan O'Riordan, Aidan Quinn, and Daniela Iacopino. Controlled assembly of Au nanorods into 1D architectures by electric field-assisted deposition. *Journal of Material Chemistry C*, 2:6810, 2014.

[19] M. Negri, S. Dhanabalan, G. Attolini, P. Lagonegro, M. Campanini, M. Bosi, F. Fabbri, and G. Salviati. Tuning the radial structure of core-shell silicon carbide nanowires. *Cryst. Eng. Comm.*, 17:1258, 2015.

[20] Shuji Nakamura, Masayuki Senoh, Naruhito Iwasa, Shin ichi Nagahama, Takao Yamada, and Takashi Mukai. Superbright green InGaN single-quantum-well-structure light-emitting diodes. *Japanese Journal of Applied Physics.*, 34(10B):L1332, 1995.

[21] Takashi Mukai, Motokazu Yamada, and Shuji Nakamura. Characteristics of InGaN-based UV/Blue/Green/Amber/Red Light-Emitting Diodes. *Japanese Journal of Applied Physics*, 38(7A):3976, 1999.

[22] Young-Ho Ko, Je-Hyung Kim, Su-Hyun Gong, Joosung Kim, Taek Kim, and Yong-Hoon Cho. Red emission of InGaN/GaN double heterostructures on GaN nanopyramid structures. *ACS Photonics*, 2(4):515, 2015.

[23] Hisashi Masui, Shuji Nakamura, Steven P. DenBaars, and Umesh K. Mishra. Nonpolar and semipolar III-nitride Light-Emitting Diodes: Achievements and challenges. *IEEE TRANSACTIONS ON ELECTRON DEVICES*, 57(1):88, 2010.

[24] Robert Koester, Daniel Sager, Wolf-Alexander Quitsch, Oliver Pfingsten, Artur Poloczek, Sarah Blumenthal, Gregor Keller, Werner Prost, Gerd Bacher, and Franz-Josef Tegude. High-speed GaN/GaInN nanowire array Light-Emitting Diode on Silicon (111). *Nano Letters*, 15(4):2318, 2015.

[25] A. Bertness, N. A. Sanford, and A. V. Davydov. GaN nanowires grown by molecular beam epitaxy. *IEEE Journal of selected topics in quantum electronics*, 17(4):847, 2011.

[26] Qian Gao, Dhruv Saxena, Fan Wang, Lan Fu, Sudha Mokkapati, Yanan Guo, Li Li, Jennifer Wong-Leung, Philippe Caroff, Hark Hoe Tan, and Chennupati Jagadish. Selective-area epitaxy of pure wurtzite InP nanowires: High quantum efficiency and room-temperature lasing. *Nano Letters*, 14(11):5206, 2014.

[27] Andrea Pescaglini, Alfonso Martín, Davide Cammi, Gediminas Juska, Carsten Ronning, Emanuele Pelucchi, and Daniela Iacopino. Hot-electron injection in Au nanorod-ZnO nanowire hybrid device for near-infrared photodetection. *Nano Letters*, 14(11):6202, 2014.

[28] B. A. Wacaser, K. A. Dick, J. Johansson, M. T. Borgström, K. Deppert, and L. Samuelson. Preferential interface nucleation: An expansion of the VLS growth mechanism for nanowires. *Advanced Materials*, 21(2):153, 2009.

[29] C. Borchers, S. Müller, D. Stichtenoth, D. Schwen, and C. Ronning. Catalyst-nanostructure interaction in the growth of 1-D ZnO nanostructures. *Journal of Physical Chemistry B*, 110(1):1656, 2006.

[30] Bodo Fuhrmann, Hartmut S. Leipner, and Hans-Reiner Höche. Ordered arrays of Silicon nanowires produced by nanosphere lithography and molecular beam epitaxy. *Nano Letters*, 5(12):2524, 2005.

[31] C. Chéze, L. Geelhaar, O. Brandt, W. M. Weber, H. Riechert, S. Münch, R. Rothemund, S. Reitzenstein, A. Forchel, T. Kehagias, P. Komninou, G. P. Dimitrakopulos, and T. Karakostas. Direct comparison of

catalyst-free and catalyst-induced GaN nanowires. *Nano Research*, 3(7):528, 2010.

[32] T. Schumann, T. Gotschke, F. Limbach, T. Stoica, and R. Calarco. Selective-area catalyst-free MBE growth of GaN nanowires using a patterned oxide layer. *Nanotechnology*, 22(9):095603, 2011.

[33] Kihyun Choi, Munetaka Arita, and Yasuhiko Arakawa. Selective-area growth of thin GaN nanowires by MOCVD. *Journal of Crystal Growth*, 357:58, 2012.

[34] K. Kishino, H. Sekiguchi, and A. Kikuchi. Improved Ti-mask selective-area growth (SAG) by RF-plasma-assisted molecular beam epitaxy demonstrating extremely uniform GaN nanocolumn arrays. *Journal of Crystal Growth*, 311(7):2063, 2009.

[35] A. Bengoechea-Encabo, F. Barbagini, S. Fernández-Garrido, J. Grandal, J. Ristić, M. A. Sánchez-García, E. Calleja, U. Jahn, E. Luna, and A. Trampert. Understanding the selective area growth of GaN nanocolumns by MBE using Ti nanomasks. *Journal of Crystal Growth*, 325(1):89, 2011.

[36] Bengoechea-Encabo, S. Albert, J. Zuñiga-Perez, P. de Mierry, A. Trampert, F. Barbagini, M. A. Sánchez-García, and E. Calleja. Selective area growth and characterization of GaN nanocolumns, with and without an InGaN insertion, on semi-polar (11-22) GaN templates. *Applied Physics Letters*, 103(24):241905, 2013.

[37] T. Koyama, T. Onuma, H. Masui, A. Chakraborty, B. A. Haskell, S. Keller, U. K. Mishra, J. S. Speck, S. Nakamura, S. P. DenBaars, T. Sota, and S. F. Chichibu. Prospective emission efficiency and in-plane light polarization of nonpolar m-plane $In_xGa_{1-x}N$/GaN blue light emitting diodes fabricated on free standing GaN substrates. *Applied Physics Letters*, 89(9):091906, 2006.

[38] P. Lefebvre, A. Morel, M. Gallart, T. Taliercio, J. Allègre, B. Gil, and H. Mathieu. High internal electric field in a graded-width InGaN/GaN quantum well: Accurate determination by time-resolved photoluminescence spectroscopy. *Applied Physics Letters*, 78(9):1252, 2001.

[39] Hon-Way Lin, Yu-Jung Lu, Hung-Ying Chen, Hong-Mao Lee, and Shangjr Gwo. InGaN/GaN nanorod array white light-emitting diode. *Applied Physics Letters*, 97(7):073101, 2010.

[40] Arpan Chakraborty, Benjamin A. Haskell, Stacia Keller, James S. Speck, Shuji Nakamura Steven P. Denbaars, and Umesh K. Mishra.

Demonstration of nonpolar m-plane InGaN/GaN Light-Emitting Diodes on free-standing m-plane GaN substrates. *Japanese Journal of Applied Physics*, 44(5):L173, 2001.

[41] Y.-L. Li, Y.-R. Huang, and Y.-H. Lai. Efficiency droop behaviors of InGaN/GaN multiple-quantum-well light-emitting diodes with varying quantum well thickness. *Applied Physics Letters*, 91(18):181113, 2007.

[42] James R. Riley, Sonal Padalkar, Qiming Li, Ping Lu, Daniel D. Koleske, Jonathan J. Wierer, George T. Wang, and Lincoln J. Lauhon. Three-dimensional mapping of quantum wells in a GaN/InGaN core-shell nanowire light-emitting diode array. *Nano Letters*, 13(9):4317, 2013.

[43] Yong-Ho Ra, Rangaswamy Navamathavam, San Kang, and Cheul-Ro Lee. Different characteristics of InGaN/GaN multiple quantum well heterostructures grown on m- and r-planes of a single n-GaN nanowire using metalorganic chemical vapor deposition. *The Journal of Materials Chemistry C*, 2:2692, 2014.

[44] J. Segura-Ruiz, G. Martinez-Criado., J. A. Sans, R. Tucoulou, P. Cloetens, I. Snigireva, C. Denker, J. Malindretos, A. Rizzi, M. Gómez-Gómez, N. Garro, and A. Cantarero. Direct observation of elemental segregation in InGaN nanowires by X-ray nanoprobe. *physica status solidi (RRL)*, 5(3):95, 2011.

[45] Christopher Hahn, Zhaoyu Zhang, Anthony Fu, Cheng Hao Wu, Yun Jeong Hwang, Daniel J. Gargas, and Peidong Yang. Epitaxial growth of InGaN nanowire arrays for Light Emitting Diodes. *ACS Nano*, 5(5):3970, 2011.

[46] T. Kuykendall, P. Ulrich, S. Aloni, and P. Young. Complete composition tunability of InGaN nanowires using a combinatorial approach. *Nature Materials*, 6(12):951, 2007.

[47] J. Segura-Ruiz, Gema Martínez-Criado, M. H. Chu, C. Denker, J. J. Malindretos, and A. Rizzi. Synchrotron nanoimaging of single In-rich InGaN nanowires. *Journal of Applied Physics*, 113(13):136511, 2013.

[48] Y.-L. Lai, C.-P. Liu, Y.-H. Lin, T.-H. Hsueh, R.-M. Lin, D.-Y. Lyu, Z.-X. Peng, , and T.-Y. Lin. Origins of efficient green light emission in phase-separated InGaN quantum wells. *Nanotechnology*, 17(15):3734, 2006.

[49] O. Brandt, C. Pfüller, C. Chéze, L. Geelhaar, and H. Riechert. Sub-meV linewidth of excitonic luminescence in single GaN nanowires: direct evidence for surface excitons. *Physical Review B*, 81(4):045302, 2010.

[50] Ilaria Zardo, Gerhard Abstreiter, and Anna Fontcuberta i Morral. *Raman Spectroscopy on Semiconductor Nanowires - Nanowires*. INTECH, 2010.

[51] Leah Bergman and Jeanne L. McHale. *Handbook of Luminescent Semiconductor Materials*. Wiley, 2012.

[52] Alan H. Chin, Tai S. Ahn, Hongwei Li, Sreeram Vaddiraju, Christopher J. Bardeen, Cun-Zheng Ning, and Mahendra K. Sunkara. Photoluminescence of GaN nanowires of different crystallographic orientations. *Nano Letters*, 7(3):626, 2007.

[53] Shatendra K. Sharna. *X-Ray Spectroscopy*. INTECH, 2012.

[54] G. E. Ice, J. D. Budai, and J. W. L. Pang. The race to X-ray microbeam and nanobeam science. *Science*, 334(6060):1234, 2011.

[55] David B. Williams and C. Barry Carter. *Transmission Electron Microscopy - A text book for Material Science*. Springer, 2009.

[56] M. Gómez-Gómez, N. Garro, J. Segura-Ruiz, G. Martínez-Criado, M. H. Chu, A. Cantarero, C. Denker andJ. Malindretos, and A. Rizzi. Radial composition of single InGaN nanowires: a combined study by EDX, Raman spectroscopy, and X-ray diffraction. *physica status solidi (RRL)*, 7(10):864, 2013.

[57] Eric C. Le Ru and Pablo G. Etchegoin. Quantifying SERS enhancements. *MRS Bulletin*, 38(8):631, 2013.

[58] Bhavya Sharma, M. Fernanda Cardinal, Samuel L. Kleinman, Nathan G. Greeneltch, Renee R. Frontiera, Martin G. Blaber, George C. Schatz, and Richard P. Van Duyne. High-performance SERS substrates: Advances and challenges. *MRS Bulletin*, 38(08):615, 2013.

[59] G. Shan, L. Xu, G. Wang, and Y. Liu. Enhanced Raman scattering of ZnO quantum dots on silver colloids. *The Journal of Physical Chemistry C*, 111(8):3290, 2007.

[60] Arne Urban. Position-controlled selective area growth of Ga-polar GaN nanocolumns by molecular beam epitaxy: A versatile approach towards semipolar GaN and the characterisation of single nanocolumns. *PhD thesis, University of Göttingen*, 2013.

[61] M. Leszczynski, H. Teisseyre, T. Suski, I. Grzegory, M. Bockowski, J. Jun, S. Porowski, K. Pakula, J. M. Baranowski, C. T. Foxon, and T. S. Cheng. Lattice parameters of gallium nitride. *Applied Physics Letters*, 69(1):73, 1996.

[62] Ü. Özgür, Ya. I. Alivov, C. Liu, A. Teke, M. A. Reshchikov, S. Doğan, V. Avrutin, S.-J. Cho, and H. Morkoç. A comprehensive review of ZnO materials and devices. *Journal of Applied Physics*, 98(4):041301, 2005.

[63] R. Liu, A. Bell, F. A. Ponce, C. Q. Chen, J. W. Yang, and M. A. Khan. Luminescence from stacking faults in gallium nitride. *Applied Physics Letters*, 86(2):021908, 2005.

[64] P. P. Paskov, R. Schifano, B. Monemar, T. Paskova, S. Figge, and D. Hommel. Emission properties of a-plane GaN grown by metal-organic chemical-vapor deposition. *Journal of Applied Physics*, 98(9):093519, 2005.

[65] P. Corfdir, P. Lefebvre, J. Ristić, P. Valvin, E. Calleja, A. Trampert, J.-D. Ganiére, and B. Deveaud-Plédran. Time-resolved spectroscopy on GaN nanocolumns grown by plasma assisted molecular beam epitaxy on Si substrates. *Journal of Applied Physics*, 105(1):013113, 2009.

[66] S. C. Jain, M. Willander, J. Narayan, and R. Van Overstraeten. III-nitrides: Growth, characterization, and properties. *Journal of Applied Physics*, 87(3):965, 2000.

[67] *http://userweb.eng.gla.ac.uk/douglas.paul/SiGe/misfit.html.*

[68] H. Morkoç. *Handbook of nitride semiconductors and devices: materials, properties and growth.* Wiley, 2008.

[69] Charles Kittel. *Introduction to Solid State Physics.* Wiley, 1996.

[70] I. Vurgaftman and J.R. Meyer. Band parameters for nitrogen-containing semiconductors. *Journal of Applied Physics*, 94(6):3675, 2003.

[71] A. Polian, M. Grimsdtitch, and I. Grzegory. Elastic constants of gallium nitride. *Journal of Applied Physics*, 79(6):3343, 1996.

[72] Daniel Fritsch, Heidemarie Schmidt, and Marius Grundmann. Band-structure pseudopotential calculation of zinc-blende and wurtzite AlN, GaN, and InN. *Physical Review B*, 67(23):235205, 2003.

[73] G. Ramirez-Flores, H. Navarro-Contreras, A. Lastras-Martínez, R. C. Powell, and J. E. Greene. Temperature-dependent optical band gap of the metastable zinc-blende structure β-GaN. *Physical Review B*, 50(12):8433, 1994.

[74] B. E. Sernelius, K. F. Berggren, Z. C. Jin, I. Hamberg, and C. G. Granqvist. Band-gap tailoring of ZnO by means of heavy Al doping. *Physical Review B*, 37(17):10244, 1988.

[75] C. Stampfl and C. G. V. de Walle. Energetics and electronic structure of stacking faults in AlN, GaN, and InN. *Physical Review B*, 57(24):R15052, 1998.

[76] G. Salviati, M. Albrecht, C. Zanotti-Fregonara, N. Armani, M. Mayer, Y. Shreter, M. Guzzi, Yu V. Melnik, K. Vassilevski, V. A. Dmitriev, and H. P. Strunk. Cathodoluminescence and transmission electron microscopy study of the influence of crystal defects on optical transitions in GaN. *physica status solidi (a)*, 171(1):325, 1999.

[77] J. Wu, W. Walukiewicz, K. M. Yu, J. W. Ager III, E. E. Haller, Hai Lu, and William J. Schaff. Small band gap bowing in $In_{1-x}Ga_xN$ alloys. *Applied Physics Letters*, 80(25):4741, 2002.

[78] W. Walukiewicz, J. W. Ager III, K. M. Yu, Z. Liliental-Weber, J. Wu, S. X. Li, R. E. Jones, and J. D. Denlinger. Structure and electronic properties of InN and In-rich group III-nitride alloys. *Journal of Physics D: Applied Physics*, 39(5):R83, 2006.

[79] W Walukiewicz, S. X Li, J Wu, K. M Yu, J. W Ager III, E. E Haller, Hai Lu, and William J Schaff. Optical properties and electronic structure of InN and In-rich group III-nitride alloys. *Journal of Crystal Growth*, 269(1):119, 2004.

[80] K. G. Belyaev, M. V. Rakhlin, V. N. Jmerik, A. M. Mizerov, Ya. V. Kuznetsova, M. V. Zamoryanskaya, S. V. Ivanov, and A. A. Toropov. Phase separation in $In_xGa_{1-x}N$ ($0.10 < x < 0.40$). *physica status solidi C*, 10(3):527, 2013.

[81] J. Segura-Ruiz, G. Martínez-Criado, C. Denker, J. Malindretos, and A. Rizzi. Phase separation in single $In_xGa_{1-x}N$ nanowires revealed through a hard X-ray synchrotron nanoprobe. *Nano Letters*, 14(3):1300, 2014.

[82] R. D. King-Smith and D. Vanderbilt. Theory of polarization of crystalline solids. *Physical Review B*, 47(3):1651, 1993.

[83] F. Bernardini, V. Fiorentini, and D. Vanderbilt. Spontaneous polarization and piezoelectric constants of III-V nitrides. *Physical Review B*, 56(16):R10024, 1997.

[84] M. Grundmann. *The Physics of Semiconductors - An Introduction including Devices and Nanophysics*. Springer, 2006.

[85] F. Bernardini, V. Fiorentini, and D. Vanderbilt. Accurate calculation of polarization-related quantities in semiconductors. *Physical Review B*, 63(19):193201, 2001.

[86] T. Takeuchi, S. Sota, M. Katsuragawa, M. Kamari, Takeuchi H, H. Amano, and I. Akasaki. Quantum-confined Stark effect due to piezoelectric fields in GaInN strained quantum wells. *Japanese Journal of Applied Physics*, 36(4A):L382, 1997.

[87] J. S. Speck and S. F. Chichibu. Nonpolar and semipolar group III nitride-based materials. *MRS Bulletin*, 34(5):304, 2009.

[88] J. Renard, R. Songmuang, G. Tourbot, C. Bougerol, B. Daudin, and B. Gayral. Evidence for quantum-confined Stark effect in GaN/AlN quantum dots in nanowires. *Physical Review B*, 80(12):121305, 2009.

[89] Raffaella Calarco, Toma Stoica, Oliver Brandt, and Lutz Geelhaar. Surface-induced effects in GaN nanowires. *Journal of Materials Research*, 26(17):2157, 2011.

[90] H. Callen, E. Callen, and Z. Kalva. Crystal symmetry and macroscopic laws II. *American Journal of Physics*, 38(11):1278, 1970.

[91] Michael A. Stroscio and Mitra Dutta. *Phonons in nanostructures.* Cambridge, 2004.

[92] J. M. Zhang, T. Ruf, M. Cardona, O. Ambacher, M. Stutzmann, J. M. Wagner, and F. Bechstedt. Raman spectra of isotopic GaN. *Physical Review B*, 56(22):14399, 1997.

[93] H.-L. Liu, C.-C. Chen, C.-T. Chia, C.-C. Yeh, C.-H. Che, M.-Y. Yu, S. Keller, and S. P. DenBaars. Infrared and Raman-scattering in single crystalline GaN nanowires. *Chemical Physics Letters*, 345(3):241, 2001.

[94] Ramon Cuscó, Esther Alarcón-Lladó, Jordi Ibánez, Luis Artús, Juan Jiménez, Buguo Wang, and Michael J. Callahan. Temperature dependence of Raman scattering in ZnO. *Physical Review B*, 75(16):165202, 2007.

[95] H. Harima. Properties of GaN and related compounds studied by means of Raman scattering. *Journal of Physics: Condensed Matter*, 14(38):R967, 2002.

[96] Yaping Wu, Xian-Hua Zhang, Fuchun Xu, Lan-Sun Zheng, and Junyong Kang. A hierarchical lattice structure and formation mechanism of ZnO nano-tetrapods. *Nanotechnology*, 20(32):325709, 2009.

[97] V. Y. Davydov, A. A. Klochikhin, V. V. Emtsev, A. N. Smirnov, I. N. Goncharuk, A. V. Sakharov, D. A. Kurdyukov, M. V. Baidakova, V. A. Vekshin, S. V. Ivanov, J. Aderhold, J. Graul, A. Hashimoto, and A. Yamamoto. Photoluminescence and Raman study of hexagonal InN and In-rich InGaN alloys. *physica status solidi (b)*, 240(2):425, 2003.

[98] H. Grille, Ch. Schnittler, and F. Bechstedt. Phonons in ternary group-III nitride alloys. *Physical Review B*, 61(9):6091, 1988.

[99] J. M. Wagner and F. Bechstedt. Phonon deformation potentials of α-GaN and -AlN: An ab initio calculation. *Applied Physics Letters*, 77(3):346, 2000.

[100] F. Demangeot, J. Frandon, P. Baules, F. Natali, F. Semond, and J. Massies. Phonon deformation potentials in hexagonal GaN. *Physical Review B*, 69(15):155215, 2004.

[101] V. Y. Davydov, N. S. Averkiev, I. N. Goncharuk, D. K. Nelson, I. P. Nikitina, A. S. Polkovnokov, A. N. Smirnov, M. A. Jacobson, and O. K. Semchinova. Raman and photoluminescence studies of biaxial strain in GaN epitaxial layers grown on 6H-SiC. *Journal of Applied Physics*, 82(10):5097, 1997.

[102] Prasana Sahoo, A. K. Tyagi, Baldev Raj, and S. Dhara. *Surface Optical Modes in Semiconductor Nanowires.* Nanowires - Implementations and Applications, Dr. Abbass Hashim (Ed.), ISBN: 978-953-307-318-7, InTech, Available from: http://www.intechopen.com/books/nanowires-implementations-andapplications/surface-optical-modes-in-semiconductor-nanowires, 2011.

[103] Q. Xiong, J. Wang, O. Reese, L. C. Lew Yan Voon, and P. C. Eklund. Raman scattering from surface phonons in rectangular cross-sectional w-ZnS nanowires. *Nano Letters*, 4(10):1991, 2004.

[104] Michael A. Stroscio, K. W. Kim, Michael A. Littlejohn, and Hsuhung Chuang. Polarization eigenvectors of surface-optical phonon modes in a rectangular quantum wire. *Physical Review B*, 42(2):1488, 1990.

[105] A. R. Bhatt, K. W. Kim, M. A. Stroscio, G. J. Iafrate, Mitra Dutta, Harold L. Grubin, Reza Haque, and X. T. Zhu. Reduction of interface phonon modes using metal-semiconductor heterostructures. *Journal of Applied Physics*, 73(5):2338, 1993.

[106] R. Gupta, Q. Xiong, G. D. Mahan, and P. C. Eklund. Surface optical phonons in gallium phosphide nanowires. *Nano Letters*, 3(12):1745, 2003.

[107] Eric C. Le Ru and Pablo G. Etchegoin. *Principles of Surface-Enhanced Raman Spectroscopy.* Elsevier, 2009.

[108] Carlo Lamberti and Giovanni Agostini. *Characterisation of Semiconductor Heterostructures and Nanostructures.* Elsevier, 2013.

[109] Manuel Cardona and G. Güntherodt. *Light Scattering in Solids II.* Springer, 1982.

[110] Peter Y. Yu and Manuel Cardona. *Fundamentals of Semiconductors.* Springer, 1996.

[111] Jaime Segura-Ruiz. Electronic and vibrational states of InN and GaInN nanocolumns. *PhD thesis, University of Valencia*, 2009.

[112] W. Hayes and R. Loudon. *Scattering of Light by Crystals.* Wiley, 1978.

[113] H. Siegle, L. Eckey, A. Hoffmann, C. Thomsen, B.K. Meyer, D. Schikora, M. Hankeln, and K. Lischka. Quantitative determination of hexagonal minority phase in cubic GaN using Raman spectroscopy. *Solid State Communications*, 96(12):943, 1995.

[114] R. Loudon. The Raman effects in crystals. *Advances in Physics*, 50(7):813, 2001.

[115] M Fleishmann, P. J. Hendra, and A. J. McQuillan. Raman spectra of pyridine adsorbed at a silver electrode. *Chemical Physics Letters*, 26:163, 1974.

[116] D. L. Jeanmaire and R. P. Van Duyne. Surface Raman spectroelectrochemistry. *Journal of Electroanalytical Chemistry*, 84:1, 1977.

[117] M. G. Albrecht and J. A. Creighton. Anomalously intense Raman spectra of pyridine at a silver electrode. *Journal of the American Chemical Society*, 99(15):5215, 1977.

[118] N.J. Halas and M. Moskovits. Surface-enhanced Raman spectroscopy: Substrates and materials for research and applications. *MRS Bulletin*, 38(8):607, 2013.

[119] S. Nie and S. R. Emory. Probing single molecules and single nanoparticles by surface-enhanced Raman scattering. *Science*, 275(5303):1102–1106, 1997.

[120] Mark Fox. *Optical Properties of Solids.* OXFORD MASTER SERIES IN CONDENSED MATTER PHYSICS, 2013.

[121] Lukas Novotny and Bert Hecht. *Principles of Nano-optics.* Cambridge University Press, 2006.

[122] C. F. Bohren and D. R. Huffman. *Absorption and Scattering of Light by Small Particles.* Wiley-VCH, 1998.

[123] Michael Möller. Optical properties of III-V nanowires and their application for charge transport and single-photon emission. *PhD thesis, University of Valencia*, 2012.

[124] Giorgio Margaritondo. *Introduction to Synchrotron Radiation*. OXFORD UNIVERSITY PRESS, 1988.

[125] Manh-Hung Chu. Structural and chemical characterisation of single Co-implanted ZnO nanowires by a hard X-ray nanoprobe. *PhD thesis, University of Grenoble*, 2014.

[126] *http://www.esrf.eu/*.

[127] The staff of ESRF. *ESRF - Foundation Phase Report*. February 1987.

[128] Jens Als-Nielsen and Des McMorrow. *Elements of Modern X-Ray Physics*. John Wiley & Sons, 2001.

[129] V. A. Solé, M. Cotte, Ph. Water, and J. Susini. A multiplatform code for the analysis of energy-dispersive X-ray fluorescence spectra. *Spectrochimica Acta B*, 62(1):63, 2007.

[130] A. P. Hammersley, S. O. Svensson, M. Hanfland, A. N. Fitch, and D. Hüsermann. Two-dimensional detector software: From real detector to idealised image or two-theta scan. *High Pressure Research*, 14(4):235, 1996.

[131] *http://bruceravel.github.io/demeter/aug/index.html*.

[132] E Calleja, M. A. Sánchez-García, F. J. Sánchez, F. Calle, F. B. Naranjo, E Muñoz, U. Jahn, and K. Ploog. Luminescence properties and defects in GaN nanocolumns grown by molecular beam epitaxy. *Physical Review B.*, 62(24):16826, 2000.

[133] Raffaella Calarco, J. Ralph Meijers, Ratan K. Debnath, Toma Stoica, Eli Sutter, and Hans Lüth. Nucleation and growth of GaN nanowires on Si(111) performed by molecular beam epitaxy. *Nano Letters*, 7(8):2248, 2007.

[134] E.O. Schäfer-Nolte, T. Stoica, T. Gotschke, F. Limbach, E. Sutter, P. Sutter, and R. Calarco. Highly polarized Raman scattering anisotropy in single GaN nanowires. *Applied Physics Letters*, 96(9):091907, 2010.

[135] R. Koester, J S Hwang, C. Durand, D. Le Si Dang, and J. Eymery. Self-assembled growth of catalyst-free GaN wires by metal-organic vapour phase epitaxy. *Nanotechnology*, 21(1):015602, 2010.

[136] X. J. Chen, B. Gayral, D. Sam-Giao, C. Bougerol, C. Durand, and J. Eymery. Catalyst-free growth of high-optical quality GaN nanowires by metal-organic vapor phase epitaxy. *Applied Physics Letters*, 99(25):251910, 2011.

[137] S. D. Hersee, X. Sun, and X. Wang. The controlled growth of GaN nanowires. *Nano Letters*, 6(8):1808, 2006.

[138] H. Sekiguchi, K. Kishino, and A. Kikuchi. Ti-mask selective-area growth of GaN by RF-plasma-assisted molecular-beam epitaxy for fabricating regularly arranged InGaN/GaN nanocolumns. *Applied Physics Express*, 1(12):124002, 2008.

[139] Y. Nagae, T. Iwatsuki, Y. Shirai, Y. Osawa, S. Naritsuka, and T. Maruyama. Effect of mask material on selective growth of GaN by RF-MBE. *Journal of Crystal Growth*, 324(1):88, 2011.

[140] T. Gotschke, T. Schumann, F. Limbach, T. Stoica, and R. Calarco. Influence of the adatom diffusion on selective growth of GaN nanowire regular arrays. *Applied Physics Letters*, 98(10):103102, 2011.

[141] Shunfeng Li, Sönke Fündling, Xue Wang, Milena Erenburg, Mohamed Aid Mansur Al-Suleiman, Jiandong Wei, Werner Bergbauer, Martin Strassburg, Hergo-Heinrich Wehmann, and Andreas Waag. Selective area growth of GaN rod structures by MOVPE: Dependence on growth conditions. *physica status solidi (c)*, 8(7):2318, 2011.

[142] J. Jeganathan, R. K. Debnath, R. Meijers, T. Stoica, R. Calarco, D. Grützmacher, and H. Lüth. Raman scattering of phonon-plasmon modes in self-assembled GaN nanowires. *Journal of Applied Physics*, 105(12):123707, 2009.

[143] J. M. Calleja, S. Lazic, J. Sánchez-Paramo, F. Agullo-Rueda, J. Ristić L. Cerutti, S. Fernández-Garrido, M. A. Sánchez-García, J. Grandal, E. Calleja, A. Trampert, and U. Jahn. Inelastic light scattering spectroscopy of semiconductor nitride nanocolumns. *physica status solidi b*, 244(8):2838, 2007.

[144] D. Gogova, P. P. Petrov, M. Buegler, M. R. Wagner, C. Nenstiel, G. Callsen, M. Schmidbauer, R. Kucharski, M. Zajac, R. Dwilinski, M. R. Phillips, A. Hoffmann, and R. Fornariv. Structural and optical investigation of non-polar (1-100) GaN grown by the ammonothermal method. *Journal of Applied Physics*, 113(20):203513, 2013.

[145] T. B. Jenichen, O. Brandt, C Pfüller, P. Dogan, M. Knelangen, and A. Trampert. Macro- and micro-strain in GaN nanowires on Si(111). *Nanotechnology*, 22(29):295714, 2011.

[146] S. Fernández-Garrido, V. M. Kaganer, C. Hauswald, B. Jenichen, M. Ramsteiner, V. Consonni, L. Geelhaar, and O. Brandt. Correlation between the structural and optical properties of spontaneously formed GaN nanowires: a quantitative evaluation of the impact of nanowire coalescence. *Nanotechnology*, 25(45):455702, 2014.

[147] P. Corfdir, P. Lefebvre, J. Levrat, D. Dussaigne, J.-D. Ganère, D. Martin, J. Ristić, T. Zhu, N. Grandjean, and B. Deveaud-Plédran. Exciton localisation on basal stacking faults in a-plane epitaxial lateral overgrown GaN grown by hybrid vapor epitaxy. *Journal of Applied Physics*, 105(4):043102, 2009.

[148] Jonas Länhemann, Oliver Brandt, Uwe Jahn, Carsten Pfüller, Claudia Roder, Pinar Dogan, Frank Grosse, Abderrezak Belabbes, Friedhelm Bechstedt, Achim Trampert, and Lutz Geelhaar. Direct experimental determination of the spontaneous polarization of GaN. *Physical Review B*, 86(8):081302(R), 2012.

[149] Ingo Tischer, Martin Feneberg, Martin Schirra, Hady Yacoub, Rolf Sauer, Klaus Thonke, Thomas Wunderer, and Ferdinand Scholz. I_2 basal plane stacking fault in GaN: Origin of the 3.32 eV luminescence band. *Physical Review B*, 83(3):035314, 2011.

[150] G. Jacopin, L. Rigutti, L. Largeau, F. Fortuna, F. Furtmayr, F. H. Julien, M. Eickhoff, and M. Tchernycheva. Optical properties of wurtzite/zinc-blende heterostructures in GaN nanowires. *Journal of Applied Physics*, 110(6):064313, 2011.

[151] M. Leroux, N. Grandjean, B. Beaumont, G. Nataf, F. Semond, J. Massies, and P. Gibart. Temperature quenching of photoluminescence intensities in undoped and doped GaN. *Journal of Applied Physics*, 86(7):3721, 1999.

[152] L. Cerutti, J. Ristić, S. Fernández-Garrido, E. Calleja, A. Trampert, K. H. Ploog, S. Lazic, and J. M. Calleja. Wurtzite GaN nanocolumns grown on Si(001) by molecular beam epitaxy. *Applied Physics Letters*, 88(21):213114, 2006.

[153] D. Hersee, A. K. Rishinaramangalam, M. N. Fairchild, L. Zhang, and P. Varangis. Threading defect elimination in GaN nanowires. *Journal of Materials Research*, 26(17):2293, 2011.

[154] Ayan Kar, Dimitri Alexson, Mitra Dutta, and Michael A. Stroscio. Evidence of compositional inhomogeneity in $In_xGa_{1-x}N$ alloys using ultraviolet and visible Raman spectroscopy. *Journal of Applied Physics*, 104:073502, 2008.

[155] H. J. Xiang, Su-Huai Wei, Juarez L. F. Da Silva, , and Jingbo Li2. Strain relaxation and band-gap tunability in ternary $In_xGa_{1-x}N$ nanowires. *Physical Review B.*, 78(19):193301, 2008.

[156] F. Scholz. Semipolar GaN grown on foreign substrates: a review. *Semiconductor Science and Technology*, 27(2):024002, 2012.

[157] Robert Koester, Jun-Seok Hwang, Damien Salomon, Xiaojun Chen, Catherine Bougerol, Jean-Paul Barnes, Daniel Le Si Dang, Lorenzo Rigutti, Andres de Luna Bugallo, Gwénolé Jacopin, Maria Tchernycheva, Christophe Durand, and Joël Eymery. M-plane core-shell InGaN/GaN multiple-quantum-wells on GaN wires for electroluminescent devices. *Nano Letters*, 11(11):4839, 2011.

[158] G. Tourbot, C. Bougerol, A. Grenier, M. Den Hertog, D. Sam-Giao, D. Cooper, P. Gilet, B. Gayral, and B Daudin. Structural and optical properties of InGaN/GaN nanowire heterostructures grown by PA-MBE. *Nanotechnology*, 22(7):075601, 2011.

[159] Yong-Ho Ra, Rangaswamy Navamathavan, Hee-Il Yoo, and Cheul-Ro Lee. Single nanowire Light-Emitting Diodes using uniaxial and coaxial InGaN/GaN multiple quantum wells synthesized by metalorganic chemical vapor deposition. *Nano Letters*, 14(3):1537, 2014.

[160] A. Y. Polyakov, N. B. Smirnov, A. V. Govorkov, H. Aamano, S. J. Pearton, I.-H. Lee, Q. Sun, J. Han, and S. Y. Karpov. Role of nonradiative recombination centers and extended defects in nonpolar GaN on light emission efficiency. *Applied Physics Letters*, 98(7):072104, 2011.

[161] M. Keplinger, T. Martensson, J. Stangl, E. Wintersberger, B. Mandl, D. Kriegner, V. Holy, G. Bauer, K. Deppert, and L. Samuelson. Structural investigations of core-shell nanowires using grazing incidence X-ray diffraction. *Nano Letters*, 9(5):1877, 2009.

[162] M. Heiss, B. Ketterer, E. Uccelli, J. R. Morante, J. Arbiol, and A. Fontcuberta i Morral. In(Ga)As quantum dot formation on group-III assisted catalyst-free InGaAs nanowires. *Nanotechnolgy.*, 22(19):195601, 2011.

[163] Jing Zhang and Nelson Tansu. Improvement in spontaneous emission rates for InGaN quantum wells on ternary InGaN substrate for light-emitting diodes. *Journal of Applied Physics*, 110(11):113110, 2011.

[164] Qiming Li and George T. Wang. Strain influenced indium composition distribution in GaN/InGaN core-shell nanowires. *Applied Physics Letters*, 97(18):181107, 2010.

[165] F. Limbach, T. Gotschke, T. Stoica, R. Calarco, E. Sutter, J. Ciston, R. Cusco , L. Artus, S. Kremling, S. Höfling, L. Worschech, and D. Grützmacher. Structural and optical properties of InGaN-GaN nanowire heterostructures grown by molecular beam epitaxy. *Journal of Applied Physics*, 109(1):014309, 2011.

[166] Gerald B. Stringfellow. *ORGANOMETALLIC VAPOR PHASE EPITAXY - Theory and Practice*. Academic Press, 1999.

[167] Duc V. Dinh. MOVPE growth of InN and InGaN with different surface orientations. *PhD thesis, University of Berlin*, 2012.

[168] V. G. Dubrovskii, N. V. Sibirev, J. C. Harmand, and F. Glas. Growth kinetics and crystal structure of semiconductor nanowires. *Physical Review B*, 78(23):235301, 2008.

[169] Hannah J. Joyce, Qiang Gao, H. Hoe Tan, C. Jagadish, Yong Kim, Jin Zou, Leigh M. Smith, Howard E. Jackson, Jan M. Yarrison-Rice, Patrick Parkinson, and Michael B. Johnston. III-V semiconductor nanowires for optoelectronic device applications. *Progress in Quantum Electronics*, 35(2):23, 2011.

[170] M. Gómez-Gómez, J. Segura-Ruiz N. Garro, G. Martinez-Criado, A. Cantarero, H. T. Mengistu, A. García-Cristóbal, S Murcia-Mascarós, C. Denker, J. Malindretos, and A. Rizzi. Spontaneous core-shell elemental distribution in In-rich $In_xGa_{1-x}N$ nanowires grown by molecular beam epitaxy. *Nanotechnology*, 25(7):075705, 2014.

[171] *http://www.ccp14.ac.uk/tutorial/powdcell.*

[172] I. Shalish, L. Kronik, G. Segal, Y. Rosenwaks, Yoram Shapira, U. Tisch, and J. Salzman. Yellow luminescence and related deep levels in unintentionally doped GaN films. *Physical Review B*, 59(15):9748, 1999.

[173] *http://www.comsol.com/comsol-multiphysics.*

[174] H. T. Mengistu and A. Garcia-Cristóbal. Generalised plane strain problem: application to heterostructure nanowires. In *Proceeding Iberian COMSOL Multiphysics Conference*, page 94, Málaga, 2014.

[175] Christy L. Haynes, Adam D. McFarland, and Richard P. Van Duyne. Surface-enhanced Raman spectroscopy. *Analytical Chemistry*, 77(17):338A, 2005.

[176] Cosmin Farcau Monica Potara, Monica Baia and Simion Astilean. Chitosan-coated anisotropic silver nanoparticles as a SERS substrate for single-molecule detection. *Nanotechnology*, 23(5):055501, 2012.

[177] M. K. Khaing Oo, C. F. Chang, Y. Sun, and X. Fan. Rapid, sensitive DNT vapor detection with UV-assisted photo-chemically synthesized gold nanoparticle SERS substrates. *Analyst*, 136:2811, 2011.

[178] Y. Zhang, Z. Wang, L. Wu, Y Pei, P. Chen, and Y. Cui. Rapid simultaneous detection of multi-pesticide residues on apple using SERS technique. *Analyst*, 139:5148, 2014.

[179] M. Sanles-Sobrido, L. Rodriguez-Lorenzo, S. Lorenzo-Abalde, A. Gonzalez-Fernandez, M. A. Correa-Duarte, R.A. Alvarez-Puebla, and L. M. Liz-Marzan. Label-free SERS detection of relevant bioanalytes on silver-coated carbon nanotubes: The case of cocaine. *Nanoscale*, 1(1):153, 2009.

[180] A. Cros. Vibrational properties of semiconductor nanowires and nanowire heterostructures: ensembles and single nanowires. *physica status solidi (RRL)*, 7(10):727, 2013.

[181] A. G. Milekhin, R. J. Meijers, T. Richter, R. Calarco, S. Montanari, H. Lüth, B. A. Paez Sierra, and D. R. T. Zahn. Raman scattering study of GaN nanostructures obtained by bottom-up and top-down approaches. *Journal of Physics: Condensed Matter*, 18(26):5825, 2006.

[182] A. G. Milekhin, N. A. Yeryukov, L. L. Sveshnikova, T. A. Duda, E. I. Zenkevich, S. S. Kosolobov, A. V. Latyshev, C. Himcinski, N. V. Surovtsev, S. V. Adichtchev, Zhe Chuan Feng, Chia Cheng Wu, Dong Sing Wuu, and D. R. T. Zahn. Surface enhanced Raman scattering of light by ZnO nanostructures. *Journal of Experimental and Theoretical Physics*, 113(6):983, 2011.

[183] Anna Rumyantseva, Sergey Kostcheev, Pierre-Michel Adam, Sergey V. Gaponenko, Svetlana V. Vaschenko, Olga S. Kulakovich, Andrey A. Ramanenka, Dmitry V. Guzatov, Dmytro Korbutyak, Volodymyr Dzhagan, Alexander Stroyuk, and Vitaliy Shvalagin. Nonresonant surface-enhanced Raman scattering of ZnO quantum dots with Au and Ag nanoparticles. *ACS Nano*, 7(4):3420, 2013.

[184] Z. Peng, H. Hu, M. I. B. Utama, L. M. Wong, K. Ghosh, R. Chen, S. Wang, Z. Shen, and Q. Xiong. Heteroepitaxial decoration of Ag nanoparticles on Si nanowires: A case study on Raman scattering and mapping. *Nano Letters*, 10(10):3940, 2010.

[185] R. Chen, D. Li, H. Hu, Y. Zhao, Y. Wang, N. Wong, S. Wang, Y. Zhang, J. Hu, Z. Shen, and Q. Xiong. Tailoring optical properties of silicon nanowires by Au nanostructure decorations: enhanced Raman scattering and photodetection. *The Journal of Physical Chemistry C*, 116(7):4416, 2012.

[186] Zhang Liu Wang. ZnO nanowire and nanobelt platform for nanotechnology. *Material Science and Engineering R*, 64(3):33, 2009.

[187] C. Soci, A. Zhang, B. Xiang, S. A. Dayeh, D. P. R. Aplin, J. Park, X. Y. Bao, Y. H. Lo, and D. Wang. ZnO nanowire UV photodetectors with high internal gain. *Nano Letters*, 7(4):1003, 2007.

[188] A. B. Djurišić, A. M. C. Ng, and X. Y. Chen. ZnO nanostructures for optoelectronics: Material properties and device applications. *Progress in Quantum Electronics*, 34(4):191, 2010.

[189] Tz-Jun Kuo, Chun-Neng Lin, Chi-Liang Kuo, and Michael H. Huang. Growth of ultralong ZnO nanowires on silicon substrates by vapor transport and their use as recyclable photocatalysts. *Chemistry of Materials*, 19(21):5143, 2007.

[190] Babak Nikoobakht and Mostafa A. El-Sayed. Preparation and growth mechanism of gold nanorods (NRs) using seed-mediated growth method. *Chemistry of Materials*, 15(10):1957, 2003.

[191] Andrea Pescaglini. Au nanorods-semiconductor nanowire hybrid nanostructures: Nanofabrication techniques and optoelectronic properties. *PhD thesis, University College of Cork*, 2014.

[192] R. Kattumenu, C. H. Lee, L. Tian, M. E. McConney, and S. Singamaneni. Nanorod decorated nanowires as highly efficient SERS-active hybrids. *Journal of Materials Chemistry*, 21(39):15218, 2011.

[193] S. Y. Sayed, F. Wang, M. Malac, A. Meldrum, R. F. Egerton, and J. M. Buriak. Heteroepitaxial growth of gold nanostructures on silicon by galvanic displacement. *ACS Nano*, 3(9):2809, 2009.

[194] S. Deng, H. M. Fan, X. Zhang, K. P. Loh, C. L. Cheng, C. H. Sow, and Y. L. Foo. An effective surface-enhanced Raman scattering template based on a Ag nanocluster-ZnO nanowire array. *Nanotechnology*, 20(17):175705, 2009.

[195] Babak Nikoobakht, Jianping Wang, and Mostafa A. El-Sayed. Surface-enhanced Raman scattering of molecules adsorbed on gold nanorods: off-surface plasmon resonance condition. *Chemical Physics Letters*, 366:17, 2002.

[196] K. Kalyanasundaram and J. K. Thomas. The conformational state of surfactants in the solid state and in micellar form. A laser-excited Raman scattering study. *The Journal of Physical Chemistry*, 80(13):1462, 1976.

[197] Benedetto Bozzini, Lucia D'Urzo, Marilena Re, and Federica Riccardis. Electrodeposition of Cu from acidic sulphate solutions containing cetyltrimethylammonium bromide (CTAB). *Journal of Applied Electrochemistry*, 8:1561, 2008.

[198] Jian Feng Li, Yi Fan Huang, Yong Ding, Zhi Lin Yang, Song Bo Li, Xiao Shun Zhou, Feng Ru Fan, Wei Zhang, Zhi You Zhou, and

De YinWu. Shell-isolated nanoparticle-enhanced Raman spectroscopy. *Nature*, 464(7287):392, 2010.

[199] Chenxu Yu, Leo Varghese, and Joseph Irudayaraj. Surface modification of cetyltrimethylammonium bromide-capped gold nanorods to make molecular probes. *Langmuir*, 23(17):9114, 2007.